



MONASH University

**Improved QCD Calculations and
Phenomenological Studies at the Large
Hadron Collider**

Nadine Fischer

B.Sc., M.Sc.

A thesis submitted for the degree of Doctor of Philosophy
at Monash University in 2017

School of Physics and Astronomy

Copyright notices

Notice 1

Under the Copyright Act 1968, this thesis must be used only under the normal conditions of scholarly fair dealing. In particular no results or conclusions should be extracted from it, nor should it be copied or closely paraphrased in whole or in part without the written consent of the author. Proper written acknowledgement should be made for any assistance obtained from this thesis.

Notice 2

I certify that I have made all reasonable efforts to secure copyright permissions for third-party content included in this thesis and have not knowingly added copyright content to my work without the owner's permission.

Contents

Abstract	i
List of research outputs	iii
Declaration	v
Additional Publications	vii
Acknowledgements	ix
1 Introduction	1
2 Quantum Chromodynamics and the Standard Model	5
2.1 Quantum Chromodynamics	5
2.2 Asymptotic Freedom and Confinement	7
2.3 Standard Model	8
2.4 Cross Sections and Matrix Elements	11
3 Monte Carlo Event Generators	15
3.1 Hard Process	15
3.2 Multi-Parton Interactions	16
3.3 Parton Shower	16
3.3.1 Parton Branching in the Collinear Limit	17
3.3.2 Coherent Branching	19
3.3.3 The Antenna Model for Shower Algorithms	21
3.3.4 The CS-Dipole Model for Shower Algorithms	22
3.3.5 Constructing the Algorithm	22
3.4 Combining Matrix Elements and Parton Showers	25
3.5 Hadronization Models	27
4 Antenna Showers and Matrix-Element Corrections	31
4.1 Published Material	32
4.2 The Shower Algorithm	80
4.3 Initial-Initial Antennae	81
4.4 Initial-Final Antennae	87

5	Correcting Ordered Showers	93
5.1	Published Material	94
5.2	CKKW-L Merging	112
6	Helicity Antenna Showers	115
6.1	Published Material	116
6.2	Helicity-Dependent Antenna Functions from DGLAP Limits	142
6.2.1	Initial-Final Antennae: Initial-State Side	143
6.2.2	Initial-Final Antennae: Final-State Side	145
6.2.3	Initial-Initial Antennae	147
6.2.4	Summary	148
7	A Trip into Fragmentation	151
7.1	Published Material	152
8	Summary and Conclusions	197
	Bibliography	201

Abstract

The particle-physics experiments at the Large Hadron Collider at CERN have entered the second long phase of data collection. Consequently, the precision of measurements rises, as does the demand for accurate and fast tools to provide theory predictions to accompany the decreasing experimental uncertainties. Monte Carlo event generators make use of random numbers to simulate realistic final states of high-energy collider experiments, making them a crucial tool to extract conclusions from experimental measurements, to analyze data, or provide comparisons between theoretical calculations and data.

This thesis focuses on new models and improvement strategies for different parts of such simulations. A very important element of the event generation is the parton shower, which models the cascade of bremsstrahlung radiation emerging in collider events. The parton shower resums effects of higher-order corrections by using approximations to radiation patterns. Different approaches exist for improving the shower approximation with perturbatively calculable transition probabilities. The ansatz used in this thesis corrects the functions driving the radiation in the parton shower by applying a correction factor based on transition probabilities and the radiation functions themselves. The rather simple correction algorithm is subsequently improved, making it more complex, but allowing more control over the calculation and an improved data description. The correction process constitutes a fairly large fraction of the computing time in the simulation of event generators. To speed up the correction, a particle property called helicity is used, which is normally not touched in the event generation. By assigning explicit helicities to particles in the parton shower, the time needed for the correcting the parton-shower approximation is decreased.

The fragmentation step in the event generation transforms the elementary particles into hadrons, composite objects observed in the experiments. A new model for obtaining the momentum of hadrons is developed, based on thermodynamical considerations. Additions to the fragmentation increase the flexibility of the model even further. A confrontation of the new model with data shows potential improvements and weaknesses, compared to the conventional model.

List of research outputs

1. Nadine Fischer, Stefan Prestel, Mathias Ritzmann, and Peter Skands, *Vincia for Hadron Colliders*, *Eur. Phys. J. C* **76** (2016), no. 11 589, doi:10.1140/epjc/s10052-016-4429-6, arXiv:1605.06142 [hep-ph]
2. Nadine Fischer and Torbjörn Sjöstrand, *Thermodynamical String Fragmentation*, *JHEP* **01** (2017) 140, doi:10.1007/JHEP01(2017)140, arXiv:1610.09818 [hep-ph]
3. Nadine Fischer and Stefan Prestel, *Combining states without scale hierarchies with ordered parton showers*, *Eur. Phys. J. C* **77** (2017) no. 9 601, doi:10.1140/epjc/s10052-017-5160-7, arXiv:1706.06218 [hep-ph]
4. Nadine Fischer, Andrew Lifson, and Peter Skands, *Helicity Antenna Showers for Hadron Colliders*, *Eur. Phys. J. C* **77** (2017) no. 10 719, doi:10.1140/epjc/s10052-017-5306-7, arXiv:1708.01736 [hep-ph]

Declaration

Declaration for thesis based or partially based on conjointly published or unpublished work

I hereby declare that this thesis contains no material which has been accepted for the award of any other degree or diploma at any university or equivalent institution and that, to the best of my knowledge and belief, this thesis contains no material previously published or written by another person, except where due reference is made in the text of the thesis.

This thesis includes three original papers published in peer reviewed journals and one submitted publication. The core theme of the thesis is the improvement and development of Monte Carlo event generators for high-energy collisions. The ideas, development and writing up of all the papers in the thesis were the principal responsibility of myself, the student, working within the School of Physics and Astronomy under the supervision of Peter Skands.

The inclusion of co-authors reflects the fact that the work came from active collaboration between researchers and acknowledges input into team-based research.

My contribution to each of the included works is declared below.

Publication Title: *Vincia for Hadron Colliders*

(Status: Published, Thesis Chapter 4)

Nature and % of student contribution

Calculated the phase-space factorization, kinematic maps, and other ingredients for ISR. Wrote the code implementation of the shower and MECs, included the LHC matrix elements. Produced the MEC plots and LHC results. Contributed to the write-up. 70%

Nature and % of co-author's contribution

- 1) Stefan Prestel: Contributed to discussions. Contributed to the write-up. 7%
 - 2) Mathias Ritzmann: Original work. Contributed to the write-up. 3%
 - 3) Peter Skands: Original work. Contributed to discussions. Responsible for the tuning and LEP results. Contributed to the write-up. 20%
-

Publication Title: *Thermodynamical String Fragmentation*
(Status: Published, Thesis Chapter 7)

Nature and % of student contribution
Wrote the code implementation and analyses. Performed the phenomenological study and produced the results. Contributed to the write-up. 70%

Nature and % of co-author's contribution
1) Torbjörn Sjöstrand: Developed the ideas. Contributed to discussions. Cross-checked the code. Contributed to the write-up. 30%

Publication Title: *Combining states without scale hierarchies with ordered parton showers*
(Status: Published, Thesis Chapter 5)

Nature and % of student contribution
Developed the ideas. Implemented the relevant code. Performed the validation. Produced the results. Contributed to the write-up. 70%

Nature and % of co-author's contribution
1) Stefan Prestel: Developed the ideas. Contributed to discussions. Implemented code for cross-checks. Contributed to the write-up. 30%

Publication Title: *Helicity Antenna Showers for Hadron Colliders*
(Status: Published (October 29, 2017), Thesis Chapter 6)

Nature and % of student contribution
Calculated, implemented, and validated the IS helicity antenna functions. Added helicity dependence to IS shower, MECs code, and matrix elements. Implemented the uncertainty bands code. Wrote the analysis and produced the results. Contributed to the write-up. 50%

Nature and % of co-author's contribution
1) Andrew Lifson* : Calculated, implemented, and validated the MHV amplitudes. Implemented the polarizer function. Contributed to the write-up. 30%
2) Peter Skands: Recalculated and reimplemented the IS helicity antenna functions. Performed the speed comparison Contributed to the write-up. 20%

* marks co-author's who were Monash students while part of the work was undertaken

I have not renumbered sections of submitted or published papers.

Student signature:



Date: September 21, 2017

The undersigned hereby certify that the above declaration correctly reflects the nature and extent of the student's and co-authors' contributions to this work. In instances where I am not the responsible author I have consulted with the responsible author to agree on the respective contributions of the authors.

Main Supervisor signature:



Date: September 21, 2017

Additional Publications

The following papers were published during the candidature, but are not part of the thesis.

Measurement of observables sensitive to coherence effects in hadronic Z decays with the OPAL detector at LEP

Nadine Fischer, Stefan Gieseke, Stefan Kluth, Simon Plätzer, Peter Skands, and the OPAL collaboration

Published in The European Physics Journal C 75 no. 12 (2015) 571

Herwig 7.0/Herwig++ 3.0 release note

Johannes Bellm, Stefan Gieseke, David Grellscheid, Simon Plätzer, Michael Rauch, Christian Reuschle, Peter Richardson, Peter Schichtel, Michael Seymour, Andrzej Siodmok, Alexandra Wilcock, Nadine Fischer, Marco Harrendorf, Graeme Nail, Andreas Papaefstathiou, and Daniel Rauch

Published in The European Physics Journal C 76 no. 4 (2016) 196

All proceedings from conferences, that took place during the candidature, are listed below (* marks the speaker).

Measurement of observables sensitive to coherence effects in hadronic Z decays with the OPAL detector at LEP

Nadine Fischer, Stefan Gieseke, Stefan Kluth, Simon Plätzer, Peter Skands, and Andrii Verbytskyi*

Conference proceedings in PoS EPS-HEP2015 (2015) 469

Coherent Showers for the LHC

Nadine Fischer* and Peter Skands

Conference proceedings in PoS RADCOR2015 (2015) 016

NLO efforts in Herwig++

Christian Reuschle*, Johannes Bellm, Stefan Gieseke, David Grellscheid, Simon Plätzer, Michael Rauch, Peter Richardson, Peter Schichtel, Michael Seymour, Andrzej Siodmok, Alexandra Wilcock, Nadine Fischer, Marco Harrendorf, Graeme Nail, Andreas Papaefstathiou, and Daniel Rauch

Conference proceedings in PoS RADCOR2015 (2015) 050

Measurement of parton shower observables with OPAL

Nadine Fischer, Stefan Gieseke, Stefan Kluth*, Simon Plätzer, Peter Skands, and the OPAL collaboration

Conference proceedings in EPJ Web Conf. 120 (2016) 05001

The Vincia Antenna Shower for Hadron Colliders

Peter Skands*, Nadine Fischer, Stefan Prestel, and Mathias Ritzmann

Conference proceedings in PoS ICHEP2016 (2016) 596

Acknowledgements

First of all, I acknowledge my supervisor Peter Skands for giving me the possibility to perform my PhD studies in his group at Monash University. During the last years, I learned a lot from him. I am thankful for his supervision, help, and support throughout my PhD and for his feedback on my thesis. I appreciate that he gave me the possibility to visit summer schools in Puri and Pittsburgh and to present my work at workshops and conferences. Furthermore, I am very grateful for the freedom to go on research trips to SLAC and to do a research project in Sweden for half a year as part of my PhD studies. I am also thankful to Michael Morgan for taking over the role as my second supervisor.

I thank the Monash University for the financial support through the Monash Graduate and Monash International Postgraduate Research Scholarship, as well as the J.L. William Scholarship from the School of Physics and Astronomy. On that note I gratefully acknowledge the financial support through CoEPP for the various travels during my candidature. I further thank the School of Physics and Astronomy and its staff for the support, in particular Jean Pettigrew, Karen Lee, and Catherine Buchanan who have been wonderful and very helpful with bureaucratic matters.

Many thanks to Stefan Prestel for the collaboration and the numerous discussions from which I learned a lot. I very much appreciate that you told me all about merging and helped me through the jungle of `Merging.cc`, `MergingHooks.cc`, and `History.cc`. Thank you so much for your constant support and help with the many smaller and larger problems during the last years.

A special thank you to Torbjörn Sjöstrand who supervised my MCnet project in Lund and always had time for discussions. Thank you for teaching me about fragmentation, for a very pleasant collaboration, and for making my time in Lund so enjoyable. I am also grateful for the many opportunities to go to conferences and to give talks during that time. Related to that, I would like to thank MCnet for providing the financial support through the short-term studentship.

For proofreading parts of the thesis I would like to thank Cody, Stefan, and Vaishali.

I would also like to thank my friends. The ones I know for many years now. The ones from study times in Karlsruhe, especially for keeping in touch or even visiting me so far away. And finally, the new ones I met in Melbourne and Lund. In partic-

ular, I thank Vaishali and Giancarlo for bearing all of my moods and still being my friends.

Ein großes Dankeschön geht an meine Eltern und meine Schwester für die jahrelange Unterstützung während Studium und Promotion, die vielen Skype-Gespräche und die Besuche in Lund und Melbourne. Ich bin sehr dankbar für meine Familie, die alte und die neue, und dass ich immer auf euch zählen kann.

Das wichtigste zum Schluss: Stefan, ohne Dich hätte ich diese Zeit nicht durchgestanden. Ich bin Dir unendlich dankbar für Deine Ermutigung, Unterstützung, Aufmerksamkeit, den Hopfentag und die vielen anderen wundervollen Momente, die wir zusammen verbracht haben, obwohl uns so viele Kilometer getrennt haben. Aber jetzt ist es endlich soweit: auf geht's in unser gemeinsames Leben!

Introduction

Particle physicists study the smallest, fundamental building blocks of nature and the forces that act between them. Classical mechanics uses physical laws to describe the motion of macroscopic objects and how they interact under the influence of forces. However, it reaches the limits of validity for very small resolution measures, that is if high velocities close to the speed of light are reached at short-distance scales such as the radius of an atomic nucleus. Much like a microscope would be used instead of the human eye to resolve small structures, quantum field theory comes into play at small resolutions to replace classical mechanics. It provides a theoretical framework for the construction of models that describe subatomic particles and their movement and interactions. In quantum field theory, particles are represented by fields, similar to how the photon is the quantum manifestation of the electromagnetic field.

The *Standard Model of particle physics* is the very elegant and fascinating quantum field theory which describes all currently known elementary particles and their interactions. It has been very successful at describing a large range of quantities measured by particle physics experiments and is therefore well established by now. The discovery of the last missing piece of the Standard Model, the so-called Higgs particle, was announced in July 2012 by ATLAS [1] and CMS [2], two experiments of the Large Hadron Collider, or LHC in short. The LHC at CERN in Geneva is the world's largest and most powerful particle collider and allows physicists to explore the highest energies and smallest distances ever probed in a laboratory setting. Two high-energy proton beams are accelerated until their velocities are close to the speed of light before they are brought together to collide. The LHC is part of a whole series of *high-energy colliders* that investigate the collision between protons and (anti)protons, electrons and positrons or protons and electrons at various energies. Following fundamental laws of nature, other particles can be created from the energy provided by the colliding objects. These newly created outgoing particles can themselves be initiators for the production of additional particles through decays or emission. Following the collision, detectors make use of the knowledge how different particles behave in the LHC's electromagnetic fields or interact with surrounding matter to identify particles and measure quantities such as their energy. The information is then analyzed and the result can be compared to expectations based on theoretical considerations.

The energy of the incoming beams at the LHC is high enough to resolve the substructure of the proton, whose constituents are quarks, antiquarks, and gluons, collectively referred to as *partons*. The theory describing the partons is called *strong force* or *Quantum Chromodynamics*, QCD in short. Just as in electromagnetism, in QCD there is a fundamental charge that the partons carry, called colour, with anti-colour being the equivalent to a negative electric charge. However, unlike in electromagnetism, three different kinds of this colour-charge exist. The accelerated colour-charges involved in the collision initiate a cascade of additional radiation, similar to the concept of *bremsstrahlung*. During the cascade, quarks and antiquarks can emit gluons, gluons can split into quark-antiquark pairs, and gluons can emit other gluons. This last process is one of the properties that makes QCD truly different from Quantum Electrodynamics, where photons do not interact directly among themselves. This is caused by photons being electrically neutral, whereas gluons do carry charges of the strong force. Another discriminating property is the observation that the potential energy increases with larger distances between colour- and anti-colour-charges. As a consequence, partons are never observed as free states in nature, but rather manifest themselves as bound states, the *hadrons*, which contain either two or three quarks. Hadrons are observed as collimated sprays of particles, called *jets*. As a wide range of physics analyses uses jets, the description of their properties and substructure with high precision is an important task.

Key players in the particle-physics community are *Monte Carlo event generators* for high-energy collisions, which make repeated use of random numbers to obtain numerical results. The primary goal of event generators is to provide an as detailed and precise picture as possible of the complete final-state dynamics. In other words, they attempt to simulate entire collider events from the incoming particles down to the observed hadrons. The lack of analytic solutions to describe the complex high-energy particle collisions requires the simulation to be factorized into different steps. The so-called *hard process* is the calculation of the transition probability for the basic, short-distance scattering. It is based on fixed-order perturbation theory, folded with the probability for finding a parton inside the proton. As discussed previously, additional radiation is produced by the incoming and, if present, outgoing partons of the hard process. The requirement for this *parton shower* is the probabilistic description of QCD *bremsstrahlung*. The radiation patterns follow simple, iteratively applied functions that approximate transition probabilities by describing the radiation without explicitly taking into account the underlying hard process. Parton showers are formulated as an evolution from short to long distances, originally based on evolution equations for single partons [3–5]. Most modern parton showers are based on the dipole-antenna picture of QCD [6–11], where multiparton states are regarded as composed of charge-anticharge pairs rather than a set of (unconnected) charges and anticharges. After the showering, the coloured par-

tons are transformed into primary hadrons, which may then decay further. This *hadronization* or *fragmentation* can not be calculated from first principles. Different QCD-inspired phenomenological models are used to describe the process, with the *string* and *cluster model* being the most common ones [12–14].

In nature, the outgoing particles at the end of the collision interact with the detector, producing even more particles. Therefore, Monte Carlo events can be processed through a detector simulation for comparisons to data. As this is a rather computationally expensive task, the usual procedure is to correct the measurements for detector effects, allowing a direct comparison between the corrected data and event generator output. This comparison makes event generators crucial for the theoretical understanding of collider physics and builds the link between experiments and theoretical calculations. Besides investigating the Standard Model and particularly the strong force, the information provided by event generators can also be used in searches for new physics. Event generators can supply an accurate modelling of potential new particles and the respective backgrounds needed to disentangle the new-physics signals from Standard-Model-initiated ones. Faster and more precise tools to provide theoretical predictions are needed to accompany the ever increasing precision of measurements reported by the experiments. The aim of this thesis is to provide new models and improvements for different parts of the event generation, in particular the parton-shower process and fragmentation.

This thesis is organized as follows: in chap. 2 the foundations of the Standard Model are reviewed, with an emphasis on the strong force. The basic elements of Monte Carlo event generators are introduced in chap. 3, focusing on the parts that are relevant later on. The following chapters present published work. The VINCIA antenna shower has so far only been able to describe radiation off outgoing partons. In chap. 4 the shower of VINCIA is extended to cover radiation associated with the incoming partons, as is the method to improve the precision of the parton-shower approximation. This method is revised and improved in chap. 5, where an alternative approach is considered in addition. To increase the speed of the calculations performed in VINCIA, chap. 6 discusses the use of helicities, the projection of the particle spin onto the direction of momentum, in the parton shower. The presentation of new LHC data led to some rethinking of the fragmentation process. In chap. 7 a new model is developed that has the capability of replacing part of Lund string fragmentation model. Finally, chap. 8 contains a summary and concluding remarks.

Quantum Chromodynamics and the Standard Model

The *Standard Model of Particle Physics* (SM) successfully describes the fundamental particles and three out of the four fundamental forces discovered in nature. The SM is based on a relativistic quantum field theory with the gauge group

$$SU(3)_C \times SU(2)_L \times U(1)_Y . \quad (2.1)$$

It contains the *strong* force, described by $SU(3)_C$, and the electromagnetic and weak forces, united in the *electroweak* sector with the gauge group $SU(2)_L \times U(1)_Y$. The force not included in the SM is gravity. The particles are described as field representations of the gauge groups. The quantized degrees of freedom, like spin and charge, give the particle character to the fields. Two groups of particles exist: fermions and bosons. In the SM fermions carry Spin 1/2 and bosons are characterized as Spin 0 or 1 particles.

Quantum Chromodynamics (QCD) is the theory behind the strong interactions. Although QCD is not exactly solvable except numerically on a discrete space-time lattice, the event generation discussed in chap. 3 strongly relies on the theory behind the strong force. With the proton as a composite object bound by QCD, effects of the latter are visible everywhere at the LHC. The thesis is centered around QCD phenomena; either based on perturbation theory or on QCD-inspired phenomenological models, both of which are encoded in the concepts of sec. 2.1, where QCD is introduced. A description of the characteristics of the strong coupling follows in sec. 2.2. Some more details of the SM are given in sec. 2.3. The chapter is closed in sec. 2.4 with a brief discussion of the cross section, as one of the key observables measured at colliders. Most of the material covered in this chapter can be found in text books, such as [15–18].

2.1 Quantum Chromodynamics

The strength of the interactions between SM particles is defined by the *coupling constants*. As the QCD coupling g_s is relatively large compared to the other couplings present in the SM, the QCD sector is named strong. The gauge group is $SU(3)_C$, where the C denotes the quantum number colour. The fermions influenced by

QCD are called *quarks* and the gauge bosons *gluons*, collectively referred to as *partons*. The six different quark flavours are represented by the fields Ψ_f with masses m_f and carry a *colour charge* (one out of the three possible, $r = \text{red}$, $g = \text{green}$, and $b = \text{blue}$). Their antiparticle, the antiquark, carries an anticolour. The gluons are described by fields G_μ^a ($a = 1\dots 8$) with eight independent colour states, the colour octet. For a representation of the colour wave-functions see e.g. [19]. Note that gluon singlets with a colour wave-function $\propto (r\bar{r} + b\bar{b} + g\bar{g})$ do not exist as they would be unconfined, see also sec. 2.2. The QCD Lagrangian provides the information that is required to calculate transition probabilities. It reads

$$\mathcal{L}_{\text{QCD}} = \sum_{f=u,d,\dots} \bar{\Psi}_f (i \gamma^\mu D_\mu - m_f) \Psi_f - \frac{1}{4} G^{a\mu\nu} G_{\mu\nu}^a. \quad (2.2)$$

Here, the covariant derivative is

$$D_\mu = \partial_\mu - i g_s T^a G_\mu^a \quad (2.3)$$

and the field strength tensors are

$$G_{\mu\nu}^a = \partial_\mu G_\nu^a - \partial_\nu G_\mu^a + g_s f^{abc} G_\mu^b G_\nu^c. \quad (2.4)$$

With $G_\mu = G_\mu^a T^a$ the eight gauge fields correspond to the eight $\text{SU}(3)_C$ generators T^a . The Lie algebra

$$[T^a, T^b] = i f^{abc} T^c \quad (2.5)$$

defines the *structure constants* f^{abc} . The generators are the Gell-Mann matrices λ in the fundamental representation for the $\text{SU}(3)_C$ gauge group, $T_{ij}^a = \lambda_{ij}^a/2$.

The first term in eq. (2.2) contains the fermionic mass terms¹ $m_f \bar{\Psi}_f \Psi_f$ and kinetic parts $\bar{\Psi}_f \gamma^\mu \partial_\mu \Psi_f$. The coupling term describes the interaction between a quark, antiquark, and a gluon, $g_s \bar{\Psi}_f \gamma^\mu G_\mu \Psi_f$, and is proportional to the strong coupling g_s . The non-abelian nature of the $\text{SU}(3)_C$ gauge group manifests itself in the *self-interactions* of the gluons,

$$\begin{aligned} \mathcal{L}_g &= -\frac{1}{4} G^{a\mu\nu} G_{\mu\nu}^a \\ &= -\frac{1}{2} \text{Tr} \left((\partial_\mu G_\nu - \partial_\nu G_\mu)^2 \right) + \frac{1}{2} g_s^2 \text{Tr} \left([G_\mu, G_\nu]^2 \right) \\ &\quad + i g_s \text{Tr} \left((\partial_\mu G_\nu - \partial_\nu G_\mu) [G^\mu, G^\nu] \right). \end{aligned} \quad (2.6)$$

The first term is the kinetic part, and the second and third term represent the four-point and three-point gluon self-interaction respectively.

¹These terms can only be introduced as QCD is treated as a separate theory. In the SM, where QCD is combined with the electroweak theory, such mass terms break symmetries and can therefore not be used.

The quantization of the gluon fields within the path integral formalism requires some modifications of the QCD Lagrangian,

$$\mathcal{L}_{\text{QCD}} \rightarrow \mathcal{L}_{\text{QCD}} + \mathcal{L}_{\text{fix}} + \mathcal{L}_{\text{ghost}} . \quad (2.7)$$

As the integration is performed over all possible gauge transformations, the functional integral is not well-defined. Faddeev and Popov introduced a gauge fixing term

$$\mathcal{L}_{\text{fix}} = -\frac{1}{2\xi} (\partial_\mu G^{a\mu})^2 \quad (2.8)$$

to remove the divergent part, see [18]. Non-Abelian gauge theories like QCD need an additional term in the Lagrangian,

$$\mathcal{L}_{\text{ghost}} = \partial_\mu \bar{\eta}^a \partial^\mu \eta^a + g_s f^{abc} \partial^\mu \eta^c G_\mu^b \eta^a , \quad (2.9)$$

to correct the unphysical timelike and longitudinal degrees of freedom of the gauge bosons. The additional fields η are called *ghost* fields.

2.2 Asymptotic Freedom and Confinement

The strong coupling $\alpha_s = g_s^2/4\pi$ changes as a function of energy; it becomes small at high energies or short distances. This scale dependence, known as *asymptotic freedom* [20, 21], allows the application of perturbative methods to calculate QCD transition probabilities at large momentum transfers. In the limit of infinitely large energy scales, quarks and gluons appear to be almost free particles.

The running of the strong coupling with the energy scale Q is described in terms of the beta function

$$\beta(\alpha_s) = Q^2 \frac{\partial \alpha_s}{\partial Q^2} = \frac{\partial \alpha_s}{\partial \ln Q^2} . \quad (2.10)$$

The beta function, derived from higher-order calculations, can be expanded in powers of α_s

$$\beta(\alpha_s) = -\alpha_s^2 (b_0 + b_1 \alpha_s + \mathcal{O}(\alpha_s^2)) , \quad (2.11)$$

with the leading-order (LO) [20, 21] and next-to-leading-order (NLO) coefficients [22, 23]

$$b_0 = \frac{33 - 2n_f}{12\pi} \quad \text{and} \quad b_1 = \frac{153 - 19n_f}{24\pi^2} . \quad (2.12)$$

The number of quark flavours is denoted by n_f , which is in turn dependent on the energy, as only the quark flavours with masses $\lesssim Q$ are active at scales $\leq Q$ and therefore contribute to the running of α_s . As the total number of observed quark flavours is six, the beta function is of negative sign and the coupling $\alpha_s(Q^2)$ decreases with increasing energy.

Solving eq. (2.10) yields the result

$$\alpha_s(Q^2) = \frac{\alpha_s(\mu^2)}{1 + b_0 \alpha_s(\mu^2) \ln(Q^2/\mu^2) + \mathcal{O}(\alpha_s^2)}. \quad (2.13)$$

A typical choice for the reference scale μ is the mass of the Z boson where the coupling has been measured to be $\alpha_s(m_Z^2) \approx 0.118$. The coupling at an arbitrary scale Q is obtained by evolving the coupling from the reference scale to Q . The running coupling in eq. (2.13) can be rewritten as

$$\alpha_s(Q^2) = \frac{1}{b_0 \ln(Q^2/\Lambda_{\text{QCD}}^2)} \quad \text{with} \quad \Lambda_{\text{QCD}}^2 = \mu^2 \exp\left(-\frac{1}{b_0 \alpha_s(\mu^2)}\right). \quad (2.14)$$

This illustrates that the coupling diverges for small enough energies (large enough distances). The scale at which α_s nominally becomes infinite and perturbation theory breaks down is $\Lambda_{\text{QCD}} \approx 200 \text{ MeV}$. This is the energy where a phenomenon called colour *confinement* takes place: coloured QCD particles produced in a scattering are not observed as free states in nature. For large distances of $\sim 1/\Lambda_{\text{QCD}} \approx 1 \text{ fm}$ the QCD force field between two colour charges is compressed into a narrow tube due to the gluon self-interactions. The further the charges move apart, the more energy will be stored in the tube. It will eventually become energetically favourable to create additional partons, which, together with the original partons, form *hadrons*. More discussion on this will follow in sec. 3.5. In collider experiments, the manifestation of confinement is the observation of collimated sprays of hadrons, called *jets*.

2.3 Standard Model

The SM combines the theory of QCD with that of electroweak interactions. The subscripts of the electroweak gauge group, $SU(2)_L \times U(1)_Y$, denote the left-handedness L and hypercharge Y .

The particle content of the SM is shown in tab. 2.1. The quarks, introduced in sec. 2.1, and the leptons are both arranged in three generations,

$$\begin{pmatrix} \nu_e \\ e \end{pmatrix}, \begin{pmatrix} \nu_\mu \\ \mu \end{pmatrix}, \begin{pmatrix} \nu_\tau \\ \tau \end{pmatrix} \quad \text{and} \quad \begin{pmatrix} u \\ d \end{pmatrix}, \begin{pmatrix} c \\ s \end{pmatrix}, \begin{pmatrix} t \\ b \end{pmatrix}.$$

The fundamental representation of the $SU(2)_L$ gauge group are the left-chiral projections of the fermion fields, $\Psi_L = \frac{1}{2}(1 - \gamma_5)\Psi$. The left-handed quarks $Q_L = (u_L, d_L)^T$ and leptons $L = (\nu_L, e_L)^T$ are doublets under the $SU(2)_L$ gauge group. Right-chiral projections $\Psi_R = \frac{1}{2}(1 + \gamma_5)\Psi$ of quarks $Q_R = (u_R, d_R)^T$ and leptons e_R are singlets under $SU(2)_L$. Note that neutrinos do not appear righthanded² and are assumed to be massless in the SM. Besides the fermions and the eight gluons,

² The Goldhaber experiment (1957) showed that neutrinos only appear lefthanded in nature.

	Charge	Mass	Spin		Charge	Mass	Spin
Fermions:							
up	u 2/3	2.2 MeV	1/2	electron	e^- -1	511 keV	1/2
down	d -1/3	4.7 MeV	1/2	muon	μ^- -1	106 MeV	1/2
charm	c 2/3	1.3 GeV	1/2	tau	τ^- -1	1.8 GeV	1/2
strange	s -1/3	96 MeV	1/2	e neutrino	ν_e 0	< 2.2 eV	1/2
top	t 2/3	173 GeV	1/2	μ neutrino	ν_μ 0	< 170 keV	1/2
bottom	b -1/3	4.2 GeV	1/2	τ neutrino	ν_τ 0	< 16 MeV	1/2
Bosons:							
gluon	g 0	0	1				
photon	γ 0	0	1				
Z boson	Z 0	91.2 GeV	1				
W boson	W^\pm ± 1	80.4 GeV	1				
Higgs	H 0	125 GeV	0				

Table 2.1: List of all particles in the Standard Model, together with their shorthand notation, electric charge, mass, and spin values. The $u/d/s$ -quark masses are estimates of so-called “current-quark masses” in a mass-independent subtraction scheme such as $\overline{\text{MS}}$ [24] at a scale ≈ 2 GeV. The masses of the c/b quark are “running” masses in the $\overline{\text{MS}}$ scheme. The t -mass is measured directly. Note that the neutrinos are assumed to be massless in the SM, but are still listed here with the upper limit on their masses. Values taken from [25].

the QCD gauge bosons introduced in sec. 2.1, the SM includes the photon γ , W and Z bosons of the electroweak theory, as well as the Higgs boson

$$g_1, \dots, g_8 \quad \text{and} \quad \gamma, W^+, W^-, Z^0 \quad \text{and} \quad H.$$

A pictorial representation including all particles and their interactions is shown in fig. 2.1.

The Lagrangian of the SM can be divided into four parts, plus the gauge-fixing and ghost terms of eqs. (2.8) and (2.9),

$$\mathcal{L}_{\text{SM}} = \mathcal{L}_{\text{boson}} + \mathcal{L}_{\text{fermion}} + \mathcal{L}_{\text{Higgs}} + \mathcal{L}_{\text{Yukawa}} + \mathcal{L}_{\text{fix}} + \mathcal{L}_{\text{ghost}}. \quad (2.15)$$

The bosonic part of the Lagrangian contains the kinetic terms of all bosons as well as the gluon self-interactions, see also sec. 2.1,

$$\mathcal{L}_{\text{boson}} = -\frac{1}{4} G^{a\mu\nu} G_{\mu\nu}^a - \frac{1}{4} B^{\mu\nu} B_{\mu\nu} - \frac{1}{4} W^{i\mu\nu} W_{\mu\nu}^i \quad (2.16)$$

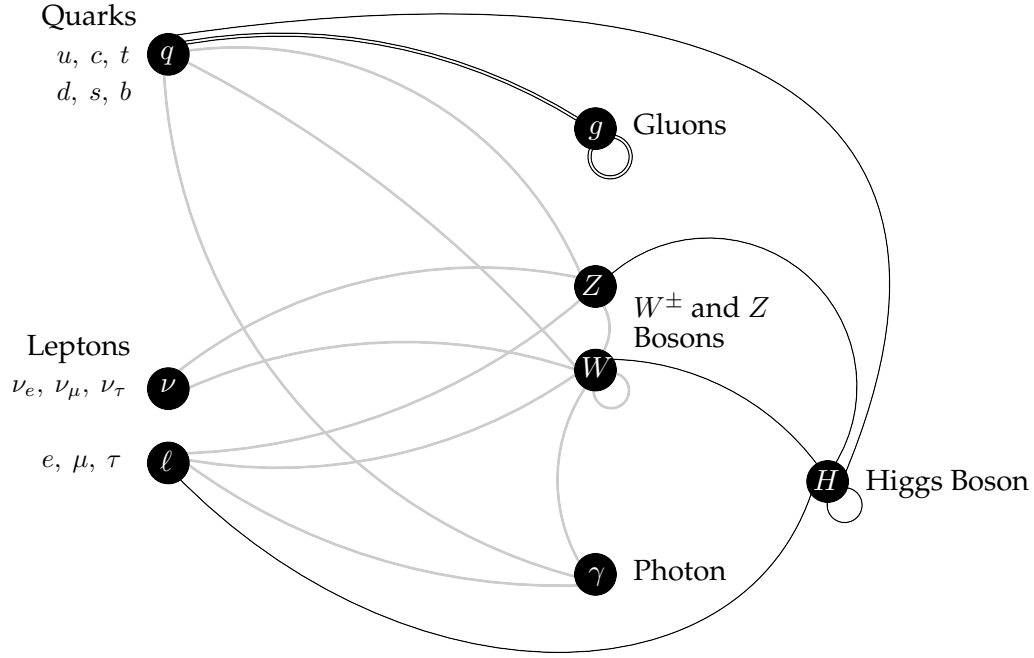


Figure 2.1: The Standard Model of particle physics, with lines indicating interactions. Electrically charged particles exchange photons; leptons and quarks interact weakly through W and Z boson exchange; W bosons interact with themselves (thick grey lines). QCD interactions include quarks exchanging gluons and gluons interacting with themselves (double lines). Every massive particle interacts with the Higgs field (black lines).

The $U(1)_Y$ gauge field is denoted by B_μ and the three $SU(2)_L$ fields by W_μ^i ($i = 1, 2, 3$). The fermionic part includes a sum over all left- and right-handed fermions and can be subdivided into a kinetic and an interaction part,

$$\begin{aligned} \mathcal{L}_{\text{fermion}} = & \sum_{\Psi_{L/R}} \bar{\Psi}_{L/R} i \gamma^\mu \partial_\mu \Psi_{L/R} + \\ & \sum_{\Psi_{L/R}} \bar{\Psi}_{L/R} \gamma^\mu (g_s I_s G_\mu + g I_w \sigma^i W_\mu^i + g' Y B_\mu) \Psi_{L/R}. \end{aligned} \quad (2.17)$$

The interaction with gluons is determined by the strong coupling g_s and the strong isospin I_s , which is unity for quarks and zero for all other fermions. The quantum number of $SU(2)_L$ is the weak isospin I_w , a half for left- and zero for right-handed fermions. Together with the dimensionless coupling g it determines the interaction between fermions and the $SU(2)_L$ gauge bosons. The last term represents the coupling of all fermions to the $U(1)_Y$ boson, which is determined by the coupling g' and the quantum number hypercharge. The latter is $Y = Q_{\text{em}} - I_w^3$, with the electric charge Q_{em} and the third component of the weak isospin I_w^3 .

The last two terms of the SM Lagrangian in eq. (2.15) involve the Higgs boson. The kinetic part of the Higgs doublet Φ , its coupling to the other gauge bosons, and the Higgs potential are

$$\mathcal{L}_{\text{Higgs}} = \left| \left(\partial_\mu - \frac{i}{2} g' B_\mu - \frac{i}{2} g \sigma^i W_\mu^i \right) \Phi \right|^2 - \mu^2 \Phi^\dagger \Phi - \lambda \left(\Phi^\dagger \Phi \right)^2. \quad (2.18)$$

With $\mu^2 < 0$, the potential is constructed such that it implies a non-vanishing vacuum expectation value, which is conveniently chosen to be $\langle \Phi \rangle = (0, v/\sqrt{2})^T$. In this way, the $SU(2)_L \times U(1)_Y$ symmetry is broken spontaneously, where a residual $U(1)_{\text{em}}$ symmetry is retained. The mechanism of spontaneous symmetry breaking (SSB) generates mass terms for two complex and one real linear combination of the B_μ and W_μ^i fields, which correspond to the physical W^\pm and Z bosons. The other linear combination corresponds to the unbroken $U(1)_{\text{em}}$ symmetry. It remains massless and is identified as the photon.

Finally, the last term in eq. (2.15) denotes the coupling of the fermions to the Higgs doublet

$$\begin{aligned} \mathcal{L}_{\text{Yukawa}} = & - \sum_{\text{leptons}} G_e \left(\bar{\Psi}_L \Phi \Psi_R + \bar{\Psi}_R \Phi^\dagger \Psi_L \right) \\ & - \sum_{\text{quarks}} \lambda_d^{ij} \bar{Q}_L^i \Psi d_R^j + i \lambda_u^{ij} \bar{Q}_L^i \tau_2 \Psi^* u_R^j + \text{h.c.} . \end{aligned} \quad (2.19)$$

The first term is the Yukawa coupling of the leptons with the dimensionless coupling constant G_e and generates mass terms of the form $-m_e(\bar{e}_L e_R + \bar{e}_R e_L)$. The second term sums over the three quark generations with the complex mixing matrices λ . The non-diagonal matrices parameterize the difference between the mass and interaction eigenstates of the quark generations Q_L^i , d_R^i , and u_R^i . For the original work on SSB and the Higgs mechanism see [26, 27].

2.4 Cross Sections and Matrix Elements

Collider experiments like the LHC or LEP are counting the occurrence of specific events; detectors therefore measure *cross sections*, the probability for certain scattering processes to happen. The *luminosity* \mathcal{L} connects the cross section σ to the event rate $\mathcal{R} = \sigma \cdot \mathcal{L}$ (with units of $\text{s}^{-1} = \text{m}^2 \cdot \text{m}^{-2} \text{s}^{-1}$). The cross section for proton A and proton B with momenta p_A and p_B to produce a specific n -particle final state is

$$\sigma(A + B \rightarrow n) = \sum_{a,b} \int_0^1 dx_a f_a(x_a, \mu_F^2) \int_0^1 dx_b f_b(x_b, \mu_F^2) \hat{\sigma}(a + b \rightarrow n). \quad (2.20)$$

This hadronic cross section *factorizes* into the partonic cross section $\hat{\sigma}_n(a + b \rightarrow n)$, calculable in perturbation theory, and the hadronic part, given by the so-called *parton distribution functions* (PDFs) $f(x, \mu^2)$. See [28–30] for the factorization ansatz.

As the incoming particles are composed of partons, all possibilities to arrive at the final state n need to be summed and integrated over. Thus, the sum contains all proton constituents, which are extracted with momentum $p_{a/b} = x_{a/b} p_{A/B}$, where $x_{a/b}$ is called the *momentum fraction*. As a first approximation, the PDFs parameterize the probability for the extraction of a parton of flavour a/b and momentum fraction $x_{a/b}$ from the proton A/B . The PDFs depend on the factorization scale μ_F , at which the physics of short and long distances is separated, i.e. factorized. As PDFs describe the properties of hadronic bound states, they can not be calculated in perturbation theory, but are extracted from measurements.

The factorization into a partonic cross section and universal PDFs is not normally an exact result, but rather only an approximation. For the Drell-Yan process however, [31] presented an explicit proof. On the final state, a similar factorization exists that splits the cross section into a short-distance part and fragmentation functions, which correspond to the probability for a parton to decay into a hadron. For the inclusive decay of a highly off-shell photon to n hadrons, $\gamma^* \rightarrow H_1 \dots H_n + X$, the factorization has been proven in [32].

The hadronic cross section in eq. (2.20) is *inclusive*, in the sense that it is the cross section for the production of the $(n + X)$ -particle final state, as the PDFs account for everything that could happen at scales below the factorization scale. In contrast, an *exclusive* quantity refers to a n - and only n -particle final state.

The most general form of the partonic cross section, i.e. including all orders in perturbation theory, is

$$\hat{\sigma}(a + b \rightarrow n) = \sum_{k=0}^{\infty} \int \mathcal{F}_{ab} \left| \sum_{l=0}^{\infty} \mathcal{M}^{(l)}(a + b \rightarrow n + k) \right|^2 d\Phi(a + b \rightarrow n + k). \quad (2.21)$$

The flux factor \mathcal{F}_{ab} is related to the relative velocities and the energies of the incoming partons and reads

$$\mathcal{F}_{ab} = \frac{1}{4\sqrt{(p_a \cdot p_b)^2 - m_a^2 m_b^2}}. \quad (2.22)$$

$\mathcal{M}^{(l)}(a + b \rightarrow n + k)$ is the *amplitude* for the n -particle final state plus k additional external legs and l additional loops. The partonic cross section in eq. (2.21) includes the sum over all possible legs and loops. The *squared matrix element* (ME), $|\sum \mathcal{M}|^2$, and flux factor are finally integrated over the Lorentz-invariant phase-space

$$d\Phi(a + b \rightarrow n + k) = (2\pi)^4 \delta^{(4)} \left(p_a + p_b - \sum_{i=1}^{n+k} p_i \right) \prod_{i=1}^{n+k} \frac{d^3 p_i}{(2\pi)^2 2E_i}. \quad (2.23)$$

In practise, the perturbative series is truncated at a fixed order in the coupling as the calculation becomes too cumbersome for large numbers of legs and/or loops. The LO partonic cross section, also referred to as *Born*, is

$$\hat{\sigma}^{\text{LO}}(a + b \rightarrow n) = \int \mathcal{F}_{ab} \left| \mathcal{M}^{(0)}(a + b \rightarrow n) \right|^2 d\Phi(a + b \rightarrow n). \quad (2.24)$$

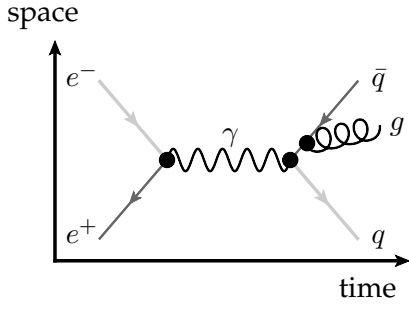


Figure 2.2: Diagrammatic representation of the annihilation amplitude of the process $e^+e^- \rightarrow \gamma \rightarrow qq\bar{q}$. Fermions are drawn with light grey lines and antifermions with dark grey lines. The photon is represented by the wavy line and the gluon by the curly line. The black dots represent vertices.

Higher-order terms correspond to real (additional legs) and virtual (additional loops) corrections. For instance the NLO cross section for the production of n particles, i.e. $k + l \leq 1$, is

$$\begin{aligned}
 \hat{\sigma}^{\text{NLO}}(a + b \rightarrow n) &= \hat{\sigma}^{\text{LO}}(a + b \rightarrow n) + \hat{\sigma}^{\text{real}}(a + b \rightarrow n) + \hat{\sigma}^{\text{virt}}(a + b \rightarrow n) \\
 &= \int \mathcal{F}_{ab} \left| \mathcal{M}^{(0)}(a + b \rightarrow n) \right|^2 d\Phi(a + b \rightarrow n) \\
 &\quad + \int \mathcal{F}_{ab} \left| \mathcal{M}^{(0)}(a + b \rightarrow n + 1) \right|^2 d\Phi(a + b \rightarrow n + 1) \\
 &\quad + \int \mathcal{F}_{ab} 2 \text{Re} \left[\mathcal{M}^{(1)}(a + b \rightarrow n) \mathcal{M}^{(0)*}(a + b \rightarrow n) \right] d\Phi(a + b \rightarrow n) \quad (2.25)
 \end{aligned}$$

with the Born cross section $\hat{\sigma}^{\text{LO}}$, real correction $\hat{\sigma}^{\text{real}}$, and virtual correction $\hat{\sigma}^{\text{virt}}$. Integrating over the full phase-space $d\Phi(ab \rightarrow n + k)$ in eq. (2.21) leads to divergences in the real corrections. Divergences in the virtual corrections are caused by the integration over the loop momentum (not explicitly shown in eq. (2.21)). By the virtue of unitarity, adding the contributions makes eq. (2.25) finite as the singularities cancel each other order by order. This is guaranteed by the KLN theorem [33, 34] and its generalization to QCD [35, 36].

The MEs are calculated with the help of *Feynman rules*, see for instance [37, 38], a set of propagator factors for internal particles, wave functions for external particles, and vertex factors for the interaction points, which can be derived from the Lagrangian introduced in this chapter. Each amplitude in eq. (2.21) can be represented graphically with a *Feynman diagram*, see fig. 2.2 for an example. Every line and point is associated with the corresponding Feynman rule, multiplied in the right order, gives an analytic expression for the amplitude. By summing over all possible diagrams and squaring the result, one obtains the ME. Those calculations are automatized by ME generators like MADGRAPH [39], such that particles with momenta distributed according to the cross section are produced at the push of a button.

Monte Carlo Event Generators

Monte Carlo event generators (MCEGs) allow the prediction of the full final-state kinematics in high-energy collisions, thereby playing an essential role in testing theory models by comparing their predictions to data. The tasks performed by MCEGs are highly non-trivial due to the larger number of particles with momenta ranging over many orders of magnitudes. The simulation of particle collisions is treated in a divide-and-conquer fashion: as a first step a subprocess at the highest energy scale of the event is computed in perturbation theory. This subprocess is the input to the parton shower, which evolves the partons downwards in scale by emitting additional radiation. As the energy scales becomes smaller and smaller, perturbation theory finally breaks down and hadronization takes over to form hadrons out of the partons. As a last step, unstable hadrons decay into the observed particles. This chapter aims at giving a basic overview of the physics behind MCEGs.

3.1 Hard Process

The first step in MCEGs is the calculation of the elementary *hard process*, the scattering process of fundamental particles. The calculation is based on fixed-order perturbation theory and convoluted with PDFs for hadronic initial states as in eq. (2.20). A large range of $2 \rightarrow \{1, 2, 3\}$ processes are included in multi-purpose MCEGs like PYTHIA 8 [40,41] or HERWIG++ [42]. These processes are traditionally implemented at LO perturbation theory. However, a lot of processes are nowadays available at NLO or even NNLO and therefore require a well-conceived combination with the parton shower, which is referred to as matching and merging. SHERPA [43], a MCEG originated in matching and merging studies, provides its own ME generator called COMIX [44]. For MCEGs to make use of the results provided by ME generators such as MADEVENT/MADGRAPH [39] or more dedicated amplitude providers like VBFNLO [45] or MCFM [46,47], the Les Houches Accord interface [48,49] specifies a standard format for the exchange of data. In HERWIG++, direct interfaces of MATCHBOX [50] to different tree-level and one-loop amplitude providers allows to set up the full calculation of LO and NLO cross sections.

To assign specific colours (and/or anticolours) to the partons of the hard process, MCEGs neglect $1/N_C$ contributions in QCD diagrams. In this limit, the colour structure of an arbitrarily complicated parton system can be decomposed as a

colour flow, represented by a set of colour lines, each connecting two partons. A colour flow F is chosen according to the relative weights

$$|\mathcal{M}^{\text{LC}}(F)|^2 / \sum_f |\mathcal{M}^{\text{LC}}(f)|^2, \quad (3.1)$$

where the denominator sums over the leading-colour (LC) ME of all possible colour structures. Together with the kinematics and energy scale of the particles of the hard process, the colour flow acts as input for the generation of additional QCD radiation in the initial- and final-state showers.

3.2 Multi-Parton Interactions

The hard process leaves behind what is left of the incoming beam particles. For hadronic initial states, the remaining *beam remnants* allow the possibility of *multiple partonic interactions* (MPIs) to occur. They manifest themselves for instance in jets and their substructure, jet shapes [51], event shapes [52], or in an enhanced activity in the region that is transverse to the direction of the hardest jet in the event [53,54].

In PYTHIA 8 and SHERPA MPIs are ordered in transverse momentum and the PDFs for each successive interaction are constructed such that the sum of x -fractions can never be greater than unity. In HERWIG++ an initial guess for the number of MPIs is used. This might eventually lead to a violation of energy-momentum conservation in the sense that the sum of the energy of the incoming partons exceeds the hadronic beam energy. If so, the generation of MPIs stops and the last interaction, which caused the violation, is removed from consideration. In the PYTHIA 8 MCEG MPIs are interleaved with the initial- and final-state showering of the hard process, whereas in HERWIG++ and SHERPA they are handled in a separate step. The MPIs themselves will be showered as well, similar to the hard process.

3.3 Parton Shower

The hard process is typically calculated according to the lowest-order ME. One possibility of obtaining higher accuracy is to extend the calculation such that higher perturbative orders of the strong coupling α_s are included. However, these corrections become more difficult to calculate with increasing order of α_s . Furthermore, while inclusive cross sections describe the momenta of the outgoing jets well, they do not give an exclusive picture of the process. To describe a collider event properly, including the substructure of jets and the characteristics of the accompanying particles, any fixed order is not sufficient.

Cross sections are enhanced for certain phase-space regions. If QCD particles are present, the ME has enhancements for two kinematic configurations:

1. The emission of a low-energy gluon ($E \rightarrow 0$, *soft* singularity).

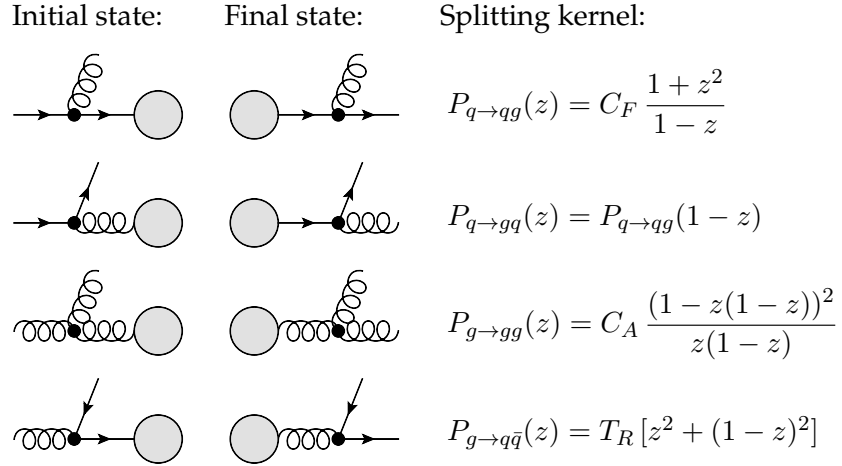


Figure 3.1: The different branching types in a QCD parton shower. Initial state branchings are shown in the left column, final state branchings in the middle column, and the corresponding DGLAP splitting kernels are shown in the right column. The grey blobs represent the hard process.

2. The splitting into two partons close in angle ($\theta \rightarrow 0$, *collinear* singularity).

Gauge theory amplitudes factorize in the soft and collinear limits of QCD [55–57]. As a result, the cross section σ_{n+1} for an arbitrary configuration with n particles, accompanied by an additional emission, can be calculated with the help of the n -particle cross section σ_n and a universal, i.e. process independent, *splitting function* (or splitting kernel). This approximation¹ is used by *parton shower* algorithms to generate emissions iteratively. While the parton kinematics and colour flow of the hard process act as input to the parton shower, additional emissions are generated independently of whether e.g. a Higgs or Z boson was present in the underlying n -particle process. As the factorization is only valid for soft and collinear emissions, a parton shower is effectively resumming the large logarithms appearing in those phase-space regions for higher orders. The parton shower is able to generate an arbitrary number of additional emissions and therefore acts as an all-orders approximation. The algorithm is typically formulated as an evolution in momentum transfer from the high scale associated with the hard process down to lower scales.

3.3.1 Parton Branching in the Collinear Limit

Consider the splitting $a \rightarrow bc$ of a final-state parton a into two partons b and c . The relevant QCD branchings for final-state legs are shown in the middle column of fig. 3.1: a quark emitting a gluon, a gluon emitting a gluon, and a gluon splitting into a quark-antiquark pair. After the splitting, parton b carries the energy fraction

¹The factorization is only correct in the soft and collinear limits and therefore an approximation away from these limits.

z of the mother parton a , $E_b = z E_a$, which leaves the energy of parton c to be $E_c = (1 - z)E_a$ due to energy conservation. In the collinear limit, i.e. where the angle θ_{bc} between partons b and c is small, the amplitude factorizes and can be written as

$$|\mathcal{M}_{n+1}|^2 \xrightarrow{\theta_{bc} \rightarrow 0} 8\pi\alpha_s \frac{P_{a \rightarrow bc}(z)}{Q^2} |\mathcal{M}_n|^2. \quad (3.2)$$

$P_{a \rightarrow bc}(z)$ denote the DGLAP (Dokshitzer-Gribov-Lipatov-Altarelli-Parisi) splitting kernels [3–5], listed on the right side of fig. 3.1. Each kernel contains a colour factor, where $C_A = N_C = 3$, $C_F = 4/3$, and $T_R = 1/2$. The propagator of the parent parton a ,

$$\frac{1}{Q^2} = \frac{1}{2p_b \cdot p_c} = \frac{1}{(p_b + p_c)^2 - m_b^2 - m_c^2}, \quad (3.3)$$

goes on-shell in the collinear limit. This causes a singularity in the ME $|\mathcal{M}_{n+1}|^2$. With eq. (3.2) the factorization of the cross section for a process accompanied by an additional parton yields

$$\sigma_{n+1} \xrightarrow{\theta_{bc} \rightarrow 0} \sigma_n \sum_{b,c} \int_{Q_{\min}^2}^{Q_{\max}^2} \frac{dQ^2}{Q^2} \frac{\alpha_s}{2\pi} \int_{z_{\min}}^{z_{\max}} dz P_{a \rightarrow bc}(z). \quad (3.4)$$

The 1-particle phase space is expressed in terms of Q^2 and z ,

$$d\Phi_{+1} = \frac{1}{16\pi^2} dQ^2 dz \frac{d\phi}{2\pi}, \quad (3.5)$$

with the generic integration boundaries $Q_{\min/\max}^2$ and $z_{\min/\max}$. The integration over the angle ϕ has already been carried out,

$$\int_0^{2\pi} \frac{d\phi}{2\pi} = 1. \quad (3.6)$$

The Q^2 integration in eq. (3.4) yields a term of the form $\ln(Q_{\max}^2/Q_{\min}^2)$ (leaving a potential Q^2 -dependence of α_s aside). This term becomes large for $Q_{\max}^2 \gg Q_{\min}^2$, which is precisely the limit that parton showers aim to describe. Therefore, shower algorithms effectively resum large logarithms.

Due to energy-momentum conservation, a $1 \rightarrow 2$ branching can not occur with all partons being on-shell. Therefore, some re-shuffling of momentum is needed, whose form depends on the chosen *recoil strategy* or *kinematics map*. In a DGLAP-based parton shower, the *recoiler* can either be a single parton as or a system of partons.

For hadronic beams the incoming partons can emit radiation before entering the hard process. This initial-state radiation is formulated as a backwards evolution [60], where the incoming partons are evolved from large scales down to the low scale associated with the beam hadron, while emitting successive radiation.

$$\begin{aligned}
\frac{d}{d \log(Q^2)} \left[\text{Diagram: White square } \rightarrow \text{Grey blob} \right]_{f_q(x, Q^2)} &= \int_x^1 \frac{dz}{z} \frac{\alpha_s}{2\pi} \left[\text{Diagram: White square } \rightarrow \text{Grey blob with gluon emission} \right]_{f_q(x/z, Q^2)}^{P_{q \rightarrow qq}(z)} + \int_x^1 \frac{dz}{z} \frac{\alpha_s}{2\pi} \left[\text{Diagram: White square } \rightarrow \text{Grey blob with quark emission} \right]_{f_q(x/z, Q^2)}^{P_{g \rightarrow q\bar{q}}(z)} \\
\frac{d}{d \log(Q^2)} \left[\text{Diagram: White square } \rightarrow \text{Grey blob with gluon emission} \right]_{f_g(x, Q^2)} &= \sum_{i=1}^{2n_f} \int_x^1 \frac{dz}{z} \frac{\alpha_s}{2\pi} \left[\text{Diagram: White square } \rightarrow \text{Grey blob with gluon emission} \right]_{f_q(x/z, Q^2)}^{P_{q \rightarrow gq}(z)} + \int_x^1 \frac{dz}{z} \frac{\alpha_s}{2\pi} \left[\text{Diagram: White square } \rightarrow \text{Grey blob with gluon emission} \right]_{f_g(x/z, Q^2)}^{P_{g \rightarrow gg}(z)}
\end{aligned}$$

Figure 3.2: Schematical representation of the DGLAP evolution of PDFs. The grey blobs represent the hard process and the white squares represent the incoming hadron. Inspired by [58] and [59].

The factorization in the collinear limit allows to derive the DGLAP evolution equations [3–5], which determine the behaviour of the PDFs as a function of the scale,

$$Q^2 \frac{df_b(x, Q^2)}{dQ^2} = \sum_{a \in \{q, g\}} \frac{\alpha_s}{2\pi} \int_x^1 \frac{dz}{z} P_{a \rightarrow bc}(z) f_a(x/z, Q^2). \quad (3.7)$$

A pictorial representation of the evolution equation is shown in fig. 3.2. Parton b , present in the beam hadron with the energy fraction x , may have been produced by parton a with the energy fraction x/z while emitting parton c into the final state. All possibilities how parton b could have been produced are summed over in eq. (3.7). As for final-state radiation, a recoiler (system) is needed to ensure energy-momentum conservation. Initial-state parton showers make use of eq. (3.7) to convert the inclusive prediction for finding parton b in the beam hadron in eq. (2.20) into an exclusive prediction for a and a specific set of additional partons, resolved at smaller scales.

3.3.2 Coherent Branching

As discussed at the beginning of sec. 3.3 MEs are not only enhanced in the collinear, but also in the soft regions of phase space. If a low-energy gluon j is emitted by two final state colour-connected partons I and K , $IK \rightarrow ijk$, the gauge theory amplitude factorization reads

$$|\mathcal{M}_{n+1}|^2 \xrightarrow{E_j \rightarrow 0} 4\pi\alpha_s \mathcal{C} S_{ijk} |\mathcal{M}_n|^2. \quad (3.8)$$

Here, \mathcal{C} is the colour factor² and S_{ijk} the universal soft eikonal factor, expressed in terms of invariants $s_{xy} = 2 p_x \cdot p_y$ and masses m^2 ,

$$S_{ijk} = \frac{2s_{ik}}{s_{ij}s_{jk}} - \frac{m_i^2}{s_{ij}^2} - \frac{m_j^2}{s_{jk}^2}. \quad (3.9)$$

The propagators of both parent partons, I and K , go on-shell simultaneously in the limit where the energy of the gluon is vanishing and thereby causing the soft

² $\mathcal{C} = C_A$ for an emission off gluons and $\mathcal{C} = 2C_F$ for an emission off quarks.

singularity in the ME. Similar to eq. (3.4) for the collinear factorization, the cross section for a configuration with one soft gluon is

$$\sigma_{n+1} \xrightarrow{E_j \rightarrow 0} \sigma_n \int \frac{ds_{ij} ds_{jk}}{s_{ij} + s_{jk} + s_{ik}} \frac{\alpha_s}{4\pi} \mathcal{C} S_{ijk}. \quad (3.10)$$

The lorentz-invariant 1-particle phase space is

$$d\Phi_{+1} = \frac{1}{16\pi^2} \frac{ds_{ij} ds_{jk}}{s_{ij} + s_{jk} + s_{ik}} \frac{d\phi}{2\pi}. \quad (3.11)$$

A transformation from the invariants (s_{ij}, s_{jk}) to (Q^2, z) connects eq. (3.5) to eq. (3.11). As before, the integration over the angle has already been carried out and the remaining integration boundaries are left unspecified.

The soft eikonal factor in eq. (3.9) can be rewritten as

$$S_{ijk} \equiv S_{ijk}^{(i)} + S_{ijk}^{(k)} = \left(\frac{1}{s_{ij}} - \frac{m_i^2}{s_{ij}^2} + \frac{s_{ik} - s_{ij}}{s_{ij}s_{jk}} \right) + \left(\frac{1}{s_{jk}} - \frac{m_j^2}{s_{jk}^2} + \frac{s_{ik} - s_{jk}}{s_{ij}s_{jk}} \right), \quad (3.12)$$

where $S_{ijk}^{(i)}$ is singular only for the gluon being collinear to parton i and may naturally be associated with the emission off parton i . Averaging over azimuthal emission angles in the limit of massless partons gives [61]

$$\langle S_{ijk}^{(i)} \rangle = \Theta(\theta_{IK} - \theta_{ij}) \frac{2}{E_j (1 - \cos \theta_{ij})}, \quad (3.13)$$

with θ_{xy} the angle between partons x and y . The contribution from $S_{ijk}^{(i)}$ is thus limited to a cone around parton I with opening angle $2\theta_{IK}$ (similarly for $S_{ijk}^{(k)}$). As a result, the opening angle of the emissions can be used as the shower ordering variable to describe the coherence property of QCD. Consider a gluon that has been produced in the hard process and emitted a hard, but collinear gluon. When calculating the probability that this process is accompanied by a soft, wide-angle gluon, two diagrams have to be summed up according to the soft factorization. As shown on the left side of fig. 3.3, each diagram corresponds to the soft gluon being radiated off either of the collinear gluons. It appears that in the region in which the softer gluon is at a larger angle than the harder one, as shown in the figure, the interference is largely destructive. One can therefore think of the wide-angle gluon as being emitted before the collinear one, pictorially shown on the right-hand side of fig. 3.3. This coherence effect [7, 62–64] is similar to the Chudakov effect in QED, where wide-angle emissions off e^+e^- pairs are absent. The reason for that is that the emission can only see the total charge of the pair, which is zero. In the QCD case the wide-angle gluon can not resolve the colour structure of the collinear gluons and therefore only sees the total colour charge of the system of partons to which it is attached.

In summary, soft gluon emission can correctly be taken into account by a parton shower based on collinear factorization if the opening angle is used as an evolution variable to order successive emissions. This implemented for instance in the

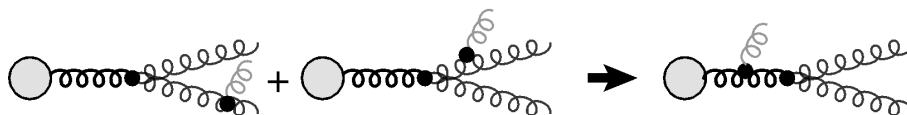


Figure 3.3: Illustration of QCD coherence. A hard, collinear gluon pair (dark grey) with a soft, wide-angle gluon (light grey), attached to any of the external partons (*left*). The contributions interfere destructively such that it appears as if the soft gluon were emitted before the smaller-angle harder gluon (*right*). The pictures do not represent Feynman diagrams, but rather serve the purpose of illustration.

angular-ordered parton shower in HERWIG++ [65]. Instead of choosing a specific evolution variable coherence can be included by imposing a veto on non-angular-ordered emissions [66]. In the following two subsections, alternative implementations of colour coherence are discussed, based on colour-connected parton pairs.

3.3.3 The Antenna Model for Shower Algorithms

As an alternative to the evolution of single partons in the DGLAP picture, emissions off parton pairs are the basis of the *antenna model*, discussed in this section, as well as the *CS-dipole model*, discussed in the next section. The foundation of both models is the large- N_C limit, characterized by infinitely many colours. As discussed in sec. 3.1, $1/N_C$ contributions in QCD diagrams are neglected and the colour structure is decomposed as a colour flow, where every colour line has a different colour. Thus, the interference between colour lines can be neglected and they can emit radiation independently of each other. So-called *colour dipoles* [6] are formed by colour-connected parton pairs during the hard process and provide the input for the antenna shower. Colour dipoles are also known as antennae in the context of fixed-order subtraction schemes [7–9]. This makes both names, dipole and antenna shower, to be used customarily to describe the same model. The antenna functions, which act as splitting kernels, are taken over from fixed-order calculations and explicitly incorporate all single-unresolved, i.e. soft and collinear, limits. They are coherent in the sense that they sum up the radiation from two sides of the leading- N_C dipole coherently, at the amplitude level. The antenna picture as a shower algorithm was first implemented in the ARIADNE program [6,67], which successfully describes the properties of final-state radiation. Instead of a backwards evolution for initial-state radiation, dipoles are spanned between the hadron remnants and the partons of the hard interactions [63]. In chap. 4 a paper is presented, where the final-state antenna shower of VINCIA [68] is extended to initial-state radiation.

In contrast to a conventional DGLAP-based parton-shower model, which evolves a single parton as emitter with one (or more) other partons acting as the recoiler (system), the antenna model treats the colour dipole as a single entity. There is no traditional role of a radiator, but rather both partons produce emissions *to-*

gether. Radiation with non-vanishing transverse momentum off gluon-antennae leads to recoil that also affects the neighbouring colour dipoles since gluons carry two colour lines. The radiation is driven by a single antenna function and a single recoil strategy, exactly factorizing the on-shell $(n + 1)$ -parton phase space into the n -parton and the $(2 \rightarrow 3)$ antenna phase space.

3.3.4 The CS-Dipole Model for Shower Algorithms

The original dipole picture, discussed in the previous section, refers to a colour-connected parton pair emitting radiation together as an entity without the distinction of the radiator and recoiler role. A Catani-Seymour (CS) partitioned dipole [10,11] corresponds, roughly speaking, to a partial-fractioning of an antenna or colour dipole into two pieces. Each partitioned dipole has a distinct radiator and recoiler. Many shower algorithms in present-day generators are based on the CS-dipole model, e.g. [69–71], and are often referred to simply as dipole shower (however, not to be confused with the dipole/antenna picture of the previous section). CS-dipole showers are naturally ordered in transverse momentum³ as the dipole approximation is based on the limit in which the scale associated with the parent colour line is much larger than the transverse momentum of the emission.

3.3.5 Constructing the Algorithm

In the DGLAP picture, the differential probability for a final-state parton a to perform a branching is, following eq. (3.2),

$$\frac{d\mathcal{P}_{\text{branch},a}}{dQ^2} = \frac{\alpha_s}{2\pi} \frac{1}{Q^2} \int_{z_{\min}}^{z_{\max}} dz \sum_{b,c} P_{a \rightarrow bc}(z), \quad (3.14)$$

with a similar equation for an initial state parton b ,

$$\frac{d\mathcal{P}_{\text{branch},b}}{dQ^2} = \frac{\alpha_s}{2\pi} \frac{1}{Q^2} \int_x^1 \frac{dz}{z} \sum_{a,c} \frac{f_a(x/z, Q^2)}{f_b(x, Q^2)} P_{a \rightarrow bc}(z), \quad (3.15)$$

that can be calculated from eq. (3.7). To construct the probability distribution of a branching, the *no-emission probability*, denoted by the symbol Π , is derived. It represents the probability that the parton does not undergo any branching at scales larger than q^2 , given a maximum possible scale of Q_{\max}^2 . Due to probability conservation the no-emission probability plus the probability that the parton does radiate have to equal unity. When changing q^2 by a small amount, the probability for the parton to not emit radiation can only change by the branching probability $d\mathcal{P}_{\text{branch}}$ if there are no branchings above q^2 . With this in mind, the differential equation for the no-emission probability is

$$\frac{d(1 - \Pi(Q_{\max}^2, q^2))}{dq^2} = - \frac{d\Pi(Q_{\max}^2, q^2)}{dq^2} = \Pi(Q_{\max}^2, q^2) \frac{d\mathcal{P}_{\text{branch}}}{dq^2}. \quad (3.16)$$

³ Transverse in the sense of relative to the axis defined by the parent colour line.

The solutions are

$$\begin{aligned} \Pi(Q_{\max}^2, q^2) &= \exp\left(-\int d\mathcal{P}_{\text{branch}}\right) \\ &= \begin{cases} \exp\left(-\int_{q^2}^{Q_{\max}^2} \frac{\alpha_s}{2\pi} \frac{dQ^2}{Q^2} \int_x^1 \frac{dz}{z} \sum_{a,c} \frac{f_a(x/z, Q^2)}{f_b(x, Q^2)} P_{a\rightarrow bc}(z)\right) & \text{ISR} \\ \exp\left(-\int_{q^2}^{Q_{\max}^2} \frac{\alpha_s}{2\pi} \frac{dQ^2}{Q^2} \int_{z_{\min}}^{z_{\max}} dz \sum_{b,c} P_{a\rightarrow bc}(z)\right) & \text{FSR} \end{cases} \end{aligned} \quad (3.17)$$

for initial-state (ISR) and final-state radiation (FSR). With this result at hand, the steps that are performed in a parton shower are the following:

- The emissions are generated according to the probability distribution given by the derivative of the no-emission probability. For that purpose, its integral, the no-emission probability itself, needs to be inverted. Therefore, the equation $\Pi(Q_{\max}^2, q^2) = \mathcal{R}$ with \mathcal{R} being a random number in the interval $[0, 1]$ is solved for q^2 , the scale of the next emission. As the branching probability \mathcal{P} is too complicated to be inverted directly, a simpler function $\hat{\mathcal{P}}$, which overestimates \mathcal{P} , is used to generate q^2 . The excess probability is then removed by accepting the scale with the probability $\mathcal{P}/\hat{\mathcal{P}}$.
- Given the singular nature of the radiation kernels and the strong coupling, it is not possible for the parton shower to describe the behaviour at arbitrarily small scale. Therefore, some lower *parton shower cutoff* μ_c is needed, which is typically around 1 GeV. If the scale q^2 generated in the previous step is below the shower cutoff, the event is passed over to the hadronization.
- If the branching has been accepted the flavours, colours, and kinematics of the post-branching partons have to be determined. The first two depend only on the parent parton(s) and the type of branching, while the latter depends on the recoil strategy.
- After the branching has been performed, the daughter partons are now in turn considered as new parent partons to undergo further branchings. The procedure is repeated until no more branchings can be performed above μ_c .

To investigate how the shower acts on the input cross section of eq. (2.20), the *Sudakov form factor*, a purely perturbative object, is introduced

$$\Delta(Q_{\max}^2, q^2) = \exp\left(-\int_{q^2}^{Q_{\max}^2} \frac{\alpha_s}{2\pi} \frac{dQ^2}{Q^2} \int_{z_{\min}}^{z_{\max}} dz \sum_{a,b,c} P_{a\rightarrow bc}(z)\right). \quad (3.18)$$

Its relation to the no-emission probability is [55]

$$\Pi(Q_{\max}^2, q^2) = \frac{f(x, q^2)}{f(x, Q_{\max}^2)} \Delta(Q_{\max}^2, q^2). \quad (3.19)$$

For final-state radiation the Sudakov factor equals the no-emission probability, whereas for the initial-state case eq. (3.19) affirms that the shower is an evolution of the PDFs. Note that eq. (3.19) is not exact, unless the shower evolution equation corresponds to the DGLAP equation (3.7), i.e. the shower uses the same splitting kernels, couplings, and scales with which the PDFs have been fitted. The shower evolution equation is nevertheless consistent with the DGLAP equation, provided that the splitting kernels have the correct (DGLAP-kernel) behaviour close to $z = 1$, as has been shown in [71].

A specific phase-space point of the input cross section, calculated at LO, reads

$$d\sigma_B = f_0(x_0, \mu_F^2) |\mathcal{M}_0|^2 \mathcal{F}_0 dx_0 d\Phi_0 . \quad (3.20)$$

Here, one PDF factor has been suppressed for the sake of simplicity and readability. The subscript zero emphasizes that flavour and energy fraction correspond to the Born state Φ_0 ; subscript one will then correspond to the Born+1 state and so on. To take the parton shower into account an *evolution operator* \mathcal{S} , acting on the differential cross section in eq. (3.20), is introduced as

$$\mathcal{S}(\mu_F^2, \mu_c^2) [d\sigma_B] . \quad (3.21)$$

It acts between the factorization scale μ_F , characterizing the Born process, and the shower cutoff μ_c . The shower operator turns the inclusive prediction into an exclusive one. Considering all possible outcomes reads

$$\begin{aligned} \mathcal{S}(\mu_F^2, \mu_c^2) [d\sigma_B] = & \underbrace{\Pi(\mu_F^2, \mu_c^2) f_0(x_0, \mu_F^2) |\mathcal{M}_0|^2 \mathcal{F}_0 dx_0 d\Phi_0}_{\text{exclusive Born+0 at the cutoff}} \\ & + \underbrace{\Pi(Q_1^2, \mu_c^2) \alpha_s \frac{f_1(x_1, Q_1^2)}{f_0(x_0, Q_1^2)} \frac{P(z_1)}{Q_1^2} \Pi(\mu_F^2, Q_1^2) f_0(x_0, \mu_F^2) |\mathcal{M}_0|^2 \mathcal{F}_1 dx_1 d\Phi_1}_{\text{exclusive Born+1 at the cutoff}} \\ & + \underbrace{\mathcal{S}(Q_2^2, \mu_c^2) \left[\alpha_s \frac{f_2(x_2, Q_2^2)}{f_1(x_1, Q_2^2)} \frac{P(z_2)}{Q_2^2} \Pi(Q_1^2, Q_2^2) \alpha_s \frac{f_1(x_1, Q_1^2)}{f_0(x_0, Q_1^2)} \frac{P(z_1)}{Q_1^2} \Pi(\mu_F^2, Q_1^2) \right.}_{\text{inclusive Born+2}} \\ & \left. f_0(x_0, \mu_F^2) |\mathcal{M}_0|^2 \mathcal{F}_2 dx_2 d\Phi_2 \right]} . \end{aligned} \quad (3.22)$$

The shower operator has been applied iteratively to construct all terms. The first line corresponds to not having any branching above the shower cutoff, represented by the no-emission probability between the shower starting and cutoff scale. The result is an exclusive Born configuration. In the next line one branching at the scale Q_1^2 occurred with no other branching above the cutoff, which results in an exclusive Born+1 configuration. The last line corresponds to having two branchings at

the scales Q_1^2 and Q_2^2 , with no emissions inbetween. This is an inclusive Born+2 configuration, as the evolution has been stopped at scale Q_2^2 and no further no-emission probabilities have been generated. The shower operator will act on this state again, for further distinguishing between the exclusive Born+2 and inclusive Born+3 configurations.

Finally, eq. (3.19) is applied to transform the no-emission probabilities into Sudakov factors. This gives the final result, which shows how the parton shower evolves the PDFs down to the scale of the cutoff,

$$\begin{aligned}
\mathcal{S}(\mu_F^2, \mu_c^2) [d\sigma_B] = & \\
& f_0(x_0, \mu_c^2) \Delta(\mu_F^2, \mu_c^2) |\mathcal{M}_0|^2 \mathcal{F}_0 dx_0 d\Phi_0 \\
& + f_1(x_1, \mu_c^2) \Delta(Q_1^2, \mu_c^2) \alpha_s P(z_1)/Q_1^2 \Delta(\mu_F^2, Q_1^2) |\mathcal{M}_0|^2 \mathcal{F}_1 dx_1 d\Phi_1 \\
& + \mathcal{S}(Q_2^2, \mu_c^2) \left[f_2(x_2, Q_2^2) \alpha_s P(z_2)/Q_2^2 \Delta(Q_1^2, Q_2^2) \alpha_s P(z_1)/Q_1^2 \Delta(\mu_F^2, Q_1^2) |\mathcal{M}_0|^2 \right. \\
& \quad \left. \mathcal{F}_2 dx_2 d\Phi_2 \right]. \tag{3.23}
\end{aligned}$$

3.4 Combining Matrix Elements and Parton Showers

An active field of MCEG development is the combination of the parton shower with higher-order MEs. While fixed-order calculations are well suited to describe hard, well-separated jets, the main strength of parton showers is to capture the soft and collinear radiation by resumming large logarithms. To illustrate one of the main difficulties in combining the parton shower and MEs with different parton multiplicities, consider, as an example, the production of Z and $Z + 1$ at LO. Since the ME for $Z + 1$ is divergent, it is restricted to cover only the phase-space region with at least one hard resolved parton, which can for instance be defined by requiring a minimum transverse momentum. Simply combining a LO cross-section calculation for Z and $Z + 1$ production and showering both leads to *double counting* of emissions. The shower off the Z state can populate the same hard region of phase space as the $Z + 1$ state.

Diagrams, as the ones shown in fig. 3.4, are used to describe the accuracy obtained by combining the parton shower with MEs. Each box represents a set of amplitudes for a process with n final-state particles plus a specific number of additional legs k and loops l , as introduced in eq. (2.21). The ME entering the calculation of the Born cross section is represented by the bottom-left box, $|\mathcal{M}_n^{(0)}|^2$, with additional legs along the horizontal axis and loops along the vertical axis. Light-grey shaded boxes indicate that the ME is used in the calculation and dark grey represents the use of the shower approximation. The top left diagram in fig. 3.4 shows the accuracy of a pure parton shower, started off the LO cross section. In the following a few

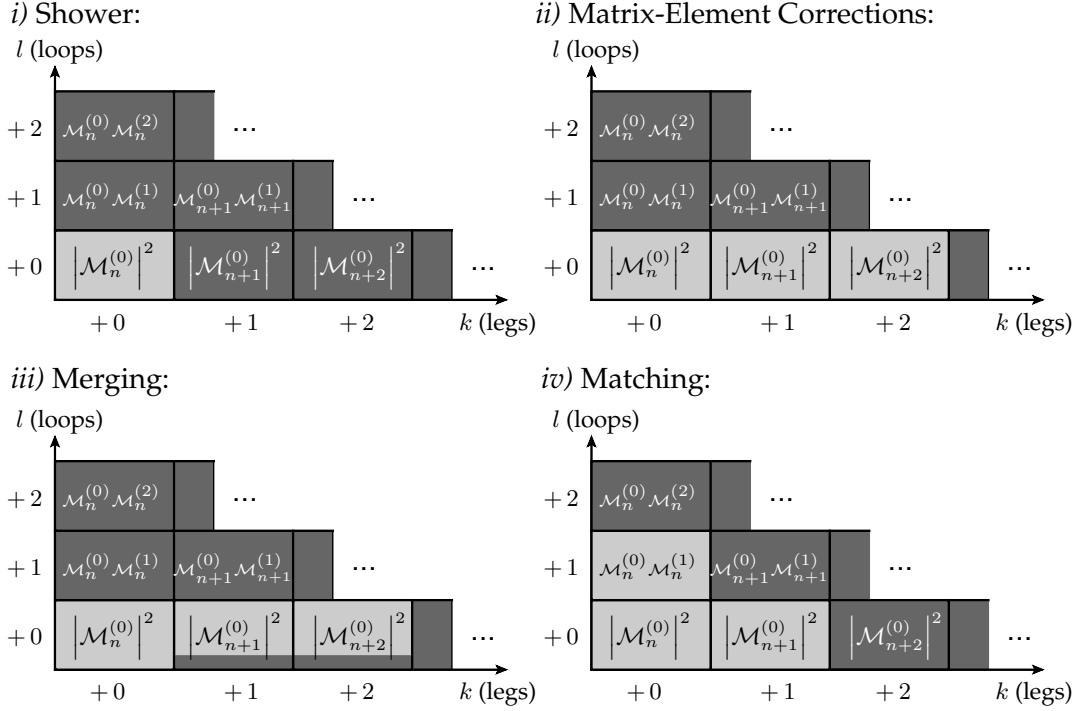


Figure 3.4: Coefficients of the perturbative series, see eq. (2.21). Loop contributions are abbreviated by $\mathcal{M}_m^{(l_1)} \mathcal{M}_m^{(l_2)} = 2 \text{Re}[\mathcal{M}_m^{(l_1)} \mathcal{M}_m^{(l_2)*}]$. Boxes shaded in light grey indicate that the ME calculation is included, whereas dark boxes are populated by the pure shower. The accuracy obtained by *i)* a pure shower, *ii)* MECs and *iii)* merging for the first two emission, and *iv)* a NLO matched calculation are shown.

methods for combining the shower with higher-order calculations are described briefly, with focus on the methods that are used in later chapters of the thesis.

To combine several LO calculations mainly two methods exist: *merging* is based on the concept of phase-space slicing, while *matrix-element corrections* (MECs) make use of unitarity. In the slicing approach the phase space is separated by the *merging scale* into two regions: a mostly hard part above the merging scale, described by the ME, and a mostly soft and collinear part below the merging scale, populated by the shower. This approach was first used in HERWIG++ to include a ME-correct first hard emission off the Born process [72, 73]. It has been generalized to include an arbitrary number of additional emissions, with CKKW [74], CKKW-L [75, 76], and MLM [77, 78] being the most well-known approaches to *multileg merging*. The bottom left diagram in fig. 3.4 shows the accuracy obtained when merging calculations for the Born process plus up to two additional emissions. In this case event samples for Born, Born+1, and Born+2 states are obtained with a ME generator. Each sample is dressed with Sudakov factors, whereby it is made sure that the samples do not produce overlap with each other. For instance a Born event, where the shower is generating an emission above the merging scale, is vetoed, as this phase-space point is present in the higher-multiplicity ME samples.

In the MECs method the all-orders approximation of the shower is used as a starting point. A finite multiplicative correction factor, namely the ratio of the ME to the shower approximation, is applied order by order in perturbation theory as the shower evolves. This leads to advantages over other LO merging schemes: no need for combining event samples with different multiplicities and improved no-emission probabilities as the correction factor is applied during the Sudakov veto algorithm. The top right diagram in fig. 3.4 shows the accuracy obtained when MECs are applied for the first two emission off the Born process⁴. The MECs approach, originally only used for the first emission beyond the hard process [66,79] has been extended in VINCIA to include an arbitrary number of additional final state emissions [80]. In chap. 4 a paper is presented, where the method has successfully been used for initial state radiation. An alternative strategy for MECs is investigated in chap. 5 and combined with CKKW-L merging.

The two traditional, subtraction-based, *matching* approaches for obtaining NLO accuracy for the hard process are MC@NLO [81,82] and POWHEG [83], shown in the bottom right diagram of fig. 3.4. Combining several NLO calculations with the shower in a consistent way is referred to as *NLO (multileg) merging*, see e.g. [84–86]. In fairly recent efforts even NNLO calculations matched to the shower have been presented [87–90].

3.5 Hadronization Models

Due to colour confinement (see also sec. 2.2), quarks and gluons do not exist as physically free states in nature, but are bound in colourless states, called hadrons. In the context of MCEGs *hadronization* or *fragmentation* denotes the process by which the partons at the end of the showering are transformed into a set of primary hadrons, which may decay further. By construction, this process happens at the cutoff scale of the shower, which is typically around 1 GeV. Hadronization can therefore not be described with perturbation theory. Instead, non-perturbative phenomenological models are deployed. The three most important models are described briefly in the following.

The oldest and simplest hadronization model, originally formulated by Field and Feynman [91,92], is called *independent fragmentation*⁵. As the name implies, the model assumes that the partons fragment independently of each other. In a first step, all gluons in the final state are split into quark-antiquark pairs which act, together with the other quarks in the event, as input to the fragmentation. To form hadrons, new pairs of quarks or diquarks are created out of the vacuum, with a transverse-momentum distribution according to a Gaussian. The fragmenting

⁴A infrared cutoff or regulator is typically used for the last corrected emission for higher orders. This is not shown in the diagram.

⁵A previous study by Artru and Mennessier [93] was the first model, but passed mostly unnoticed.

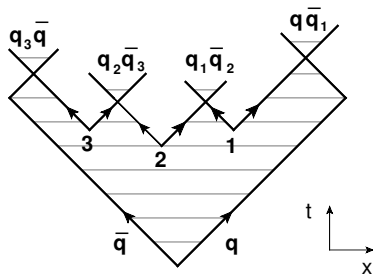


Figure 3.5: The dynamics of a string in space-time coordinates. As the $q\bar{q}$ pair moves apart the string (grey colour) is stretched between them, with the energy of the string being proportional to its length. Several string breaks occur via the creation of additional $q_i\bar{q}_i$ pairs.

quark is combined with the new (di)quark into a hadron, which leaves a (di)quark with less energy behind, that in turn will now fragment. The fragmentation stops once the leftover energy falls below a cutoff. The remainder of this process is a free (di)quark for every chain of fragmenting initial quarks. This, as well as the violation of momentum conservation are the two main weaknesses of the model. Nevertheless, independent fragmentation has been used quite successfully in describing the broad features of two- and three-jet final states in e^+e^- annihilation at moderate energies [55].

The underlying idea of the *string model of hadronization* is an important result of lattice QCD known as *linear confinement*, see for instance [94–96]: the potential of the field between the colour- and anticolour-charge of a singlet state grows linearly with the separation of the charges, for distances larger than about a femtometer. The field lines are believed to be compressed into tubelike regions, the strings, as observed by lattice QCD [97–101]. The potential of the flux tubes is $V(r) = \kappa r$, where the short-distance Coulomb term proportional to $1/r$ is neglected. The string constant κ , i.e. the amount of energy per unit length of the tube, is known to be $\kappa \approx 1 \text{ GeV/fm} \approx 0.2 \text{ GeV}^2$. As a consequence, if the two colour-charges of a singlet state move apart, the energy stored in the string increases constantly. With enough energy in the string, it will eventually be energetically favourable that the string breaks. As before, investigations in lattice QCD support the string model of hadronization [102–110]. Among several other hadronization models based on strings the so-called Lund model [12,13] is most widely used. In this picture gluons build kinks on the strings, which leads to the absorbance of very soft gluons. For the formation of hadrons, a phenomenological model based on a tunneling analogy provides fluctuations in the string in terms of gluons splitting into (di)quark pairs. Those break the sting by absorbing energy from it, see fig. 3.5. As in the independent fragmentation, the break-up pairs receive a transverse-momentum contribution according to a Gaussian distribution. String fragmentation is carried out iteratively from both string ends inwards to the center of the string, where the fragmentation off the two different sides is alternated randomly. In chap. 7 a publication is presented which deals with an extension to the conventional string fragmentation model.

A property of parton showers called *preconfinement* [111] is the basis of the *cluster model of hadronization*. For scales much smaller than the scale of the hard process,

clusters are formed from colour singlet combinations of partons. The invariant mass distribution of the clusters is universal, i.e. depends only on the current scale of the parton shower and not on the hard process. The distribution has a maximum at low masses of some GeV and falls fast for higher masses. Similar to independent fragmentation, the gluons in the final state are split into (di)quark pairs before forming the primary clusters from colour-connected parton pairs. Clusters with very high masses decay into lighter clusters, before decaying into hadrons. The cluster hadronization model is for instance used in HERWIG++ [14].

Antenna Showers and Matrix-Element Corrections

Combining higher-order QCD effects with the parton-shower framework has been the focus of attention in the development of MCEGs during the last decade(s): the matching of NLO calculations to the parton shower [50, 81, 83, 112–117] and the merging of LO [74, 75, 118–125] and NLO [85, 126–130] matched results for various jet multiplicities. Therefore, the development on the parton-shower side is rather manageable [68–70, 131, 132].

The traditional parton-shower approaches implemented in HERWIG++ [133, 134], PYTHIA 8 [60, 135], and SHERPA [136, 137] have been supplemented or replaced by CS-dipole- or antenna-based shower algorithms [68–70, 131, 132]. As those shower algorithms are based on dipole or antenna factorization respectively, the combination with higher-order QCD calculations becomes somewhat more feasible. Another intrinsic feature of those algorithms is the description of QCD coherence, see sec. 3.3.2.

The basis of the VINCIA parton shower is the colour-dipole picture in the large- N_C limit, introduced in sec. 3.3.3. The repeated factorization of two quantities permits to maintain a probabilistic description of emissions in the QCD antenna picture: the exact factorization of the emission phase space in terms of $2 \rightarrow 3$ branchings and the approximate factorization of amplitudes around the soft and collinear limits. This allows a treatment of QCD radiation that is separated from the remainder of the event. The VINCIA antenna shower has so far only been available for final-state radiation. One of the major complications when going from leptonic to hadronic initial states is the composite nature of the beams, which is accounted for by the PDFs introduced in sec. 2.4. PDFs are extracted from experimental data at relatively low scales, typically of the order of a few GeV, and evolved to higher scales with the help of DGLAP kernels. A direct inversion of the PDF evolution would therefore require the application of a DGLAP-based parton shower. However, as the antenna functions reproduce the DGLAP limits, the hadronic nature of the beams is still properly reflected in each evolution step by the presence of PDF ratios in the no-emission probability.

The state-of-the-art LO merging methods combine event samples with different parton multiplicities with the parton shower and remove the overlap between the

samples. As discussed in sec. 3.4, LO merging is based on phase-space slicing and therefore introduces a dependence on the merging scale. Consequently, the emission pattern of the shower is only corrected in the hard part of phase space. The no-emission probabilities are not altered by the LO merging. The iterative MECs method, introduced in sec. 3.4, corrects the emission as well as the no-emission patterns over the whole phase space in a single chain of evolution.

In the publication presented in sec. 4.1 we extend the antenna shower and iterated MECs method of VINCIA to hadronic initial states. More details of the VINCIA antenna shower algorithm for the initial state are given: the different steps to construct a branching are given in sec. 4.2, followed by details for initial-initial and initial-final antennae in secs. 4.3 and 4.4. The additional information is of a rather technical nature and is not required to follow the publication. Note that some information contained in the publication is repeated to achieve a mostly self-consistent write-up.

4.1 Published Material

Vincia for Hadron Colliders

Nadine Fischer, Stefan Prestel, Mathias Ritzmann, and Peter Skands

Published in The European Physics Journal C 76 no. 11 (2016) 589

DOI: 10.1140/epjc/s10052-016-4429-6

e-Print: [arXiv:1605.06142](https://arxiv.org/abs/1605.06142) [hep-ph]

With kind permission of The European Physical Journal (EPJ).

Begins overleaf.

VINCIA for hadron colliders

N. Fischer^{1,a}, S. Prestel², M. Ritzmann^{3,4}, P. Skands¹¹ School of Physics and Astronomy, Monash University, Clayton, VIC 3800, Australia² SLAC National Accelerator Laboratory, Menlo Park, CA 94025, USA³ Nikhef, Theory Group, Science Park 105, 1098 XG Amsterdam, The Netherlands⁴ Institut de Physique Théorique, CEA Saclay, 91191 Gif-sur-Yvette Cedex, FranceReceived: 15 June 2016 / Accepted: 10 October 2016 / Published online: 28 October 2016
© The Author(s) 2016. This article is published with open access at Springerlink.com

Abstract We present the first public implementation of antenna-based QCD initial- and final-state showers. The shower kernels are $2 \rightarrow 3$ antenna functions, which capture not only the collinear dynamics but also the leading soft (coherent) singularities of QCD matrix elements. We define the evolution measure to be inversely proportional to the leading poles, hence gluon emissions are evolved in a p_{\perp} measure inversely proportional to the eikonal, while processes that only contain a single pole (e.g., $g \rightarrow q\bar{q}$) are evolved in virtuality. Non-ordered emissions are allowed, suppressed by an additional power of $1/Q^2$. Recoils and kinematics are governed by exact on-shell $2 \rightarrow 3$ phase-space factorisations. This first implementation is limited to massless QCD partons and colourless resonances. Tree-level matrix-element corrections are included for QCD up to $\mathcal{O}(\alpha_s^4)$ (4 jets), and for Drell–Yan and Higgs production up to $\mathcal{O}(\alpha_s^3)$ ($V/H + 3$ jets). The resulting algorithm has been made publicly available in VINCIA 2.0.

Contents

1	Introduction	2
2	VINCIA’s Antenna showers	3
2.1	Notation and conventions	4
2.2	Initial–initial configurations	5
2.3	Initial–final configurations	6
2.4	Final–final configurations	8
2.5	The shower generator	9
2.6	Colour coherence and colour indices	10
2.7	Uncertainty estimations	11
2.8	Limitations	12

3	Matrix-element corrections	12
3.1	Hard jets in non-QCD processes	13
3.2	Strong ordering compared with tree-level matrix elements	14
3.3	Smooth ordering compared with tree-level matrix elements	17
3.4	Smooth ordering vs. strong ordering	20
	Leading logarithms	20
	Hadronic Z decays	22
	Drell–Yan	23
3.5	Hard jets in QCD processes	23
3.6	Matrix-element corrections with MADGRAPH 4	23
4	Preliminary results and tuning	25
4.1	The strong coupling	25
4.2	VINCIA 2.0 default tune	27
	Hadronic Z decays	27
	Drell–Yan	30
	Underlying event	31
	QCD jets	34
5	Summary and conclusions	37
A	Details of the shower algorithm	37
A.1	Construction of the post-branching momenta	38
	Initial–initial antennae	38
	Initial–final antennae	38
	Final–final antennae	38
A.2	Collinear limits of the antenna functions	39
	Initial–initial antennae	39
	Initial–final antennae	39
	Final–final antennae	40
A.3	Phase-space variables and limits	40
B	Comparison with matrix elements	41
	References	44

Virtual Numerical Collider with Interleaved Antennae: <http://vincia.hepforge.org>.^a e-mail: nadine.fischer@monash.edu

1 Introduction

The basic differential equations governing renormalisation-group-improved (resummed) perturbation theory for initial-state partons were derived in the 1970s [1–3]. The resulting DGLAP¹ equations remain a cornerstone of high-energy phenomenology, underpinning our understanding of perturbative corrections and scaling in many contexts, in particular the structure of QCD jets, parton distribution functions, and fragmentation functions.

In the context of event generators [4], DGLAP splitting kernels are still at the heart of several present-day parton showers (including, e.g., [5–9]). Although the DGLAP kernels themselves are derived in the collinear (small-angle) limit of QCD, which is dominated by radiation off a single hard parton, the destructive-interference effects [10] which dominate for wide-angle soft-gluon emission can also be approximately accounted for in this formalism; either by choosing the shower evolution variable to be a measure of energy times angle [11] or by imposing a veto on non-angular-ordered emissions [12]. The resulting parton-shower algorithms are called *coherent*. A third alternative, increasingly popular and also adopted in this work, is to replace the parton-based DGLAP picture by so-called colour dipoles [13] (known as antennae in the context of fixed-order subtraction schemes [14–18]),² which incorporate all single-unresolved (i.e., both soft and collinear) limits explicitly. In the context of shower algorithms, this approach was originally pioneered by the ARIADNE program [13, 21] and is now widely used [22–30]. We note that the word “coherence” is used in different contexts, such as angular ordering. When we use coherence in the context of antenna functions, we define it at the lowest level, as follows: antenna functions sum up the radiation from two sides of the leading- N_C dipole coherently, at the amplitude level; see also Ref. [27].

In addition, shower algorithms rely on several further improvements that go beyond the LO DGLAP picture, including: exact momentum conservation (related to the choice of recoil strategy), colour-flow tracing (in the leading- N_C limit, related to coherence at both the perturbative and non-perturbative levels), and higher-order-improved scale choices (including the use of $\mu_R = p_\perp$ for gluon emissions and the so-called CMW scheme translation which applies in the soft limit [31, 32]). Each of these are associated with ambiguities, with Sect. 2 containing the details of our choices and motivations.

¹ Dokshitzer–Gribov–Lipatov–Altarelli–Parisi. We mourn the recent passing of Guido Altarelli (1941–2015), a founder of this field and a great inspirer.

² Note that a “Catani–Seymour” dipole [19, 20] corresponds roughly speaking to a partial-fractioning of an antenna or Lund colour dipole into two pieces.

Finally, in the context of initial-state parton showers, the evolution from a high factorisation scale to a low one corresponds to an evolution in spacelike (negative) virtualities, “backwards” towards lower resolution. The correct equations for backwards parton-shower evolution were first derived by Sjöstrand [33]; in particular it is essential to multiply the evolution kernels by ratios of parton distribution functions (PDFs), to recover the correct low-scale structure of the incoming beam hadrons. We shall use a generalisation of backwards evolution to the case of simultaneous evolution of the two incoming-hadron PDFs, similar to that presented in [26].

The merits of different shower algorithms is a frequent topic of debate, with individual approaches differing by which compromises are made and by the effective higher-order terms that are generated. We emphasise the following three attractive properties of antenna showers:

- They are intrinsically coherent, in the sense that the correct eikonal structure is generated for each single-unresolved soft gluon, up to corrections suppressed by at least $1/N_C^2$. Especially for initial–final antennae, where gluon emission off initial- and final-state legs interfere, has some challenges.³ In the final–final case which was already testable with previous VINCIA versions, a recent OPAL study of 4-jet events [37] found good agreement between VINCIA and several recently proposed coherence-sensitive observables [38].
- They are extremely simple, relying on local and universal $2 \rightarrow 3$ phase-space maps which represent an exact factorisation of the n -particle phase spaces not only in the soft and collinear regions but over all of phase space. This makes for highly tractable analytical expansions on which our accompanying matrix-element correction formalism is based [39]. The pure shower is in some sense merely a skeleton for generating the leading singularities, with corrections for both hard and soft emissions regarded as an intrinsic part of the formalism, restoring

³ Older parton-shower models often treat initial-state (ISR) and final-state (FSR) evolution in disjoint sequences. In this case, it is challenging to ensure that FSR evolution from the enlarged and changed parton ensemble after ISR evolution recovers the coherent features. Implementations of a combined simultaneous evolution chain for ISR and FSR may also be challenging. The current p_\perp -ordered showers in PYTHIA 8 [8, 34, 35] do, for example, not account for the coherence structure of the hardest gluon emission in $t\bar{t}$ events [36]. In contrast, we suspect that due to the fact that physical output states (parsed through hadronisation) are only constructed at the end of the evolution, the angular-ordered algorithms of HERWIG [6] and HERWIG++ [7] produce coherent sequences of emission angles in IF configurations correctly. This assessment relies on the assumption that the algorithms ensure that the angular constraints on final-state emission variables are unchanged by the ISR shower evolution, and vice versa.

the emission patterns to at least LO accuracy up to the matched orders.

- There is a close correspondence with the antenna-subtraction formalism used in fixed-order calculations [16–18], which is based on the same subtraction terms and phase-space maps. This property was already utilised in [40] to implement a simple and highly efficient procedure for NLO corrections to gluon emission off a $q\bar{q}$ antenna. Highly non-trivial fixed-order results which have recently been obtained within the antenna formalism include NNLO calculations for $Z + \text{jet}$ [41], $H + \text{jet}$ [42] (for $m_t \rightarrow \infty$), $gg \rightarrow gg$ [43], and leading-colour $q\bar{q} \rightarrow t\bar{t}$ [44] production at hadron colliders. While it is (far) beyond the scope of the present work to connect directly with these calculations, their feasibility is encouraging to us, and provides a strong motivation for future developments of the antenna-shower formalism.

The aim with this work is to present the first full-fledged and publicly available antenna shower for hadron colliders, extending from previous work on final-state antenna showers developed in [23, 39] and building on the proof-of-concept studies for hadronic initial states reported in [29, 45]. The model is implemented in—and defines—version 2.0 of the VINCIA plug-in to the PYTHIA 8 event generator [34]. This article is also intended to serve as the first physics manual for VINCIA 2.0. It is accompanied by a more technical HTML User Reference documenting each of the user-modifiable parameters and switches at the technical level [46] and an author’s compendium documenting more detailed algorithmic aspects [47]; both of these auxiliary documents are included with the code package, which is publicly available via the HepForge repository at <http://vincia.hepforge.org>.

In Sect. 2 we introduce the basic antenna-shower formalism, including our notation and conventions. We mainly focus on initial–initial and initial–final configurations and summarise final–final configurations only briefly, as a more extensive description is available in [23, 39]. Our conventions for colour flow are specified in Sect. 2.6. These are intended to maximise information on coherence while simultaneously generating a state in which all colour tags obey the index-based treatment of subleading-colour correlations proposed in [48, 49]. By assigning these indices after each branching and tracing them through the shower evolution, rather than statistically assigning them at the end of the evolution as was done in [49], we remove the risk of accidentally generating unphysical colour flows.⁴ We therefore believe the procedure proposed here represents an improvement on the one in [49].

⁴ E.g., in our treatment the case illustrated by [49, Fig. 19b] cannot occur: $Z \rightarrow qg\bar{q}$ with the two gluons collinear to each other, non-collinear to any of the quarks, and in a singlet state.

The extension of VINCIA’s automated treatment of perturbative shower uncertainties to hadron collisions is documented in Sect. 2.7.

In Sect. 3, we present the extension of the GKS⁵ matrix-element-correction (MEC) formalism [39] to initial-state partons, starting with the case of a basic process accompanied by one or more jets whose scales are nominally harder than that of the basic process in Sect. 3.1. In Sect. 3.2, we present some basic numerical comparisons between tree-level matrix elements and our shower formalism expanded to the equivalent level (i.e., setting all Sudakov factors and coupling constants to unity), to validate that combinations of $2 \rightarrow 3$ antenna branchings do produce a reasonable agreement with the full n -parton matrix elements. We discuss our extension of “smooth ordering” [39] to reach non-ordered parts of phase space in Sect. 3.3, again focusing on the initial-state context. Section 3.5 summarises the application of smooth ordering to the specific case of hard jets in QCD processes. In Sect. 3.6 we extend and document VINCIA’s existing use of MADGRAPH 4 [50] matrix elements.

The set of numerical parameters which define the default “tune” of VINCIA 2.0 is documented in Sect. 4, including our preferred convention choice for α_s , the most important parameter of any shower algorithm. A set of comparisons to a selection of salient experimentally measured distributions for hadronic Z decays, Drell–Yan, and QCD jet production are included to document and validate the performance of the shower algorithm with these parameters.

Finally, in Sect. 5, we summarise and give an outlook. Additional material, as referred to in the text, is collected in the Appendices.

2 VINCIA’s Antenna showers

A QCD antenna represents a colour-connected parton pair which undergoes a (coherent) $2 \rightarrow 3$ branching process [13–16, 51]. In contrast to conventional shower models (including both DGLAP and Catani–Seymour dipole ones) which single out one parton as the “emitter” with one (or more) other partons acting as “recoiler(s)”, the antenna formalism treats the two pre-branching “parent” partons as a single entity, with a single radiation kernel (an antenna function) driving the amount of radiation and a single “kinematics map” governing the exact relation between the pre-branching and post-branching momenta. Formally, the antenna function represents the approximate (to leading order in the vanishing invariant(s)) factorisation between the pre- and post-branching squared amplitudes, while the kinematics map encapsulates the exact on-shell factorisation of the $(n + 1)$ -

⁵ Giele–Kosower–Skands [39].

parton phase space into the n -parton one and the $(2 \rightarrow 3)$ antenna phase space.

Note that for branching processes involving flavour changes of the parent partons, such as $g \rightarrow q\bar{q}$, a distinction between “emitter” and “recoiler” and thus a treatment independent of the above description is possible. However, this is not compulsory and we are therefore still using the same $(2 \rightarrow 3)$ antenna phase-space and kinematics map as in the case of gluon emission. Moreover, applying a $2 \rightarrow 3$ branching amounts to using the lowest number of involved partons which admit an on-shell to on-shell mapping.

In this section we briefly review the notation and conventions that will be used throughout this paper (Sect. 2.1), followed by definitions for all of the phase-space convolutions or factorisations, respectively, antenna functions, and evolution variables on which VINCIA’s treatment of initial–initial, initial–final, and final–final configurations are based (Sects. 2.2, 2.3, and 2.4). The expressions for final–final configurations are unchanged relative to those in [23, 39], with the default antenna functions chosen to be those of [52] averaged over helicities. Some further details on the explicit kinematics constructions are collected in Appendix A. The explicit form of the shower-generation algorithm is presented in Sect. 2.5. Finally, we round off in Sect. 2.8 with comments on some features of earlier incarnations of VINCIA which have not (yet) been made available in VINCIA 2.0.

2.1 Notation and conventions

We use the following notation for labelling partons: capital letters for pre-branching (parent) and lower-case letters for post-branching (daughter) partons. We label incoming partons with the first letters of the alphabet, a, b , and outgoing ones with i, j, k . Thus, for example, a branching occurring in an initial–final antenna (a colour antenna spanned between an initial–state parton and a final–state one) would be labelled $AK \rightarrow ajk$. This is consistent with the conventions used in the most recent VINCIA papers [29, 39].⁶ The recoiler or recoiling system will be denoted by R and r respectively (compared with R' and R in [29]).

We restrict our discussion to massless partons and denote the Lorentz-invariant momentum four-product between two partons 1 and 2 by

$$s_{12} \equiv 2p_1^\mu p_{2\mu} = (p_1 + p_2)^2, \quad (1)$$

which is always positive regardless of whether the partons involved are in the initial or final state. Momentum conservation then yields

⁶ The earliest VINCIA paper on final–final antennae [23] used an alternative convention: $\hat{a} + \hat{b} \rightarrow a + r + b$.

$$\text{FF} : s_{IK} = s_{ij} + s_{jk} + s_{ik}, \quad (2)$$

$$\text{IF} : s_{AK} = s_{ak} + s_{aj} - s_{jk}, \quad (3)$$

$$\text{II} : s_{AB} = s_{ab} - s_{aj} - s_{jb}, \quad (4)$$

for final–final (FF), initial–final (IF), and initial–initial (II) branchings, respectively.

The evolution variable, which we denote t , is evaluated on the post-branching partons, hence, e.g., $t_{\text{FF}} = t(s_{ij}, s_{jk})$. It serves as a dynamic factorisation scale for the shower, separating resolved from unresolved regions. As such, it must vanish for singular configurations. Generally, we define the evolution variable for each branching type to vanish with the same power of the momentum invariants as the leading poles of the corresponding antenna functions, see below. The complementary phase-space variable will be denoted ζ .

Colour Factors \mathcal{C} We use the following convention: for gluon emission the colour factors are $\mathcal{C} = C_A = 3$ for gluon-only antennae, $\mathcal{C} = 2C_F = 8/3$ for quark-only antennae, and the mean, $\mathcal{C} = (C_A + 2C_F)/2$, for quark-gluon antennae. For gluon splitting the colour factor is $\mathcal{C} = 2T_R = 1$. Note that symmetry factors, taking into account that gluons contribute to two antennae, are included in the antenna functions.

Shower Basics A shower algorithm is based on the probability that no branching occurs between two scales t_n and t_{n+1} , with $t_n > t_{n+1}$. (For an introduction to conventional showers, see, e.g., [53, Chp. 40] or [4]. For antenna showers more specifically, see [39, 40]). In the case of initial-state radiation in the antenna picture the no-emission probability is

$$\Pi_n(t_n, t_{n+1}) = \exp \left(- \sum_i \in \{n \rightarrow n+1\} \int_{t_{n+1}}^{t_n} d\Phi_{\text{ant}} 4\pi\alpha_s(t) \mathcal{C} \bar{a}_i(t, \zeta) R_{\text{pdf}i} \right), \quad (5)$$

with the colour- and coupling-stripped antenna function \bar{a} and the (double) ratio of PDFs,

$$R_{\text{pdf}} = \frac{f_a(x_a, t) f_b(x_b, t)}{f_A(x_A, t) f_B(x_B, t)}. \quad (6)$$

Note that although the integral over $d\Phi_{\text{ant}}$ in Eq. (5) is three-dimensional, we only explicitly wrote down the boundaries in the evolution variable t , with integration over the complementary invariant, ζ , and over the azimuth angle, ϕ , implied. Given specific choices for t and ζ as functions of the phase-space invariants, the boundaries of the ζ integral are derived from energy-momentum conservation, as usual for shower algorithms (see, [4, 23, 47, 54]). This generates modifications to the LL structure which—since (E, p) conservation is a genuine physical effect—is expected to improve the shower approximation at the subleading level. (We are not aware of a rigorous proof of this statement, however.)

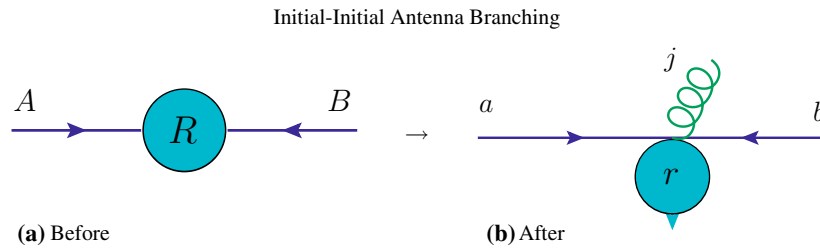


Fig. 1 Illustration of pre-branching (left) and post-branching (right) on-shell momenta, for an initial–initial antenna branching, emphasising the transverse kick imparted to the hard system, R , which consists of all particles produced in the collision $A + B \rightarrow R$. The hard system is treated as a rigid body (i.e., any internal invariants are not modified) by

the branching. It is subjected to a single overall Lorentz transformation, $R \rightarrow r$, equivalent to a frame reinterpretation required to orient the new incoming partons along the z axis. Note that we define our kinematics maps to preserve not only the invariant mass but also the rapidity of the recoiling system: $m_r^2 = m_R^2$ and $y_r = y_R$, cf. Appendix A.1

The sum in Eq. (5) runs over all possible $(n + 1)$ -parton states that can be created from the n -parton state, and will be implicit from here on. $d\Phi_{\text{ant}}$ is the antenna phase space, providing a mapping from two to three on-shell partons while preserving energy and momentum. The specific form for the two configurations, initial–initial and initial–final, are defined below, along with the specific forms of the evolution variable.

We define the Sudakov factor as

$$\Delta_n(t_n, t_{n+1}) = \exp \left(- \sum_{i \in \{n \rightarrow n+1\}} \int_{t_{n+1}}^{t_n} d\Phi_{\text{ant}} \frac{x_A x_B}{x_a x_b} 4\pi \alpha_s(t) C \tilde{a}_i(t, \zeta) \right). \tag{7}$$

This object does not depend on parton distribution functions or other non-perturbative input and may thus be regarded as a purely perturbative object. Following the arguments of [30], we define the no-emission probability in terms of the Sudakov factor, as follows (generalised from [55]):

$$\Pi_n(t_n, t_{n+1}) = \frac{f_A(x_A, t_{n+1}) f_B(x_B, t_{n+1})}{f_A(x_A, t_n) f_B(x_B, t_n)} \Delta_n(t_n, t_{n+1}). \tag{8}$$

This in turn implicitly defines the evolution equation for the antenna shower, which, as shown in [30], is consistent with the DGLAP equation, provided the antenna functions used in VINCIA have the correct (AP-kernel) behaviour close to $z = 1$, where z is an energy-sharing variable.⁷ This is shown in Appendix A.2, in which the collinear limits of all antenna functions used in this work are given. Note that a similar strategy of using Eq. (8) as a definition was also used when

⁷ The resulting evolution equation will contain objects that are very close to the unintegrated parton densities of [56,57].

defining perturbative states in [58]. For final–final configurations, Eq. (8) simplifies to $\Pi_n(t_n, t_{n+1}) = \Delta_n(t_n, t_{n+1})$.

2.2 Initial–initial configurations

We denote the pre- and post-branching partons participating in an initial–initial branching by $AB \rightarrow abj$ and the (system of) particles produced by the collision by $R \rightarrow r$, cf. the illustrations in Fig. 1. In the following, we specify the phase-space convolution, antenna functions, evolution variables and the resulting no-emission probability.

Phase space The phase-space convolution reads

$$\int \frac{dx_a}{x_a} \Theta(1-x_a) \frac{dx_b}{x_b} \Theta(1-x_b) d\Phi_2(p_a, p_b \rightarrow p_j, p_r) = \int \frac{dx_A}{x_A} \Theta(1-x_A) \frac{dx_B}{x_B} \Theta(1-x_B) d\Phi_1(p_A, p_B \rightarrow p_R) d\Phi_{\text{ant}}^{\text{II}} \tag{9}$$

with the antenna phase space

$$d\Phi_{\text{ant}}^{\text{II}} = \frac{1}{16\pi^2} \frac{s_{AB}}{s_{ab}^2} \Theta(x_a - x_A) \Theta(x_b - x_B) ds_{aj} ds_{jb} \frac{d\phi}{2\pi}. \tag{10}$$

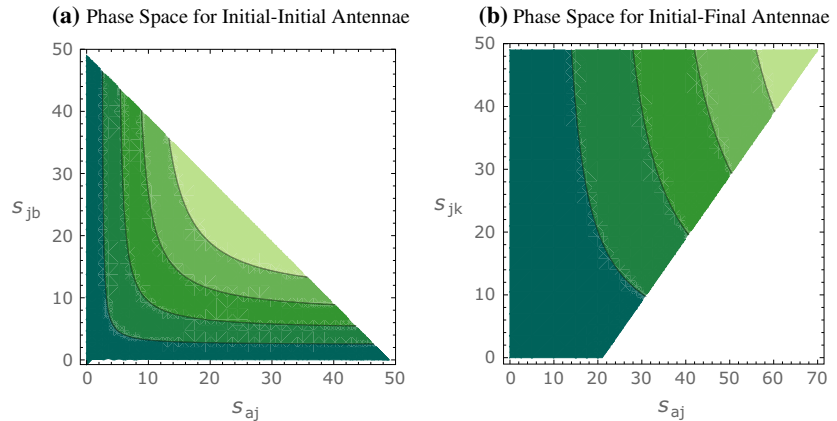
See Appendix A.1 for the explicit construction of the post-branching momenta.

Antenna functions The gluon-emission antenna functions are

$$\tilde{a}_{q\bar{q}g}^{\text{II}} = \tilde{a}(a_q, b_{\bar{q}}, j_g) = \frac{1}{s_{AB}} \left(2 \frac{s_{ab}s_{AB}}{s_{aj}s_{jb}} + \frac{s_{jb}}{s_{aj}} + \frac{s_{aj}}{s_{jb}} \right), \tag{11}$$

$$\begin{aligned} \tilde{a}_{ggg}^{\text{II}} &= \tilde{a}(a_g, b_g, j_g) \\ &= \frac{1}{s_{AB}} \left(2 \frac{s_{ab}s_{AB}}{s_{aj}s_{jb}} + 2 \frac{s_{jb}}{s_{aj}} \frac{s_{ab}}{s_{AB}} + 2 \frac{s_{jb}}{s_{aj}} \frac{s_{AB}}{s_{ab} + s_{aj}} \right. \\ &\quad \left. + 2 \frac{s_{aj}}{s_{jb}} \frac{s_{ab}}{s_{AB}} + 2 \frac{s_{aj}}{s_{jb}} \frac{s_{AB}}{s_{ab} + s_{jb}} \right), \end{aligned} \tag{12}$$

Fig. 2 Contours of constant gluon-emission evolution variable for **a** initial–initial and **b** initial–final configurations. For **a** the recoiler is chosen to be a Higgs boson, $s_{AB} = m_H^2$, and for **b** $s_{AK} = 10500 \text{ GeV}^2$ and $x_A = 0.3$. For both cases, the total hadronic $\sqrt{s} = 7 \text{ TeV}$



$$\begin{aligned} \bar{a}_{qg}^{\text{II}} = \bar{a}(a_q, b_g, j_g) &= \frac{1}{s_{AB}} \left(2 \frac{s_{ab}s_{AB}}{s_{aj}s_{jb}} + \frac{s_{jb}}{s_{aj}} \right. \\ &\left. + 2 \frac{s_{aj}}{s_{jb}} \frac{s_{ab}}{s_{AB}} + 2 \frac{s_{aj}}{s_{jb}} \frac{s_{AB}}{s_{ab} + s_{jb}} \right). \end{aligned} \tag{13}$$

The antenna function for a gluon evolving backwards to a quark (and similarly to an antiquark) is

$$\bar{a}_{q\bar{q}}^{\text{II}} = \bar{a}(a_q, b_x, j_q) = \frac{1}{2s_{aj}} \frac{s_{jb}^2 + s_{ab}^2}{s_{AB}^2}, \tag{14}$$

and for a quark evolving backwards into a gluon

$$\bar{a}_{g\bar{q}}^{\text{II}} = \bar{a}(a_g, b_x, j_{\bar{q}}) = \frac{1}{s_{AB}} \left(-2 \frac{s_{jb}s_{AB}}{s_{aj}(s_{ab} - s_{aj})} + \frac{s_{ab}}{s_{aj}} \right). \tag{15}$$

In Appendix A.2 we show that the antenna functions correctly reproduce the DGLAP splitting kernels in the collinear limit.

Evolution variables We evolve gluon emission in the physical transverse momentum of the emission (relative to the p_a - p_b -axis),

$$t_{\text{II}}^{\text{emit}} = p_{\perp \text{II}}^2 = \frac{s_{aj}s_{jb}}{s_{ab}}, \tag{16}$$

which exhibits the same “antenna-like” $a \leftrightarrow b$ symmetry as the leading (double) poles of the corresponding antenna functions, Eqs. (11)–(13) above. The upper phase-space limit for this variable is $p_{\perp \text{II}}^2 \leq (s - s_{AB})^2 / (4s)$, where s denotes the hadronic centre-of-mass energy squared.

Figure 2a shows constant contours of $p_{\perp \text{II}}^2$, as a function of the two branching invariants s_{aj} and s_{jb} . As the phase space is symmetric in s_{aj} and s_{jb} it has a triangular shape whose hypotenuse is defined by the upper phase-space bound $s_{AB} + s_{aj} + s_{jb} \leq s$. For branchings with flavour changes in the initial state (gluon evolving backwards to a quark or vice versa) for which the antenna functions only contain single poles, cf. Eqs. (14)–(15) above, we use the corresponding invariant, s_{aj} or s_{jb} , respectively,

$$t_{\text{II}}^{\text{conv}} = Q_{\text{II}}^2 = \begin{cases} s_{aj} & \text{for } a \text{ converting to/from a gluon} \\ s_{jb} & \text{for } b \text{ converting to/from a gluon} \end{cases}, \tag{17}$$

where the phase-space limit is $s_{xj} \leq s - s_{AB}$. Note that the conversion measure is equivalent to the Mandelstam $|t|$ variable for the relevant diagrams. Since only one parton can convert at a time—either A or B —these diagrams are unique, with no interferences, as is also reflected by the corresponding antenna functions containing only single (collinear) poles.

No-emission probability With the definitions given above (5) for initial–initial configurations reads

$$\begin{aligned} \Pi_n(t_n, t_{n+1}) &= \exp \left(- \int_{s_{aj_{n+1}}}^{s_{aj_n}} ds_{aj} \Theta(x_a - x_A) \right. \\ &\times \int_{s_{jb_{n+1}}}^{s_{jb_n}} ds_{jb} \Theta(x_b - x_B) \int_0^{2\pi} \frac{d\phi}{2\pi} \\ &\times \frac{\alpha_s(t)}{4\pi} \frac{s_{AB}}{s_{ab}^2} \mathcal{C} \bar{a}(s_{aj}, s_{jb}, s_{AB}) \frac{f_a(x_a, t)}{f_A(x_A, t)} \\ &\left. \times \frac{f_b(x_b, t)}{f_B(x_B, t)} \right), \end{aligned} \tag{18}$$

with $t = t_{\text{II}}(s_{aj}, s_{jb}, s_{ab})$. The subscript of the s_{aj} and s_{jb} integration limits indicates the association with the branching scales t_n and t_{n+1} , respectively.

2.3 Initial–final configurations

In traditional (DGLAP-based) parton-shower formulations, the radiation emitted by a colour line flowing from the initial to the final state is handled by two separate algorithms, one for ISR and one for FSR. Coherence can still be imposed by letting these algorithms share information on the angles between colour-connected partons and limiting radiation to

In the following, we describe the phase-space convolution, antenna functions and resulting no-emission probability used for initial–final evolution.

Phase space The phase-space convolution reads

$$\int \frac{dx_a}{x_a} \Theta(1-x_a) \frac{dx_B}{x_B} \Theta(1-x_B) d\Phi_3(p_a, p_B \rightarrow p_R, p_j, p_k) = \int \frac{dx_A}{x_A} \Theta(1-x_A) \frac{dx_B}{x_B} \Theta(1-x_B) d\Phi_2(p_A, p_B \rightarrow p_R, p_K) d\Phi_{\text{ant}}^{\text{IF}} \tag{19}$$

with the antenna phase space

$$d\Phi_{\text{ant}}^{\text{IF}} = \frac{1}{16\pi^2} \frac{s_{AK}}{(s_{AK} + s_{jk})^2} \Theta(x_a - x_A) ds_{aj} ds_{jk} \frac{d\phi}{2\pi} \tag{20}$$

See Appendix A.1 for the explicit construction of the post-branching momenta.

Antenna functions The gluon-emission antenna functions are

$$\bar{a}_{qqg}^{\text{IF}} = \bar{a}(a_q, k_q, j_g) = \frac{1}{s_{AK}} \left(2 \frac{s_{ak}s_{AK}}{s_{aj}s_{jk}} + \frac{s_{jk}}{s_{aj}} + \frac{s_{aj}}{s_{jk}} \right), \tag{21}$$

$$\bar{a}_{ggg}^{\text{IF}} = \bar{a}(a_g, k_g, j_g) = \frac{1}{s_{AK}} \left(2 \frac{s_{ak}s_{AK}}{s_{aj}s_{jk}} + 2 \frac{s_{jk}}{s_{aj}} \frac{s_{ak}}{s_{AK}} + 2 \frac{s_{jk}s_{AK}}{s_{aj}(s_{AK} + s_{jk})} + \frac{s_{aj}}{s_{jk}} \frac{s_{ak}}{s_{AK}} \right), \tag{22}$$

$$\bar{a}_{qgg}^{\text{IF}} = \bar{a}(a_q, k_g, j_g) = \frac{1}{s_{AK}} \left(2 \frac{s_{ak}s_{AK}}{s_{aj}s_{jk}} + \frac{s_{jk}}{s_{aj}} + \frac{s_{aj}}{s_{jk}} \frac{s_{ak}}{s_{AK}} \right), \tag{23}$$

$$\bar{a}_{gqg}^{\text{IF}} = \bar{a}(a_g, k_q, j_g) = \frac{1}{s_{AK}} \left(2 \frac{s_{ak}s_{AK}}{s_{aj}s_{jk}} + 2 \frac{s_{jk}}{s_{aj}} \frac{s_{ak}}{s_{AK}} + 2 \frac{s_{jk}s_{AK}}{s_{aj}(s_{AK} + s_{jk})} + \frac{s_{aj}}{s_{jk}} \right). \tag{24}$$

The antenna function for a gluon evolving backwards to a quark (and similarly to an antiquark) is

$$\bar{a}_{q\bar{q}q}^{\text{IF}} = \bar{a}(a_q, k_x, j_q) = \frac{1}{2s_{aj}} \frac{s_{jk}^2 + s_{ak}^2}{s_{AK}^2}, \tag{25}$$

for a quark evolving backwards to a gluon

$$\bar{a}_{g\bar{x}\bar{q}}^{\text{IF}} = \bar{a}(a_g, k_x, j_{\bar{q}}) = \frac{1}{s_{AK}} \left(-2 \frac{s_{jk}(s_{AK} - s_{aj})}{s_{aj}(s_{AK} + s_{jk})} + \frac{s_{ak}}{s_{aj}} \right), \tag{26}$$

and for a final-state gluon splitting

$$\bar{a}_{x\bar{q}q}^{\text{IF}} = \bar{a}(a_x, k_q, j_{\bar{q}}) = \frac{1}{2s_{jk}} \frac{s_{aj}^2 + s_{ak}^2}{s_{AK}^2}. \tag{27}$$

In Appendix A.2 we show that the antenna functions correctly reproduce the DGLAP splitting kernels in the collinear limit.

Evolution variables We evolve gluon emission in the transverse momentum of the emission, defined as

$$t_{\text{IF}}^{\text{emit}} = p_{\perp \text{IF}}^2 = \frac{s_{aj}s_{jk}}{s_{AK} + s_{jk}} = \frac{s_{aj}s_{jk}}{s_{aj} + s_{ak}}, \tag{28}$$

with the phase-space limit $p_{\perp \text{IF}}^2 \leq s_{AK}(1-x_A)/x_A$. Figure 2b shows constant contours of $p_{\perp \text{IF}}^2$, as a function of the two branching invariants s_{aj} and s_{jk} . Note that the phase space is limited by $s_{jk} \leq s_{AK}(1-x_A)/x_A$ and $s_{aj} \leq s_{AK} + s_{jk}$.

For branchings with flavour changes in the initial or final state we use the corresponding invariant, s_{aj} or s_{jk} , respectively,

$$t_{\text{IF}}^{\text{conv}} = Q_{\text{IF}}^2 = \begin{cases} s_{aj} & \text{for } a \text{ converting to/from a gluon} \\ s_{jk} & \text{for } K \rightarrow q\bar{q} \end{cases}, \tag{29}$$

with the phase-space limits $s_{aj} \leq s_{AK}/x_A$ and $s_{jk} \leq s_{AK}(1-x_A)/x_A$.

No-emission probability With the definitions given above (5) for initial–final configurations reads

$$\Pi_n(t_n, t_{n+1}) = \exp \left(- \int_{s_{aj_{n+1}}}^{s_{aj_n}} ds_{aj} \int_{s_{jk_{n+1}}}^{s_{jk_n}} ds_{jk} \int_0^{2\pi} \frac{d\phi}{2\pi} \times \frac{\alpha_s(t)}{4\pi} \frac{s_{AK}}{(s_{AK} + s_{jk})^2} \mathcal{C} \bar{a}(s_{aj}, s_{jk}, s_{AK}) \times \frac{f_a(x_a, t)}{f_A(x_A, t)} \right), \tag{30}$$

with $t = t_{\text{IF}}(s_{aj}, s_{jk}, s_{ak})$. The subscript of the s_{aj} and s_{jk} integration limits indicates the association with the branching scales t_n and t_{n+1} , respectively.

2.4 Final–final configurations

We denote the pre- and post-branching partons participating in a final–final branching by $IK \rightarrow ijk$, with no recoils outside the antenna. In the following, we specify the phase-space factorisation, antenna functions, evolution variables and the resulting no-emission probability. More extensive descriptions of VINCIA’s final-state antenna-shower formalism can be found in [23,39].

Phase space The phase-space factorisation reads

$$d\Phi_3(P \rightarrow p_i, p_j, p_k) = d\Phi_2(P \rightarrow p_I, p_K) d\Phi_{\text{ant}}^{\text{FF}} \tag{31}$$

with the antenna phase space

$$d\Phi_{\text{ant}}^{\text{FF}} = \frac{1}{16\pi^2} \frac{1}{s_{IK}^2} ds_{ij} ds_{jk} \frac{d\phi}{2\pi}. \tag{32}$$

See Appendix A.1 for the explicit construction of the post-branching momenta.

Antenna functions The default final–final antenna functions are chosen to be the ones of [52] averaged over helicities. For gluon-emission antennae, these are

$$\bar{a}_{q\bar{q}g}^{\text{FF}} = \bar{a}(i_q, k_{\bar{q}}, j_g) = \frac{1}{s_{IK}} \left(2 \frac{s_{ik}s_{IK}}{s_{ij}s_{jk}} + \frac{s_{jk}}{s_{ij}} + \frac{s_{ij}}{s_{jk}} + 1 \right), \tag{33}$$

$$\begin{aligned} \bar{a}_{ggg}^{\text{FF}} &= \bar{a}(i_g, k_g, j_g) \\ &= \frac{1}{s_{IK}} \left(2 \frac{s_{ik}s_{IK}}{s_{aj}s_{jb}} + \frac{s_{jk}}{s_{ij}} + \frac{s_{ij}}{s_{jk}} - \frac{s_{jk}^2}{s_{ij}s_{IK}} \right. \\ &\quad \left. - \frac{s_{ij}^2}{s_{jk}s_{IK}} + \frac{3}{2} + \frac{s_{ij} + s_{jk}}{2s_{IK}} \right), \end{aligned} \tag{34}$$

$$\bar{a}_{q\bar{q}g}^{\text{FF}} = \bar{a}(i_q, k_{\bar{q}}, j_g) = \frac{1}{s_{IK}} \left(2 \frac{s_{ik}s_{IK}}{s_{aj}s_{jb}} + \frac{s_{jk}}{s_{ij}} + \frac{s_{ij}}{s_{jk}} - \frac{s_{ij}^2}{s_{jk}s_{IK}} + \frac{3}{2} \right). \tag{35}$$

For a final-state gluon splitting, the default is

$$\bar{a}_{xq\bar{q}}^{\text{FF}} = \bar{a}(i_x, k_q, j_{\bar{q}}) = \frac{1}{2s_{jk}} \frac{s_{ij}^2 + s_{ik}^2}{s_{IK}^2} + \frac{1}{2} \frac{s_{jk}}{s_{IK}^2} + \frac{s_{ik}}{s_{IK}^2}. \tag{36}$$

In Appendix A.2 we show that the antenna functions correctly reproduce the DGLAP splitting kernels in the collinear limit.

Evolution variables We evolve gluon emission either in transverse momentum, which is the default choice, or in the antenna mass,

$$t_{\text{FF}}^{\text{emit}} = \begin{cases} p_{\perp, \text{FF}}^2 = 4 \frac{s_{ij}s_{jk}}{s_{IK}} \\ m_{\text{AFF}}^2 = 2 \min(s_{ij}, s_{jk}) \end{cases}. \tag{37}$$

The upper phase-space limit is the parent antenna mass, $t_{\text{FF}}^{\text{emit}} \leq s_{IK}$. Gluon splittings are evolved in the invariant mass of the quark-antiquark pair,

$$t_{\text{FF}}^{\text{conv}} = Q_{\text{FF}}^2 = \begin{cases} s_{ij} & \text{for } i \text{ being the gluon} \\ s_{jk} & \text{for } k \text{ being the gluon} \end{cases}, \tag{38}$$

with the same phase-space limit as before.

No-emission probability With the definitions given above (5) for final–final configurations reads

$$\begin{aligned} \Pi_n(t_n, t_{n+1}) &= \Delta_n(t_n, t_{n+1}) \\ &= \exp \left(- \int_{s_{ij_{n+1}}}^{s_{ij_n}} ds_{ij} \int_{s_{jk_{n+1}}}^{s_{jk_n}} ds_{jk} \right. \\ &\quad \left. \times \int_0^{2\pi} \frac{d\phi}{2\pi} \frac{\alpha_s(t)}{4\pi} \frac{1}{s_{IK}^2} \mathcal{C} \bar{a}(s_{ij}, s_{jk}, s_{IK}) \right), \end{aligned} \tag{39}$$

with $t = t_{\text{FF}}(s_{ij}, s_{jk}, s_{IK})$. The subscript of the s_{ij} and s_{jk} integration limits indicates the association with the branching scales t_n and t_{n+1} , respectively.

2.5 The shower generator

We now illustrate how the shower algorithm generates branchings, starting from trial branchings generated according to a simplified version of the no-emission probability in Eq. (5). For definiteness we consider the specific example of initial–initial antennae, initial–final ones being handled in much the same way, with a PDF ratio that only involves one of the beams, and final–final ones not involving any PDF ratios at all. The full antenna-shower evolution (II+IF+FF) is combined with PYTHIA’s p_{\perp} -ordered multiple-parton-interactions (MPI) model, in a common interleaved sequence of evolution steps [8].

With the explicit form of the antenna phase space the no-emission probability reads

$$\begin{aligned} \Pi_n(t_{\text{start}}, t_{n+1}) &= \exp \left(- \int_{t_{n+1}}^{t_{\text{start}}} ds_{aj} ds_{jb} \frac{\alpha_s(t) \mathcal{C}}{4\pi} \right. \\ &\quad \left. \times \frac{s_{AB}}{s_{ab}^2} \bar{a}(s_{aj}, s_{jb}, s_{AB}) R_{\text{pdf}} \right) \\ &= \exp \left(- \int_{t_{n+1}}^{t_{\text{start}}} ds_{aj} ds_{jb} a(s_{aj}, s_{jb}, s_{AB}) R_{\text{pdf}} \right), \end{aligned} \tag{41}$$

where the integral is written in terms of the invariants s_{aj} and s_{jb} and we have suppressed the trivial integration over ϕ . In the second line, colour and coupling factors, as well as leftover factors coming from the antenna phase space are absorbed into a redefined antenna function, $a(s_{aj}, s_{jb}, s_{AB})$. To impose the evolution measure, we first change the integration variables from s_{aj} and s_{jb} to t and ζ , where t has dimension GeV^2 and ζ is dimensionless. The definition of ζ is in somewhat arbitrary, as long as it is linearly independent of t and there exists a one-to-one map back and forth between (s_{aj}, s_{jb}) and (t, ζ) . Generally, the freedom to choose ζ can

be utilised to make the (t, ζ) integrands and phase-space boundaries as simple and efficient as possible. Transformed to arbitrary (t, ζ) , Eq. (41) now reads

$$\Pi_n(t_{\text{start}}, t_{n+1}) = \exp\left(-\int_{t_{n+1}}^{t_{\text{start}}} dt d\zeta |J| a(s_{aj}, s_{jb}, s_{AB}) R_{\text{pdf}}\right), \quad (42)$$

with the Jacobian $|J|$ associated with the transformation from (s_{aj}, s_{jb}) to (t, ζ) . Rather than solving the exact expression, we make three simplifications, the effects of which we will later cancel by use of the veto algorithm:

- Instead of the physical antenna functions, a , we use simpler (trial) overestimates, $\hat{a}(s_{aj}, s_{jb}, s_{AB})$. For instance the trial antenna function for gluon emission off an initial-state quark–antiquark pair is chosen to be

$$\hat{a}_{q\bar{q}g}^{\text{II}} = 2 \frac{s_{ab}^2}{s_{AB} s_{aj} s_{jb}}. \quad (43)$$

- Instead of the PDF ratio, R_{pdf} , we use the overestimate

$$\hat{R}_{\text{pdf}} = \left(\frac{x_A x_B}{x_a x_b}\right)^\alpha \frac{f_a(x_A, t_{\min}) f_b(x_B, t_{\min})}{f_A(x_A, t_{\min}) f_B(x_B, t_{\min})}, \quad (44)$$

where t_{\min} is the lower limit of the range of evolution variable under consideration and α a parameter, whose value is, wherever possible, chosen differently, depending on the type of branching, to give a good performance.

- In cases where the physical ζ boundaries depend on the evolution variable t , we allow trial branchings to be generated in a larger hull encompassing the physical phase space, with ζ boundaries that only depend on the t integration limits.

Having the trial no-emission probability, $\hat{\Pi}_n(t_{\text{start}}, t_{n+1})$, at hand we solve

$$\hat{\Pi}_n(t_{\text{start}}, t_{n+1}) = \mathcal{R} \quad \text{with} \quad \mathcal{R} \in [0, 1] \quad (45)$$

for t_{n+1} to obtain the scale of the next branching. Due to the simplifications discussed above, this can be done analytically. We then generate another uniformly distributed random number, \mathcal{R}_ζ , from which we obtain a trial ζ value by solving (again analytically),

$$\mathcal{R}_\zeta = \frac{\hat{I}_\zeta(\hat{\zeta}_{\min}, \zeta)}{\hat{I}_\zeta(\hat{\zeta}_{\min}, \hat{\zeta}_{\max})} \quad (46)$$

where \hat{I} is the integral over all ζ dependence in $\hat{\Pi}_n(t_{\text{start}}, t_{n+1})$.

Finally, a uniformly distributed trial $\phi = 2\pi\mathcal{R}_\phi$ can be generated, furnishing the last branching variable. We now make use of the veto algorithm to recover the exact integral

in Eq. (42), as shown in [62]. First, any trial branching outside the physical phase space is rejected. Each physical trial branching is then accepted with the probability

$$\mathcal{O}(\hat{t}, t_{n+1}) P^{\text{shower}} = \mathcal{O}(\hat{t}, t_{n+1}) \frac{a(s_{aj}, s_{jb}, s_{AB}) R_{\text{pdf}}}{\hat{a}(s_{aj}, s_{jb}, s_{AB}) \hat{R}_{\text{pdf}}}, \quad (47)$$

where $\mathcal{O}(\hat{t}, t_{n+1})$ represents the ordering condition with respect to some scale \hat{t} . In traditional, strongly ordered showers this scale is equal to the scale of the last branching t_n and the ordering condition therefore is

$$\mathcal{O}(\hat{t}, t_{n+1}) = \mathcal{O}(t_n, t_{n+1}) = \Theta(t_n - t_{n+1}). \quad (48)$$

For more details on the algorithm see Appendix A.3 and the VINCIA compendium distributed alongside with the code.

2.6 Colour coherence and colour indices

When assigning colour indices to represent colour flow after a branching, we adopt a set of conventions that are designed to approximately capture correlations between partons that are not LC-connected, based on the arguments presented in [49]. Specifically, we let the last digit of the "Les Houches (LH) colour tag" [63, 64] run between 1 and 9, and refer to this digit as the "colour index". LC-connected partons have matching LH colour tags and therefore also matching colour/anticolour indices, while colours that are in a relative octet state are assigned non-identical colour/anticolour indices. Hence the last digit of a gluon colour tag will never have the same value as that of its anticolour tag. This does not change the LC structure of the cascade; if using only the LH tags themselves to decide between which partons string pieces should be formed, the extra information is effectively just ignored. It does, however, open for the possibility of allowing strings to form between non-LC-connected partons that "accidentally" end up with matching indices, in a way that at least statistically gives a more faithful representation of the full SU(3) group weights than the strict-LC one [49].

The new aspect we introduce here is to assign colour indices after each branching, whereas the model in [49] operated at the purely non-perturbative stage just before hadronisation. Furthermore, for gluon emissions, we choose to let the colour tag of the parent antenna be inherited by the daughter antenna with the largest invariant mass, while the one with the smaller invariant mass is assigned a new colour tag (subject to the rules described above). This is intended to preserve the coherence structure as seen by the rest of the event, so that, for instance, the new colour created in a near-collinear branching is attributed to the new small antenna, while the colour tag of the parent antenna continues on as the tag of the larger of the daughters. An advantage of this approach is

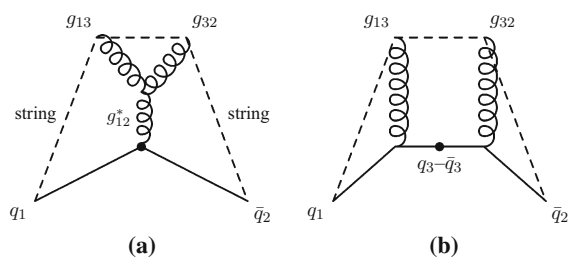


Fig. 4 Illustration of *colour flow* in $Z \rightarrow qgg\bar{q}$, using subscripts to denote *colour indices*. Note that both x and y axes illustrate spatial dimensions, with time indicated roughly by the distance from the location of the original Z , denoted by *bullet symbol*. Two Feynman diagrams contribute to the same leading-colour string topology

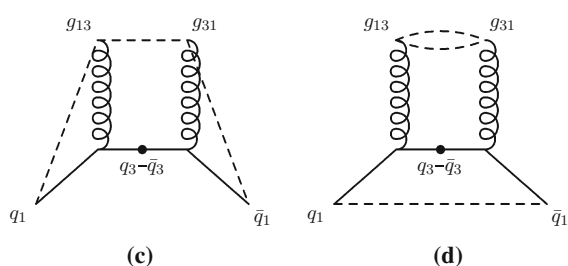


Fig. 5 With a probability suppressed by $1/N_C^2$, the same *colour index* may occur twice in the diagram shown in Fig. 4b, illustrated here in the *left-hand pane*. When this occurs, the string topology shown in the *right-hand pane* is also possible (The model of [49] invokes a string-length minimisation argument to decide which is realised)

that the octet nature of intermediate gluons, e.g. in collinear $g \rightarrow gg$ branchings, is preserved by our treatment, which is not the case in the implementation of [49].

In Figs. 4 and 5 we illustrate our approach, and the ambiguity it addresses. For definiteness, and for simplicity, we consider the specific case of $Z \rightarrow qgg\bar{q}$, but the arguments are general. The two diagrams in Fig. 4 show the outgoing partons, produced by a Z boson decaying at the point denoted by \bullet . Both axes correspond to spatial dimensions, hence time is indicated roughly by the radial distance from the Z decay point. Examples of the colour indices defined above are indicated by subscripts, hence e.g., g_{13} denotes a gluon carrying anticcolour index 1 and colour index 3. Due to our selection rule, the type of assignment represented by Fig. 4a is always selected when m_{gg} is small, $s_{gg} < s_{qg}$, while the one represented by Fig. 4b is selected when $s_{qg} < s_{gg}$ (when the second emission occurs in the $q-g$ antenna, and completely analogously when it occurs in the $g-\bar{q}$ one). The subleading-colour ambiguity illustrated by Fig. 5 can only occur for the latter type of assignment, hence will be absent in our treatment for collinear $g \rightarrow gg$ branchings (where the flow represented by Fig. 4a dominates), in agreement with the collinearly branching gluon having to be an octet. We regard this as an improvement on the treatment in [49], in which there was no mechanism to prevent collinear

gluons from ending up in an overall singlet state; see also the remarks accompanying [49, Fig. 15].

As a last point, we remark that this new assignment of colour tags is currently left without impact, but is implemented in order to enable future studies, such as colour reconnection within VINCIA.

2.7 Uncertainty estimations

Traditionally, shower uncertainties are evaluated by systematic up/down variations of each model parameter, which mandates the generation of multiple event sets, one for each variation. To avoid this time-consuming procedure, VINCIA instead generates a vector of variation weights for each event [39], where each of the weights corresponds to varying a different parameter. A separate publication details the formal proof of the validity of the method [65], which we have here extended to cover both the initial- and final-state showers in VINCIA. (**Note added in proof:** during the publication of this manuscript, two further papers appeared reporting similar implementations in HERWIG and SHERPA, see [66,67].) In this section, we only give a brief overview of the implementation, referring to [39,65] for details and illustrations. Technical specifications for how to switch the uncertainty bands on and off in the code, and how to access them, are provided in VINCIA's HTML User Reference [46].

During the shower step, in which a trial branching gets accepted with the probability P_{def} given in Eq. (47), the probability of the same branching to occur with a variation in e.g. the choice of renormalisation scale or antenna function is calculated,

$$P_{\text{var}} = \frac{\text{VAR}}{\text{DEF}} P_{\text{def}} \quad (49)$$

where DEF and VAR are symbols representing the default and variation choice, respectively. In the case of an accepted branching the variation weight of the event gets simply multiplied with $P_{\text{var}}/P_{\text{def}}$, and for rejected branchings with

$$\frac{1 - P_{\text{var}}}{1 - P_{\text{def}}} \quad (50)$$

to correctly take the no-emission probability into account.

The variations currently implemented in VINCIA are the following:

- VINCIA's default settings, with default antenna functions, scale choices and colour factors.
- Variation of the renormalisation scale. Using $\alpha_s(t/k_\mu)$ and $\alpha_s(t k_\mu)$, with a user-specifiable value of the additional scaling factor k_μ .
- Variation of the antenna functions. Using antenna sets with large and small nonsingular terms, representing

unknown (but finite) process-dependent LO matrix-element terms. Note that these are cancelled by LO MECs (up to the matched orders).

- α_s -suppressed counterparts of the finite-term variations above⁸ which are not cancelled by (LO) MECs.
- Variation of the colour factors. All gluon emissions use the colour factor of either $C_A = 3$ or $2C_F = 8/3$.
- Modified P_{imp} factor,

$$P'_{\text{imp}} = \frac{\hat{t}^2}{\hat{t}^2 + t^2}. \quad (51)$$

Note that, except for the first one, the variations are taken with respect to the user-defined settings. All of these variations are applied in the shower and the MECs, and they are limited to branchings in the hard system, i.e. they are for instance not applied in the showering of multi-parton interactions.

2.8 Limitations

For completeness, we note that a few options and extensions of the existing VINCIA final-state shower have not yet been implemented in VINCIA 2.0. These will remain available in earlier versions of the code (limited to pure final-state radiation hence mostly of interest for e^+e^- studies) and may reappear in future versions, subject to interest and available manpower. Briefly summarised, this concerns the following features:

- Sector showers [28]: a variant of the antenna-shower formalism in which a single term is responsible for generating all contributions to each phase-space point. It has some interesting and unique properties including being one-to-one invertible and producing fewer (one) term at each order of GKS matrix-element corrections leading to the numerically fastest matching algorithm we are aware of (see [28]), at the price of requiring more complicated antenna functions with more complicated phase-space boundaries. For the initial-state extension of VINCIA we have so far focussed on the technically simpler case of “global” (as opposed to sector) antennae.
- One-loop matrix-element corrections. The specific case of one-loop corrections for hadronic Z decays up to and including 3 jets was studied in detail by HLS [40]. The extension of this method to hadronic initial states, and a more systematic approach to one-loop corrections in VINCIA in general, will be a major goal of future efforts.
- Helicity dependence [52]. The shower and matrix-element-correction algorithms described in this paper

pertain to unpolarised partons. Although this is fully consistent with the unpolarised nature of the initial-state partons obtained from conventional parton distribution functions (PDFs), we note that an extension to a helicity-dependent formalism could nonetheless be a relatively simple future development. Moreover, we expect this would provide useful speed gains for the GKS matrix-element correction algorithm equivalent to those observed for the final-state algorithm [52].

- Full-fledged fermion mass effects [68]. Our treatment of mass effects for initial-state partons is so far limited to one paralleling the simplest treatment in conventional PDFs, the “zero-mass-variable-flavour-number (ZMVF) scheme”. In this scheme, heavy-quark PDFs are set to zero below the corresponding mass threshold(s) and are radiatively generated above them by $g \rightarrow Q\bar{Q}$ splittings, with m_Q formally set to zero in those splittings and for the subsequent heavy-quark evolution. Thus, in VINCIA 2.0, all partons are assigned massless kinematics, but $g \rightarrow Q\bar{Q}$ splittings are switched off (also in the final state) below the physical mass thresholds. This only gives a very rough approximation of mass effects [69, 70] but at least avoids generating unphysical singularities. Beyond the strict ZMVF scheme, optionally and for final-state branchings only, we allow for a set of universal antenna mass corrections to be applied and/or for tighter phase-space constraints to be imposed, with the latter obtained from the would-be massive phase-space boundaries. We note that a mixed treatment similar to the one currently employed by PYTHIA, with massive/massless kinematics for outgoing/incoming partons, respectively, would not be straightforward to adopt in VINCIA as it would be inconsistent with the application of on-shell matrix-element corrections.
- The so-called “Ariadne factor” [21] for gluon splitting antennae

$$P_{\text{Ari}} = \frac{2s_N}{s_N + s_P}, \quad (52)$$

with s_N the invariant mass squared of the colour neighbour on the other side of the splitting gluon and s_P the invariant mass squared of the parent (splitting) antenna is limited to its original purpose, that of improving the description of 4-jet observables in Z decay, and is not applied outside that context.

3 Matrix-element corrections

In this section we focus on the MEC formalism in VINCIA and discuss our strategy for reaching the non-ordered parts of phase space, both with respect to the factorisation scale in

⁸ Up to and including VINCIA 2.001, these variations were erroneously applied by multiplying or dividing the antenna functions by $(1 + \alpha_s)$, which is degenerate with the renormalisation-scale variations.

the case of the first branching and with respect to previous branching scales.

Note that in this paper all matrix elements are generated with MADGRAPH [50,71]. The output is suitably modified to extract the leading-colour matrix element, i.e. to not sum over colour permutations, but pick the (diagonal) entry in MADGRAPH’s colour matrix that corresponds to the colour order of interest. All plots shown in this paper are based on leading-colour matrix elements.

3.1 Hard jets in non-QCD processes

In this section we describe our formalism to combine events which are accompanied by at least one very hard jet, with the ones which are not. We emphasise that the considerations are general and apply to any processes that do not exhibit QCD jets at the Born level.

We first consider the Born inclusive cross section, differential in the Born phase space,

$$d\sigma_B^{\text{incl}}(t_{\text{fac}}) = f_0(x_0, t_{\text{fac}}) |\mathcal{M}_B|^2 d\Phi_B, \tag{53}$$

where t_{fac} is the factorisation scale, subscript zero emphasises that flavour and energy fraction correspond to the state Φ_B (subscript one will then correspond to the state Φ_{B+1} and so on), and the second PDF factor has been dropped for the sake of readability.

Since the ISR shower formally corresponds to a “backwards” evolution of the PDFs [33], the factorisation scale represents the natural upper bound (starting scale) for the initial-state shower evolution. This implies that any phase-space points with $t > t_{\text{fac}}$ will not be populated by the shower, potentially leaving a “dead zone” for high- t emissions. In principle, the freedom in choosing the evolution variable can be exploited to define t in such a way that the entire physical phase space becomes associated with scales $t < t_{\text{fac}}$ [30], including points with physical $p_{\perp}^2 \gg t_{\text{fac}}$. Here, however, we wish to maintain a close correspondence between the evolution variable and the physical (kinematic) p_{\perp} , requiring the development of a different strategy.

The approach used internally in PYTHIA is that of “power showers” (with [72] or without [73] matrix-element corrections): starting the shower from a scale t_{start} that is higher than the factorisation scale. This method has been criticised for producing too hard jet emission spectra and violating the factorisation ansatz. Though the improved power showers defined in [74,75] are better behaved (dampening the LL $1/p_{\perp}^2$ kernels to explicitly subleading Q^2/p_{\perp}^4 ones for emissions above the Q scale of the basic process), shortcomings are still present. Consider, for example, the Born exclusive

cross section at an arbitrary shower cutoff, differential in the Born phase space, scale t_{cut} ,

$$\begin{aligned} d\sigma_B^{\text{excl}}(t_{\text{cut}}) &= \Pi_0(t_{\text{start}}, t_{\text{cut}}) f_0(x_0, t_{\text{fac}}) |\mathcal{M}_B|^2 d\Phi_B \tag{54} \\ &= \frac{f_0(x_0, t_{\text{fac}})}{f_0(x_0, t_{\text{start}})} f_0(x_0, t_{\text{cut}}) \Delta_0(t_{\text{start}}, t_{\text{cut}}) |\mathcal{M}_B|^2 d\Phi_B. \tag{55} \end{aligned}$$

Unless $t_{\text{start}} = t_{\text{fac}}$, there appears an undesired PDF ratio, which reflects the difference in the factorisation and shower starting scale. To avoid this problem, we introduce two separate event samples, both initiated by the same matrix element with the same factorisation scale, as in Eq. (53). They are generated simultaneously, producing a single stream of ordinary randomly mixed, weighted events, with no need for external recipes to combine them. The first sample creates events that do not have a hard jet, by starting the shower at the factorisation scale (hence leaving the region $t > t_{\text{fac}}$ unpopulated). The second event sample is responsible for all events with at least one jet with scale $t > t_{\text{fac}}$. This sample is initialised by first reweighting the Born-level events such that the (temporary) factorisation scale is set to the phase-space maximum, t_{max} , and the shower algorithm is started from that scale. Events that do not produce at least one branching before the original (Born-level) factorisation scale is reached are vetoed, resulting in a total contribution to the inclusive cross section in Eq. (53) of

$$\frac{f_0(x_0, t_{\text{max}})}{f_0(x_0, t_{\text{fac}})} f_0(x_0, t_{\text{fac}}) (1 - \Pi_0(t_{\text{max}}, t_{\text{fac}})) |\mathcal{M}_B|^2 d\Phi_B. \tag{56}$$

Adding the two event samples together yields the new inclusive cross section,

$$\begin{aligned} d\sigma_B^{\text{incl}}(t_{\text{fac}}) &= f_0(x_0, t_{\text{fac}}) |\mathcal{M}_B|^2 d\Phi_B + f_0(x_0, t_{\text{start}}) (1 \\ &\quad - \Pi_0(t_{\text{start}}, t_{\text{fac}})) |\mathcal{M}_B|^2 d\Phi_B \\ &= f_0(x_0, t_{\text{fac}}) |\mathcal{M}_B|^2 d\Phi_B \\ &\quad + \int_{t_{\text{fac}}}^{t_{\text{start}}} dt f_1(x_1, t) \mathcal{A}(t) \Delta_0(t_{\text{start}}, t) |\mathcal{M}_B|^2 d\Phi_B, \tag{57} \end{aligned}$$

where $\mathcal{A}(t)$ contains all antenna functions, coupling and colour factors. By virtue of adding and subtracting $f_0(x_0, t_{\text{fac}}) |\mathcal{M}_B|^2 d\Phi_B \Delta_0(t_{\text{start}}, t_{\text{fac}})$ and using the DGLAP equation

$$\begin{aligned} f_0(x_0, t_{\text{start}}) &= f_0(x_0, t_{\text{fac}}) \Delta_0(t_{\text{start}}, t_{\text{fac}}) \\ &\quad + \int_{t_{\text{fac}}}^{t_{\text{start}}} dt f_1(x_1, t) \mathcal{A}(t) \Delta_0(t_{\text{start}}, t) \tag{58} \end{aligned}$$

this becomes

$$d\sigma_B^{\text{incl}}(t_{\text{fac}}) = f_0(x_0, t_{\text{start}}) |\mathcal{M}_B|^2 d\Phi_B + f_0(x_0, t_{\text{fac}}) (1 - \Delta_0(t_{\text{start}}, t_{\text{fac}})) |\mathcal{M}_B|^2 d\Phi_B. \quad (59)$$

Expanding (57) to $\mathcal{O}(\alpha_s)$ yields

$$d\sigma_B^{\text{incl}}(t_{\text{fac}}) = f_0(x_0, t_{\text{fac}}) |\mathcal{M}_B|^2 d\Phi_B + \int_{t_{\text{fac}}}^{t_{\text{start}}} dt f_1(x_1, t) \mathcal{A}(t) |\mathcal{M}_B|^2 d\Phi_B. \quad (60)$$

Expanding (59) instead yields

$$d\sigma_B^{\text{incl}}(t_{\text{fac}}) = f_0(x_0, t_{\text{start}}) |\mathcal{M}_B|^2 d\Phi_B + f_0(x_0, t_{\text{fac}}) \int_{t_{\text{fac}}}^{t_{\text{start}}} dt \mathcal{A}(t) |\mathcal{M}_B|^2 d\Phi_B, \quad (61)$$

which is seemingly at odds with (60). The problem is that both (60) and (61) have been derived by expanding, so that their relation through the DGLAP equation is lost. The crucial point—which is obscured after expanding—is already contained in (57): the inclusive cross section is calculated with a sensible factorisation scale t_{fac} , while all branchings with scales $t > t_{\text{fac}}$ contribute, in a controlled way, at higher orders. Section 4 contains some illustrations of the effects of these corrections for physical observables such as the dilepton rapidity and p_{\perp} spectra in Drell–Yan processes.

The inclusive cross section obtained from Eq. (57) does not reduce to the zero-parton Born cross section, the changes being only due to hard emissions which have not been incorporated in the first term in (57). This differs from cross section changes in CKKW-inspired merging prescriptions [76, 77], which arise from real–virtual mismatches at the merging scale,⁹ or from the definition of the inclusive cross section in unitarised merging schemes [78, 79]. In the latter, the inclusive cross section is almost entirely given by the first term in (57), and only changed by “incomplete” states which cannot be associated with valid parton–shower histories. The definition of what is deemed an “incomplete state” is not conventional and thus may depend on the details of a particular implementation. Note, however, that [78–80] do not advocate including the factors “ Δ_0 ” when reweighting “incomplete” states. This could lead to interesting differences in observables relying on very boosted Z-boson momenta.

We note that, although the described method of adding hard jets in non-QCD processes is the default choice in VINCIA, we include the possibility to perform an ordinary shower, starting off the factorisation scale t_{fac} . This is the recommended option when combining VINCIA’s shower with external matching and merging schemes.

⁹ The value of merging scales is typically well below t_{fac} .

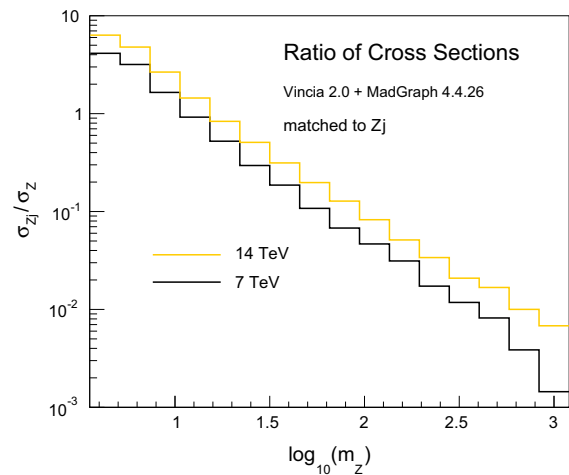


Fig. 6 Ratio of cross sections in Z production as a function of the Z mass for $\sqrt{s} = 7$ GeV (black) and $\sqrt{s} = 14$ GeV (orange)

In Fig. 6 we show the relative contribution of the two event samples in Z production, as a function of the Z mass,

$$\frac{\sigma_{Zj}}{\sigma_Z}(m_Z) = \frac{f_0(x_0, s) (1 - \Pi_0(s, m_Z^2)) |\mathcal{M}_{Zj}|^2 \Phi_{Zj}}{f_0(x_0, m_Z^2) |\mathcal{M}_Z|^2 \Phi_Z}, \quad (62)$$

with $\sqrt{s} = 7$ GeV (black) and $\sqrt{s} = 14$ GeV (orange). As expected, the contribution of events with at least one hard jets is larger for decreasing Z masses and increasing centre-of-mass energies. For both values of \sqrt{s} the Born event sample eventually dominates for Z masses above $\mathcal{O}(10)$ GeV.

3.2 Strong ordering compared with tree-level matrix elements

To validate the quality of the antenna shower, we use large samples of $pp \rightarrow Zjj$ phase-space points, generated with RAMBO [81] (an implementation of which is included in VINCIA). We cluster all of the phase-space points back to the corresponding $pp \rightarrow Z$ phase-space point, using the exact inverse of the $2 \rightarrow 3$ recoil prescription used in the shower as a clustering algorithm; see Appendix A for the kinematics map used here. This allows one to reconstruct all possible ways in which the shower could have populated a certain phase-space point, analogously to the study carried out for final-state radiation in [39] (see also [82]). Comparing the shower approximation with the LO matrix element for $q_1 \bar{q}_2 \rightarrow Zg_3g_4$ yields the tree-level PS-to-ME ratio

$$R_4 \equiv \frac{\Theta(t_{\hat{4}3} - t_3) C_{qg} C_{q\bar{q}}^{\text{IF}}(1, 4, 3) C_{q\bar{q}}^{\text{II}}(1\hat{3}, 2, \hat{4}3) |\mathcal{M}_Z(Z)|^2}{|\mathcal{M}_{Zgg}(1, 2; Z, 3, 4)|^2}$$

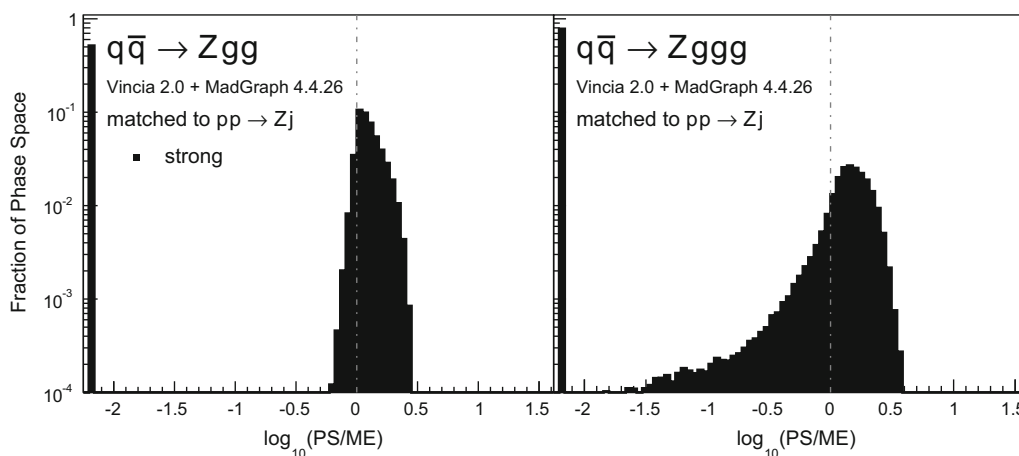


Fig. 7 Antenna shower, compared to matrix elements: distribution of $\log_{10}(\text{PS}/\text{ME})$ in a flat phase-space scan of the full phase space. Contents normalised to the number of generated points. Gluon emission only

$$+ \frac{\Theta(t_{\hat{3}4} - t_4) C_{\bar{q}gg} \bar{a}_{\bar{q}gg}^{\text{IF}}(2, 3, 4) C_{q\bar{q}g} \bar{a}_{q\bar{q}g}^{\text{II}}(1, \hat{2}4, \hat{3}4) |\mathcal{M}_Z(Z)|^2}{|\mathcal{M}_{Zgg}(1, 2; Z, 3, 4)|^2} \tag{63}$$

where the strong-ordering condition is incorporated by the Θ step functions and the hatted variables \hat{a}_j denote clustered momenta. The two terms correspond to the two possible shower histories—obtained from starting by clustering either gluon 3 or 4, respectively—with the sequential clustering scales

$$t_3 = p_{\perp\text{IF}}^2(g_3) \quad \text{and} \quad t_{\hat{4}3} = p_{\perp\text{II}}^2(g_{\hat{4}3}), \tag{64}$$

$$t_4 = p_{\perp\text{IF}}^2(g_4) \quad \text{and} \quad t_{\hat{3}4} = p_{\perp\text{II}}^2(g_{\hat{3}4}). \tag{65}$$

R_4 therefore gives a measure of how much the shower under- or overcounts the tree-level matrix element. With the first emission already corrected¹⁰ Eq. (63) reduces to

$$R_4 = \frac{\Theta(t_{\hat{4}3} - t_3) C_{qgg} \bar{a}_{qgg}^{\text{IF}}(1, 4, 3) |\mathcal{M}_{Zg}(\hat{1}3, 2, \hat{4}3)|^2}{|\mathcal{M}_{Zgg}(1, 2; Z, 3, 4)|^2} + \frac{\Theta(t_{\hat{3}4} - t_4) C_{\bar{q}gg} \bar{a}_{\bar{q}gg}^{\text{IF}}(2, 3, 4) |\mathcal{M}_{Zg}(1, \hat{2}4, \hat{3}4)|^2}{|\mathcal{M}_{Zgg}(1, 2; Z, 3, 4)|^2}. \tag{66}$$

Higher-order PS-to-ME ratios are constructed in a similar way.

Histograms showing the logarithmic distribution of the PS-to-ME ratios for $q\bar{q} \rightarrow Zgg$ and $q\bar{q} \rightarrow Zggg$, in a flat scan over the full phase space, comparing a strongly ordered

¹⁰ This is trivial for $q\bar{q} \rightarrow Zgg$ as the corresponding antenna function already is the ratio of the LO matrix elements.

shower with the LO amplitude squared, are shown in Fig. 7. The spike on the very left of the histograms corresponds to the part of phase space where there are no ordered shower histories. Note that about 35 % of the whole phase space in a flat scan of $q\bar{q} \rightarrow Zgg$ does not have an ordered shower path, a significantly higher fraction than the roughly 2 % found for the final-state phase spaces in [39]. We interpret this as due to the significantly larger size of the initial-state phase space, which is not limited by the original antenna invariant mass but only by the hadronic CM energy. The binning of the histogram is chosen such that the two bins around 0 (marked with a grey dashed line) correspond to the shower having less than 10 % deviation to the tree-level matrix element. For the shower with strong ordering about 10 % of the total number of phase-space points, corresponding to about 15 % of the phase space with at least one ordered path, populate these two bins.

To gain an understanding of where in phase space significant deviations between the shower approximation and the LO amplitudes squared occur, we consider the 2D distributions presented in Figs. 8 and 9. For all plots, the x axes represent the degree of ordering of the first ($Z \rightarrow Zg$) emission, while the y axis represents the degree of ordering of the second ($Zg \rightarrow Zgg$) emission, defined more precisely below. Note that, since the phase spaces have more than 2 dimensions, each bin still represents an average of different phase-space points with the same x and y coordinates. Since the ratios on the axis are plotted logarithmically, zero denotes the border between ordered and unordered paths. The black-framed box in the lower left-hand corner of the plots highlights the strongly ordered region defined by $p_{\perp\text{IF}}^2 \ll p_{\perp\text{II}}^2 \ll m_Z^2$, in which any (coherent) LL shower approximation is expected to give reasonable results. In the left-hand panes, grey colours signify less than 20 % deviation

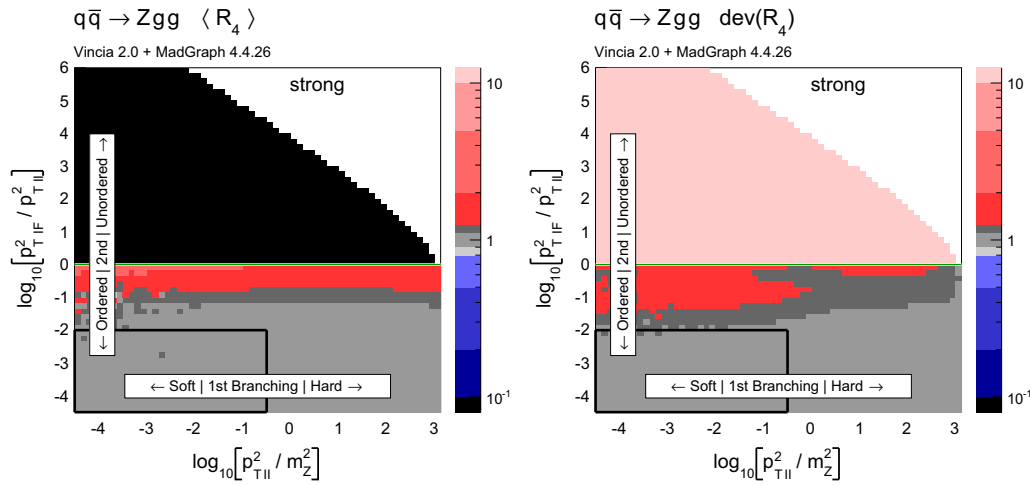


Fig. 8 The value of $\langle R_4 \rangle$ (left) and $\text{dev}(R_4)$ (right), differentially over the 4-parton phase space, with p_{\perp}^2 ratios characterizing the first and second emissions on the x- and y axis, respectively. Strong ordering in the shower, with gluon emission only

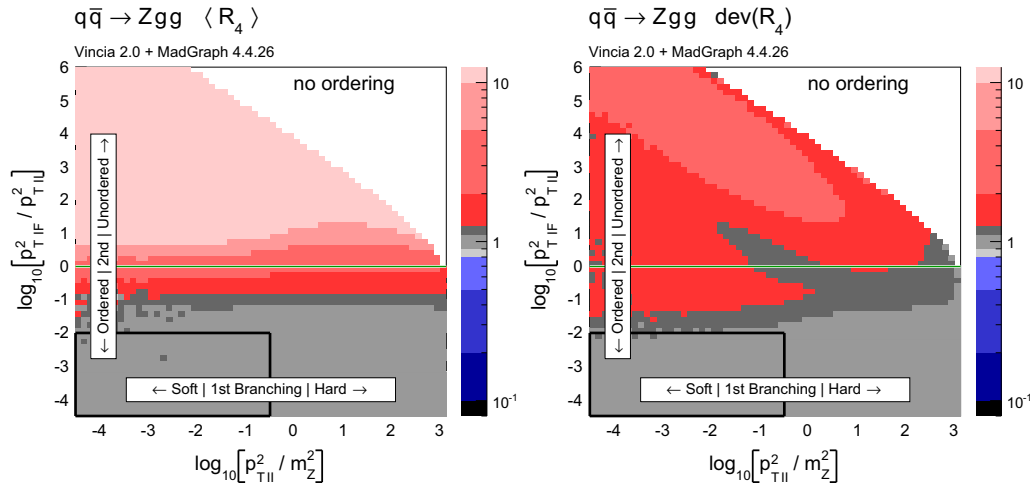


Fig. 9 The value of $\langle R_4 \rangle$ (left) and $\text{dev}(R_4)$ (right), differentially over the 4-parton phase space, with p_{\perp}^2 ratios characterizing the first and second emissions on the x- and y axis, respectively. No ordering in the shower, with gluon emission only

tion from a ratio unity (with the middle shade corresponding to less than 10 % deviation, corresponding to near-perfect agreement). Red shades signify increasingly large deviations, with contours at 2, 5, and 10. Blue contours extend to 1/2, 1/5, and 1/10, while black indicates regions where the shower answer is less than one tenth of the matrix-element answer. In the right-hand panes, the same colour scale is used to show a measure of the width of the R_4 distribution in each bin, defined below. These plots are intended to ensure that an average good agreement in the left-hand pane is not merely accidental, but also corresponds to a narrow distribution.

In Fig. 8, the left-hand pane provides a clear illustration of the dead zone for the process $q\bar{q} \rightarrow Zgg$ in a strongly p_{\perp}^2 -

ordered antenna shower. Each bin of the two-dimensional histogram shows the average of the value of R_4 in Eq. (66) over all phase-space points populating that bin. For every phase-space point there are two possible (not necessarily ordered) shower histories, with different scales for the first branching, $p_{\perp II}^2$, and second one, $p_{\perp IF}^2$. The combination of scales that correspond to the path with the smaller scale of the second branching is used to characterise the phase-space point. The black region in Fig. 8 for strong ordering corresponds to the spike in Fig. 7. Since there are two shower histories, there is in principle the possibility that the second history (which was not used to characterise the phase-space point) contributes as an ordered history, but this does not appear to happen any-

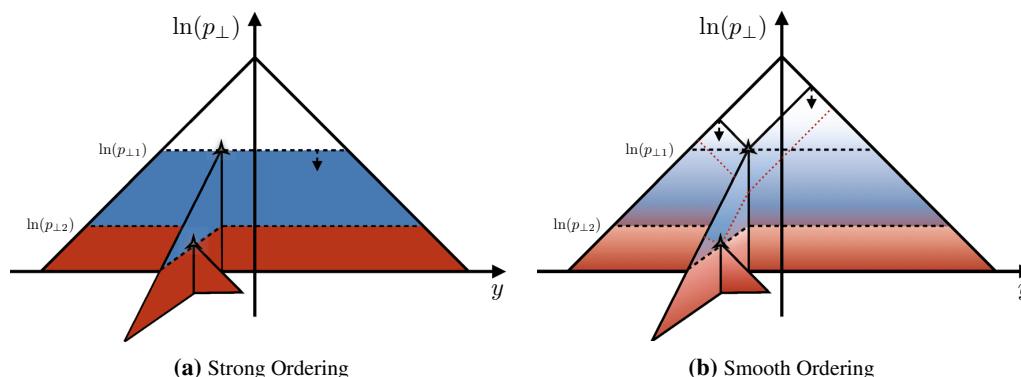


Fig. 10 Illustration of the phase-space coverage of p_{\perp} -ordered dipole/antenna showers with **a** strong and **b** smooth ordering, in the “origami” plane of $\ln p_{\perp}$ vs. rapidity

where in the region classified as unordered. The plot on the right shows the deviation within each bin, which we define to be

$$\text{dev}(R_4) = 10^{\sqrt{(\log_{10}^2(R_4)) - (\log_{10}(R_4))^2}}, \tag{67}$$

since the distribution of R_4 is naturally a logarithmic one. We assign a deviation of 10 to the dead zone, since the log would otherwise not be defined. As mentioned above, the deviation is intended to illustrate whether an average value in the left plot is achieved by a broad or a narrow distribution.

One could force the dead zone to disappear by simply removing the ordering condition and starting the shower at the phase-space maximum for each antenna. However, as can be seen from Fig. 9, this would highly overcount the matrix elements in the unordered region, again parallelling the observations for the equivalent case of final-state radiation in [39]. The strong-ordering condition is clearly a better approximation to QCD, even if it does not fill all of phase space. To improve the shower, we will therefore need to allow the shower to access the whole phase space while suppressing the overcounting in the unordered region.

3.3 Smooth ordering compared with tree-level matrix elements

As we saw in the previous section, a strongly ordered shower has a significant dead zone for hard emissions, especially in the initial-state sector. We now want to focus on how to remove them by generalising VINCIA’s “smooth ordering” [39] to initial-state phase spaces. Reference [39] shows that replacing the step function of an ordered shower with a smooth suppression factor leads to a surprisingly good description of the unordered region in Z decay. Based on this study, an improved version of the shower accept probability in Eq. (47), which allows one to take “unordered” branchings into account is

$$\mathcal{O}(\hat{t}, t) P^{\text{shower}} = P_{\text{imp}} P^{\text{shower}} = \frac{\hat{t}}{\hat{t} + t} P^{\text{shower}}, \tag{68}$$

where t is the scale of the trial branching at hand and \hat{t} is the reference scale.

The difference between conventional strong ordering and VINCIA’s P_{imp} -suppressed smooth ordering can be illustrated by considering so-called origami diagrams [83–85], in which the antenna (or, equivalently, dipole) phase space is depicted in terms of $\ln(p_{\perp}^2)$ versus rapidity. Defining these by our gluon-emission evolution variable, $p_{\perp}^2 = m_{12}^2 m_{23}^2 / m^2$ and by $y = \frac{1}{2} \ln(m_{12}^2 / m_{23}^2)$, respectively, for an antenna with total invariant mass m splitting into two smaller antennae with masses m_{12} and m_{23} , the leading (double-logarithmic) contribution to the branching probability is transformed to just a constant over the antenna phase space,

$$dP \sim \frac{\mathcal{C} \alpha_s}{2\pi} d \ln p_{\perp}^2 dy, \tag{69}$$

where \mathcal{C} is the colour factor normalised so that $\mathcal{C} \rightarrow N_C$ in the leading-colour limit. The phase-space boundary for gluon emissions with $p_{\perp} \ll m$ is determined by $y_{\text{max}}(p_{\perp}) = \frac{1}{2} \ln(m^2 / p_{\perp}^2)$, so that the rapidity range available for emissions at a given p_{\perp} defines a triangular region,

$$\Delta y(p_{\perp}) = \ln(m^2 / p_{\perp}^2) = \ln(m^2) - \ln(p_{\perp}^2), \tag{70}$$

corresponding to the outer hulls of the diagrams shown in Fig. 10.

For an emission at any given value of $p_{\perp1}^2 = m_{12}^2 m_{23}^2 / m^2$, the total rapidity range (at that p_{\perp} value) is unchanged by the branching,

$$\begin{aligned} \Delta y(p_{\perp1}) &= \underbrace{\ln(m^2) - \ln(p_{\perp1}^2)}_{\text{pre-branching}} \\ &= \underbrace{\ln(m_{12}^2) - \ln(p_{\perp1}^2) + \ln(m_{23}^2) - \ln(p_{\perp1}^2)}_{\text{post-branching}}, \end{aligned} \tag{71}$$

cf. the dashed line at $\ln(p_{\perp}) = \ln(p_{\perp 1})$ in the figure. For soft emissions, however, say at a reference value of $p_{\perp} = 1$ GeV, the post-branching configuration covers a total rapidity range which is larger by

$$\begin{aligned} \Delta y(1 \text{ GeV})_{\text{post}} - \Delta y(1 \text{ GeV})_{\text{pre}} \\ = \ln(m_{12}^2) + \ln(m_{23}^2) - \ln(m^2) = \ln(p_{\perp}^2). \end{aligned} \quad (72)$$

The additional phase space “opened up” by the branching can hence be represented by adding a double-sided isocles right triangle to the origami diagram, with side lengths $\ln(p_{\perp 1})$, which—for lack of a better direction—is drawn pointing out of the original plane. Restricting the subsequent shower evolution to populate only the region below the $p_{\perp 1}$ scale produces a strongly ordered shower, illustrated in Fig. 10a with the blue and red shaded regions representing the phase space accessible to a second and third branching, respectively. The case of smooth ordering is illustrated in Fig. 10b for the same sequence of branchings. In this case, each of the antennae produced by the first branching are allowed to evolve over their full phase spaces, and their respective full phase-space triangles are therefore now included in the diagram, using solid black lines for the first branching and red dotted lines for the phase-space limits after the second branching. The suppression of the branching probability near and above the branching scale is illustrated by reducing the amount of shading of the corresponding regions. Comparing the figures, one can see that we expect no change in the total range or integrated rate of soft emissions (at the bottom of the diagrams). The only effects occur near and above the branching scale where the strongly ordered (LL) shower formalism is anyway unproductive. In Sect. 3.4 below, we show explicitly that the leading-logarithmic structure of smoothly ordered showers is identical to that of strongly ordered ones, but for the remainder of this section we constrain our attention to comparisons with fixed-order matrix elements.

A further point that must be addressed in the context of the ordering criterion is that our matrix-element-correction formalism, discussed below, requires a Markovian (history-independent) definition of the \hat{t} variable in the P_{imp} factor in Eq. (68). Rather than using the scale of the preceding branching directly (which depends on the shower path and hence would be history-dependent), we therefore compute this scale in a Markovian way as follows: Given a n -parton state we determine the values of the evolution variable corresponding to all branchings the shower could have performed to get from any $(n - 1)$ - to the given n -parton state. The reference scale \hat{t} is then taken as the minimum of those scales. The dead zone, equivalent to the unordered region, is now populated by allowing branchings of a restricted set of antennae to govern the full relevant phase space. Such antennae are called unordered, while other antennae are called ordered. It is in principle permissible to treat all antennae in an event as unordered. To mimic the structure of effective $2 \rightarrow 4$ and

higher branchings, we, however, only tag those antennae which are connected to partons that partook in the branching that gave rise to the chosen value for \hat{t} as unordered. Branchings of ordered antennae may then contribute below the scale \hat{t} .

For example, consider the case of a gluon emission being associated with the smallest value of the evolution variable. In this case the gluon as well as the two partons playing the role of the parent antenna that emitted the gluon, are marked for unordering and therefore all antennae in which these three partons participate are allowed to restart the evolution at their phase-space limits. This limited unordering reflects that no genuinely new region of phase space would be opened up by allowing partons/antennae completely unrelated to the “last branching” to be unordered, as these will already have explored their full accessible phase spaces during the prior evolution.

We note that for the final state the available phase space reduces for each successive branching, limiting the effect of the smooth ordering. In [40] it is shown that, for final-state radiation, the damping factor in Eq. (68) does not modify the LL $1/t$ behaviour and only generates explicitly subleading \hat{t}/t^2 corrections in the strongly unordered limit, $t \gg \hat{t}$. For the initial state, the phase-space boundaries are governed by the hadronic centre-of-mass energy leading to possibly large unordered regions and therefore a rather large effect of the smooth ordering. As the main purpose of the smooth ordering is to fill all available phase space for the MECs, we restrict it to the ME corrected branchings by default and keep all following shower emissions strongly ordered. In this case, all damping factors get replaced by the MEC weight, see Sect. 3.6, by virtue of the Sudakov veto algorithm.

We compare the logarithmic distributions of the ratio of the shower approximation to the matrix element for $q\bar{q} \rightarrow Zgg$ and $q\bar{q} \rightarrow Zggg$ for both strong and smooth ordering in Fig. 11. When applying smooth ordering, the distribution gets narrower on the side where the shower overcounts the tree-level matrix element, and that the dead-zone spike is replaced by an extended tail towards low ratios on the other side. This tail is due to configurations that look like a hard-QCD process accompanied with a radiated Z . Such phase-space points should in principle be populated by an electroweak shower, such as the one presented in [86]; not having developed the required formalism in the antenna context yet, however, we still allow our QCD shower to populate this region of phase space; it will in any case be corrected with matrix elements, see Sect. 3. To focus on the improvement in the QCD regions of phase space we apply a cut on the transverse mass of the Z boson and require it to be larger than the branching scale of the path that has been chosen to characterise the phase-space point,

$$p_{\perp \text{IF}}^2 < m_{\perp Z}^2 = k_{\perp Z}^2 + m_Z^2. \quad (73)$$

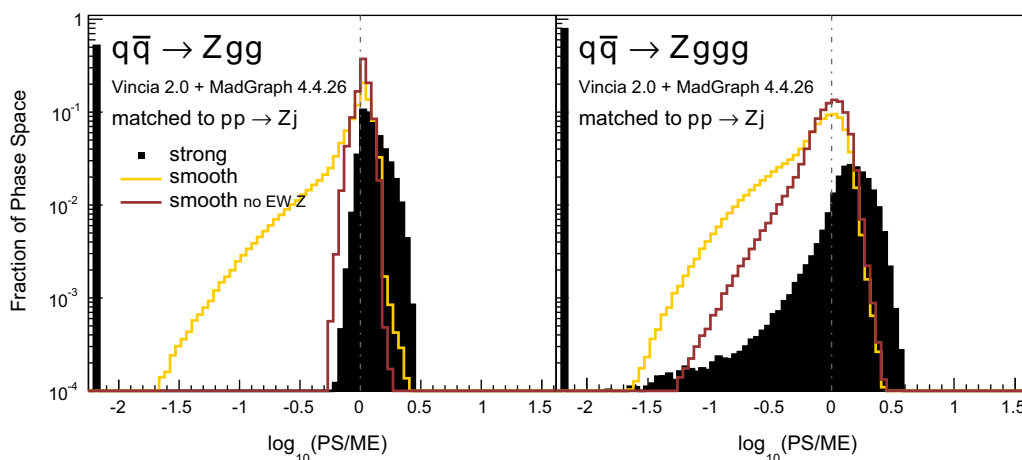


Fig. 11 Antenna shower, compared to matrix elements: distribution of $\log_{10}(\text{PS}/\text{ME})$ in a flat phase-space scan of the full phase space with strong and smooth ordering and smooth ordering with a cut on $m_{\perp Z}^2$. Contents normalised to the number of generated points. Gluon emission only

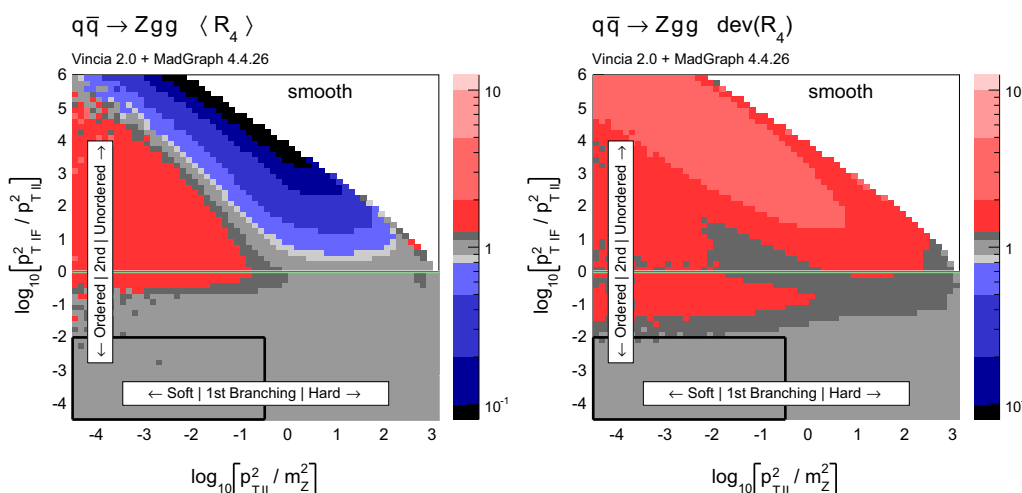


Fig. 12 The value of $\langle R_4 \rangle$ (left) and $\text{dev}(R_4)$ (right), differentially over the 4-parton phase space, with p_{\perp}^2 ratios characterising the first and second emissions on the x and y axis, respectively. Smooth ordering in the shower, with gluon emission only

We define $k_{\perp Z}^2$ to be the minimum of all possible

$$k_{\perp Z}^2 = \min(E_Z^2, E_q^2)(1 - \cos \theta_{Zq}). \tag{74}$$

The resulting distributions are shown in red in Fig. 11. Applying the cut leads to a removal of the part of phase space where the Z should have been generated as an emission rather than as part of the hard process. The distribution is now dominated by QCD and the smoothly ordered shower produces a narrower as well as more symmetric distribution, compared to the strongly ordered shower.

Similarly we repeat the two-dimensional histograms for the smoothly ordered antenna shower in Fig. 12 without and in Fig. 13 with the cut on $m_{\perp Z}^2$. As expected, we obtain an

improved description as compared to both the strong and unordered showers, Figs. 8 and 9 respectively. Due to the form of the improvement factor in Eq. (68) we get a factor of 0.5 at the green line, around where the scales of the two branchings coincide, leading to a better description already of this region. Once again these plots show that the shower undercounts the region where the Z boson is very soft and should have been generated with a weak shower, representing a path that is not available in VINCIA yet. The strongly unordered region remains somewhat overcounted, though by less than a factor 2, far better and with narrower distributions than was the case for the fully unordered shower, Fig. 9.

An extended set of plots, including Higgs production processes, can be found in Appendix B.

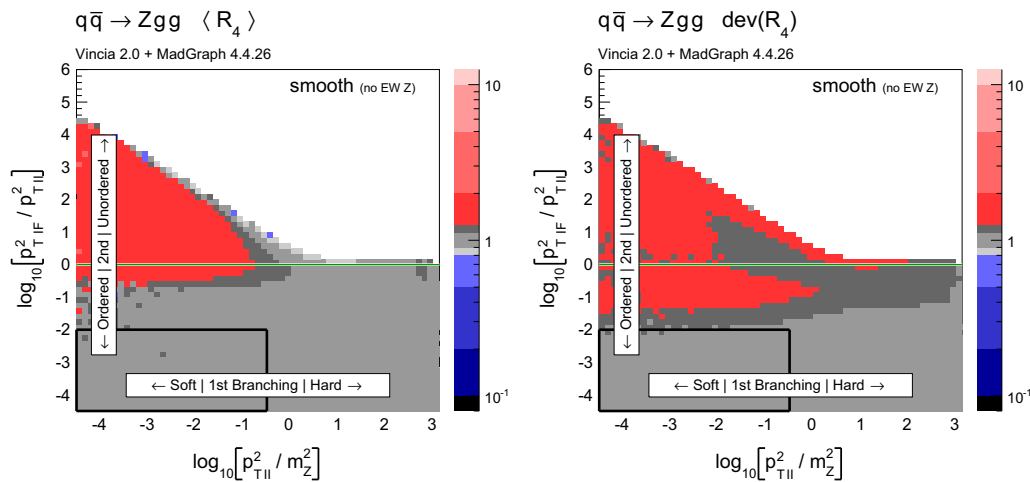


Fig. 13 The value of $\langle R_4 \rangle$ (left) and $\text{dev}(R_4)$ (right), differentially over the 4-parton phase space, with p_{\perp}^2 ratios characterizing the first and second emissions on the x and y axis, respectively. Smooth ordering in the shower, with a cut on $m_{\perp Z}^2$ and gluon emission only

3.4 Smooth ordering vs. strong ordering

This section presents a comparison of strong and smooth ordering, first in terms of their analytical leading-logarithmic structures, and then using jet clustering scales, investigating the processes $e^+e^- \rightarrow$ jets as well as $pp \rightarrow Z$ +jets. The analyses are adapted from the code used in [30], originally written by Höche. In order to focus on the shower properties we present parton-level distributions, with MECs switched off, a fixed strong coupling with $\alpha_s(m_Z) = 0.13$, and a very low cutoff, 10^{-3} GeV for $e^+e^- \rightarrow$ jets and 10^{-2} GeV for $pp \rightarrow Z$ +jets. To furthermore put the magnitude of the differences between smooth and strong ordering into perspective, an $\alpha_s(m_Z)$ -variation band for the strongly ordered result is included in Figs. 14 and 15.

We emphasise that, even leaving the α_s and cutoff settings aside, the distributions in this section are meant for validation only. The event generation modus used below does not make use of VINCIA’s matrix-element correction features. When using MECs, the main purpose of the smooth ordering is to fill the available phase space with non-vanishing weight, which allows a reweighting to reproduce the correct LO matrix-element result. Keeping this disclaimer in mind, it is still useful to investigate how the phase space is filled before MECs are applied.

Leading logarithms

As discussed in the preceding section, the leading (double-pole) behaviour of the gluon-emission antenna functions is just a constant over phase space when expressed in terms of the origami variables $\ln(p_{\perp})$ and y . We begin by considering

a conventional strongly ordered antenna shower, such as that of ARIADNE [13,21] (or VINCIA with strong ordering). The leading contribution to the Sudakov factor $\Delta(Q_{\perp}^2, p_{\perp}^2)$ representing the no-branching probability between two resolution scales $Q_{\perp}^2 > p_{\perp}^2$ (e.g., following a preceding branching which happened at the scale Q_{\perp}), is then, cf. Eq. (70),

$$\begin{aligned}
 -\ln \Delta_{\text{strong}} &\stackrel{\text{LL}}{\sim} \frac{C\alpha_s}{2\pi} \int_{\ln p_{\perp}^2}^{\ln Q_{\perp}^2} d \ln q_{\perp}^2 \int_{-\ln(m/q_{\perp})}^{\ln(m/q_{\perp})} dy \\
 &= \frac{C\alpha_s}{2\pi} \int_{\ln p_{\perp}^2}^{\ln Q_{\perp}^2} d \ln q_{\perp}^2 \ln \left[\frac{m^2}{q_{\perp}^2} \right] \tag{75}
 \end{aligned}$$

$$= \frac{C\alpha_s}{2\pi} \left(\frac{1}{2} \ln^2 \left[\frac{Q_{\perp}^2}{p_{\perp}^2} \right] + \ln \left[\frac{Q_{\perp}^2}{p_{\perp}^2} \right] \ln \left[\frac{m^2}{Q_{\perp}^2} \right] \right), \tag{76}$$

for a final-final antenna¹¹ with invariant mass m and assuming $p_{\perp}^2 \ll m^2$. This agrees with the LL limit for dipole showers derived in [30]. We note that the second term is absent from [87, Eq. (8)] due to a phase-space restriction placed in Eq. (2) of that paper, which we believe is appropriate to remove double-counting of soft emissions in showers based on DGLAP kernels. In the context of antenna showers, however, the antenna functions already have the correct (eikonal) soft limits, and the imposition of this additional phase-space constraint would have the (undesired) effect of removing the added rapidity range corresponding to the extra origami fold discussed in Sect. 3.3, producing an “undercounting”

¹¹ For initial-initial antennae, replace m in the phase-space limit on the rapidity integral in Eq. (75) by $\sqrt{s} = \sqrt{s_{AB}/(x_A x_B)}$, assuming $x_A x_B \ll 1$. For initial-final antennae, replace it by $\sqrt{s_{AK}/x_A}$ assuming $x_A \ll 1$.

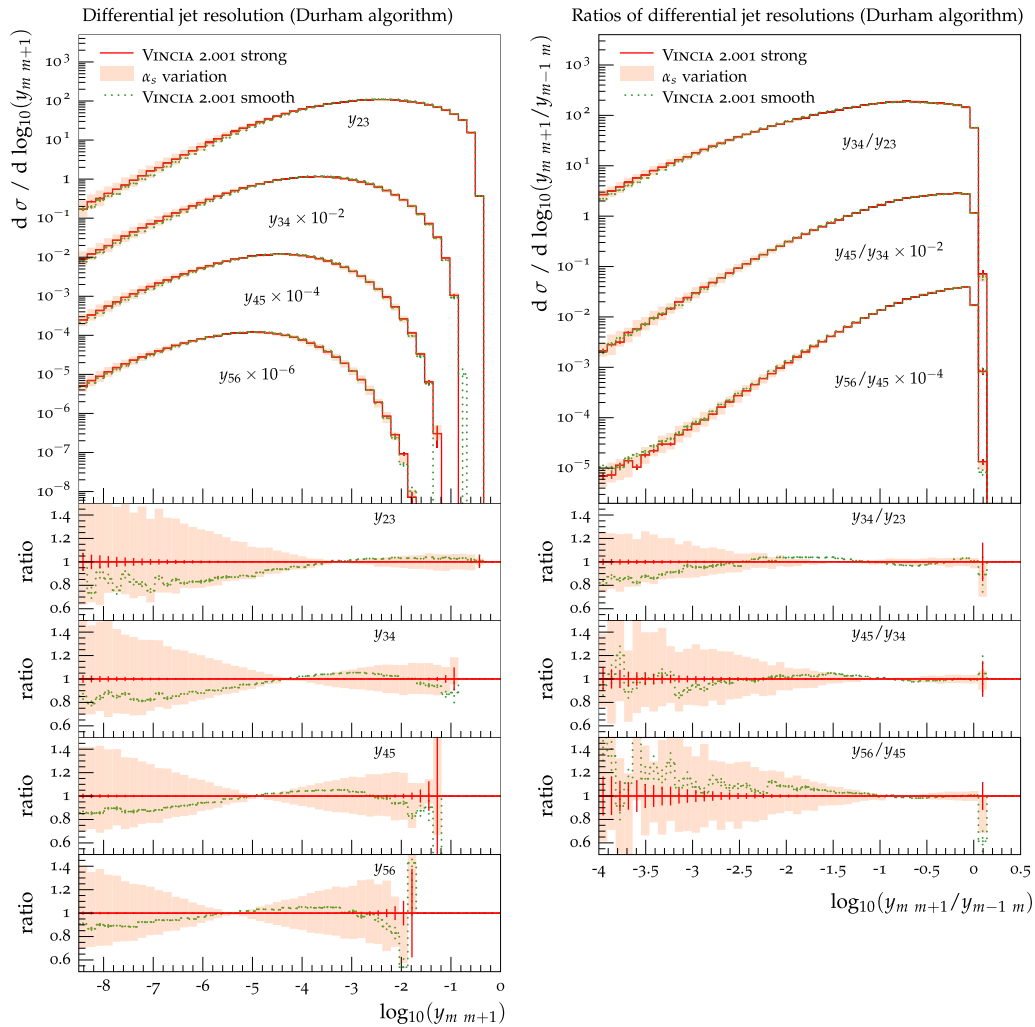


Fig. 14 Logarithmic distributions of differential jet resolutions and their ratios for heavy Z decays ($m_Z = 1000$ GeV). Predictions of VINCIA 2.0 with strong (*smooth*) ordering are shown in *solid red* (*dotted*)

green) lines. The *red band* shows an α_s variation with $\alpha_s(m_Z) = 0.12$ and $\alpha_s(m_Z) = 0.14$

of soft emissions. We therefore regard the expression above, Eq. (76), as the reference expression which an LL-correct antenna shower should reproduce.

A counter-example, illustrating an incorrect LL behaviour, can be furnished by considering a so-called “power shower” [73] in which the upper boundary of the integral above is replaced by m^2 rather than Q_\perp^2 (e.g., letting newly created antennae evolve over their full phase spaces, irrespective of the ordering scale, and without any suppression). This produces an extra logarithm which is not present in the strongly ordered case:

$$-\ln \Delta_{\text{pwr}} \stackrel{\text{LL}}{\sim} \frac{C\alpha_s}{2\pi} \left(\frac{1}{2} \ln^2 \left[\frac{Q_\perp^2}{p_\perp^2} \right] \right)$$

$$+ \ln \left[\frac{Q_\perp^2}{p_\perp^2} \right] \ln \left[\frac{m^2}{Q_\perp^2} \right] + \frac{1}{2} \ln^2 \left[\frac{m^2}{Q_\perp^2} \right] \Bigg), \tag{77}$$

where we have rewritten the $\frac{1}{2} \ln^2(m^2/p_\perp^2)$ result to make the two first terms identical to the ones produced in the strongly ordered case, so that the third term, highlighted in red, represents the difference.

For smooth ordering, with the P_{imp} suppression factor defined in Eq. (68), the relevant integral is

$$\int_{p_\perp^2}^{m^2} \frac{1}{1 + \frac{q_\perp^2}{Q_\perp^2}} \frac{dq_\perp^2}{q_\perp^2} \ln \left[\frac{m^2}{q_\perp^2} \right], \tag{78}$$

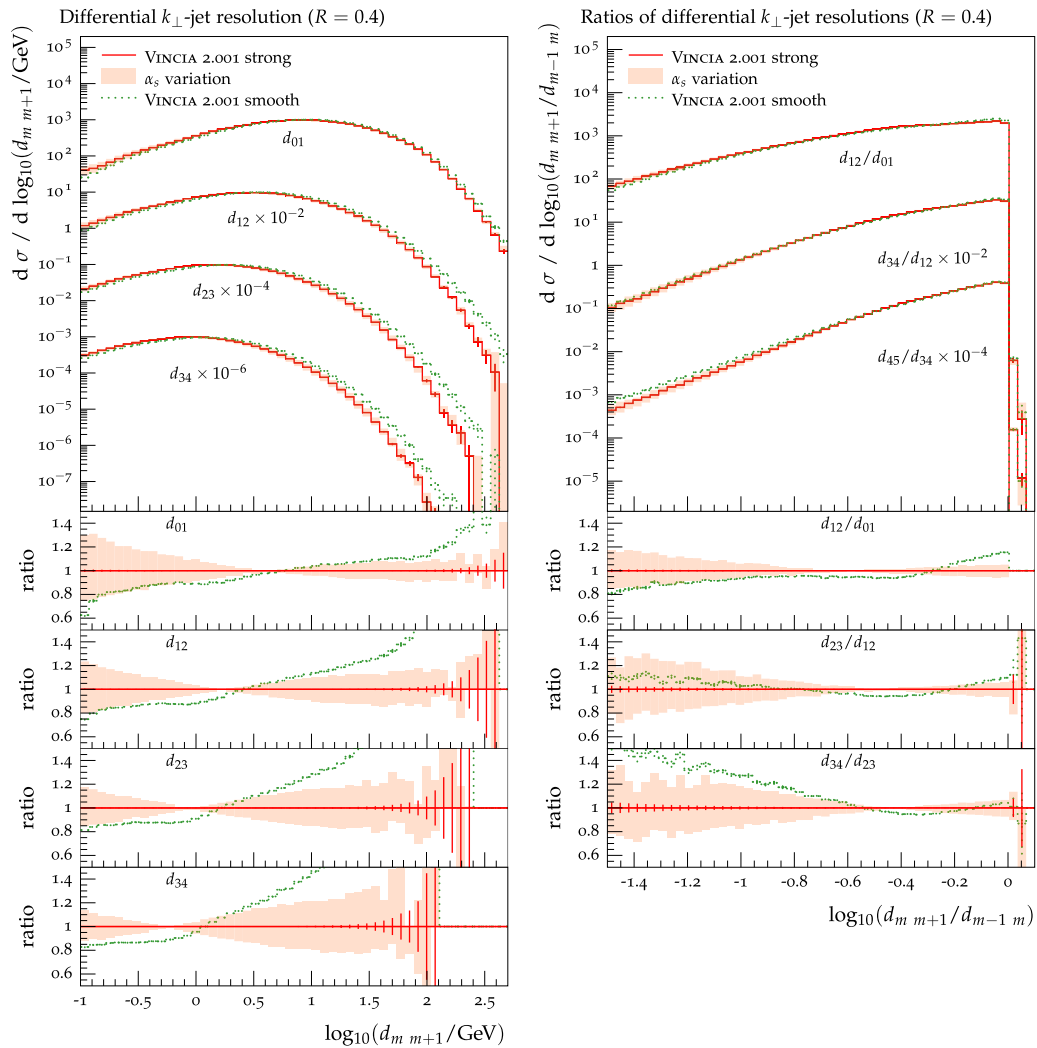


Fig. 15 Logarithmic distributions of differential jet resolutions and their ratios for Z+jets events. Predictions of VINCIA 2.0 with strong (*smooth*) ordering are shown in *solid red* (*dotted green*) lines. The *red band* shows an α_s variation with $\alpha_s(m_Z) = 0.12$ and $\alpha_s(m_Z) = 0.14$

which after a bit of algebra can be cast in the following form:

$$\frac{1}{2} \ln^2 \left[\frac{Q_{\perp}^2}{p_{\perp}^2} \right] + \ln \left[\frac{Q_{\perp}^2}{p_{\perp}^2} \right] \ln \left[\frac{m^2}{Q_{\perp}^2} \right] + \ln \left[1 + \frac{p_{\perp}^2}{Q_{\perp}^2} \right] \ln \left[\frac{m^2}{p_{\perp}^2} \right] - \text{Li}_2 \left[\frac{-Q_{\perp}^2}{m^2} \right] - \text{Li}_2 \left[\frac{-p_{\perp}^2}{Q_{\perp}^2} \right] - \frac{\pi^2}{6}, \tag{79}$$

where the two first terms are again identical to those of Eq. (76). In the third term, $\ln(1 + p_{\perp}^2/Q_{\perp}^2) \rightarrow 0$ for $p_{\perp}^2/Q_{\perp}^2 \rightarrow 0$, and the fourth and fifth terms are bounded by $-\pi^2/12 < \text{Li}_2(-x) < 0$ (with 0 corresponding to the limit $x \rightarrow 0$ and $-\pi^2/12$ for $x \rightarrow 1$). We thus conclude that the LL properties of the antenna shower are not spoiled by changing from strong to smooth ordering.

Hadronic Z decays

To increase the available phase space we used a heavy Z with $m_Z = 1000$ GeV which decays hadronically. In Fig. 14 we present the parton-level result for four successive jet resolution measures, $y_{m,m+1}$ (with $m \in \{2, 3, 4, 5\}$), and their ratios $y_{m,m+1}/y_{m-1,m}$, using the Durham jet algorithm. Jet resolution scales exhibit a Sudakov suppression for low values, and exhibit fixed-order behaviour for large values. We note that in realistic calculations (and in experimental data), low-scale values are typically strongly affected by hadronisation corrections, which are absent here since we are at parton level, with a fixed α_s . We also exclude values of $y_{m,m+1}$ corresponding to scales below the shower cutoff. Small values of the ratios $y_{m,m+1}/y_{m-1,m}$ highlight the modelling in the region

of large scale separation, i.e. where effects of resummation become relevant. Large values of y_{m+1}/y_{m-1} are associated with the region of validity of fixed-order calculations.

In the distributions of the jet resolution scales themselves we observe moderate differences between the different ordering modes, up to $\mathcal{O}(20\%)$. Smooth ordering generates more events with larger y_{m+1} separation and, consequently, fewer events with small separation, compared to strong ordering.

While the prediction with smooth ordering lies below the strongly ordered one for small values of the y_{34}/y_{23} ratio, it eventually slightly exceeds the strong ordering in the y_{56}/y_{45} ratio. This behaviour is a combination of two effects: Smooth ordering allows more phase-space coverage, while at the same time, the Markovian restart scale means that emissions from “ordered” antennae have more stringent phase-space restrictions than in the strongly ordered case. Thus, if more ordered antennae are present, which is only the case after several branchings, the Markovian restarting scale may lead to a softer multi-emission pattern than in the strongly ordered case. However, recall that MECs are an essential ingredient in the evolution, and that, for emissions beyond the highest ME multiplicity, no smooth ordering is applied. This means that, for lower multiplicities, the effect of smooth ordering is effectively removed and replaced by the full fixed-order result. For higher multiplicities, the shape change due to the Markovian restart scale is also absent, since smooth ordering is not applied. This suggests that smooth ordering of the entire cascade, and without MECs, exhibits some undesirable features. However, it is worth noting that the differences are largest in the soft region, where non-perturbative physics and tuning are expected to have large impact, as e.g. exemplified by a large dependence on the value of $\alpha_s(m_Z)$. Finally we note that the prediction with smooth ordering lies well within the $\alpha_s(m_Z)$ -variation band of the strong ordering.

Drell–Yan

The parton-level results for Z +jets events are presented in Fig. 15: four successive jet resolution measures, d_{m+1} (with $m \in \{0, 3\}$), and their ratios d_{m+1}/d_{m-1} , using the longitudinally invariant k_\perp jet algorithm with $R = 0.4$. As before, jet resolution scales show a fixed-order behaviour for large values, a Sudakov suppression and potentially large non-perturbative corrections for low values. The ratios y_{m+1}/y_{m-1} are used to more clearly reveal the successive scale hierarchies.

The observations for both, the jet resolution scales, and their ratios, are qualitatively similar to the $e^+e^- \rightarrow$ jets case, though quantitatively the effects here are larger. We notice the same turn-over when going from d_{12}/d_{01} to d_{34}/d_{23} we saw for Z decays, with the explanation being very similar to the case before. Smooth ordering will allow

additional phase-space regions to be filled with harder emission (cf. Fig. 10). Due to the unitarity of the parton-shower algorithm, this naively means that fewer soft emissions occur. This is counter-acted by the Markovian restart scale, which means that the smoothly ordered shower yields softer emissions from “ordered” antennae. At low multiplicity, the former dominates, as all antennae are allowed to fill their available phase space, while at higher multiplicity, the latter drives the differences. Figure 15 shows trends in d_{01} and d_{12} similar to the ones visible in Figs. 10 and 20 of [87]. Note again that the additional, compensating effect of the Markovian restarting scale starts playing an important role for higher multiplicities.

3.5 Hard jets in QCD processes

We already discussed our strategy to include hard branchings in non-QCD processes in Sect. 3.1. For processes with QCD jets in the final state we apply a different formalism, as the Born process already comes with a QCD scale. The first branching is allowed to populate all of phase space; however, the region with scales above the factorisation scale, $t > t_{\text{fac}}$, is treated with smooth ordering, as described in Sect. 3.3. In Fig. 16 we show the PS-to-ME ratios for $gg \rightarrow ggg$ and $q\bar{q} \rightarrow ggg$ where the factorisation scale is chosen to be the transverse momentum of the final-state partons in the Born $2 \rightarrow 2$ process. We show a comparison of strong ordering, i.e. not including $t > t_{\text{fac}}$, smooth ordering with $\hat{t} = t_{\text{fac}}$ in the P_{imp} factor, and no ordering, which corresponds to adding an event sample with $t > t_{\text{fac}}$. The plots indicate that the smooth ordering is preferred over adding hard jets as a separate event sample. Note that the asymmetric distribution of the PS-to-ME ratio for $gg \rightarrow ggg$ is the result of combining the distributions of different colour flows.

One could imagine applying the same treatment to non-QCD processes as well. However, this is not done in VINCIA as the factorisation scale in these processes is not a QCD scale and therefore not suited to enter the P_{imp} factor.

3.6 Matrix-element corrections with MADGRAPH 4

In this section we review the GKS procedure for iterative matrix-element corrections (MECs) [39]. To first order, the formalism is equivalent to that by Bengtsson and Sjöstrand in Refs. [5, 12], and to the approach used for real corrections in POWHEG [88, 89]. In the context of final-state showers, the approach was generalised to multiple emissions in [39] where it was successfully used to include MECs through $\mathcal{O}(\alpha_s^4)$ for hadronic Z decays. A generalisation at the one-loop level has also been developed [40], though so far limited to $\mathcal{O}(\alpha_s^2)$. Here, we focus on tree-level corrections only.

Matrix-element corrections take the all-orders approximation of the shower as their starting point, and apply ME-based

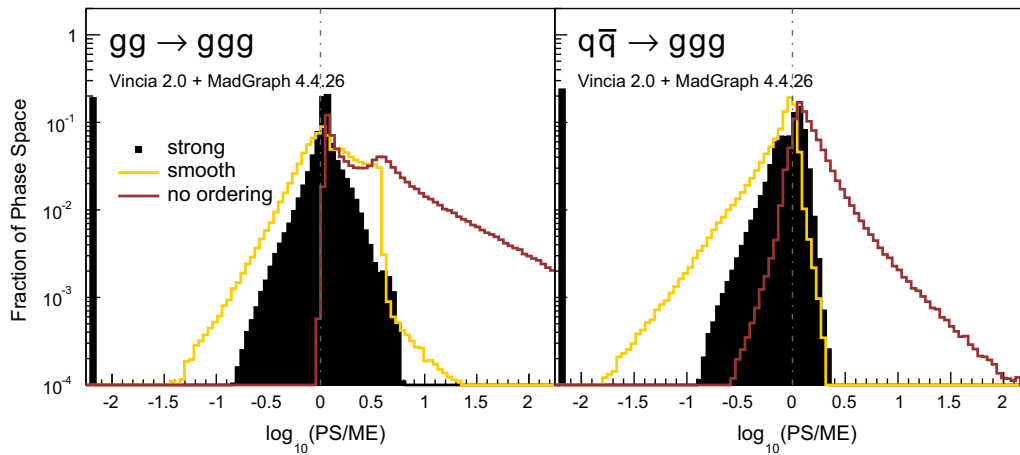


Fig. 16 Antenna shower, compared to matrix elements: distribution of $\log_{10}(\text{PS}/\text{ME})$ in a flat phase-space scan of the full phase space with strong, smooth, and no ordering with respect to the factorisation scale

of the Born process. Contents normalised to the number of generated points. Gluon emission only

corrections to this structure order by order in perturbation theory. At tree level, the following multiplicative correction factor is applied to each antenna function for matching to leading-colour matrix elements,

$$C_i \bar{a}_i \rightarrow C_i \bar{a}_i P_n^{\text{ME}} \quad \text{with} \quad P_n^{\text{ME}} = \frac{|\mathcal{M}_n|^2}{\sum_j C_j \bar{a}_j |\mathcal{M}_{n-1}|^2}, \tag{80}$$

with the n -particle matrix element squared $|\mathcal{M}_n|^2$, see Eqs. (81) and (82) for more details on colour ordering. Given VINCIA's invertible kinematics maps and the explicit forms of the physical antenna functions defined in Sect. 2, the denominator is exactly calculable (taking the smooth ordering P_{imp} factors defined in the previous section into account). The numerator is obtained by using amplitudes derived from MADGRAPH 4 [50], stored in VINCIA's `interfaces/MG4` subdirectory. Minor extensions were required to include processes with initial-state coloured partons, and several new matrix-element routines were added in the context of this work. The F77 syntax for calling a VINCIA-modified MG4 matrix element is (using the specific example of a $b\bar{b} \rightarrow Hgg$ matrix element):

```
SUBROUTINE Sbbx2gggh (MCMODE, ICOL, P1,
HEL1, ANS)
```

where

- INTEGER MCMODE selects between Leading Colour (0), VINCIA Colour (1), and Full Colour (2), as defined below,
- INTEGER ICOL selects which colour ordering is desired for MCMODE=0, 1,

- DOUBLE PRECISION P1(0:3, NEXTERNAL) the momenta of the particles (in this example NEXTERNAL=6),
- INTEGER HEL1(4) holding up to 4 helicity configurations to be summed over, sufficient to average over an unpolarised initial 2-parton state or decaying vector boson, with specified final-state helicities. The enumeration of helicity configurations follows MADGRAPH's normal helicity-counting convention.
- The requested matrix element squared is saved in the double-precision ANS variable, which in VINCIA always has only a single element.

From within VINCIA these matrix elements are accessed via C++ wrappers accessible via the `VinciaPlugin::mgInterface.ME2()` methods, with definitions contained in the `MG4interface.h` and `MG4interface.cc` files. The input is a number of particles with partons being colour ordered, i.e. ordered in colour chains such as $q - g - g - \bar{q}$, where initial partons are crossed into the final state. The diagonal entry in MADGRAPH's colour matrix, C_{ii}^{MG} , associated with the given colour order, is chosen with ICOL. Using the more recent convention of MADGRAPH 5 [90]¹² we define the leading-colour matrix element as

$$|\mathcal{M}_n|^2 = C_{ii}^{\text{MG}} \left| \mathcal{J}_n^{(i)} \right|^2, \tag{81}$$

with the colour-stripped n -particle amplitude $\mathcal{J}_n^{(i)}$ corresponding directly to a JAMP in MADGRAPH's nomenclature.

¹² In MADGRAPH 4 the colour matrix for amplitudes with multiple quark pairs is more complicated and required a decomposition by hand to separate the leading- from the subleading-colour parts, as is now done automatically by MADGRAPH 5.

Full-colour matrix-element corrections: The full matrix element contains contributions that cannot be associated with a single colour ordering, i.e. the off-diagonal entries of the colour matrix, representing interferences between different colour orderings. To include those subleading-colour contributions while remaining within a formalism that provides strictly positive-definite correction factors, we use the following prescription [39] (VINCIA colour):

$$|\mathcal{M}_n|^2 = c_{ii}^{\text{MG}} \left| \mathcal{J}_n^{(i)} \right|^2 \rightarrow c_{ii}^{\text{MG}} \left| \mathcal{J}_n^{(i)} \right|^2 \frac{\sum_{j,k} c_{jk}^{\text{MG}} \mathcal{J}_n^{(j)} \mathcal{J}_n^{(k)*}}{\sum_j c_{jj}^{\text{MG}} \left| \mathcal{J}_n^{(j)} \right|^2}. \quad (82)$$

The matrix element for each colour structure gets a correction from the subleading-colour part of the full matrix element that is proportional to the relative weight of that colour structure such that the sum over all colour flows reproduces the full-colour-summed matrix element norm squared.

Note that, though we show all matrix-element comparisons with leading colour, the conclusions do not change when replacing leading with full colour.

Interference between different Born-level processes: In previous versions of VINCIA the interference contributions from different Born-level processes were ignored; e.g., the interference between $Z \rightarrow d\bar{d}(g \rightarrow u\bar{u})$ and $Z \rightarrow u\bar{u}(g \rightarrow d\bar{d})$ contributing to $Z \rightarrow d\bar{d}u\bar{u}$ was not included. As those interferences can become fairly large and are already present for the first branching, e.g., $qg \rightarrow qgg$ can arise from $gg \rightarrow gg$ or $qg \rightarrow qg$ Born-level processes, we developed a more general formalism capable of handling these cases. Yet more interesting and illustrative are the interferences between $gg \rightarrow H$ and $Q\bar{Q} \rightarrow H$ Born processes, which both contribute to $Qg \rightarrow QH$ (with Q a heavy quark) but involve completely different types and orders of couplings. For this special case of Higgs production and decay we provide an option to allow/disallow such interferences.

Impact of matrix-element corrections: In Fig. 17 we show parton-level predictions of VINCIA in Z production events, i.e. multi-parton-interactions and hadronisation turned off, to focus solely on the shower properties and the impact of successive MECs. Comparisons to data

increasing orders of MECs included to ATLAS [91] and CMS [92] data. The inclusive cross section and the azimuthal angle between the reconstructed Z boson and the hardest jet (shown in the upper panel of Fig. 17) clearly highlight that MECs improve the description of data sensitive to multiple hard emissions. The progressive improvements that are introduced through iterated MECs is particularly obvious in the inclusive jet multiplicity. It is worthwhile mentioning that jet multiplicities beyond the third jet are only described by the approximate shower result. However, the combination of MECs up to third order seems to yield a good starting point for the shower, such that also high jet multiplicities are well described. Note that correcting only the hardest emission leads only to a modest improvement, since VINCIA's antenna functions already provide a good approximation of the Z + jet matrix element. The lower panel of Fig. 17 shows the jet transverse momentum in exclusive Z + jet events. This observable should be dominated by the MEC of the hardest emission. Indeed, the description improves over plain showering, and is very stable upon iteratively including MECs to higher multiplicities. This showcases that MECs to higher-multiplicity states do not degrade the quality of the description of lower-multiplicity observables.

4 Preliminary results and tuning

4.1 The strong coupling

All components of VINCIA (i.e., both matrix-element corrections and showers) use a single reference value for strong coupling constant, with the default value $\alpha_s^{\overline{\text{MS}}}(M_Z) = 0.118$, in agreement with the current world average [53,93]. By default, we use two-loop running expressions, with the number of active flavours changing at each quark-mass threshold (including at m_t), though options for one-loop running or even fixed α_s values are provided as well. The inclusion of three-loop running effects is not relevant at the present (LO+LL) level of precision of the shower. In the infrared, the behaviour of α_s is regulated by allowing to evaluate it at a slightly displaced scale, $\alpha_s(\mu) \rightarrow \alpha_s(\mu + \mu_0)$ and by imposing an upper bound $\alpha_s < \alpha_s^{\text{max}}$. The set of default parameter values are:

```
Vincia:alphaSvalue = 0.118 ! Default alphaS(mZ) MSbar
Vincia:alphaSorder = 2 ! Default is two-loop running
Vincia:alphaSmuFreeze = 0.4 ! mu0 scale in alphaS argument, in GeV
Vincia:alphaSmax = 1.2 ! max numerical value of alphaS
```

including multi-parton-interactions and hadronisation will be presented in the section Sect. 4. We compare VINCIA with

Within the context of an LO+LL calculation, however, the value $\alpha_s(M_Z) = 0.118$ produces a poor agreement with collider measurements; direct “tunings” at the LO+LL level

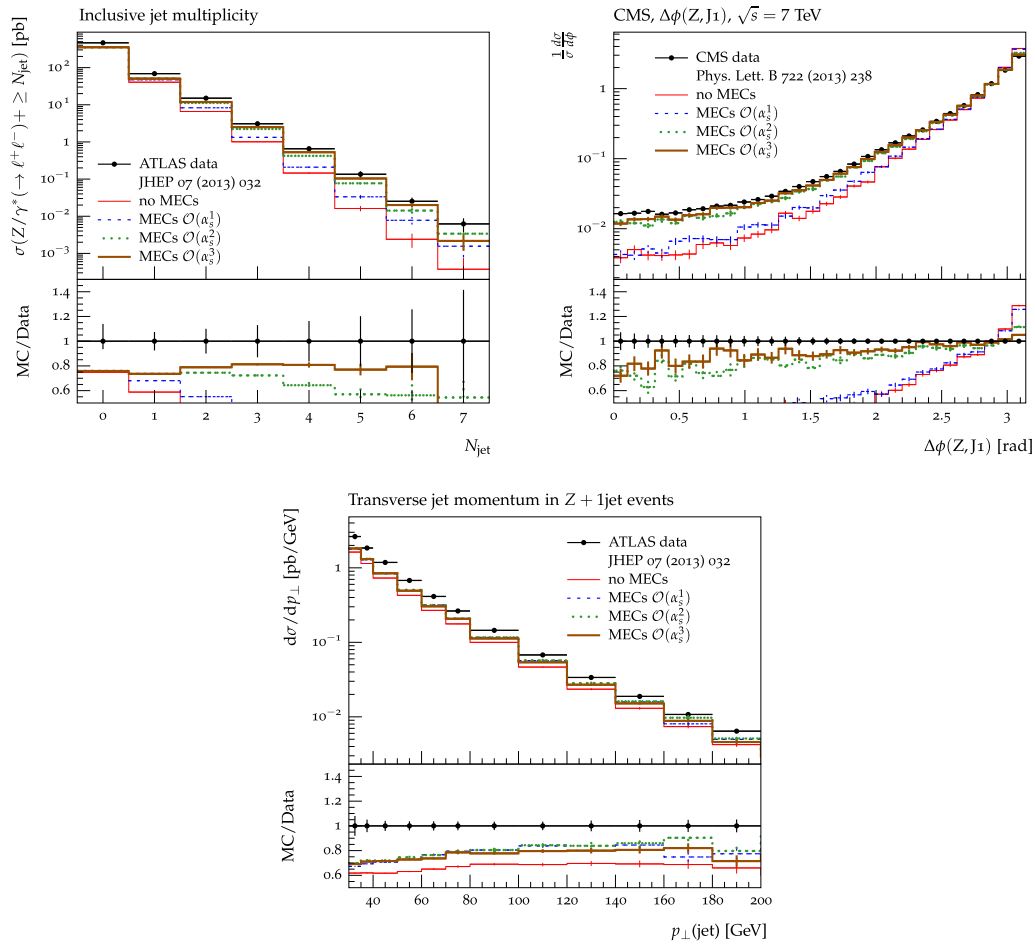


Fig. 17 Inclusive cross section for the Drell-Yan lepton pair plus $\geq N$ jets (top left), distribution of the azimuthal angle between the Z boson and the hardest jet (top right), and jet p_{\perp} in Z + 1 jet events (bottom).

Parton-level predictions of VINCIA 2.0 for increasing order of MECs included, compared to ATLAS data from [91] and CMS data from [92]

typically find effective values closer to $\alpha_s(M_Z) = 0.140$, see e.g. [39,94]. To permit analogous tunings of VINCIA, a user-specifiable prefactor is applied to the renormalisation-scale argument for each branching type,

$$\text{Gluon Emission} : \alpha_s(p_{\perp}) \rightarrow \alpha_s(k_{\mu} p_{\perp}), \tag{83}$$

$$\text{Gluon Splitting} : \alpha_s(m_{qq}) \rightarrow \alpha_s(k_{\mu}^{\text{split}} m_{qq}), \tag{84}$$

with equivalent parameters for splittings involving initial-state partons. The k_{μ} and k_{μ}^{split} parameters provide the same range of tuning possibilities for the effective coupling constant as in other parton-shower models, while they are simultaneously straightforward to interpret e.g. in the context of NLO matrix-element merging schemes.

The VINCIA shower algorithms do nonetheless incorporate a translation (on by default) between the $\overline{\text{MS}}$ value given above and the so-called CMW (or MC) scheme which is

appropriate for soft-gluon emission in coherent parton showers [32]. Since this translation is only rigorously defined in the limit of vanishing gluon energy, there is an ambiguity as to precisely how it should be applied to finite gluon energies. We address this by applying the CMW translation only to the coupling constant accompanying the eikonal (double-pole) term of the gluon-emission antenna functions,

$$\alpha_s^{\overline{\text{MS}}} a_{\text{Emit}} = \alpha_s^{\overline{\text{MS}}} (a_{\text{eik}} + a_{\text{coll}} + a_{\text{hard}}) \tag{85}$$

$$\rightarrow \alpha_s^{\text{CMW}} a_{\text{eik}} + \alpha_s^{\overline{\text{MS}}} (a_{\text{coll}} + a_{\text{hard}}), \tag{86}$$

with a few different options provided for how the eikonal term should be extrapolated to finite gluon energies. In a future study we shall aim to bring these ambiguities under better control by systematic application of one-loop corrected antenna functions, but this is still (far) beyond the scope of the present work.

4.2 VINCIA 2.0 default tune

Two main tools were used to perform the analyses: VINCIA's own ROOT-based analysis tool, VINCIAROOT [39], and RIVET [95]. For the hadron-collider distributions, we compare VINCIA 2.0 with PYTHIA 8.2. For the $e^+e^- \rightarrow$ hadrons analyses, we also include VINCIA 1.2, since this version included NLO corrections to $e^+e^- \rightarrow 3$ jets which have not yet been migrated to VINCIA 2.0. Note, however, that even without the NLO corrections the two VINCIA versions are not exactly identical due to a slightly revised definition of the smooth-ordering criterion, to make it truly Markovian.

We note that these tunings were done manually (by “eye”), rather than by automated minimisation of χ^2 or equivalent measures. The latter is not as straightforward as it may sound, due to correlations between measurements and the influence of regions of low theoretical accuracy. These issues can be at least partially addressed by combining global knowledge and experience to (subjectively) choose binwise weighting factors. Nevertheless, manual and automated approaches may be considered complementary, with the former certainly competitive for the purpose of determining a set of “reasonable default values”, which is our principal aim here.

```
Vincia:cutoffScaleFF = 0.9 ! Cutoff value in GeV for FF antennae
StringZ:aLund        = 0.5 ! Lund a parameter
StringZ:bLund        = 1.15 ! Lund b parameter
StringZ:aExtraDiquark= 1.12 ! (extra for diquarks)
StringPT:sigma       = 0.295 ! Soft pT in string breaks
```

Hadronic Z decays

The final-state showering and hadronisation parameters are constrained using hadronic Z decays, mainly from the LEP experiments. In the context of VINCIA 2.0, the rates of perturbative final-state branchings depend on the effective renormalisation scheme and scale choice, cf. Eq. (83), for which we have chosen the default values:

```
Vincia:CMWtypeFF    = 2 ! CMW rescaling for FF antennae
Vincia:alphaSkMuF   = 0.6 ! muR prefactor for gluon emissions
Vincia:alphaSkMuSplitF = 0.5 ! muR prefactor for gluon splittings
! (g -> qqbar)
```

Figure 18 shows the event-shape observables¹³ that were used as the primary tuning constraints, compared with light-flavour tagged data from the L3 experiment [96]. In the main (top) plot panes, experimental data is represented by black square symbols, with $1\text{-}\sigma$ and $2\text{-}\sigma$ uncertainties represented by black vertical error bars and light-grey extensions, respec-

tively. In the ratio panes, the inner (green) bands indicate the $1\text{-}\sigma$ uncertainties on the data; outer (yellow) bands represent $2\text{-}\sigma$.

Note that, since VINCIA 2.0 does not incorporate the NLO corrections to $Z \rightarrow 3$ jets internally (unlike VINCIA 1.2 [40]), we have chosen to allow the default tune to undershoot the reference data slightly in regions dominated by hard, resolved 3-jet events. This hopefully produces a more universal global tuning which should also be appropriate for use with the NLO merging strategies that are available within PYTHIA, notably UNLOPS [97].

The Lund string model [98–100] is used for hadronisation, with parameters (re)optimised for use with VINCIA's shower model. The main parameters are the shower IR cutoff, the Lund fragmentation-function a and b parameters—which are defined by

$$f(z) \propto \frac{(1-z)^a}{z} \exp\left(\frac{-bm_{\perp}^2}{z}\right), \quad (87)$$

with $z = E_{\text{hadron}}/E_{\text{parton}}$ and $m_{\perp}^2 = m^2 + p_{\perp}^2$ —and the transverse-momentum broadening in string breaks, expressed as a Gaussian with width $\sigma_{\perp} \sim \mathcal{O}(\Lambda_{\text{QCD}})$. The default VINCIA 2.001 hadronisation-parameter values are,

The inclusive charged-particle multiplicity distribution and momentum ($x_p = 2|p|/E_{\text{cm}}$) spectrum is shown in Fig. 19, again compared with light-flavour tagged L3 data from [96].

Finally, we show the rates for identified light-flavour mesons and baryons in Fig. 20; these hardly change between the PYTHIA, VINCIA 1, and VINCIA 2 defaults. Note that we

here compare to the reference measurement values derived for the Monash tune [94] of PYTHIA 8, which are not identical to the corresponding PDG values in particular for some of the baryon rates, see [94].

The corresponding full set of default parameter values are:

¹³ For definitions, see e.g. [96].

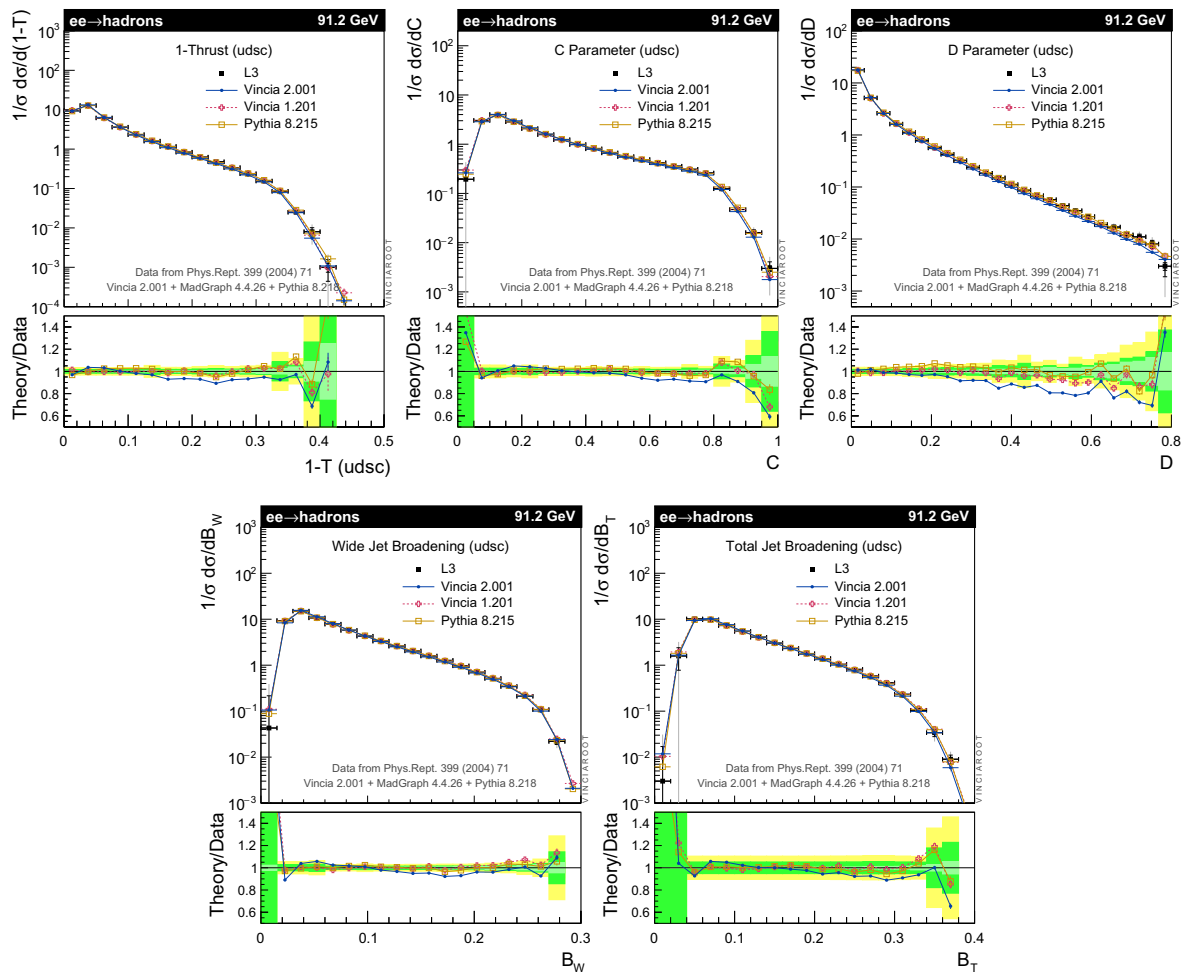


Fig. 18 Event-shape variables compared with measurements performed by the L3 experiment

```

! * String breakup flavour parameters
StringFlav:probStoUD      = 0.21    ! Strangeness-to-UD ratio
StringFlav:mesonUDvector  = 0.45    ! Light-flavour vector suppression
StringFlav:mesonSvector   = 0.555   ! Strange vector-meson suppression
StringFlav:mesonCvector   = 1.03    ! Charm vector-meson suppression
StringFlav:mesonBvector   = 2.2     ! Bottom vector-meson suppression
StringFlav:probQQtoQ      = 0.077   ! Diquark rate (for baryon production)
StringFlav:probSQtoQQ     = 1.0     ! Optional Strange diquark suppression
StringFlav:probQQ1toQQ0   = 0.027   ! Vector diquark suppression
StringFlav:etaSup         = 0.53    ! Eta suppression
StringFlav:etaPrimeSup    = 0.105   ! Eta' suppression
StringFlav:decupletSup    = 1.0     ! Optional Spin-3/2 Baryon Suppression
StringFlav:popcornSpair   = 0.9     ! Popcorn
StringFlav:popcornSmeson  = 0.5     ! Popcorn
StringZ:rFactC            = 1.60    ! Bowler parameter for c quarks
StringZ:rFactB            = 1.1     ! Bowler parameter for b quarks
StringZ:useNonstandardB   = true    ! Special treatment for b quarks

```

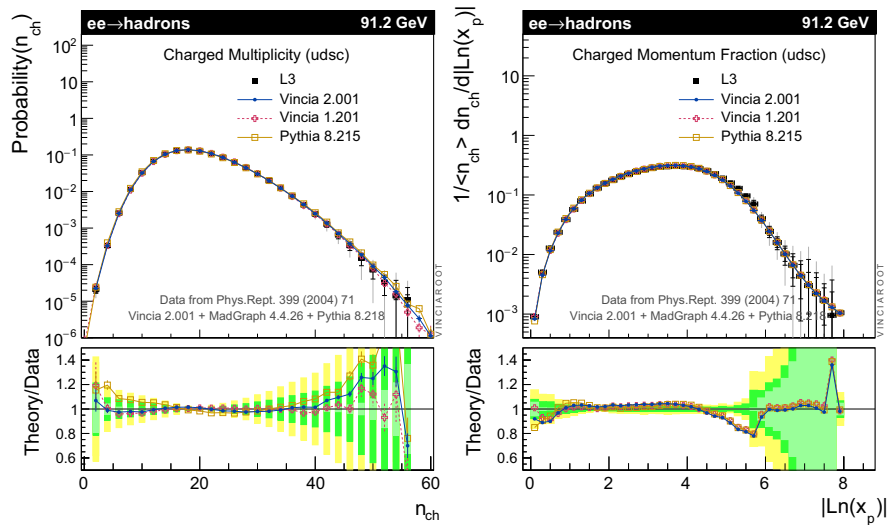


Fig. 19 Charged-track multiplicity and momentum spectra, compared with measurements performed by the L3 experiment

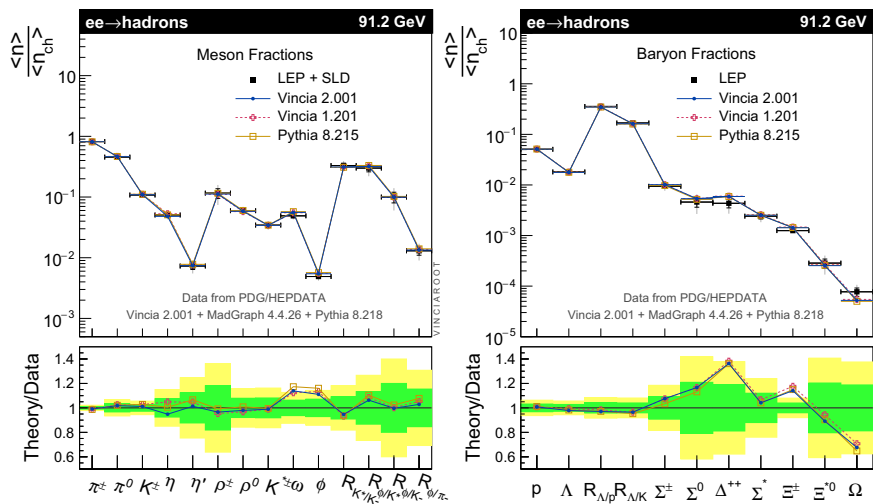


Fig. 20 Identified-particle rates (expressed as fractions of the charged-particle multiplicity, or as indicated by *R* symbols), compared with the Monash 2013 reference values

StringZ:aNonstandardB = 0.82 ! a parameter for b quarks
 StringZ:bNonstandardB = 1.4 ! b parameter for b quarks

Note that the last 6 parameters govern *c*- and particularly *b*-quark fragmentation. Since massive-quark effects are not explicitly addressed in this version of VINCIA, these parameters have been chosen merely on a “best-effort” basis. We plan to return to this in a future update. A minimal set of checks on the level of agreement with heavy-quark spectra can be carried out using the vincia03-root and vincia05-root example programs included with the

code. The former includes cross checks on the $g \rightarrow c\bar{c}$ and $g \rightarrow b\bar{b}$ rates as well as a D^* spectrum, sensitive to *c*-quark fragmentation, while the latter focuses on constraints from *b*-tagged events. For completeness, the D^* and *B*-hadron spectra produced by these example programs are reproduced in Fig. 21.

For the SLD x_B spectrum, be advised that the current distribution of VINCIA (version 2.001) contains the spectrum obtained from the HepData archive [104] at the time of writ-

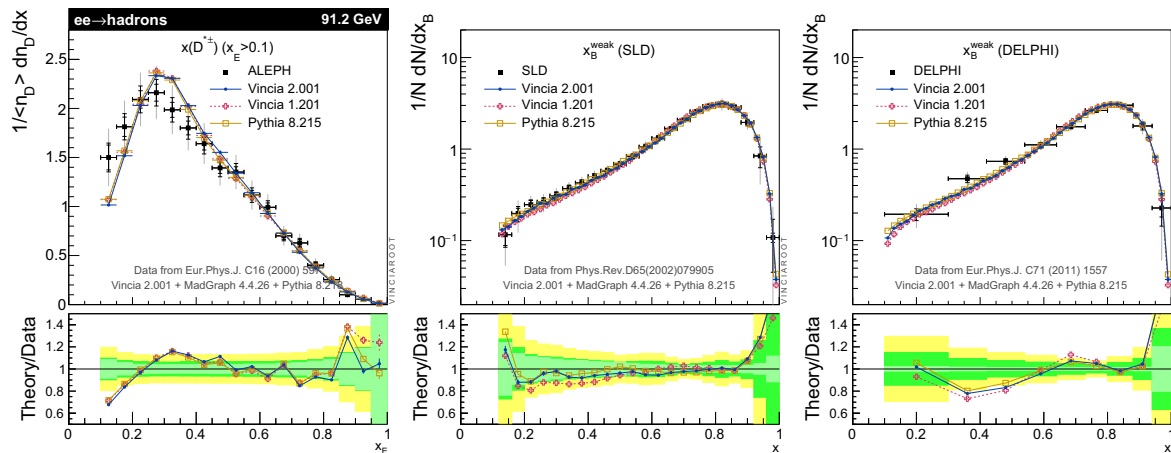


Fig. 21 Distributions sensitive to heavy-quark fragmentation. *Left* the energy-fraction spectrum of charged D^* mesons compared with ALEPH data [101]. *Center and right* the momentum-fraction spec-

trum of weakly decaying B hadrons compared to measurements by SLD [102] and DELPHI [103], respectively

ing. However, the corrections contained in an erratum subsequently published by SLD [102] were missing from this table. The figure we show here contains the updated values (from the erratum). The updated table will be included in the next public release of VINCIA, with corresponding updates expected in the HepData archive in due course.

Drell–Yan

In Figs. 22, 23 and 24 we show a set of observables in Drell–Yan events with ATLAS data from [105] and [106] and CMS data from [92] and [107]. We show predictions of default VINCIA 2.0 in red, VINCIA 2.0 wimpy (representing an ordinary shower, starting at the factorisation scale, i.e. no hard jets, no MECs, and strong ordering) in green, and PYTHIA 8.2 in blue. The VINCIA 2.001 results correspond to the following default parameter choices:

```
# Perturbative shower parameters
Vincia:CMWtypeII      = 2      ! CMW rescaling of Lambda for II antennae
Vincia:CMWtypeIF      = 2      ! CMW rescaling of Lambda for IF antennae
Vincia:alphaSkMuI     = 0.75  ! Renormalisation-scale prefactor for ISR
                          ! emissions
Vincia:alphaSkMuSplitI = 0.7   !  "-- for g->qq splittings
Vincia:alphaSkMuConv  = 0.7   !  "-- for ISR conversions
# Shower IR cutoff and primordial kT
Vincia:cutoffScaleII  = 1.0    ! Cutoff value (in GeV) for II antennae
Vincia:cutoffScaleIF  = 0.9    ! Cutoff value (in GeV) for IF antennae
BeamRemnants:primordialkThard = 1.05 ! Primordial kT for hard interactions
BeamRemnants:primordialkTsoft = 0.7 ! Primordial kT for soft interactions
```

Figure 22 shows angular correlations and the transverse-momentum spectrum of the Drell–Yan lepton pair. As one

would expect the spectrum of VINCIA 2.0 wimpy dies out at the Z mass. The prediction of default VINCIA 2.0 shows too much activity in the hard tail of the spectrum which is caused by the reweighting of the event sample that includes high- p_{\perp} jets, see Sect. 3.1. The tuning of the renormalisation-scale prefactor was chosen to produce as good a compromise as possible between the regions above and below $p_{\perp} \sim m_Z/2$.

Figure 23 shows the improved predictions when MECs are included. The left plot shows the relative azimuthal angle between the Z boson and the hardest jet, $\Delta\phi(Z, J_1)$, where multiple shower emissions are required to obtain values below π . This plots shows that although PYTHIA's power shower is matrix-element corrected for the first emission and results in a very good description of the Z transverse momentum, its prediction for $\Delta\phi(Z, J_1)$ is worse than that of VINCIA 2.0 wimpy. For this observable as well as for the thrust in the right plot in Fig. 23 default VINCIA 2.0 agrees well with the data.

Figure 24 shows the inclusive cross section for the Drell–Yan lepton pair plus $\geq N$ jets, the transverse-momentum

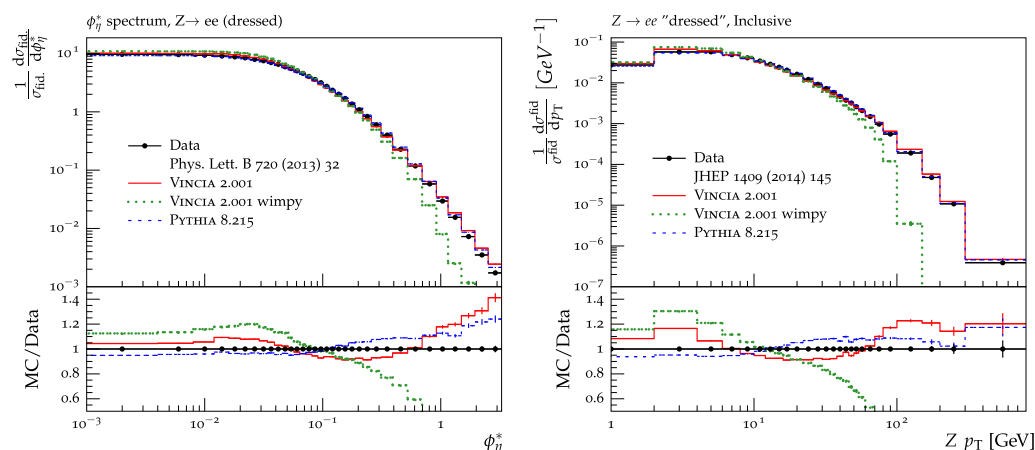


Fig. 22 Angular correlations (*left*) and the transverse-momentum spectrum (*right*) of the Drell-Yan lepton pair. Predictions of default VINCIA 2.0 in *red*, VINCIA 2.0 wimpy in *green*, and PYTHIA 8.2 in *blue*, compared to ATLAS data from [105] and [106]

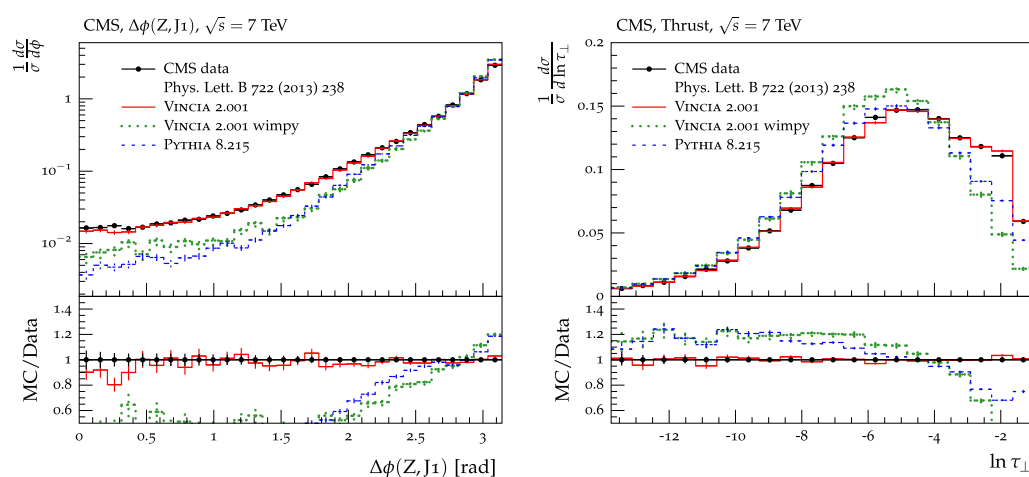


Fig. 23 Distribution of the azimuthal angle between the Z boson and the hardest jet (*left*) and thrust (*right*). Predictions of default VINCIA 2.0 in *red*, VINCIA 2.0 wimpy in *green*, and PYTHIA 8.2 in *blue*, compared to CMS data from [92]

and the pseudorapidity spectrum of the leading jet. For all observables we find default VINCIA 2.0 to produce a fairly good description of the data. As expected, VINCIA 2.0 wimpy is not able to produce enough jets and cannot populate the full spectrum of the transverse momentum of the hardest jet.

Underlying event

Although soft-inclusive QCD physics is not the main focus of this version of VINCIA, it is nonetheless relevant to verify

that a reasonable description of the underlying event (UE) is obtained. We rely on the basic multi-parton-interaction (MPI) modelling of PYTHIA 8 [8,34,108] including its default colour-reconnection (CR) model, with parameters reoptimised for use with VINCIA's initial- and final-state showers.

The MPI and CR parameter choices for the default VINCIA 2.001 tune are as follows:

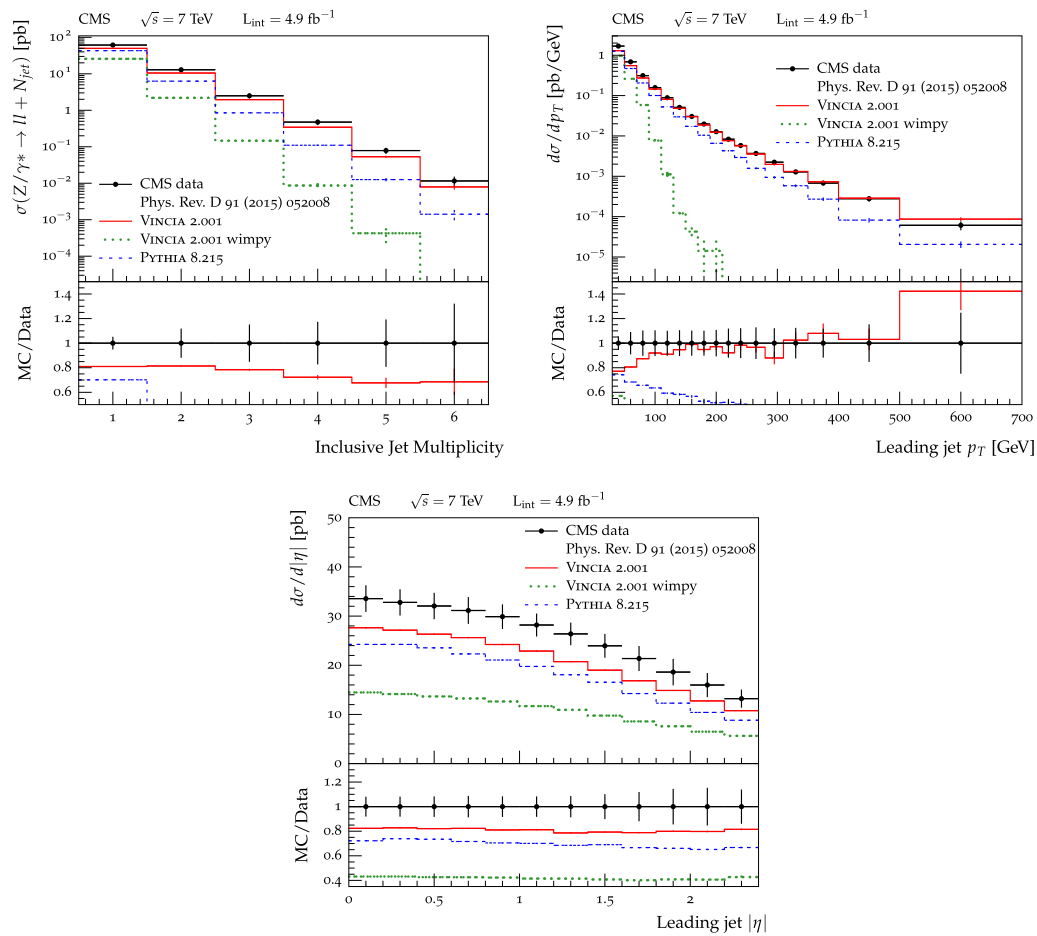


Fig. 24 Inclusive cross section for the Drell–Yan lepton pair plus $\geq N$ jets (*top left*), the transverse-momentum (*top right*) and the pseudo-rapidity spectrum of the leading jet (*bottom*). Predictions of default

VINCIA 2.0 in red, VINCIA 2.0 wimpy in green, and PYTHIA 8.2 in blue, compared to CMS data from [107]

```

! UE/MPI tuning parameters
SigmaProcess:alphaSvalue           = 0.118
SigmaProcess:alphaSorder           = 2
MultiPartonInteractions:alphaSvalue = 0.119
MultiPartonInteractions:alphaSorder = 2
MultiPartonInteractions:pT0ref     = 2.00
MultiPartonInteractions:expPow     = 1.75
MultiPartonInteractions:ecmPow     = 0.21
! Parameters for PYTHIA 8's baseline CR model
ColourReconnection:reconnect       = on
ColourReconnection:range           = 1.75
! VINCIA is not compatible with perturbative diffraction
Diffraction:mMinPert               = 1000000.0

```

Note that we choose two-loop running for α_s , analogously to the rest of VINCIA, whereas the default PYTHIA 8.2 Monash tune [94] uses one-loop running. We also set the $\alpha_s(M_Z)$

reference value for hard processes (SigmaProcess:alphaSvalue) to the same value (0.118) as used for the showers, and use a similar value (0.119) for MPI,

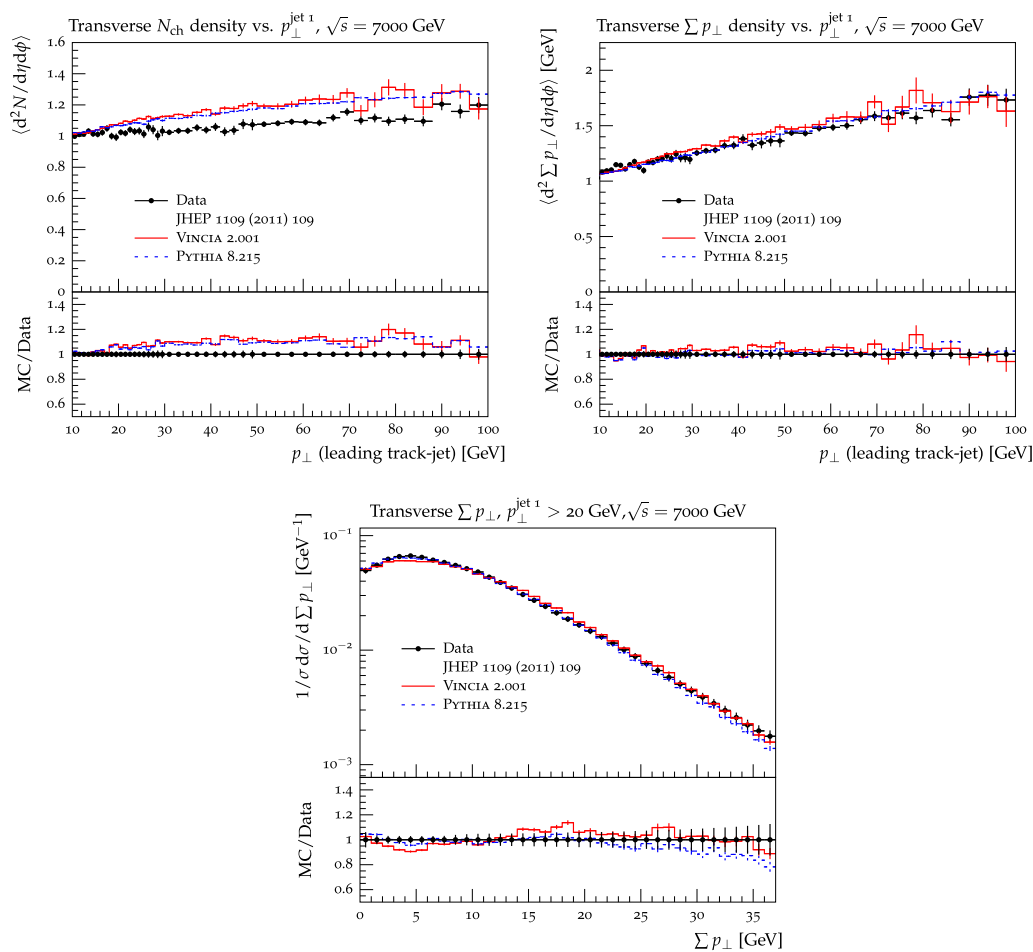


Fig. 25 The underlying event in pp collisions at 7 TeV: Measurement of charged particles with $p_{\perp} > 0.5$ GeV and $|\eta| < 2$ in the transverse region; average multiplicity (top left) and average scalar $\sum p_{\perp}$ (top right) as a function of the transverse momentum of the leading track-jet, and normalised scalar $\sum p_{\perp}$ distribution for leading

track-jets with $p_{\perp} > 20$ GeV (bottom). Predictions of default VINCIA 2.0 in red and PYTHIA 8.2 in blue, compared to CMS data from [110]. Note that we use a cut of $p_{\perp} > 15$ GeV in the hard process for the MC predictions and are therefore not showing the region of $1 \text{ GeV} < p_{\perp} (\text{leading track-jet}) < 10 \text{ GeV}$ for the top histograms

whereas the default PYTHIA tune employ larger values ~ 0.13 . The remaining MPI parameters were optimised using the 7-TeV charged-track summed- p_{\perp} and number densities from [109], as well as their 900-GeV equivalents to constrain the energy-scaling parameter. The colour-reconnection strength was determined using the high-multiplicity region of the $\langle p_{\perp} \rangle$ (N_{ch}) distribution measured by ATLAS [109] in minimum-bias events. It should be noted, however, that VINCIA is not suitable for (low-multiplicity) minimum-bias physics in its present form. This is partly related to the last parameter, which is included to switch off PYTHIA's perturbative treatment of hard diffraction, with which VINCIA is not yet compatible.

In Fig. 25, we compare default VINCIA 2.0 with default PYTHIA 8.2, to three basic observables measuring the level of activity in the region transverse to the leading (hardest) charged-particle jet in the central pseudorapidity region, $|\eta| < 2$, for LHC collisions at 7 TeV. We use the conventional definition of the transverse region, spanning $60^{\circ} < \Delta\phi < 120^{\circ}$ in azimuth with respect to the leading charged-particle jet, and compare to CMS data [110]. These comparisons satisfy us that at least the global properties of the UE are in acceptable agreement with the measurements, in particular in regards to the average p_{\perp} density (top right-hand plot) and its event-to-event fluctuations (bottom right-hand plot). The charged-track multiplicity (top left-hand plot) is a more dif-

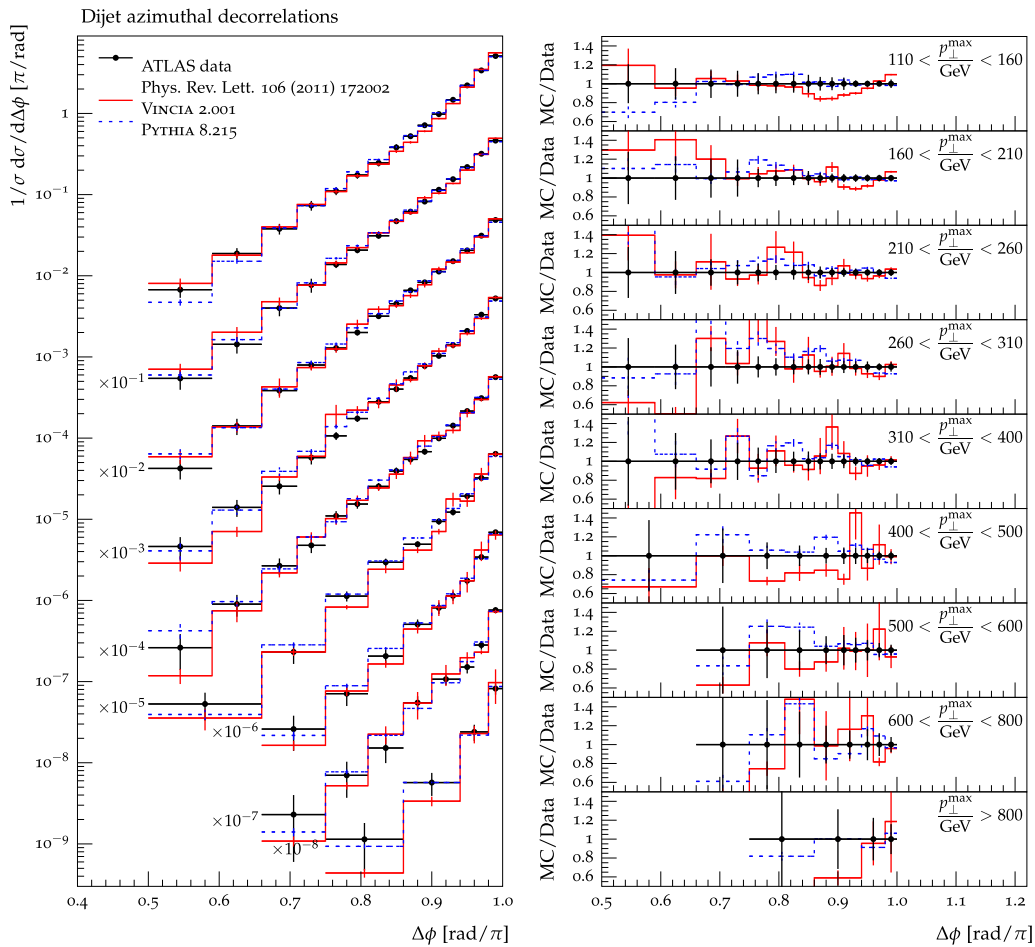


Fig. 26 Distribution of dijet azimuthal decorrelations; predictions of VINCIA 2.0 in red and PYTHIA 8.2 in blue, compared to ATLAS data from [112]

difficult observable to predict since it is less IR safe and hence more dependent on details of the hadronisation modelling; we presume that the small ($\mathcal{O}(10\%)$) discrepancies observed for both PYTHIA and VINCIA in this observables may be due to imperfections in PYTHIA's still rather crude modelling of colour reconnections.

QCD jets

As our final set of validation checks, we consider the following observables in hard-QCD events: azimuthal dijet decorrelations, jet cross sections, and jet shapes. A technical aspect is that, due to the steeply falling nature of the jet p_{\perp} spectrum, we use weighted events for all MC results in this section. The basic $2 \rightarrow 2$ QCD process at the scale \hat{p}_{\perp} is oversampled by an amount of $(\hat{p}_{\perp}/10)^4$, while the compensating event weight is $(10/\hat{p}_{\perp})^4$. This allows one to fill the low-cross-section tails of the distributions with a reasonable amount

of events. Note, however, that, for observables that are not identical to the biasing variable (which are all observables since no one-to-one measurement of the partonic \hat{p}_{\perp} is possible), rare events with large weights can then produce “spurious” peaks or dips in distributions, accompanied by large error bars. Such features are to be expected in some of the distributions we show below; removing them would require generating substantially more events. While these features appear in the predictions of VINCIA, they are not present in PYTHIA's distributions. The reason is as follows: The aforementioned event weight becomes large for small values of \hat{p}_{\perp} . As this value serves as the starting scale in PYTHIA's shower, the event will not produce any high- p_{\perp} jets. In VINCIA, however, the full phase space for the first emission is explored with the suppression factor P_{imp} which is necessary for the application of MECs. In the rare cases, where VINCIA produces a jet with $p_{\perp j} \gg \hat{p}_{\perp}$, the large event weight becomes visible in distributions which require high- p_{\perp} jets.

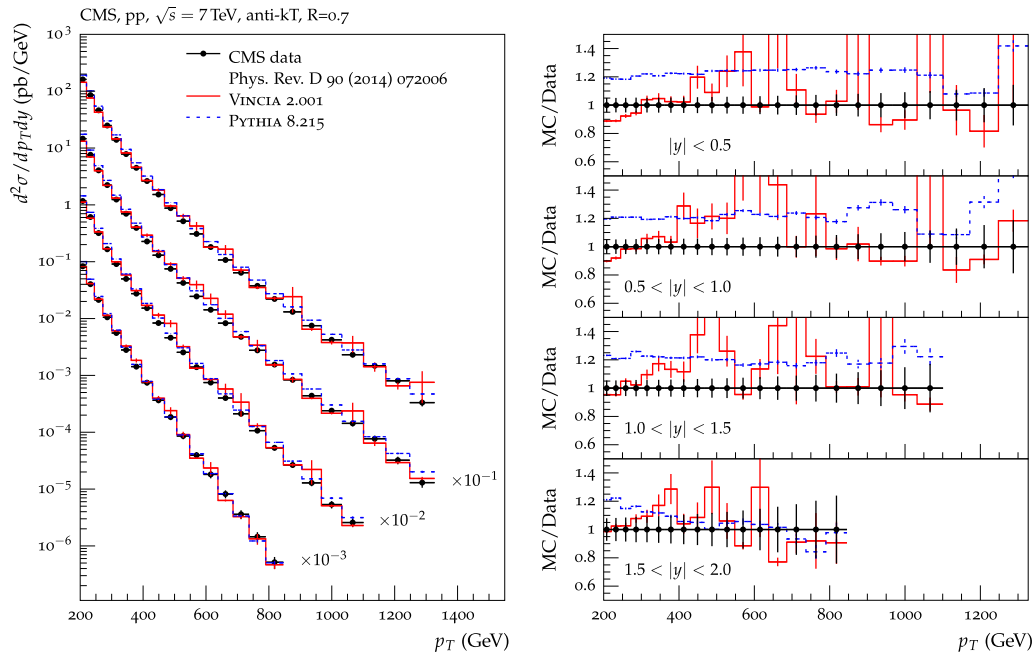


Fig. 27 Inclusive jet cross section for 4 different rapidity bins as a function of the jet p_{\perp} . Predictions of VINCIA 2.0 in red and PYTHIA 8.2 in blue. Data from CMS [113]

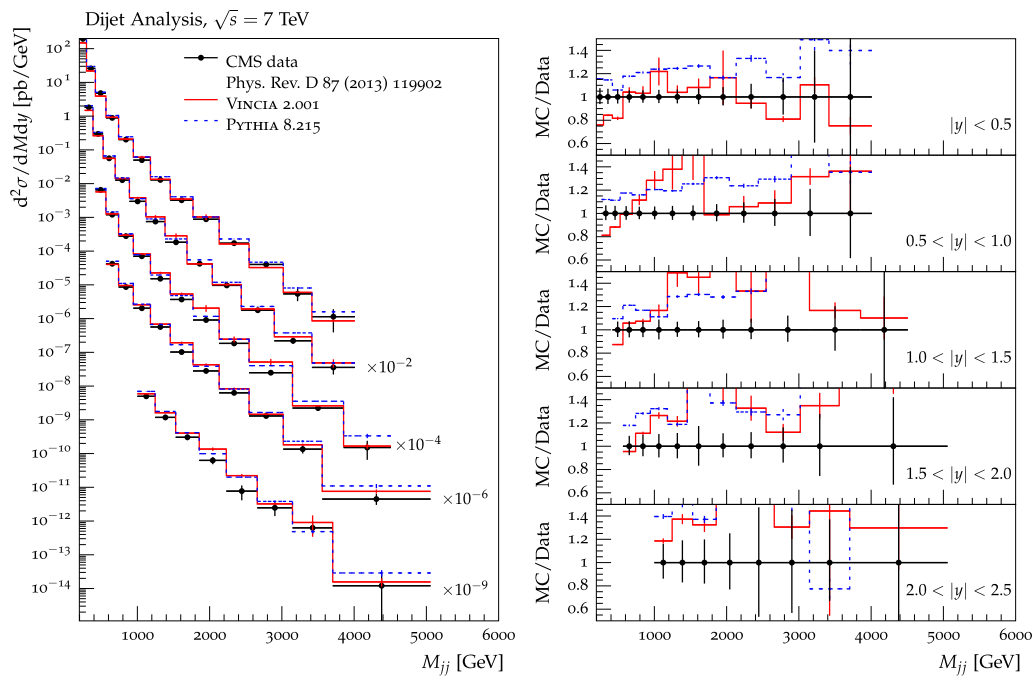


Fig. 28 Inclusive dijet cross sections for 5 different rapidity bins as a function of the dijet mass. Predictions of VINCIA 2.0 in red and PYTHIA 8.2 in blue. Data from CMS [114]

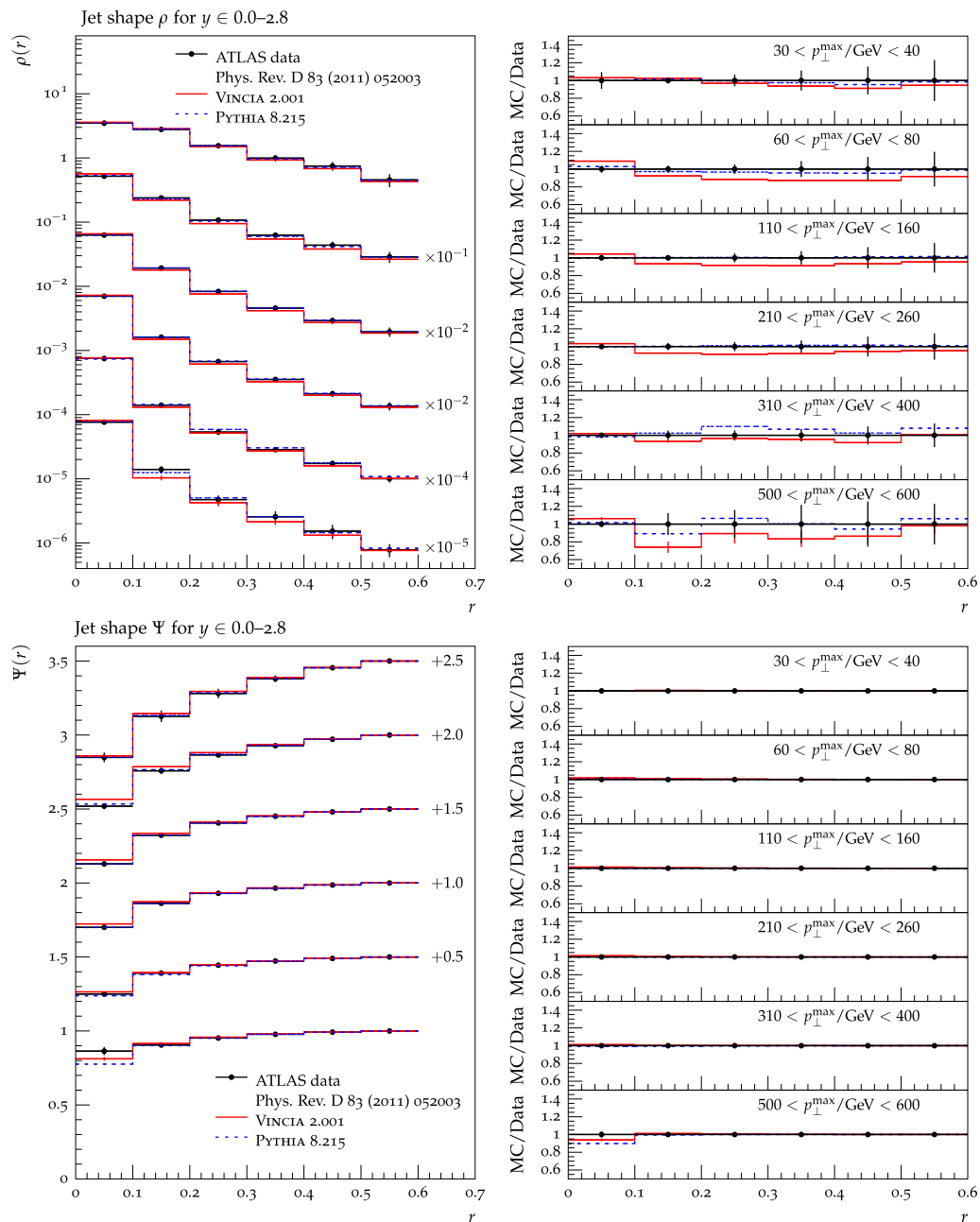


Fig. 29 Distributions of the jet shape variables $\rho(r)$ (top) and $\Psi(r)$ (bottom) for different ranges of the jet transverse momentum. Predictions of VINCIA 2.0 in red and PYTHIA 8.2 in blue, compared to ATLAS data from [115]

A second technical aspect is that, as shown in Fig. 16, the PS-to-ME ratios for QCD processes result in rather broad distributions already for the first-order correction with gluon emission only. This complicates including MECs for QCD processes, as violations in the Sudakov veto algorithm for generating emission and no-emission probabilities in the

shower become more likely. By default, we neglect such violations. It is, however, possible for the user to check the effect of taking the violations into account properly via the procedure outlined in Ref. [111], which has been included in VINCIA.

In Fig. 26 we show the predictions of VINCIA 2.0 and PYTHIA 8.2 for dijet azimuthal decorrelations for different ranges of the jet transverse momentum and compare to ATLAS data from [112]. While we observe no glaring discrepancies with the data—the general trends of the distributions are well reproduced by both VINCIA and PYTHIA—there still appears to be some room for improvement, in particular with VINCIA undershooting the precisely measured data points around $\Delta\phi \sim 0.9$ in the lower two p_{\perp}^{\max} bins by about 10–20 %.

Figures 27 and 28 show the transverse-momentum and jet mass spectra for different ranges of the jet rapidity and compare the MC predictions to CMS data from [113] and [114] respectively. We note that, whereas PYTHIA lies systematically above the data here, the lower default α_s value chosen in VINCIA causes the VINCIA normalisations to be substantially lower, even to the point of undershooting the measurements. This is not surprising given that the inclusive-jet cross section in PYTHIA/VINCIA is calculated at LO. The tails of the distributions unfortunately suffer from rather large weight-fluctuation effects, as was discussed above; nonetheless we note that the bins for which a reasonable statistical precision is obtained are generally closer to the data than the PYTHIA reference comparison.

Finally, in Fig. 29 we show the differential jet shape variable $\rho(r)$ and its cumulative integral $\Psi(r)$ for different ranges of the jet transverse momentum, compared with ATLAS data from [115]. This validates that the FSR broadening of QCD jets is in reasonable agreement with the experimental measurements, though we note that VINCIA's distributions may be slightly too narrow, which we again regard as being consistent with the LL nature of VINCIA's antenna functions and analogous to the slightly too narrow thrust distribution we allowed in the e^+e^- event shapes. As far as a first default set of parameters goes, we are satisfied with this level of tuning, with future directions being informed both by lessons from combinations with external matrix-element matching and merging schemes and by attempts to integrate NLO antenna-function corrections into the shower itself, e.g. in the spirit of [40].

5 Summary and conclusions

We presented the first publicly available antenna shower for initial and final state in VINCIA 2.0, with focus on antenna functions and kinematic maps for initial-state radiation. VINCIA 2.0 includes two different methods to explore the full phase space for the first emission, depending on the hard process at hand, without the disadvantages of a “power shower”. The full phase space of subsequent emissions is populated in a Markovian way. We compare explicitly to tree-level matrix

elements for $pp \rightarrow Z/H jj(j)$ and $pp \rightarrow jjj$ to check the validity of our approximations.

We extended the iterative MEC approach to the initial state and include MECs for QCD up to $\mathcal{O}(\alpha_s^4)$ (4 jets), and for Drell–Yan and Higgs production up to $\mathcal{O}(\alpha_s^3)$ ($V/H + 3$ jets). This is the first time MECs beyond one leg have been applied to hadron collisions. However, this implementation was not without its complications; the large phase space available for initial-state branchings implies that “unordered” emissions account for a larger fraction of the full phase space than was the case for FSR, and the MEC factors are less well behaved and therefore more difficult / less efficient to implement, compared to pure final-state MECs. We also saw in Sect. 4.2 that biased event samples result in larger weight fluctuations for VINCIA than in the case of pure PYTHIA, presumably due to unordered emissions in VINCIA allowing a larger range of corrections to each event. In the context of future developments of VINCIA, these aspects will therefore merit further consideration.

We presented first validation results with VINCIA 2.0 for the main benchmark processes for FSR and ISR, including hadronic Z decays, Drell–Yan, and QCD jets. We observe good agreement with experimental data from the LEP/SLD and LHC experiments.

The development of a more highly automated interface to MADGRAPH 5 is among the main development targets for the near future. The feasibility of an interface to NJET2 [116] is also being explored.

Acknowledgements We thank the HepForge project, www.hepforge.org [117] for providing the hosting and repository services used for developing and maintaining the VINCIA code. HepForge is funded via the UK STFC and hosted at the Durham IPPP. We thank Johannes Bellm for useful discussions on [87]. This work was supported in part by the ARC Centre of Excellence for Particle Physics at the Terascale. SP is supported by the US Department of Energy under contract DE-AC02-76SF00515. The work of MR was supported by the European Research Council under Advanced Investigator Grant ERC-AdG-228301 and ERC Advanced Grant No. 320651, “HEPGAME”. PS is the recipient of an Australian Research Council Future Fellowship, FT130100744: “Virtual Colliders: high-accuracy models for high energy physics”.

Open Access This article is distributed under the terms of the Creative Commons Attribution 4.0 International License (<http://creativecommons.org/licenses/by/4.0/>), which permits unrestricted use, distribution, and reproduction in any medium, provided you give appropriate credit to the original author(s) and the source, provide a link to the Creative Commons license, and indicate if changes were made. Funded by SCOAP³.

A Details of the shower algorithm

In this section we present some details of the shower algorithm, starting with the construction of the kinematics after the branching. Thereafter we will give a brief overview on

how the antenna functions correctly reproduce the DGLAP functions in the collinear limit.

A.1 Construction of the post-branching momenta

The antenna picture does not distinguish between the emitter/splitter and recoiler. Therefore, we have one mapping for each configuration, initial–initial, initial–final, and final–final. We express the momenta in terms of branching invariants only which leads to very simple expressions.

Initial–initial antennae

For a branching of type $AB \rightarrow abj$, the invariant mass and rapidity of the recoiler, $R \rightarrow r$, are not changed. The kinematics are constructed in the lab frame, where the post-branching momenta read as follows:

$$p_a^\mu = \sqrt{\frac{s_{ab} s_{AB} + s_{jb}}{s_{AB} s_{AB} + s_{aj}}} p_A^\mu, \quad (88)$$

$$p_b^\mu = \sqrt{\frac{s_{ab} s_{AB} + s_{aj}}{s_{AB} s_{AB} + s_{jb}}} p_B^\mu, \quad (89)$$

$$p_j^\mu = \sqrt{\frac{s_{jb}^2 s_{AB} + s_{jb}}{s_{ab} s_{AB} s_{AB} + s_{aj}}} p_A^\mu + \sqrt{\frac{s_{aj}^2 s_{AB} + s_{aj}}{s_{ab} s_{AB} s_{AB} + s_{jb}}} p_B^\mu + \sqrt{\frac{s_{aj} s_{jb}}{s_{ab}}} p_\perp^\mu, \quad (90)$$

$$p_r^\mu = p_a^\mu + p_b^\mu - p_j^\mu, \quad (91)$$

with $p_\perp = (0, \cos \phi, \sin \phi, 0)$, where ϕ is chosen uniformly in $[0, 2\pi]$.

Initial–final antennae

For a branching of type $AK \rightarrow akj$ the kinematics are constructed in the centre-of-mass frame of the parent antenna, which we define to be the rest frame of $p_A + p_K$ here, rotated so they are aligned with the z axis (the inverse of the corresponding Lorentz transformation is applied afterwards to bring the system back to the lab frame). The post-branching momenta read as follows:

$$p_a^\mu = \frac{s_{AK} + s_{jk}}{s_{AK}} p_A^\mu, \quad (92)$$

$$p_k^\mu = \frac{s_{jk} s_{aj}}{s_{AK} (s_{AK} + s_{jk})} p_A^\mu + \frac{s_{ak}}{s_{AK} + s_{jk}} p_K^\mu - \sqrt{\frac{s_{jk} s_{ak} s_{aj}}{s_{AK} + s_{jk}}} p_\perp^\mu, \quad (93)$$

$$p_j^\mu = \frac{s_{jk} s_{ak}}{s_{AK} (s_{AK} + s_{jk})} p_A^\mu + \frac{s_{aj}}{s_{AK} + s_{jk}} p_K^\mu + \sqrt{\frac{s_{jk} s_{ak} s_{aj}}{s_{AK} + s_{jk}}} p_\perp^\mu, \quad (94)$$

with p_\perp defined as in the previous paragraph.

Final–final antennae

For a branching of type $IK \rightarrow ijk$ the kinematics are constructed in the centre-of-mass frame of the parent antenna, with the direction of parton I defining the positive z axis (The inverse of the corresponding Lorentz transformation is applied afterwards to bring the system back to the lab frame). A first set of post-branching momenta is constructed with parton i aligned with the z axis and using the xz plane to represent the branching plane,

$$p_i^\mu = E_i(1, 0, 0, 1), \quad (95)$$

$$p_k^\mu = E_k(1, \sin \theta_{ik}, 0, \cos \theta_{ik}), \quad (96)$$

$$p_j^\mu = E_j(1, -\sin \theta_{ij}, 0, \cos \theta_{ij}), \quad (97)$$

with the energies

$$E_i = \frac{s_{IK} - s_{jk}}{2\sqrt{s_{IK}}}, \quad E_k = \frac{s_{IK} - s_{ij}}{2\sqrt{s_{IK}}}, \quad E_j = \frac{s_{IK} - s_{ik}}{2\sqrt{s_{IK}}}, \quad (98)$$

and angles between the partons

$$\cos \theta_{ik} = \frac{2E_i E_k - s_{ik}}{2E_i E_k}, \quad \cos \theta_{ij} = \frac{2E_i E_j - s_{ij}}{2E_i E_j}. \quad (99)$$

The azimuth angle of the emitted gluon in the xy plane (defining the orientation of the branching plane) is generated by rotating the above momenta around the z axis by a uniformly chosen random angle ϕ .

Finally, there remains one more global orientation angle, which can be cast as the angle between parton i and the original parton I , ψ_{Ii} , around an axis perpendicular to the branching plane (still in the centre-of-mass frame), i.e., specifying the degree to which p_i is not aligned with the z axis after the branching. Different choices are implemented in VINCIA (see [21, 23]), with the default being

$$\psi_{Ii} = 1 + \frac{2y_{ii}}{s_{IK} - s_{jk}} \quad \text{with} \\ y_{ii} = -\frac{(1 - \rho)s_{ik}/s_{IK} + 2fs_{ij}s_{jk}/s_{IK}^2}{2(1 - s_{ij}/s_{IK})}, \\ f = \frac{s_{jk}}{s_{ij} + s_{jk}}, \quad \rho = \sqrt{1 + 4f(1 - f)s_{ij}s_{jk}/s_{ik}s_{IK}}.$$

The final post-branching momenta are constructed by rotating the ijk system by the angle ψ_{Ii} around the axis perpendicular to the branching plane, and then finally performing the inverse Lorentz transform to bring the post-branching partons back to the lab frame.

A.2 Collinear limits of the antenna functions

In this paragraph, we collect, for convenience of the reader, the collinear limits of the antenna functions used in VINCIA. We also relate the antenna functions in this limit to corresponding DGLAP splitting kernels, which we will denote $P(x \rightarrow yz)$. Note that the apparent difference in colour factors for DGLAP splitting kernels and antenna functions is due to the phase-space and coupling factor, which, for antennae, is

$$\frac{\alpha_s C_{\text{ant}}}{4\pi} \quad \text{with } C_{\text{ant}} \in [C_A, 2C_F, T_R], \tag{100}$$

whereas DGLAP kernels are conventionally defined with

$$\frac{\alpha_s C_{\text{DGLAP}}}{2\pi} \quad \text{with } C_{\text{DGLAP}} \in [C_A, C_F, T_R/2]. \tag{101}$$

We note that antenna functions with gluons as parent partons only reproduce half of a DGLAP kernel, as gluons take part in two antennae. In addition a factor of $1/z$ will multiply the DGLAP kernels in the case of initial-state radiation.

The collinear limits of the antenna functions below agree with the limits found in Refs. [16–18, 118].

Initial–initial antennae

In the case of initial–initial antenna functions the energy-sharing variable is $z = s_{AB}/s_{ab}$ and we arbitrarily pick the invariant mass of one of the parton pairs, $Q^2 = s_{aj}$, and its scaled version, $y = Q^2/s_{AB}$. For an easy comparison with the DGLAP kernels we rewrite the antenna functions in terms of these variables,

$$\bar{a}_{q\bar{q}g}^{\text{II}} = \frac{1}{Q^2} \frac{1}{z} \left(2 \frac{z}{1-z-zy} + (1-z-zy) \right) + \mathcal{O}(Q^2), \tag{102}$$

$$\begin{aligned} \bar{a}_{ggg}^{\text{II}} = & 2 \frac{1}{Q^2} \frac{1}{z} \left(\frac{z}{1-z-zy} + \frac{1}{z} - 1 - y \right. \\ & \left. + (1-z-zy) \frac{z}{1+zy} \right) + \mathcal{O}(Q^2), \end{aligned} \tag{103}$$

$$\bar{a}_{q\bar{q}q}^{\text{II}} = \frac{1}{2} \frac{1}{Q^2} \frac{1}{z} \left(\frac{(1-z-zy)^2 + 1}{z} \right), \tag{104}$$

$$\bar{a}_{g\bar{q}\bar{q}}^{\text{II}} = \frac{1}{Q^2} \frac{1}{z} \left(1 - 2z + 2 \frac{z^2}{1-zy} \right). \tag{105}$$

Note that we made use of $s_{jb} = s_{AB}(1-z-zy)/z$ and wrote the terms in the gluon-emission antennae that do not contain $1/Q^2$ singularities as $\mathcal{O}(Q^2)$, as they will vanish in the unresolved limit anyway.

Given this new form of the antenna functions, the collinear limits, $y \rightarrow 0$, are simple to read off,

$$\bar{a}_{q\bar{q}g}^{\text{II}} \rightarrow \frac{1}{Q^2} \frac{1}{z} \left(\frac{1+z^2}{1-z} \right) = \frac{1}{Q^2} \frac{1}{z} P(q \rightarrow qg), \tag{106}$$

$$\begin{aligned} \bar{a}_{ggg}^{\text{II}} \rightarrow & 2 \frac{1}{Q^2} \frac{1}{z} \left(\frac{z}{1-z} + \frac{1-z}{z} + z(1-z) \right) \\ = & \frac{1}{Q^2} \frac{1}{z} P(g \rightarrow gg) \end{aligned} \tag{107}$$

$$\bar{a}_{q\bar{q}q}^{\text{II}} \rightarrow \frac{1}{2} \frac{1}{Q^2} \frac{1}{z} \left(\frac{(1-z)^2 + 1}{z} \right) = \frac{1}{2} \frac{1}{Q^2} \frac{1}{z} P(q \rightarrow gq), \tag{108}$$

$$\bar{a}_{g\bar{q}\bar{q}}^{\text{II}} \rightarrow \frac{1}{Q^2} \frac{1}{z} \left(z^2 + (1-z)^2 \right) = \frac{1}{Q^2} \frac{1}{z} P(g \rightarrow q\bar{q}). \tag{109}$$

Note in particular that the second and fourth antenna functions include the full DGLAP kernels for $g \rightarrow gg$ and $g \rightarrow q\bar{q}$, respectively. This is different from their final-state counterparts (see below) in which two neighbouring antenna functions must be summed over to recover the full DGLAP kernels. This difference arises from the fact that there is no “emission into the initial state”—the initial-state gluon only occurs as a hard leg, not as the emitted parton.

Initial–final antennae

We start with the collinear limit of the initial-state side, $Q^2 = s_{aj}$ and $y = Q^2/s_{AK}$, and energy-sharing variable $z = s_{AK}/(s_{AK} + s_{jk})$ and rewrite the antenna functions,

$$\bar{a}_{q\bar{q}g}^{\text{IF}} = \frac{1}{Q^2} \frac{1}{z} \left(\frac{1+z^2-2zy}{1-z} \right) + \mathcal{O}(Q^2), \tag{110}$$

$$\begin{aligned} \bar{a}_{ggg}^{\text{IF}} = & 2 \frac{1}{Q^2} \frac{1}{z} \left(\frac{z(1-zy)}{1-z} + \frac{(1-z)(1-zy)}{z} \right. \\ & \left. + z(1-z) \right) + \mathcal{O}(Q^2), \end{aligned} \tag{111}$$

$$\bar{a}_{q\bar{q}q}^{\text{IF}} = \frac{1}{2} \frac{1}{Q^2} \frac{1}{z} \left(\frac{(1-z)^2 + (1-zy)^2}{z} \right), \tag{112}$$

$$\bar{a}_{g\bar{q}\bar{q}}^{\text{IF}} = \frac{1}{Q^2} \frac{1}{z} \left(z(1-2z)y + z^2 + (1-z)^2 \right). \tag{113}$$

Note that we made use of $s_{jk} = s_{AK}(1-z)/z$ and $s_{ak} = s_{AK}(1-yz)/z$ and, as before, wrote the terms in the gluon-emission antennae that do not contain $1/Q^2$ singularities as $\mathcal{O}(Q^2)$.

Given this new form of the antenna functions, the collinear limits, $y \rightarrow 0$, are simple to read off,

$$\bar{a}_{qqg}^{\text{IF}} \rightarrow \frac{1}{Q^2} \left(\frac{1+z^2}{1-z} \right) = \frac{1}{Q^2} \frac{1}{z} P(q \rightarrow qg), \quad (114)$$

$$\begin{aligned} \bar{a}_{ggg}^{\text{IF}} &\rightarrow 2 \frac{1}{Q^2} \frac{1}{z} \left(\frac{z}{1-z} + \frac{1-z}{z} + z(1-z) \right) \\ &= \frac{1}{Q^2} \frac{1}{z} P(g \rightarrow gg) \end{aligned} \quad (115)$$

$$\begin{aligned} \bar{a}_{q^xq}^{\text{IF}} &\rightarrow \frac{1}{2} \frac{1}{Q^2} \frac{1}{z} \left(\frac{(1-z)^2 + 1}{z} \right) \\ &= \frac{1}{2} \frac{1}{Q^2} \frac{1}{z} P(q \rightarrow gq), \end{aligned} \quad (116)$$

$$\bar{a}_{g^x\bar{q}}^{\text{IF}} \rightarrow \frac{1}{Q^2} \frac{1}{z} (z^2 + (1-z)^2) = \frac{1}{Q^2} \frac{1}{z} P(g \rightarrow q\bar{q}). \quad (117)$$

Now we continue with the collinear limit of the final-state side, $Q^2 = s_{jk}$ and $y = Q^2/s_{AK}$, and energy-sharing variable $z = s_{ak}/s_{AK}$. The antenna functions, rewritten in terms of the new variables and using $s_{aj} = s_{AK}(1-z+y)$, read

$$\bar{a}_{qqg}^{\text{IF}} = \frac{1}{Q^2} \frac{1}{z} \left(\frac{2z + (1-z+y)^2}{1-z+y} \right) + \mathcal{O}(Q^2), \quad (118)$$

$$\bar{a}_{ggg}^{\text{IF}} = \frac{1}{Q^2} \left(2 \frac{z}{1-z+y} + z(1-z) \right) + \mathcal{O}(Q^2), \quad (119)$$

$$\bar{a}_{xq\bar{q}}^{\text{IF}} = \frac{1}{2} \frac{1}{Q^2} \left((1-z+y)^2 + z^2 \right). \quad (120)$$

Given this new form of the antenna functions, the collinear limits, $y \rightarrow 0$, are simple to read off,

$$\bar{a}_{qqg}^{\text{IF}} \rightarrow \frac{1}{Q^2} \left(\frac{1+z^2}{1-z} \right) = \frac{1}{Q^2} P(q \rightarrow qg), \quad (121)$$

$$\begin{aligned} \bar{a}_{ggg}^{\text{IF}} + \bar{a}_{ggg}^{\text{IF}}[z \leftrightarrow 1-z] &\rightarrow 2 \frac{1}{Q^2} \\ &\times \left(\frac{z}{1-z} + \frac{1-z}{z} + z(1-z) \right) = \frac{1}{Q^2} P(g \rightarrow gg) \end{aligned} \quad (122)$$

$$\bar{a}_{xq\bar{q}}^{\text{IF}} \rightarrow \frac{1}{2} \frac{1}{Q^2} \left((1-z)^2 + z^2 \right) = \frac{1}{2} \frac{1}{Q^2} P(g \rightarrow q\bar{q}). \quad (123)$$

Final-final antennae

In the case of final-final antenna functions the energy-sharing variable is $z = s_{ik}/s_{IK}$ and we arbitrarily pick the invariant mass of one of the parton pairs, $Q^2 = s_{jk}$, and its scaled version, $y = Q^2/s_{IK}$. For an easy comparison with the DGLAP kernels we rewrite the antenna functions in terms of these variables (leaving out the finite parts as their choice is arbitrary),

$$\bar{a}_{q\bar{q}g}^{\text{FF}} = \frac{1}{Q^2} \left(\frac{2z + (1-z-y)^2}{1-z-y} \right) + \mathcal{O}(Q^2), \quad (124)$$

$$\bar{a}_{ggg}^{\text{FF}} = \frac{1}{Q^2} \left(2 \frac{z}{1-z-y} + (1-z-y)(z+y) \right) + \mathcal{O}(Q^2), \quad (125)$$

$$\bar{a}_{xq\bar{q}}^{\text{FF}} = \frac{1}{2} \frac{1}{Q^2} \left((1-z-y)^2 + z^2 \right). \quad (126)$$

Note that we made use of $s_{ij} = s_{IK}(1-z-y)$ and, as before, wrote the terms in the gluon-emission antennae that do not contain $1/Q^2$ singularities as $\mathcal{O}(Q^2)$.

Given this new form of the antenna functions, the collinear limits, $y \rightarrow 0$, are simple to read off,

$$\bar{a}_{q\bar{q}g}^{\text{FF}} \rightarrow \frac{1}{Q^2} \left(\frac{1+z^2}{1-z} \right) = \frac{1}{Q^2} P(q \rightarrow qg), \quad (127)$$

$$\begin{aligned} \bar{a}_{ggg}^{\text{FF}} + \bar{a}_{ggg}^{\text{FF}}[z \leftrightarrow 1-z] &\rightarrow 2 \frac{1}{Q^2} \\ &\times \left(\frac{z}{1-z} + \frac{1-z}{z} + z(1-z) \right) = \frac{1}{Q^2} P(g \rightarrow gg) \end{aligned} \quad (128)$$

$$\bar{a}_{xq\bar{q}}^{\text{FF}} \rightarrow \frac{1}{2} \frac{1}{Q^2} \left((1-z)^2 + z^2 \right) = \frac{1}{2} \frac{1}{Q^2} P(g \rightarrow q\bar{q}). \quad (129)$$

A.3 Phase-space variables and limits

In Table 1 we give an overview on combinations of the evolution variable t and complementary phase-space variable ζ that are used in the shower.

Table 1 Definitions of the evolution variable t and the complementary phase-space variable ζ for II, IF and FF configurations, with the ζ boundaries in the last two columns

	Evolution Variable t	Definition of ζ	ζ Boundaries ζ_{\min}	ζ_{\max}
II	$\frac{s_{aj}s_{jb}}{s_{ab}}$	$\frac{s_{aj}}{s_{ab}}$	$\frac{s-s_{AB}}{s} - \sqrt{\frac{t_{\max}-t}{s}}$	$\frac{s-s_{AB}}{s} + \sqrt{\frac{t_{\max}-t}{s}}$
		$\frac{s_{aj}}{s_{AB}}$	$\frac{s-s_{AB}}{2s_{AB}} - \frac{1}{s_{AB}}\sqrt{s(t_{\max}-t)}$	$\frac{s-s_{AB}}{2s_{AB}} + \frac{1}{s_{AB}}\sqrt{s(t_{\max}-t)}$
	s_{aj}	$\frac{s_{jb}}{s_{AB}}$	$\frac{s-s_{AB}}{2s_{AB}} - \frac{1}{s_{AB}}\sqrt{s(t_{\max}-t)}$	$\frac{s-s_{AB}}{2s_{AB}} + \frac{1}{s_{AB}}\sqrt{s(t_{\max}-t)}$
		$\frac{s_{ab}}{s_{AB}}$	$\frac{s_{AB}+t}{s_{AB}}$	$\frac{s}{s_{AB}}$
IF	$\frac{s_{aj}s_{jk}}{s_{AK}+s_{jk}}$	$\frac{s_{ab}}{s_{AB}}$	$\frac{s_{AB}+t}{s_{AB}}$	$\frac{s}{s_{AB}}$
		$\frac{s_{jk}+s_{AK}}{s_{AK}}$	$\frac{s_{AK}+t}{s_{AK}}$	$\frac{1}{x_A}$
FF	s_{aj}	$\frac{s_{aj}}{s_{AK}+s_{jk}}$	$\frac{t \cdot x_A}{s_{AK}(1-x_A)}$	1
		$\frac{s_{aj}}{s_{jk}}$	$\frac{t \cdot x_A}{s_{AK}(1-x_A)^2}$	$\frac{s_{AK}+t}{t}$
	s_{jk}	$\frac{s_{jk}+s_{AK}}{s_{AK}}$	$\max\left(1, \frac{t}{s_{AK}}\right)$	$\frac{1}{x_A}$
		$\frac{s_{aj}}{s_{AK}+s_{jk}}$	0	1
FF	$4 \frac{s_{ij}s_{jk}}{s_{IK}}$	$\frac{s_{ij}}{s_{ij}+s_{jk}}$	$\frac{1}{2} \left(1 - \sqrt{1 - \frac{t}{s_{IK}}}\right)$	$\frac{1}{2} \left(1 + \sqrt{1 - \frac{t}{s_{IK}}}\right)$
		$\frac{s_{jk}}{s_{IK}}$	0	$\frac{s_{IK}-t}{s_{IK}}$
	s_{jk}	$\frac{s_{ij}}{s_{IK}}$	0	$\frac{s_{IK}-t}{s_{IK}}$

B Comparison with matrix elements

In this section we show an extended set of plots where we compare the shower approximation to leading-order matrix elements; see Sects. 3.2 and 3.3 for a description of the observables. We show the one- and two-dimensional distributions

of the PS-to-ME ratios for $gg \rightarrow Zq\bar{q}(g)$ in Figs. 30 and 31, for $q\bar{q} \rightarrow Hgg(g)$ in Figs. 32 and 33, and for $gg \rightarrow Hgg(g)$ in Figs. 34 and 35. As before, see Eqs. (73) and (74), we include distributions with a cut on the transverse mass of the boson, $m_{\perp Z}^2$ (labelled “no EW Z”) and $m_{\perp H}^2$ (labelled “no EW H”), respectively.

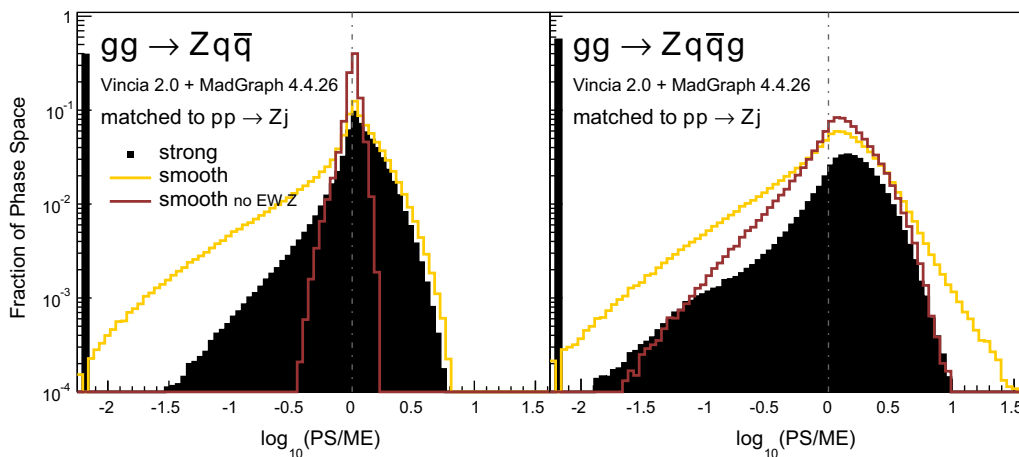


Fig. 30 Antenna shower, compared to matrix elements: distribution of $\log_{10}(\text{PS}/\text{ME})$ in a flat phase-space scan of the full phase space. Contents normalised to the number of generated points

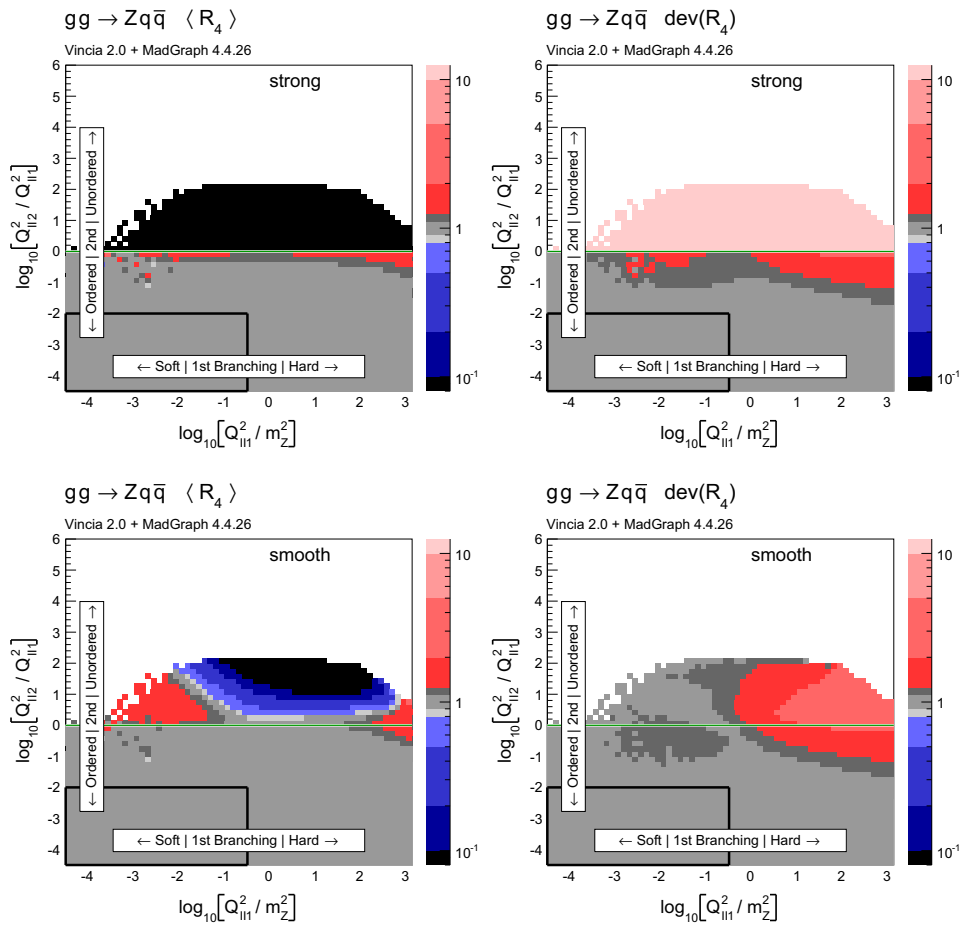
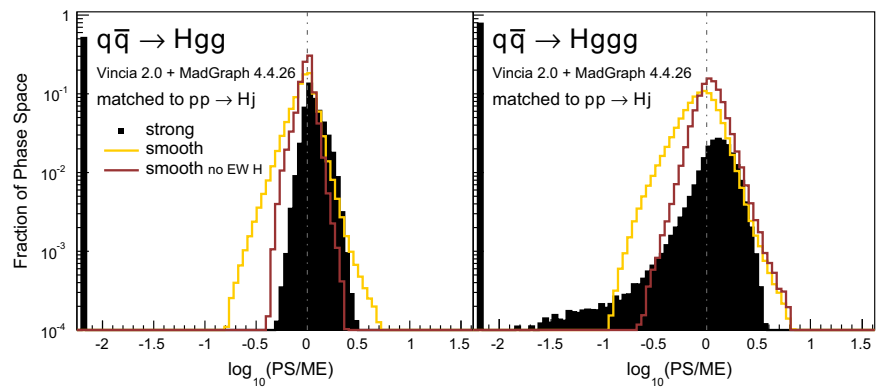


Fig. 31 The value of $\langle R_4 \rangle$ (left) and $\text{dev}(R_4)$ (right), differentially over the 4-parton phase space, with Q^2 ratios characterising the first and second emissions on the x and y axis, respectively. Strong (top) and smooth (bottom) ordering in the shower

Fig. 32 Antenna shower, compared to matrix elements: distribution of $\log_{10}(\text{PS}/\text{ME})$ in a flat phase-space scan of the full phase space. Contents normalised to the number of generated points. Gluon emission only



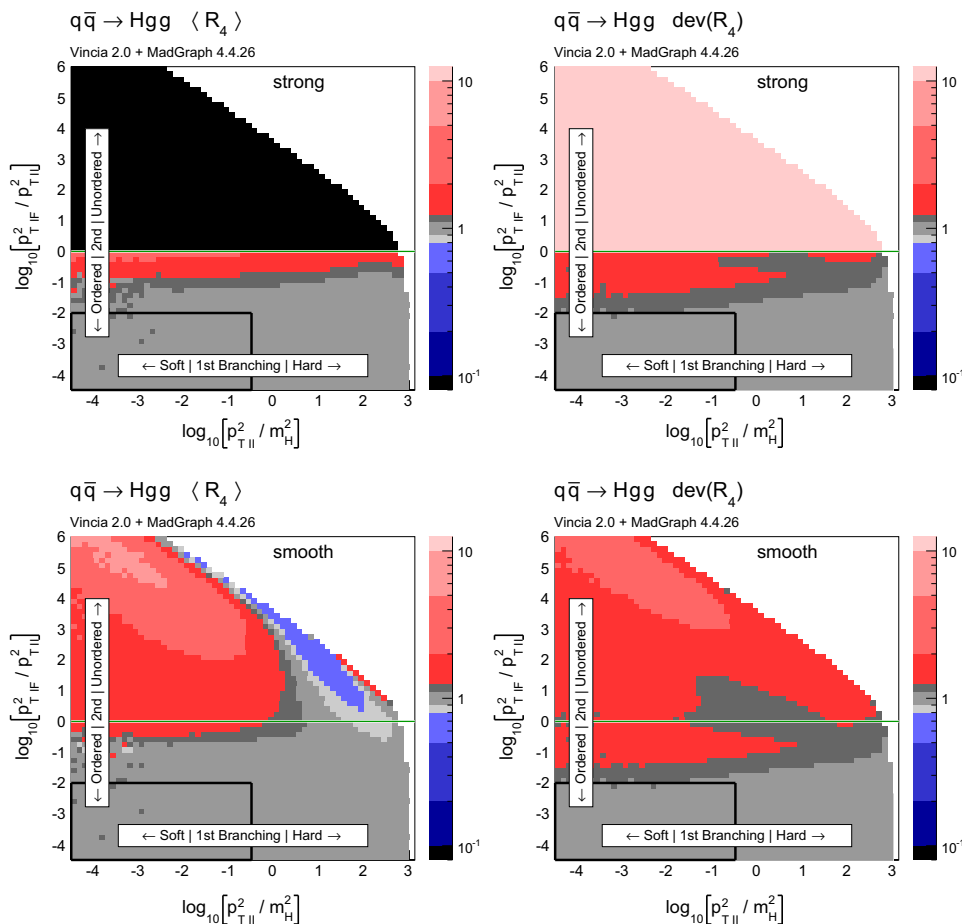
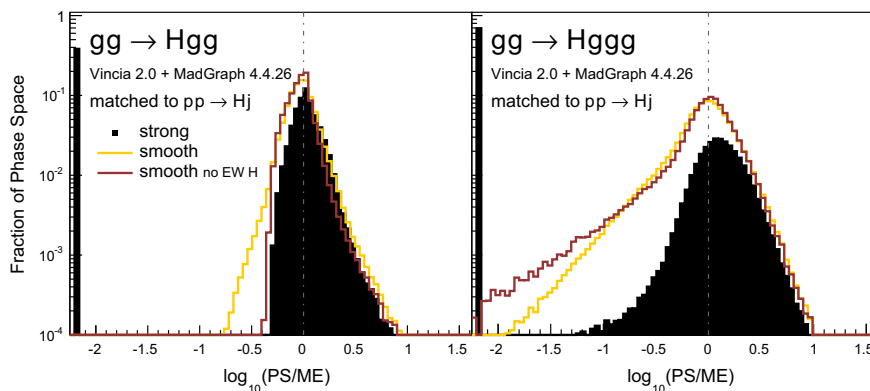


Fig. 33 The value of $\langle R_4 \rangle$ (left) and $\text{dev}(R_4)$ (right), differentially over the 4-parton phase space, with p_T^2 ratios characterising the first and second emissions on the x and y axis, respectively. Strong (top) and smooth (bottom) ordering in the shower, with gluon emission only

Fig. 34 Antenna shower, compared to matrix elements: distribution of $\log_{10}(\text{PS}/\text{ME})$ in a flat phase-space scan of the full phase space. Contents normalised to the number of generated points. Gluon emission only



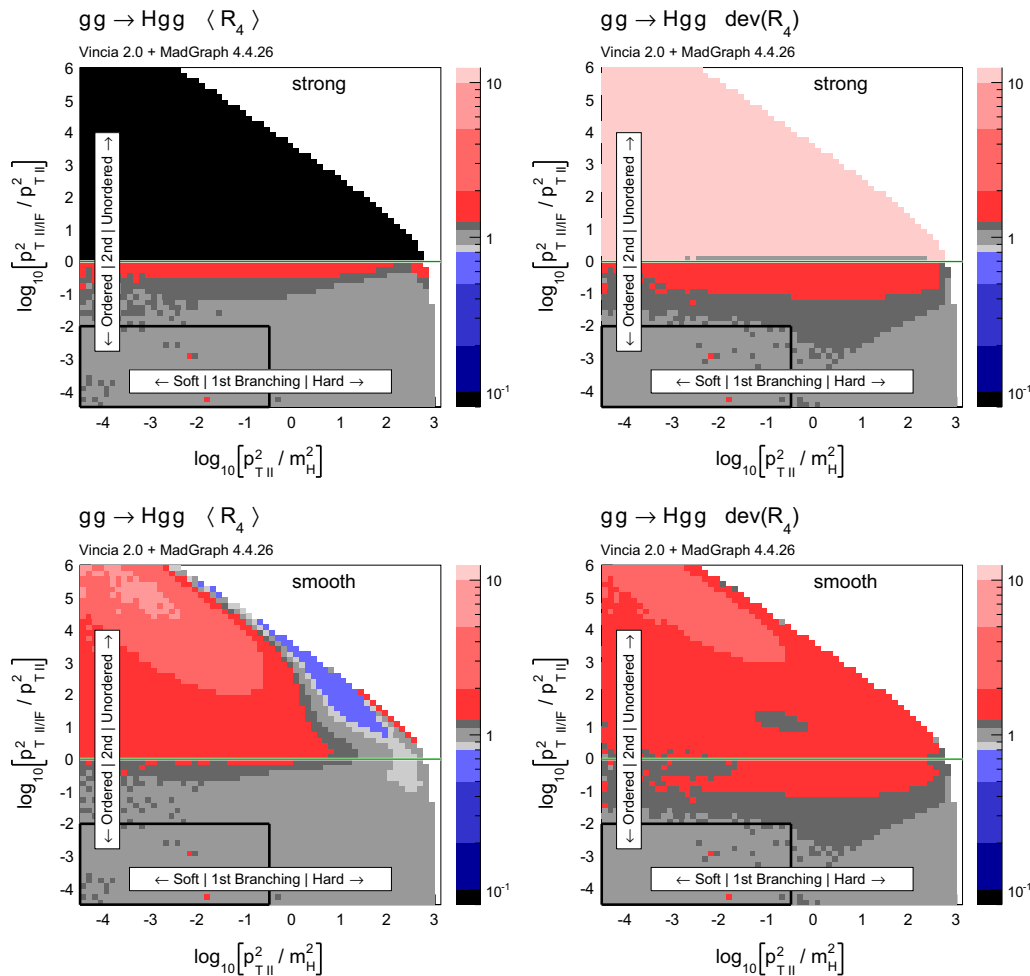


Fig. 35 The value of $\langle R_4 \rangle$ (left) and $\text{dev}(R_4)$ (right), differentially over the 4-parton phase space, with p_{\perp}^2 ratios characterising the first and second emissions on the x and y axis, respectively. Strong (top) and smooth (bottom) ordering in the shower, with gluon emission only

References

1. V.N. Gribov, L.N. Lipatov, Deep inelastic $e - p$ scattering in perturbation theory. *Sov. J. Nucl. Phys.* **15**, 438–450 (1972)
2. Y.L. Dokshitzer, Calculation of the structure functions for deep inelastic scattering and e^+e^- annihilation by perturbation theory in quantum chromodynamics. *Sov. Phys. JETP* **46**, 641–653 (1977)
3. G. Altarelli, G. Parisi, Asymptotic freedom in parton language. *Nucl. Phys. B* **126**, 298–318 (1977)
4. A. Buckley et al., General-purpose event generators for LHC physics. *Phys. Rep.* **504**, 145–233 (2011). [arXiv:1101.2599](https://arxiv.org/abs/1101.2599)
5. M. Bengtsson, T. Sjöstrand, Coherent parton showers versus matrix elements: implications of PETRA - PEP data. *Phys. Lett. B* **185**, 435 (1987)
6. G. Marchesini, B.R. Webber, Monte Carlo simulation of general hard processes with coherent QCD radiation. *Nucl. Phys. B* **310**, 461 (1988)
7. S. Gieseke, P. Stephens, B. Webber, New formalism for QCD parton showers. *JHEP* **12**, 045 (2003). [arXiv:hep-ph/0310083](https://arxiv.org/abs/hep-ph/0310083)
8. T. Sjöstrand, P.Z. Skands, Transverse-momentum-ordered showers and interleaved multiple interactions. *Eur. Phys. J. C* **39**, 129 (2005). [arXiv:hep-ph/0408302](https://arxiv.org/abs/hep-ph/0408302)
9. F. Krauss, A. Schlicke, G. Soff, APACIC++ 2.0: a parton cascade in C++. *Comput. Phys. Commun.* **174**, 876–902 (2006). [arXiv:hep-ph/0503087](https://arxiv.org/abs/hep-ph/0503087)
10. A. Bassetto, M. Ciafaloni, G. Marchesini, Jet structure and infrared sensitive quantities in perturbative QCD. *Phys. Rep.* **100**, 201–272 (1983)
11. G. Marchesini, B.R. Webber, Simulation of QCD jets including soft gluon interference. *Nucl. Phys. B* **238**, 1 (1984)
12. M. Bengtsson, T. Sjöstrand, A comparative study of coherent and noncoherent parton shower evolution. *Nucl. Phys. B* **289**, 810 (1987)
13. G. Gustafson, U. Petterson, Dipole formulation of QCD cascades. *Nucl. Phys. B* **306**, 746 (1988)
14. Y.I. Azimov, Y.L. Dokshitzer, V.A. Khoze, S.I. Troian, The string effect and QCD coherence. *Phys. Lett. B* **165**, 147–150 (1985)
15. D.A. Kosower, Antenna factorization of gauge theory amplitudes. *Phys. Rev. D* **57**, 5410–5416 (1998). [arXiv:hep-ph/9710213](https://arxiv.org/abs/hep-ph/9710213)

16. A.G. De Ridder, T. Gehrmann, E.W.N. Glover, Antenna subtraction at NNLO. *JHEP* **09**, 056 (2005). [arXiv:hep-ph/0505111](#)
17. A.G. De Ridder, T. Gehrmann, E.W.N. Glover, Quark-gluon antenna functions from neutralino decay. *Phys. Lett. B* **612**, 36–48 (2005). [arXiv:hep-ph/0501291](#)
18. A.G. De Ridder, T. Gehrmann, E.W.N. Glover, Gluon-gluon antenna functions from Higgs boson decay. *Phys. Lett. B* **612**, 49–60 (2005). [arXiv:hep-ph/0502110](#)
19. S. Catani, M.H. Seymour, The Dipole formalism for the calculation of QCD jet cross-sections at next-to-leading order. *Phys. Lett. B* **378**, 287–301 (1996). [arXiv:hep-ph/9602277](#)
20. S. Catani, M.H. Seymour, A general algorithm for calculating jet cross-sections in NLO QCD. *Nucl. Phys. B* **485**, 291 (1997). [arXiv:hep-ph/9605323](#). [Erratum: *Nucl. Phys. B* **510**, 503 (1998)]
21. L. Lönnblad, ARIADNE version 4: a program for simulation of QCD cascades implementing the color dipole model. *Comput. Phys. Commun.* **71**, 15–31 (1992)
22. Z. Nagy, D.E. Soper, Matching parton showers to NLO computations. *JHEP* **10**, 024 (2005). [arXiv:hep-ph/0503053](#)
23. W.T. Giele, D.A. Kosower, P.Z. Skands, A simple shower and matching algorithm. *Phys. Rev. D* **78**, 014026 (2008). [arXiv:0707.3652](#)
24. M. Dinsdale, M. Ternick, S. Weinzierl, Parton showers from the dipole formalism. *Phys. Rev. D* **76**, 094003 (2007). [arXiv:0709.1026](#)
25. S. Schumann, F. Krauss, A Parton shower algorithm based on Catani–Seymour dipole factorisation. *JHEP* **03**, 038 (2008). [arXiv:0709.1027](#)
26. J.-C. Winter, F. Krauss, Initial-state showering based on colour dipoles connected to incoming parton lines. *JHEP* **07**, 040 (2008). [arXiv:0712.3913](#)
27. S. Plätzer, S. Gieseke, Coherent parton showers with local recoils. *JHEP* **01**, 024 (2011). [arXiv:0909.5593](#)
28. J.J. Lopez-Villarejo, P.Z. Skands, Efficient matrix-element matching with sector showers. *JHEP* **11**, 150 (2011). [arXiv:1109.3608](#)
29. M. Ritzmann, D.A. Kosower, P. Skands, Antenna showers with hadronic initial states. *Phys. Lett. B* **718**, 1345–1350 (2013). [arXiv:1210.6345](#)
30. S. Höche, S. Prestel, The midpoint between dipole and parton showers. *Eur. Phys. J. C* **75**(9), 461 (2015). [arXiv:1506.0505](#)
31. D. Amati, A. Bassetto, M. Ciafaloni, G. Marchesini, G. Veneziano, A Treatment of Hard Processes Sensitive to the Infrared Structure of QCD. *Nucl. Phys. B* **173**, 429 (1980)
32. S. Catani, B.R. Webber, G. Marchesini, QCD coherent branching and semiinclusive processes at large x . *Nucl. Phys. B* **349**, 635–654 (1991)
33. T. Sjöstrand, A model for initial state parton showers. *Phys. Lett. B* **157**, 321 (1985)
34. T. Sjöstrand, S. Ask, J.R. Christiansen, R. Corke, N. Desai, P. Ilten, S. Mrenna, S. Prestel, C.O. Rasmussen, P.Z. Skands, An introduction to PYTHIA 8.2. *Comput. Phys. Commun.* **191**, 159–177 (2015). [arXiv:1410.3012](#)
35. R. Corke, T. Sjöstrand, Interleaved parton showers and tuning prospects. *JHEP* **03**, 032 (2011). [arXiv:1011.1759](#)
36. P. Skands, B. Webber, J. Winter, QCD coherence and the top quark asymmetry. *JHEP* **07**, 151 (2012). [arXiv:1205.1466](#)
37. OPAL Collaboration, N. Fischer, S. Gieseke, S. Kluth, S. Plätzer, P. Skands, Measurement of observables sensitive to coherence effects in hadronic Z decays with the OPAL detector at LEP. [arXiv:1505.0163](#)
38. N. Fischer, S. Gieseke, S. Plätzer, P. Skands, Revisiting radiation patterns in e^+e^- collisions. *Eur. Phys. J. C* **74**(4), 2831 (2014). [arXiv:1402.3186](#)
39. W.T. Giele, D.A. Kosower, P.Z. Skands, Higher-order corrections to timelike jets. *Phys. Rev. D* **84**, 054003 (2011). [arXiv:1102.2126](#)
40. L. Hartgring, E. Laenen, P. Skands, Antenna showers with one-loop matrix elements. *JHEP* **10**, 127 (2013). [arXiv:1303.4974](#)
41. A.G. De Ridder, T. Gehrmann, E.W.N. Glover, A. Huss, T.A. Morgan, NNLO QCD corrections for Z boson plus jet production. In *Proceedings, 12th International Symposium on Radiative Corrections (Radcor 2015) and LoopFest XIV (Radiative Corrections for the LHC and Future Colliders)*, 2016. [arXiv:1601.0456](#)
42. X. Chen, T. Gehrmann, N. Glover, M. Jaquier, Higgs plus one jet production at NNLO. (2016). [arXiv:1604.0408](#)
43. J. Currie, A. G. De Ridder, E.W.N. Glover, J. Pires, NNLO QCD corrections to jet production at hadron colliders from gluon scattering. *JHEP* **01**, 110 (2014). [arXiv:1310.3993](#)
44. G. Abelof, A.G. De Ridder, I. Majer, Top quark pair production at NNLO in the quark-antiquark channel. *JHEP* **12**, 074 (2015). [arXiv:1506.0403](#)
45. N. Fischer, P. Skands, Coherent showers for the LHC. (2016). [arXiv:1604.0480](#)
46. P. Skands et al., VINCIA user reference (2016). CoEPP-MN-16-12 <http://vincia.hepforge.org/current/share/Vincia/htmldoc/>
47. P. Skands et al., VINCIA Authors' Compendium (2016). CoEPP-MN-16-13, <http://vincia.hepforge.org/current/share/Vincia/htmldoc/compendium.pdf>
48. C. Bierlich, G. Gustafson, L. Lönnblad, A. Tarasov, Effects of overlapping strings in pp collisions. *JHEP* **03**, 148 (2015). [arXiv:1412.6259](#)
49. J.R. Christiansen, P.Z. Skands, String formation beyond leading colour. *JHEP* **08**, 003 (2015). [arXiv:1505.0168](#)
50. J. Alwall, P. Demin, S. de Visscher, R. Frederix, M. Herquet, F. Maltoni, T. Plehn, D.L. Rainwater, T. Stelzer, MadGraph/MadEvent v4: the new web generation. *JHEP* **09**, 028 (2007). [arXiv:0706.2334](#)
51. Y.L. Dokshitzer, G. Marchesini, Monte Carlo and large angle gluon radiation. *JHEP* **03**, 117 (2009). [arXiv:0809.1749](#)
52. A.J. Larkoski, J.J. Lopez-Villarejo, P. Skands, Helicity-dependent showers and matching with VINCIA. *Phys. Rev. D* **87**(5), 054033 (2013). [arXiv:1301.0933](#)
53. K.A. Olive et al., Review of particle physics. *Chin. Phys. C* **38**, 090001 (2014)
54. S. Gieseke, Uncertainties of Sudakov form-factors. *JHEP* **01**, 058 (2005). [arXiv:hep-ph/0412342](#)
55. R.K. Ellis, W.J. Stirling, B.R. Webber, in *QCD and Collider Physics*, edn 1. Cambridge Monographs on Particulate Physics, Nuclear physics and Cosmology, vol. 8. (Cambridge University Press, Cambridge, 1996). ISBN:0521545897
56. M.A. Kimber, A.D. Martin, M.G. Ryskin, Unintegrated parton distributions and prompt photon hadroproduction. *Eur. Phys. J. C* **12**, 655–661 (2000). [arXiv:hep-ph/9911379](#)
57. M.A. Kimber, A.D. Martin, M.G. Ryskin, Unintegrated parton distributions. *Phys. Rev. D* **63**, 114027 (2001). [arXiv:hep-ph/0101348](#)
58. Z. Nagy, D.E. Soper, On the transverse momentum in Z-boson production in a virtuality ordered parton shower. *JHEP* **03**, 097 (2010). [arXiv:0912.4534](#)
59. A. Banfi, G.P. Salam, G. Zanderighi, Phenomenology of event shapes at hadron colliders. *JHEP* **06**, 038 (2010). [arXiv:1001.4082](#)
60. M. Dasgupta, A. Fregoso, S. Marzani, G.P. Salam, Towards an understanding of jet substructure. *JHEP* **09**, 029 (2013). [arXiv:1307.0007](#)
61. G. Parisi, R. Petronzio, Small transverse momentum distributions in hard processes. *Nucl. Phys. B* **154**, 427 (1979)
62. T. Sjöstrand, S. Mrenna, P.Z. Skands, PYTHIA 6.4 physics and manual. *JHEP* **05**, 026 (2006). [arXiv:hep-ph/0603175](#)
63. E. Boos, M. Dobbs, W. Giele, I. Hinchliffe, J. Huston, et al., Generic user process interface for event generators. [arXiv:hep-ph/0109068](#)

64. J. Alwall, A. Ballestrero, P. Bartalini, S. Belov, E. Boos et al., A standard format for Les Houches event files. *Comput. Phys. Commun.* **176**, 300 (2007). [arXiv:hep-ph/0609017](#)
65. S. Mrenna, P. Skands, Automated parton-shower variations in Pythia 8. [arXiv:1605.0835](#)
66. J. Bellm, S. Plätzer, P. Richardson, A. Siódmok, S. Webster, Reweighting parton showers. [arXiv:1605.0825](#)
67. E. Bothmann, M. Schönherr, S. Schumann, Reweighting QCD matrix-element and parton-shower calculations. [arXiv:1606.0875](#)
68. A.G. De Ridder, M. Ritzmann, P.Z. Skands, Timelike Dipole-Antenna showers with massive fermions. *Phys. Rev. D* **85**, 014013 (2012). [arXiv:1108.6172](#)
69. E. Norrbin, T. Sjöstrand, QCD radiation off heavy particles. *Nucl. Phys. B* **603**, 297–342 (2001). [arXiv:hep-ph/0010012](#)
70. R.S. Thorne, Effect of changes of variable flavor number scheme on parton distribution functions and predicted cross sections. *Phys. Rev. D* **86**, 074017 (2012). [arXiv:1201.6180](#)
71. H. Murayama, I. Watanabe, K. Hagiwara, HELAS: HELicity amplitude subroutines for Feynman diagram evaluations
72. G. Miu, T. Sjöstrand, W production in an improved parton shower approach. *Phys. Lett. B* **449**, 313–320 (1999). [arXiv:hep-ph/9812455](#)
73. T. Plehn, D. Rainwater, P.Z. Skands, Squark and gluino production with jets. *Phys. Lett. B* **645**, 217–221 (2007). [arXiv:hep-ph/0510144](#)
74. P.Z. Skands, Tuning Monte Carlo generators: the Perugia tunes. *Phys. Rev. D* **82**, 074018 (2010). [arXiv:1005.3457](#)
75. R. Corke, T. Sjöstrand, Improved parton showers at large transverse momenta. *Eur. Phys. J. C* **69**, 1–18 (2010). [arXiv:1003.2384](#)
76. S. Catani, F. Krauss, R. Kuhn, B.R. Webber, QCD matrix elements + parton showers. *JHEP* **11**, 063 (2001). [arXiv:hep-ph/0109231](#)
77. J. Alwall et al., Comparative study of various algorithms for the merging of parton showers and matrix elements in hadronic collisions. *Eur. Phys. J. C* **53**, 473–500 (2008). [arXiv:0706.2569](#)
78. L. Lönnblad, S. Prestel, Unitarising matrix element + parton shower merging. *JHEP* **02**, 094 (2013). [arXiv:1211.4827](#)
79. S. Plätzer, Controlling inclusive cross sections in parton shower + matrix element merging. *JHEP* **08**, 114 (2013). [arXiv:1211.5467](#)
80. J. Bellm, Higher order corrections to multi jet final states at collider. PhD thesis, KIT, Karlsruhe, IKP, 2015
81. R. Kleiss, W.J. Stirling, S.D. Ellis, A New Monte Carlo treatment of multiparticle phase space at high-energies. *Comput. Phys. Commun.* **40**, 359 (1986)
82. B. Andersson, G. Gustafson, C. Sjögren, Comparison of the dipole cascade model versus $O(\alpha_s^2)$ matrix elements and color interference in e^+e^- annihilation. *Nucl. Phys. B* **380**, 391–407 (1992)
83. B. Andersson, G. Gustafson, A. Nilsson, C. Sjögren, Fluctuations and anomalous dimensions in QCD cascades. *Z. Phys. C* **49**, 79–90 (1991)
84. G. Gustafson, A. Nilsson, Fractal structures and intermittency in perturbative QCD cascades. *Nucl. Phys. B* **355**, 106–122 (1991)
85. B. Andersson, G. Gustafson, J. Samuelsson, Discrete QCD: a new approximation for QCD cascades. *Nucl. Phys. B* **463**, 217–237 (1996)
86. J.R. Christiansen, T. Sjöstrand, Weak Gauge Boson radiation in parton showers. *JHEP* **04**, 115 (2014). [arXiv:1401.5238](#)
87. J. Bellm, G. Nail, S. Plätzer, P. Schichtel, A. Siódmok, Parton shower uncertainties with Herwig 7: benchmarks at leading order. [arXiv:1605.1338](#)
88. S. Frixione, P. Nason, C. Oleari, Matching NLO QCD computations with Parton Shower simulations: the POWHEG method. *JHEP* **11**, 070 (2007). [arXiv:0709.2092](#)
89. P. Nason, A New method for combining NLO QCD with shower Monte Carlo algorithms. *JHEP* **11**, 040 (2004). [arXiv:hep-ph/0409146](#)
90. J. Alwall, R. Frederix, S. Frixione, V. Hirschi, F. Maltoni, O. Mattelaer, H.S. Shao, T. Stelzer, P. Torrielli, M. Zaro, The automated computation of tree-level and next-to-leading order differential cross sections, and their matching to parton shower simulations. *JHEP* **07**, 079 (2014). [arXiv:1405.0301](#)
91. ATLAS Collaboration, G. Aad et al., Measurement of the production cross section of jets in association with a Z boson in pp collisions at $\sqrt{s} = 7$ TeV with the ATLAS detector. *JHEP* **07**, 032 (2013). [arXiv:1304.7098](#)
92. C.M.S. Collaboration, S. Chatrchyan et al., Event shapes and azimuthal correlations in Z + jets events in pp collisions at $\sqrt{s} = 7$ TeV. *Phys. Lett. B* **722**, 238 (2013). [arXiv:1301.1646](#)
93. D. d’Enterria, P.Z. Skands, eds., High-precision α_s measurements from LHC to FCC-ee (2015)
94. P. Skands, S. Carrazza, J. Rojo, Tuning PYTHIA 8.1: the Monash 2013 tune. *Eur. Phys. J. C* **74**(8), 3024 (2014). [arXiv:1404.5630](#)
95. A. Buckley, J. Butterworth, L. Lönnblad, D. Grellscheid, H. Hoeth, J. Monk, H. Schulz, F. Siegert, Rivet user manual. *Comput. Phys. Commun.* **184**, 2808 (2013). [arXiv:1003.0694](#)
96. L3 Collaboration, P. Achard et al., Studies of hadronic event structure in e^+e^- annihilation from 30-GeV to 209-GeV with the L3 detector. *Phys. Rep.* **399**, 71–174 (2004). [arXiv:hep-ex/0406049](#)
97. L. Lönnblad, S. Prestel, Merging multi-leg NLO matrix elements with parton showers. *JHEP* **03**, 166 (2013). [arXiv:1211.7278](#)
98. B. Andersson, G. Gustafson, B. Söderberg, A general model for jet fragmentation. *Z. Phys. C* **20**, 317 (1983)
99. B. Andersson, G. Gustafson, G. Ingelman, T. Sjöstrand, Parton fragmentation and string dynamics. *Phys. Rep.* **97**, 31–145 (1983)
100. B. Andersson, The Lund model. *Camb. Monogr. Part. Phys. Nucl. Phys. Cosmol.* (1997)
101. ALEPH Collaboration, R. Barate et al., Study of charm production in Z decays. *Eur. Phys. J. C* **16**, 597–611 (2000). [arXiv:hep-ex/9909032](#)
102. SLD Collaboration, K. Abe et al., Measurement of the b quark fragmentation function in Z0 decays. *Phys. Rev. D* **65**, 092006 (2002). [arXiv:hep-ex/0202031](#). [Erratum: *Phys. Rev. D* **66**, 079905 (2002)]
103. DELPHI Collaboration, J. Abdallah et al., A study of the b-quark fragmentation function with the DELPHI detector at LEP I and an averaged distribution obtained at the Z Pole. *Eur. Phys. J. C* **71**, 1557 (2011). [arXiv:1102.4748](#)
104. A. Buckley, M. Whalley, HepData reloaded: reinventing the HEP data archive. *PoS ACAT2010*, 067 (2010). [arXiv:1006.0517](#)
105. ATLAS Collaboration, G. Aad et al., Measurement of angular correlations in Drell-Yan lepton pairs to probe Z/gamma* boson transverse momentum at $\sqrt{s}=7$ TeV with the ATLAS detector. *Phys. Lett. B* **720**, 32 (2013). [arXiv:1211.6899](#)
106. ATLAS Collaboration, G. Aad et al., Measurement of the Z/γ^* boson transverse momentum distribution in pp collisions at $\sqrt{s} = 7$ TeV with the ATLAS detector. *JHEP* **09**, 145 (2014). [arXiv:1406.3660](#)
107. CMS Collaboration, V. Khachatryan et al., Measurements of jet multiplicity and differential production cross sections of Z+ jets events in proton-proton collisions at $\sqrt{s} = 7$ TeV. *Phys. Rev. D* **91**(5), 052008. [arXiv:1408.3104](#)
108. T. Sjöstrand, M. van Zijl, A Multiple interaction model for the event structure in hadron collisions. *Phys. Rev. D* **36**, 2019 (1987)
109. ATLAS Collaboration, G. Aad et al., Measurement of underlying event characteristics using charged particles in pp collisions at $\sqrt{s} = 900\text{ GeV}$ and 7 TeV with the ATLAS detector. *Phys. Rev. D* **83**, 112001 (2011). [arXiv:1012.0791](#)
110. CMS Collaboration, S. Chatrchyan et al., Measurement of the underlying event activity at the LHC with $\sqrt{s} = 7$ TeV and comparison with $\sqrt{s} = 0.9$ TeV. *JHEP* **09**, 109 (2011). [arXiv:1107.0330](#)

111. S. Hoeche, S. Schumann, F. Siegert, Hard photon production and matrix-element parton-shower merging. *Phys. Rev. D* **81**, 034026 (2010). [arXiv:0912.3501](#)
112. ATLAS Collaboration, G. Aad et al., Measurement of Dijet Azimuthal Decorrelations in pp Collisions at $\sqrt{s} = 7$ TeV. *Phys. Rev. Lett.* **106**, 172002 (2011). [arXiv:1102.2696](#)
113. CMS Collaboration, S. Chatrchyan et al., Measurement of the ratio of inclusive jet cross sections using the anti- k_T algorithm with radius parameters $R=0.5$ and 0.7 in pp collisions at $\sqrt{s} = 7$ TeV. *Phys. Rev. D* **90**(7), 072006 (2014). [arXiv:1406.0324](#)
114. CMS Collaboration, S. Chatrchyan et al., Measurements of differential jet cross sections in proton-proton collisions at $\sqrt{s} = 7$ TeV with the CMS detector. *Phys. Rev. D* **87**(11), 112002 (2013). [arXiv:1212.6660](#). [Erratum: *Phys. Rev. D* **87**(11), 119902 (2013)]
115. ATLAS Collaboration, G. Aad et al., Study of Jet Shapes in Inclusive Jet Production in pp Collisions at $\sqrt{s} = 7$ TeV using the ATLAS detector. *Phys. Rev. D* **83**, 052003 (2011). [arXiv:1101.0070](#)
116. S. Badger, B. Biedermann, P. Uwer, V. Yundin, Computation of multi-leg amplitudes with NJet. *J. Phys. Conf. Ser.* **523**, 012057 (2014). [arXiv:1312.7140](#)
117. A. Buckley, M.R. Whalley, W.J. Stirling, J.M. Butterworth, E. Nurse, B. Waugh, HepForge: a lightweight development environment for HEP software. In *15th International Conference on Computing in High Energy and Nuclear Physics (CHEP 2006) Mumbai, Maharashtra, India, February 13–17, 2006*, (2006). [arXiv:hep-ph/0605046](#)
118. A. Daleo, T. Gehrmann, D. Maitre, Antenna subtraction with hadronic initial states. *JHEP* **04**, 016 (2007). [arXiv:hep-ph/0612257](#)

4.2 The Shower Algorithm

The parton-shower algorithm is based on solving

$$\Pi \equiv \Pi(t_n, t_{n+1}) = \mathcal{R} \quad (4.1)$$

for the scale of the next branching t_{n+1} . Here, \mathcal{R} is a random number distributed flat in the interval $[0, 1]$. The same symbol will be used throughout this chapter to denote random numbers. The no-emission probability integrates over the differential kernels $d\mathcal{A}$ which are non-trivial functions of the evolution t and a complementary phase-space variable ζ ,

$$\begin{aligned} \Pi &= \exp\left(-\int d\mathcal{A}(t_n, t_{n+1})\right) = \exp\left(-\int d\Phi_{\text{ant}} g_s^2(t) \mathcal{C} \bar{a}(t, \zeta) R_{\text{pdf}}\right) \\ &= \exp\left(-\int_{t_{n+1}}^{t_n} dt \int_{\zeta_-(t)}^{\zeta_+(t)} d\zeta \int_0^{2\pi} \frac{d\phi}{2\pi} \left(\frac{x_A x_B}{x_a x_b}\right)^2 \frac{\alpha_s(t) \mathcal{C}}{4\pi} \frac{\bar{a}(t, \zeta)}{s_{\text{ant}}} R_{\text{pdf}} |J|\right). \end{aligned} \quad (4.2)$$

The variables t and ζ are functions of the antenna invariant mass squared s_{ant} and the branching invariants s_{12} and s_{23} , $t \equiv t(s_{12}, s_{23}, s_{\text{ant}})$ and $\zeta \equiv \zeta(s_{12}, s_{23}, s_{\text{ant}})$. Here, the numbers 1, 2, 3 refer to the post-branching momenta, i.e. $s_{12} = s_{aj}$ and $s_{23} = s_{jb}$ or s_{jk} for initial-initial or initial-final antennae respectively. The antenna phase space $d\Phi_{\text{ant}}$ is typically expressed in terms of s_{12} and s_{23} . The transformation from the invariants (s_{12}, s_{23}) to the evolution parameters (t, ζ) introduces the Jacobian

$$J = \det\left(\frac{\partial\{s_{12}, s_{23}\}}{\partial\{t, \zeta\}}\right) = \left(\frac{\partial t}{\partial s_{12}} \frac{\partial \zeta}{\partial s_{23}} - \frac{\partial \zeta}{\partial s_{12}} \frac{\partial t}{\partial s_{23}}\right)^{-1}. \quad (4.3)$$

The functional form of ζ is required to be linearly independent of the evolution variable t , to be not a candidate for t itself. Furthermore, contours of constant ζ should intersect contours of constant t only once for all $t > 0$, such that the Jacobian in eq. (4.3) is well defined. In the DGLAP picture, the z variable corresponds to the energy fraction of the emission, which not only assigns a physical meaning to the complementary variable, but is also particularly convenient for initial-state radiation, as will be discussed below.

The PDF ratio has the general form

$$R_{\text{pdf}} = \frac{f_a(x_a, t) f_b(x_b, t)}{f_A(x_A, t) f_B(x_B, t)}. \quad (4.4)$$

The no-emission probability in eq. (4.2) holds for all types of antennae. If one or both of the initial-state partons are left unchanged by the branching, the ratio of x -values and PDFs automatically cancel.

The complexity of eq. (4.2) requires introducing overestimates of the splitting kernels \bar{a} , PDF ratio R_{pdf} , and the ζ -integral I_ζ ,

$$\bar{a}, R_{\text{pdf}}, I_\zeta(\zeta_-(t), \zeta_+(t)) \longrightarrow \hat{a}, \hat{R}_{\text{pdf}}, I_\zeta(\zeta_-(t_{\text{min}}), \zeta_+(t_{\text{min}})), \quad (4.5)$$

such that eq. (4.1) can be solved. The functional forms of \hat{a} are given in secs. 4.3.4 and 4.4.4. The ζ -integral includes all ζ -dependent terms of eq. (4.2) and is overestimated by applying integration boundaries that are evaluated at the scale t_{\min} . The PDF ratio is overestimated by

$$\hat{R}_{\text{pdf}} = \frac{x_a^\epsilon f_a(x_A, t_{\min})}{x_A^\epsilon f_A(x_A, t_{\min})} \frac{x_b^\epsilon f_b(x_B, t_{\min})}{x_B^\epsilon f_B(x_B, t_{\min})}. \quad (4.6)$$

Here, t_{\min} is the lower limit of the range of evolution variable under consideration. If the ζ variable corresponds to the energy-sharing x_A/x_a x_B/x_b (or the inverse), as it is the case in DGLAP showers, the overestimate of the PDF ratio can be controlled by choosing a value of $\epsilon \neq 0$.

This allows to propose a branching in terms of the three evolution parameters, by solving the following equations for t_{n+1} , ζ , and ϕ ,

$$\hat{\Pi}(t_n, t_{n+1}) = \mathcal{R}_t, \quad (4.7)$$

$$\frac{I_\zeta(\zeta_-(t_{\min}), \zeta)}{I_\zeta(\zeta_-(t_{\min}), \zeta_+(t_{\min}))} = \mathcal{R}_\zeta, \quad (4.8)$$

$$\phi/2\pi = \mathcal{R}_\phi. \quad (4.9)$$

In eq. (4.8), the boundary values $(\zeta_-(t_{\min}), \zeta_+(t_{\min}))$ must be the same as those that were used in the overestimate of I_ζ . The angle ϕ is generated in the rest frame of the parent antenna. The proposed branching is rejected if it is unphysical, e.g. if ζ is outside the physical phase space, or if

$$P_{\text{LL}} \cdot P_{\text{ME}} = \frac{\bar{a}}{\hat{a}} \frac{R_{\text{pdf}}}{\hat{R}_{\text{pdf}}} \cdot P_{\text{ME}} < \mathcal{R}. \quad (4.10)$$

Here, P_{LL} denotes the accept probability of the pure shower and P_{ME} represents an additional term due to MECs. By the virtue of the veto algorithm [138], this will remove the excess emissions introduced due to the overestimates. To construct the post-branching kinematics, the variables t and ζ must be inverted to reobtain the branching invariants (s_{12}, s_{23}) .

The follow sections give the details required to follow the previous instructions for initial-initial and initial-final antennae.

4.3 Initial-Initial Antennae

The integration kernel for initial-initial configurations reads

$$d\mathcal{A}^{\text{II}}(t_n^{\text{II}}, t_{n+1}^{\text{II}}) = dt^{\text{II}} d\zeta \frac{d\phi}{2\pi} \frac{\alpha_s(t^{\text{II}}) \mathcal{C}_{s_{AB}}}{4\pi s_{ab}^2} \bar{a}^{\text{II}}(t^{\text{II}}, \zeta) R_{\text{pdf}} |J|. \quad (4.11)$$

The calculation of the initial-initial antenna phase space $d\Phi_{\text{ant}}^{\text{II}}$ is discussed in sec. 4.3.1. The functional form of the variables t^{II} and ζ is given in sec. 4.3.2, with

a brief discussion of their kinematical limits. The Jacobian J , which transforms the invariants (s_{aj}, s_{jb}) to the evolution parameters (t^{II}, ζ) , is given in sec. 4.3.3. The overestimates for the antenna functions, required to solve eq. (4.1), is given in sec. 4.3.4. Finally, the different pieces are put together into the evolution integrals in sec. 4.3.5, and solved to find values for ζ and t^{II} in sec. 4.3.6 and sec. 4.3.7 respectively. As a last step, the transformation from t^{II} and ζ back to the branching invariants s_{aj} and s_{jb} is given in sec. 4.3.8.

4.3.1 Phase-Space Factorization

To calculate the phase-space factorization the mapping from the momenta before the branching, $AB \rightarrow R$, to the ones after the branching, $ab \rightarrow jr$, has to be known; see fig. 1 in sec. 4.1 for a graphical illustration. The final state particles are combined into the massive recoiler system R/r ; all other partons are considered massless here. Keeping the direction of the incoming partons A and B fixed, two degrees of freedom remain to construct the post-branching momenta. The following choices are made:

1. The invariant mass of the final state recoiler system R is kept invariant. Applying momentum conservation, $p_R = p_A + p_B$ and $p_j + p_r = p_a + p_b$, yields

$$p_R^2 = p_r^2 \Leftrightarrow s_{AB} = s_{ab} - s_{aj} - s_{jb}. \quad (4.12)$$

2. The rapidity of the final state recoiler system is kept invariant,

$$y_R = y_r \Leftrightarrow \frac{p_{R+}}{p_{R-}} = \frac{p_{r+}}{p_{r-}} \Leftrightarrow \frac{x_A}{x_B} = \frac{x_a(s_{ab} - s_{jb})}{x_b(s_{ab} - s_{aj})}. \quad (4.13)$$

With eqs. (4.12) and (4.13) at hand, we can proceed to the calculation of the phase-space factorization. The full phase space consists of the two-particle phase space $d\Phi_2(p_a, p_b \rightarrow p_j, p_r)$ and a part describing the incoming partons,

$$d\Phi_2^{\text{II}} = \frac{dx_a}{x_a} \frac{dx_b}{x_b} d\Phi_2(p_a, p_b \rightarrow p_j, p_r), \quad (4.14)$$

The two-particle phase space is

$$\begin{aligned} & d\Phi_2(p_a, p_b \rightarrow p_j, p_r) \\ &= \frac{1}{(2\pi)^2} \frac{d^3 p_j}{2E_j} d^4 p_r \theta(E_r) \delta(p_r^2 - m_r^2) \delta^{(4)}(p_a + p_b - p_r - p_j) \\ &= \frac{1}{8\pi^2} E_j dE_j d\cos\theta_j d\phi_j \theta(E_a + E_b - E_j) \delta(s_{ab} - s_{aj} - s_{jb} - m_r^2). \end{aligned} \quad (4.15)$$

Performing the transformation from the variables $(E_j, \cos\theta_j, x_a, x_b)$ to $(s_{aj}, s_{jb}, x_A, x_B)$ introduces a 4-dimensional Jacobian factor,

$$J = \det \left(\frac{\partial \{s_{aj}, s_{jb}, x_A, x_B\}}{\partial \{E_j, \cos\theta_j, x_a, x_b\}} \right). \quad (4.16)$$

This requires the new variables to be written solely in terms of the old variables,

$$s_{aj} = x_a \sqrt{s} E_j (1 - \cos \theta_j) \quad (4.17)$$

$$s_{jb} = x_b \sqrt{s} E_j (1 + \cos \theta_j) \quad (4.18)$$

$$x_A = \sqrt{\frac{x_a(s_{ab} - s_{jb})}{x_b(s_{ab} - s_{aj})} \frac{s_{ab} - s_{aj} - s_{jb}}{s}} \quad (4.19)$$

$$x_B = \sqrt{\frac{x_b(s_{ab} - s_{aj})}{x_a(s_{ab} - s_{jb})} \frac{s_{ab} - s_{aj} - s_{jb}}{s}}. \quad (4.20)$$

The hadronic center-of-mass energy is denoted by s . Using MATHEMATICA [139] to calculate the Jacobian gives the simple result

$$J^{-1} = 2 E_j s_{ab}. \quad (4.21)$$

Plugging eqs. (4.15) and (4.21) into the expression for the full phase space, eq. (4.14) reads

$$\begin{aligned} d\Phi_2^{\text{II}} &= \frac{dx_A}{x_a} \frac{dx_B}{x_b} \frac{1}{8\pi^2} E_j ds_{aj} ds_{jb} d\phi_j \frac{1}{2E_j s_{ab}} \delta(s_{ab} - s_{aj} - s_{jb} - m_r^2) \\ &= \frac{dx_A}{x_A} \frac{dx_B}{x_B} 2\pi \delta(s_{ab} - s_{aj} - s_{jb} - m_r^2) \frac{1}{16\pi^2} \frac{s_{AB}}{s_{ab}^2} ds_{aj} ds_{jb} \frac{d\phi_j}{2\pi} \\ &= \frac{dx_A}{x_A} \frac{dx_B}{x_B} d\Phi_1(p_A, p_B \rightarrow p_R) d\Phi_{\text{ant}}^{\text{II}}. \end{aligned} \quad (4.22)$$

The phase space is now written in terms of the one-particle phase space

$$\begin{aligned} d\Phi_1(p_A, p_B \rightarrow p_R) &= 2\pi d^4 p_R \delta(p_R^2 - m_R^2) \delta^{(4)}(p_A + p_B - p_R) \\ &= 2\pi \delta(s_{AB} - m_R^2) \end{aligned} \quad (4.23)$$

and the antenna phase space

$$d\Phi_{\text{ant}}^{\text{II}} = \frac{1}{16\pi^2} \frac{s_{AB}}{s_{ab}^2} ds_{aj} ds_{jb} \frac{d\phi_j}{2\pi}. \quad (4.24)$$

4.3.2 Evolution Variables and ζ Definitions

Branchings are evolved in the following variables,

$$t^{\text{II}} = \begin{cases} t_{\text{emit}}^{\text{II}} = \frac{s_{aj} s_{jb}}{s_{ab}} & \text{for gluon emission} \\ t_{\text{conv}}^{\text{II}} = s_{aj} \text{ or } s_{jb} & \text{for } a \text{ or } b \text{ converting to/from a gluon.} \end{cases} \quad (4.25)$$

The upper phase-space limits are $t_{\text{emit}}^{\text{II}} \leq (s - s_{AB})^2 / (4s)$ and $t_{\text{conv}}^{\text{II}} \leq s - s_{AB}$. From here on, whenever the two initial sides are treated separately, we will only consider branchings involving leg A . Branchings off leg B are treated similarly.

Our choices for the functional form of the ζ variable are

$$\zeta_1 = \frac{s_{aj}}{s_{ab}} = \frac{s_{aj}}{s_{AB} + s_{aj} + s_{jb}}, \quad \zeta_2 = \frac{s_{jb}}{s_{AB}}, \quad \text{and} \quad \zeta_3 = \frac{s_{ab}}{s_{AB}} = \frac{x_a x_b}{x_A x_B}. \quad (4.26)$$

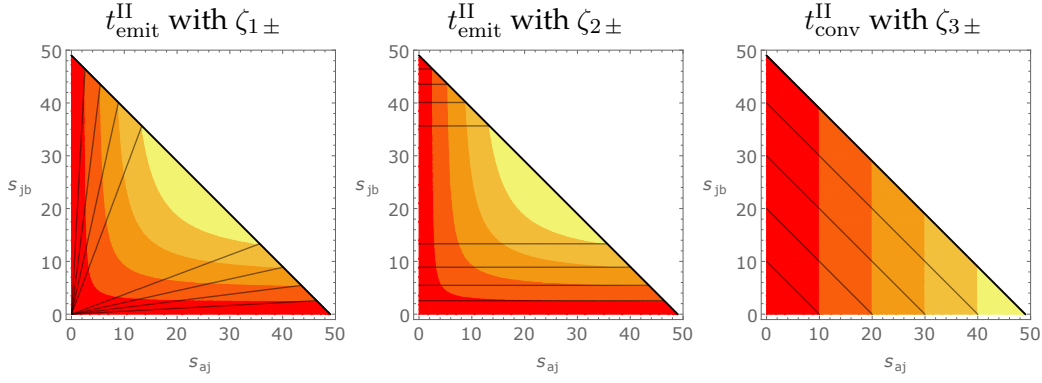


Figure 4.1: Contours of constant values of the evolution variable are shown in color. The grey lines represent the corresponding ζ -integration boundaries. The recoiler has chosen to be a Higgs boson, $s_{AB} = m_H^2 = (125 \text{ GeV})^2$. The phase space limit $s_{aj} + s_{jb} \leq s - s_{AB}$ is visualized by the thick black line.

The ζ -integration boundaries are denoted by ζ_{\pm} . For a given value of the evolution variable, $t_{\text{emit}}^{\text{II}}$ or $t_{\text{conv}}^{\text{II}}$ respectively, the boundaries are

$$\zeta_{1-}(t_{\text{emit}}^{\text{II}}) = \frac{s_{xj-}}{s} \quad \zeta_{1+}(t_{\text{emit}}^{\text{II}}) = \frac{s_{xj+}}{s}, \quad (4.27)$$

$$\zeta_{2-}(t_{\text{emit}}^{\text{II}}) = \frac{s_{xj-}}{s_{AB}} \quad \zeta_{2+}(t_{\text{emit}}^{\text{II}}) = \frac{s_{xj+}}{s_{AB}}, \quad (4.28)$$

$$\zeta_{3-}(t_{\text{conv}}^{\text{II}}) = \frac{s_{AB} + t_{\text{conv}}^{\text{II}}}{s_{AB}} \quad \zeta_{3+}(t_{\text{conv}}^{\text{II}}) = \frac{s}{s_{AB}}, \quad (4.29)$$

with $2s_{xj\pm} = s - s_{AB} \pm \sqrt{(s - s_{AB})^2 - 4t_{\text{emit}}^{\text{II}}s}$. Plots of contours of constant values of the different evolution variables, together with the corresponding ζ limits are shown in fig. 4.1.

4.3.3 Jacobians

The Jacobian factors for the transformation from the phase-space variables (s_{aj}, s_{jb}) to the shower variables (t^{II}, ζ) are

$$|J(t_{\text{emit}}^{\text{II}}, \zeta_1)| = s_{ab} (\zeta_1(1 - \zeta_1))^{-1}, \quad (4.30)$$

$$|J(t_{\text{emit}}^{\text{II}}, \zeta_2)| = s_{ab}^2 (s_{jb}(1 + \zeta_2))^{-1}, \quad (4.31)$$

$$|J(t_{\text{conv}}^{\text{II}}, \zeta_3)| = s_{AB}. \quad (4.32)$$

4.3.4 Trial Antenna Functions

To overestimate the physical antenna functions we make use of $s_{ab} > s_{AB}$ and $s_{ab} > s_{aj/jb}$. The following list presents the physical antenna functions \bar{a}^{II} for initial-initial configurations together with the overestimate \hat{a}^{II} ,

$$\bar{a}_{q\bar{q}g}^{\text{II}} = \frac{1}{s_{AB}} \left(\frac{2 s_{ab} s_{AB}}{s_{aj} s_{jb}} + \frac{s_{aj}}{s_{jb}} + \frac{s_{jb}}{s_{aj}} \right) \Rightarrow \hat{a}_{\text{soft}}^{\text{II}} = \frac{1}{s_{AB}} \frac{2 s_{ab}^2}{s_{aj} s_{jb}}, \quad (4.33)$$

$$\bar{a}_{gxg}^{\text{II}} - \bar{a}_{\text{soft}}^{\text{II}} = \frac{2}{s_{AB}} \left(\frac{s_{jb} s_{ab}}{s_{aj} s_{AB}} + \frac{s_{jb} s_{AB}}{s_{aj} s_{ab} + s_{aj}} \right) \Rightarrow \hat{a}_{gxg}^{\text{II}} = 2 \frac{s_{ab}^2}{s_{AB}^2} \frac{1}{s_{aj}}, \quad (4.34)$$

$$\bar{a}_{gx\bar{q}}^{\text{II}} = \frac{1}{s_{AB}} \left(-2 \frac{s_{jb} s_{AB}}{s_{aj} (s_{ab} - s_{aj})} + \frac{s_{ab}}{s_{aj}} \right) \Rightarrow \hat{a}_{gx\bar{q}}^{\text{II}} = \frac{s_{ab}}{s_{AB}} \frac{1}{s_{aj}}, \quad (4.35)$$

$$\bar{a}_{qxq}^{\text{II}} = \frac{1}{2 s_{aj}} \frac{s_{jb}^2 + s_{ab}^2}{s_{AB}^2} \Rightarrow \hat{a}_{qxq}^{\text{II}} = \frac{s_{ab}^2}{s_{AB}^2} \frac{1}{s_{aj}}. \quad (4.36)$$

Note that the overestimate of the soft eikonal term $\hat{a}_{\text{soft}}^{\text{II}}$ already includes the collinear singularities of the parent quarks. However, if a parent parton is a gluon, the overestimate of the eikonal term is not large enough. In those cases an additional term $\hat{a}_{gxg}^{\text{II}}$ is introduced. It contains only the singularities associated with the emission being collinear to the parent gluon and is independent of the flavour of the other parent parton, x .

4.3.5 Evolution Integrals

The integration kernel in eq. (4.11) contains the angle ϕ . As the integration over $d\phi$ is trivial, we will drop it in this section. Using the Jacobian factors in eqs. (4.30) to (4.32) and the trial antenna functions in eqs. (4.33) to (4.36), the trial integration kernels $d\hat{\mathcal{A}}$ can be written in terms of t and ζ ,

$$d\hat{\mathcal{A}}_{\text{soft}}^{\text{II}} = \frac{\alpha_s \mathcal{C}}{2\pi} \hat{R}_{\text{pdf}} \frac{dt_{\text{emit}}^{\text{II}}}{t_{\text{emit}}^{\text{II}}} \frac{d\zeta_1}{\zeta_1(1-\zeta_1)}, \quad (4.37)$$

$$d\hat{\mathcal{A}}_{gxg}^{\text{II}} = \frac{\alpha_s \mathcal{C}}{2\pi} \hat{R}_{\text{pdf}} \frac{dt_{\text{emit}}^{\text{II}}}{t_{\text{emit}}^{\text{II}}} \frac{d\zeta_2}{1+\zeta_2}, \quad (4.38)$$

$$d\hat{\mathcal{A}}_{gx\bar{q}}^{\text{II}} = \frac{\alpha_s \mathcal{C}}{4\pi} \left(\frac{x_a x_b}{x_A x_B} \right)^\alpha \hat{R}_{\text{pdf}} \frac{dt_{\text{conv}}^{\text{II}}}{t_{\text{conv}}^{\text{II}}} \frac{d\zeta_3}{\zeta_3^{1+\alpha}}, \quad (4.39)$$

$$d\hat{\mathcal{A}}_{qxq}^{\text{II}} = \frac{\alpha_s \mathcal{C}}{4\pi} \left(\frac{x_a x_b}{x_A x_B} \right)^\alpha \hat{R}_{\text{pdf}} \frac{dt_{\text{conv}}^{\text{II}}}{t_{\text{conv}}^{\text{II}}} \frac{d\zeta_3}{\zeta_3^\alpha}. \quad (4.40)$$

For the last two processes the general factor α helps to control the overestimate of the PDF ratio, as discussed in sec. 4.2.

4.3.6 ζ Integrals and Trial ζ

The ζ integrals that appear in the trial evolution kernels in eqs. (4.37) to (4.40) are

$$I_{\zeta_{1/2}} = \int_{\zeta_a}^{\zeta_b} \frac{d\zeta}{\zeta^\rho(1\pm\zeta)} = \ln \left(\frac{\zeta_b^\rho(1\pm\zeta_b)^{\pm 1}}{\zeta_a^\rho(1\pm\zeta_a)^{\pm 1}} \right) \quad \text{with } \rho \in \{0, 1\}, \quad (4.41)$$

$$I_{\zeta_3} = \int_{\zeta_a}^{\zeta_b} \frac{d\zeta}{\zeta^\kappa} = \begin{cases} (\zeta_b^{1-\kappa} - \zeta_a^{1-\kappa}) / (1-\kappa) & \text{for } \kappa \neq 1 \\ \ln(\zeta_b/\zeta_a) & \text{for } \kappa = 1 \end{cases}. \quad (4.42)$$

Here, $\kappa = \alpha$ for eq. (4.40), $\kappa = 1 + \alpha$ for eq. (4.39), $\rho = 1$ for eq. (4.37), and $\rho = 0$ for eq. (4.38). A trial value for the ζ variable is generated according to

$$\zeta_{1/2} = \left[\frac{1 \pm \zeta_{\min}}{\zeta_{\min}^\rho} \left(\frac{\zeta_{\min}^\rho (1 \pm \zeta_{\max})}{\zeta_{\max}^\rho (1 \pm \zeta_{\min})} \right)^{\mathcal{R}_{\zeta_{1/2}}} \mp 1 \right]^{\pm 1}, \quad (4.43)$$

$$\zeta_3 = \begin{cases} (\mathcal{R}_{\zeta_3} (\zeta_{\min}^{1-\kappa} - \zeta_{\max}^{1-\kappa}) + \zeta_{\max}^{1-\kappa})^{\frac{1}{1-\kappa}} & \text{for } \kappa \neq 1 \\ \zeta_{\max} (\zeta_{\min}/\zeta_{\max})^{\mathcal{R}_{\zeta_3}} & \text{for } \kappa = 1 \end{cases}. \quad (4.44)$$

4.3.7 Generation of Trial Evolution Scale

In the discussion so far we have not considered the strong coupling. We distinguish between two cases: a constant and running α_s . For a constant α_s the integral over the evolution is scale is

$$\alpha_s X \int_{t_{n+1}^{\text{II}}}^{t_n^{\text{II}}} \frac{dt^{\text{II}}}{t^{\text{II}}} = \alpha_s X \ln t^{\text{II}} \Big|_{t_{n+1}^{\text{II}}}^{t_n^{\text{II}}} = \alpha_s X \ln \frac{t_n^{\text{II}}}{t_{n+1}^{\text{II}}}. \quad (4.45)$$

X represents all terms in eqs. (4.37) to (4.40) that do not depend on the scale. The solution for the next trial scale t_{n+1}^{II} is

$$t_{n+1}^{\text{II}} = t_n^{\text{II}} \mathcal{R}^{(\alpha_s X)^{-1}}. \quad (4.46)$$

To include one-loop running of the strong coupling we use $\alpha_s^{-1}(t) = b_0 \ln(k_R^2 t/\Lambda^2)$. The arbitrary scaling factor k_R includes the compound effect of any renormalization scale prefactor choices. The integral over the evolution scale changes to

$$X \int_{t_{n+1}^{\text{II}}}^{t_n^{\text{II}}} \frac{dt^{\text{II}}}{t^{\text{II}} \ln\left(\frac{k_R^2 t^{\text{II}}}{\Lambda^2}\right)} = X \ln\left(\ln\left(\frac{k_R^2 t^{\text{II}}}{\Lambda^2}\right)\right) \Big|_{t_{n+1}^{\text{II}}}^{t_n^{\text{II}}} = X \ln\left(\frac{\ln\left(\frac{k_R^2 t_n^{\text{II}}}{\Lambda^2}\right)}{\ln\left(\frac{k_R^2 t_{n+1}^{\text{II}}}{\Lambda^2}\right)}\right). \quad (4.47)$$

The solution for the next trial scale t_{n+1}^{II} is

$$t_{n+1}^{\text{II}} = \frac{\Lambda^2}{k_R^2} \left(\frac{k_R^2 t_n^{\text{II}}}{\Lambda^2} \right)^{\mathcal{R}^{1/X}}. \quad (4.48)$$

4.3.8 Inverse Transforms

After a set of shower variables has been generated, the (t^{II}, ζ) choices must be inverted to reobtain the branching invariants (s_{aj}, s_{jb}) which are used to construct the kinematics of the trial branching. These inversions are the following:

$$t_{\text{emit}}^{\text{II}} \text{ with } \zeta_1: \quad s_{aj} = \frac{t_{\text{emit}}^{\text{II}} + \zeta_1 s_{AB}}{1 - \zeta_1} \quad s_{jb} = \frac{t_{\text{emit}}^{\text{II}}}{\zeta_1} \quad (4.49)$$

$$t_{\text{emit}}^{\text{II}} \text{ with } \zeta_2: \quad s_{aj} = \frac{t_{\text{emit}}^{\text{II}}(1 + \zeta_2)}{\zeta_2 - t_{\text{emit}}^{\text{II}}/s_{AB}} \quad s_{jb} = \zeta_2 s_{AB} \quad (4.50)$$

$$s_{aj} \text{ with } \zeta_3: \quad s_{aj} = t_{\text{conv}}^{\text{II}} \quad s_{jb} = s_{AB}(\zeta_3 - 1) - t_{\text{conv}}^{\text{II}} \quad (4.51)$$

4.4 Initial-Final Antennae

The integration kernel for initial-final configurations reads

$$d\mathcal{A}^{\text{IF}}(t_n^{\text{IF}}, t_{n+1}^{\text{IF}}) = dt^{\text{IF}} d\zeta \frac{d\phi}{2\pi} \frac{\alpha_s(t^{\text{IF}}) \mathcal{C} s_{AK}}{4\pi(s_{AK} + s_{jk})^2} \bar{a}^{\text{IF}}(t^{\text{IF}}, \zeta) R_{\text{pdf}} |J|. \quad (4.52)$$

The following sections are structured as for initial-initial antennae: the phase space $d\Phi_{\text{ant}}^{\text{IF}}$ is calculated in sec. 4.4.1, the t^{IF} and ζ variables are given in sec. 4.4.2, the Jacobian factors J in sec. 4.4.3, the overestimates for the antenna functions in sec. 4.4.4, the trial evolution integrals in sec. 4.4.5, values for ζ and t^{IF} are found in sec. 4.4.6 and sec. 4.4.7 respectively, and the transformation from t^{IF} and ζ back to the branching invariants s_{aj} and s_{jk} is given in sec. 4.4.8.

4.4.1 Phase-Space Factorization

To calculate the phase-space factorization the mapping from the momenta before the branching, $AB \rightarrow KR$, to the ones after the branching, $ab \rightarrow jkr$, has to be known; see fig. 3 in sec. 4.1 for a graphical illustration. . The final state particles, except for the parton K , are combined into the massive recoiler system R/r ; all other partons are considered massless here. Keeping the direction of the incoming partons A and B fixed and not allowing recoil outside of the antenna, i.e. $b = B$ and $r = R$, fully fixes the degrees of freedom. With this choice of recoil strategy momentum conservation is

$$p_j + p_k - p_a = p_K - p_A \Leftrightarrow s_{AK} + s_{jk} = s_{ak} + s_{aj}. \quad (4.53)$$

The ratio of the energy fractions of the incoming parton is $x_A/x_a = s_{AK}/(s_{AK} + s_{jk})$.

The full phase space consists of the three-particle phase space $d\Phi_3(p_a, p_B \rightarrow p_j, p_k, p_R)$ and a part describing the incoming parton,

$$d\Phi_3^{\text{IF}} = \frac{dx_a}{x_a} d\Phi_3(p_a, p_B \rightarrow p_j, p_k, p_R), \quad (4.54)$$

Note that no integration over $x_b = x_B$ enters, as the other incoming parton does not change its momentum. The three-particle phase space is

$$\begin{aligned} d\Phi_3(p_a, p_B \rightarrow p_j, p_k, p_R) &= \frac{1}{(2\pi)^5} \frac{d^3 p_j}{2E_j} \frac{d^3 p_k}{2E_k} d^4 p_R \theta(E_R) \delta(p_R^2 - m_R^2) \delta^{(4)}(p_a + p_B - p_j - p_k - p_R) \\ &= \frac{1}{4(2\pi)^5} E_j dE_j d\cos\theta_j d\phi_j E_k dE_k d\cos\theta_k d\phi_k \delta((p_a + p_B - p_j - p_k)^2 - m_R^2). \end{aligned} \quad (4.55)$$

Performing the transformation from the variables $(E_j, \cos\theta_j, \cos\theta_k, x_a)$ to $(s_{aj}, s_{jk}, s_{AK}, x_A)$ introduces a 4-dimensional Jacobian factor,

$$J = \det \left(\frac{\partial\{s_{aj}, s_{jk}, x_A, s_{AK}\}}{\partial\{E_j, \cos\theta_j, x_a, \cos\theta_k\}} \right). \quad (4.56)$$

This requires the new variables to be written solely in terms of the old variables,

$$s_{aj} = x_a \sqrt{s} E_j (1 - \cos \theta_j) \quad (4.57)$$

$$s_{ak} = x_a \sqrt{s} E_k (1 - \cos \theta_k) \quad (4.58)$$

$$s_{AK} = x_A \sqrt{s} (E_j (1 - \cos \theta_j) + E_k (1 - \cos \theta_k)) \quad (4.59)$$

$$s_{jk} = -s_{AK} + s_{ak} + s_{aj} \quad (4.60)$$

$$x_A = \frac{1}{\sqrt{s}} \left(x_a \sqrt{s} \left(1 + \frac{p_{\perp K}^2}{s_{aj} + s_{ak}} \right) - E_j (1 + \cos \theta_j) - E_k (1 + \cos \theta_k) \right) \quad (4.61)$$

Using MATHEMATICA [139] to calculate the Jacobian gives the simple result

$$J^{-1} = 2 E_j E_k (s_{AK} + s_{jk}) x_A \sqrt{s} = 2 E_j E_k \frac{(s_{AK} + s_{jk})^2}{s_{AK}} \frac{x_A^2}{x_a} \sqrt{s}. \quad (4.62)$$

Plugging eqs. (4.55) and (4.62) into the expression for the full phase space, eq. (4.54) reads

$$\begin{aligned} d\Phi_3^{\text{IF}} &= \frac{dx_A}{x_A} \frac{1}{4(2\pi)^5} \frac{s_{AK}}{2(s_{AK} + s_{jk})^2 x_A \sqrt{s}} ds_{AK} ds_{aj} \\ &\quad ds_{jk} d\phi_j d\phi_k dE_k \delta((p_a + p_B - p_j - p_k)^2 - m_R^2). \end{aligned} \quad (4.63)$$

To carry out the integration dE_k we rewrite the remaining delta-function as

$$\delta \left(s_{ab} - s_{aj} - s_{jb} + \frac{x_b - x_a}{x_a} s_{ak} - 2 x_b \sqrt{s} E_k - m_R^2 \right). \quad (4.64)$$

With the result of the integration, $(2 x_B \sqrt{s})^{-1}$, the phase space reduces to

$$\begin{aligned} &\int \frac{dx_a}{x_a} d\Phi_3(p_a, p_b \rightarrow p_j, p_k, p_R) \\ &= \int \frac{dx_A}{x_A} \frac{ds_{AK}}{(2\pi)^2 s_{AB}} \frac{d\phi_k}{16\pi^2} \frac{s_{AK}}{(s_{AK} + s_{jk})^2} ds_{aj} ds_{jk} \frac{d\phi_j}{2\pi} \\ &= \int \frac{dx_A}{x_A} d\Phi_2(p_A, p_B \rightarrow p_K, p_R) d\Phi_{\text{ant}}^{\text{IF}}. \end{aligned} \quad (4.65)$$

To verify this result we calculate the two-particle phase space

$$\begin{aligned} &d\Phi_2(p_A, p_B \rightarrow p_K, p_R) \\ &= \frac{1}{(2\pi)^2} \frac{d^3 p_K}{2E_K} d^4 p_R \theta(E_R) \delta(p_R^2 - m_R^2) \delta^{(4)}(p_A + p_B - p_R - p_K) \\ &= \frac{1}{2(2\pi)^2 x_A \sqrt{s}} ds_{AK} d\phi_K dE_K \delta((p_A + p_B - p_K)^2 - m_R^2). \end{aligned} \quad (4.66)$$

A factor of $(x_A \sqrt{s} E_K)^{-1}$ arises due to the variable transformation from $\cos \theta_K$ to s_{AK} . The remaining delta-function can be rewritten as

$$\delta \left(s_{AB} + \frac{x_B - x_A}{x_A} s_{AK} - 2 x_B \sqrt{s} E_K - m_R^2 \right). \quad (4.67)$$

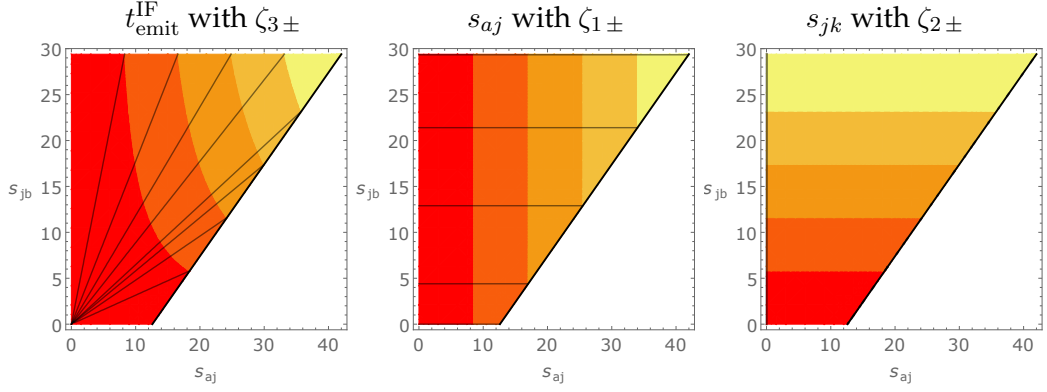


Figure 4.2: Contours of constant values of the evolution variable are shown in color with the choices $s_{AK} = 12.6 \text{ TeV}^2$ and $x_A = 0.3$. The grey lines represent the corresponding ζ -integration boundaries. The phase space limit $s_{aj} \leq s_{AK} + s_{jk}$ is visualized by the thick black line.

With the result of the dE_K integration, $(2x_B\sqrt{s})^{-1}$, the two-particle phase space reduces to

$$d\Phi_2(p_A, p_B \rightarrow p_K, p_R) = \frac{ds_{AK} d\phi_K}{(2\pi)^2 s_{AB}}. \quad (4.68)$$

Comparing eqs. (4.65) and eq. (4.68) gives the result for the initial-final antenna phase space for local recoils

$$d\Phi_{\text{ant}}^{\text{IF}} = \frac{1}{16\pi^2} \frac{s_{AK}}{(s_{AK} + s_{jk})^2} ds_{aj} ds_{jk} \frac{d\phi_j}{2\pi}. \quad (4.69)$$

4.4.2 Evolution Variables and ζ Definitions

Branchings are evolved in the following variables,

$$t^{\text{IF}} = \begin{cases} t_{\text{emit}}^{\text{IF}} = \frac{s_{aj}s_{jk}}{s_{AK} + s_{jk}} & \text{for gluon emission} \\ t_{\text{conv}}^{\text{IF}} = \begin{cases} s_{aj} & \text{for } a \text{ converting to/from a gluon} \\ t_{\text{conv}}^{\text{IF}} = s_{jk} & \text{for final state gluon splitting.} \end{cases} \end{cases} \quad (4.70)$$

The upper phase-space limits are $t_{\text{IF}}^{\text{emit}} \leq s_{AK}(1 - x_A)/x_A$, $s_{aj} \leq s_{AK}/x_A$, and $s_{jk} \leq s_{AK}(1 - x_A)/x_A$.

Our choices for the functional form of the ζ variable are

$$\zeta_1 = \frac{s_{jk} + s_{AK}}{s_{AK}} = \frac{x_a}{x_A}, \quad \zeta_2 = \frac{s_{aj}}{s_{AK} + s_{jk}}, \quad \text{and} \quad \zeta_3 = \frac{s_{aj}}{s_{jk}}. \quad (4.71)$$

For a given value of the evolution variable, $t_{\text{emit}}^{\text{IF}}$, s_{aj} , or s_{jk} respectively, the ζ -integration boundaries are

$$\zeta_{1-}(t_{\text{emit}}^{\text{IF}}) = \frac{t_{\text{emit}}^{\text{IF}} + s_{AK}}{s_{AK}} \quad \zeta_{1+}(t_{\text{emit}}^{\text{IF}}) = \frac{1}{x_A}, \quad (4.72)$$

$$\zeta_{2-}(t_{\text{emit}}^{\text{IF}}) = \frac{t_{\text{emit}}^{\text{IF}} x_A}{s_{AK}(1-x_A)} \quad \zeta_{2+}(t_{\text{emit}}^{\text{IF}}) = 1, \quad (4.73)$$

$$\zeta_{3-}(t_{\text{emit}}^{\text{IF}}) = \frac{t_{\text{emit}}^{\text{IF}} x_A}{s_{AK}(1-x_A)^2} \quad \zeta_{3+}(t_{\text{emit}}^{\text{IF}}) = \frac{s_{AK} + t_{\text{emit}}^{\text{IF}}}{t_{\text{emit}}^{\text{IF}}}, \quad (4.74)$$

$$\zeta_{1-}(s_{aj}) = \max\left(1, \frac{s_{aj}}{s_{AK}}\right) \quad \zeta_{1+}(s_{aj}) = \frac{1}{x_A}, \quad (4.75)$$

$$\zeta_{2-}(s_{jk}) = 0 \quad \zeta_{2+}(s_{jk}) = 1. \quad (4.76)$$

Plots of contours of constant values of the different evolution variables, together with the corresponding ζ limits are shown in fig. 4.2.

4.4.3 Jacobians

The Jacobian factors for the transformation from the phase-space variables (s_{aj}, s_{jk}) to the shower variables (t^{IF}, ζ) are

$$|J(t_{\text{emit}}^{\text{IF}}, \zeta_1)| = (s_{AK} + s_{jk})s_{AK}/s_{jk}, \quad (4.77)$$

$$|J(t_{\text{emit}}^{\text{IF}}, \zeta_2)| = (s_{AK} + s_{jk})^2/s_{aj}, \quad (4.78)$$

$$|J(t_{\text{emit}}^{\text{IF}}, \zeta_3)| = (s_{AK} + s_{jk})^2 (\zeta_3(2s_{AK} + s_{jk}))^{-1}, \quad (4.79)$$

$$|J(s_{aj}, \zeta_1)| = s_{AK}, \quad (4.80)$$

$$|J(s_{jk}, \zeta_2)| = s_{AK} + s_{jk}. \quad (4.81)$$

4.4.4 Trial Antenna Functions

To overestimate the physical antenna functions we make use of $s_{AK} + s_{jk} = s_{ak} + s_{aj}$ and replacing for instance s_{ak} with $s_{ak} + s_{aj} = s_{AK} + s_{jk} > s_{ak}$. The following list presents the physical antenna functions \bar{a}^{IF} for initial-final configurations together with the overestimate \hat{a}^{IF} ,

$$\bar{a}_{\text{soft}}^{\text{IF}} = 2 \frac{s_{ak}}{s_{aj}s_{jk}} \Rightarrow \hat{a}_{\text{soft}}^{\text{IF}} = \frac{(2s_{AK} + s_{jk})(s_{AK} + s_{jk})}{s_{aj}s_{jk}s_{AK}}, \quad (4.82)$$

$$\bar{a}_{qg}^{\text{IF}} - \bar{a}_{\text{soft}}^{\text{IF}} = \frac{1}{s_{AK}} \frac{s_{jk}}{s_{aj}} \Rightarrow \hat{a}_{qg}^{\text{IF}} = \frac{1}{s_{AK}} \frac{s_{jk} + s_{AK}}{s_{aj}}, \quad (4.83)$$

$$\bar{a}_{xqg}^{\text{IF}} - \bar{a}_{\text{soft}}^{\text{IF}} = \frac{1}{s_{AK}} \frac{s_{aj}}{s_{jk}} \Rightarrow \hat{a}_{xqg}^{\text{IF}} = \frac{1}{s_{AK}} \frac{s_{jk} + s_{AK}}{s_{jk}}, \quad (4.84)$$

$$\bar{a}_{gxg1}^{\text{IF}} - \bar{a}_{\text{soft}}^{\text{IF}} = \frac{2}{s_{AK}} \frac{s_{jk}}{s_{aj}} \frac{s_{ak}}{s_{AK}} \Rightarrow \hat{a}_{gxg1}^{\text{IF}} = 2 \frac{(s_{AK} + s_{jk})^2}{s_{AK}^2 s_{aj}}, \quad (4.85)$$

$$\bar{a}_{gxg2}^{\text{IF}} - \bar{a}_{\text{soft}}^{\text{IF}} = \frac{2}{s_{aj}(s_{AK} + s_{jk})} \Rightarrow \hat{a}_{gxg2}^{\text{IF}} = \frac{2}{s_{aj}}, \quad (4.86)$$

$$\bar{a}_{xgg}^{\text{IF}} - \bar{a}_{\text{soft}}^{\text{IF}} = \frac{1}{s_{AK}} \frac{s_{aj}}{s_{jk}} \frac{s_{ak}}{s_{AK}} \Rightarrow \hat{a}_{xgg}^{\text{IF}} = \frac{1}{s_{AK}} \frac{s_{aj}}{s_{jk}} \frac{s_{AK} + s_{jk}}{s_{AK}}, \quad (4.87)$$

$$\bar{a}_{qxq}^{\text{IF}} = \frac{1}{2 s_{aj}} \frac{s_{ak}^2 + s_{jk}^2}{s_{AK}^2} \Rightarrow \hat{a}_{qxq}^{\text{IF}} = \frac{1}{s_{aj}} \frac{(s_{AK} + s_{jk})^2}{s_{AK}^2}, \quad (4.88)$$

$$\bar{a}_{gx\bar{q}}^{\text{IF}} = \frac{1}{s_{AK}} \frac{s_{ak}}{s_{aj}} - \frac{2}{s_{AK}} \frac{s_{jk}}{s_{aj}} \frac{s_{AK} - s_{aj}}{s_{AK} + s_{jk}} \Rightarrow \hat{a}_{gx\bar{q}}^{\text{IF}} = \frac{2}{s_{AK}} \frac{s_{AK} + s_{jk}}{s_{aj}}, \quad (4.89)$$

$$\bar{a}_{xq\bar{q}}^{\text{IF}} = \frac{1}{2 s_{jk}} \frac{s_{ak}^2 + s_{aj}^2}{s_{AK}^2} \Rightarrow \hat{a}_{xq\bar{q}}^{\text{IF}} = \frac{1}{2 s_{jk}} \frac{(s_{AK} + s_{jk})^2}{s_{AK}^2}. \quad (4.90)$$

As a first step we find an overestimate for the soft eikonal term, present in all gluon emission antenna functions. In a second step we analyze the collinear terms individually, eqs. (4.83) to eq. (4.87). Finally we find overestimates for the antenna functions that involve flavour changes.

4.4.5 Evolution Integrals

As for initial-initial antennae, the integration over $d\phi$ will be dropped in this section. Using the Jacobian factors in eqs. (4.77) to (4.81) and the trial antenna functions in eqs. (4.82) to (4.90), the trial integration kernels $d\hat{\mathcal{A}}$ can be written in terms of t and ζ ,

$$d\hat{\mathcal{A}}_{\text{soft}}^{\text{IF}} = \frac{\alpha_s \mathcal{C}}{4\pi} \hat{R}_{\text{pdf}} \frac{dt_{\text{emit}}^{\text{IF}}}{t_{\text{emit}}^{\text{IF}}} \frac{d\zeta_3}{\zeta_3}, \quad (4.91)$$

$$d\hat{\mathcal{A}}_{qxg}^{\text{IF}} = \frac{\alpha_s \mathcal{C}}{4\pi} \left(\frac{x_a x_b}{x_A x_B} \right)^\beta \hat{R}_{\text{pdf}} \frac{dt_{\text{emit}}^{\text{IF}}}{t_{\text{emit}}^{\text{IF}}} \frac{d\zeta_1}{\zeta_1^{1+\beta}}, \quad (4.92)$$

$$d\hat{\mathcal{A}}_{xqg}^{\text{IF}} = \frac{\alpha_s \mathcal{C}}{4\pi} \hat{R}_{\text{pdf}} \frac{dt_{\text{emit}}^{\text{IF}}}{t_{\text{emit}}^{\text{IF}}} d\zeta_2, \quad (4.93)$$

$$d\hat{\mathcal{A}}_{gxg1}^{\text{IF}} = \frac{\alpha_s \mathcal{C}}{2\pi} \left(\frac{x_a x_b}{x_A x_B} \right)^\beta \hat{R}_{\text{pdf}} \frac{dt_{\text{emit}}^{\text{IF}}}{t_{\text{emit}}^{\text{IF}}} \frac{d\zeta_1}{\zeta_1^\beta}, \quad (4.94)$$

$$d\hat{\mathcal{A}}_{gxg1}^{\text{IF}} = \frac{\alpha_s \mathcal{C}}{2\pi} \left(\frac{x_a x_b}{x_A x_B} \right)^\beta \hat{R}_{\text{pdf}} \frac{dt_{\text{emit}}^{\text{IF}}}{t_{\text{emit}}^{\text{IF}}} \frac{d\zeta_1}{\zeta_1^\beta}, \quad (4.95)$$

$$d\hat{\mathcal{A}}_{gxg2}^{\text{IF}} = \frac{\alpha_s \mathcal{C}}{2\pi} \left(\frac{x_a x_b}{x_A x_B} \right)^\beta \hat{R}_{\text{pdf}} \frac{dt_{\text{emit}}^{\text{IF}}}{t_{\text{emit}}^{\text{IF}}} \frac{d\zeta_1}{\zeta_1^{2+\beta}}, \quad (4.96)$$

$$d\hat{\mathcal{A}}_{xgg}^{\text{IF}} = \frac{\alpha_s \mathcal{C}}{4\pi} \frac{x_a x_b}{x_A x_B} \hat{R}_{\text{pdf}} \frac{dt_{\text{emit}}^{\text{IF}}}{t_{\text{emit}}^{\text{IF}}} \zeta_2 d\zeta_2, \quad (4.97)$$

$$d\hat{\mathcal{A}}_{gx\bar{q}}^{\text{IF}} = \frac{\alpha_s \mathcal{C}}{2\pi} \left(\frac{x_a x_b}{x_A x_B} \right)^\alpha \hat{R}_{\text{pdf}} \frac{dt_{\text{conv}}^{\text{IF}}}{t_{\text{conv}}^{\text{IF}}} \frac{d\zeta_1}{\zeta_1^{1+\beta}}, \quad (4.98)$$

$$d\hat{\mathcal{A}}_{qxq}^{\text{IF}} = \frac{\alpha_s \mathcal{C}}{4\pi} \left(\frac{x_a x_b}{x_A x_B} \right)^\alpha \hat{R}_{\text{pdf}} \frac{dt_{\text{conv}}^{\text{IF}}}{t_{\text{conv}}^{\text{IF}}} \frac{d\zeta_1}{\zeta_1^\beta}, \quad (4.99)$$

$$d\hat{\mathcal{A}}_{xq\bar{q}}^{\text{IF}} = \frac{\alpha_s \mathcal{C}}{8\pi} \frac{x_a x_b}{x_A x_B} \hat{R}_{\text{pdf}} \frac{dt_{\text{conv}}^{\text{IF}}}{t_{\text{conv}}^{\text{IF}}} d\zeta_2. \quad (4.100)$$

For some processes the general factor β helps to control the overestimate of the PDF ratio, as discussed in sec. 4.2.

4.4.6 ζ Integrals and Trial ζ

The general form of the ζ integrals appearing in the trial evolution kernels in eqs. (4.91) to (4.100) is

$$I_\zeta = \int_{\zeta_a}^{\zeta_b} \frac{d\zeta}{\zeta^\kappa} = \begin{cases} (\zeta_b^{1-\kappa} - \zeta_a^{1-\kappa}) / (1-\kappa) & \text{for } \kappa \neq 1 \\ \ln(\zeta_b/\zeta_a) & \text{for } \kappa = 1 \end{cases}. \quad (4.101)$$

Here, $\kappa = \beta$ for eqs. (4.95) and (4.99), $\kappa = 1 + \beta$ for eqs. (4.92) and (4.98), $\kappa = 2 + \beta$ for eq. (4.96), $\kappa = 1$ for eq. (4.91), $\kappa = 0$ for eq. (4.93), and $\kappa = -1$ for eq. (4.91). A trial value for the ζ variable is generated according to

$$\zeta = \begin{cases} (\mathcal{R}_\zeta(\zeta_{\min}^{1-\kappa} - \zeta_{\max}^{1-\kappa}) + \zeta_{\max}^{1-\kappa})^{\frac{1}{1-\kappa}} & \text{for } \kappa \neq 1 \\ \zeta_{\max} (\zeta_{\min}/\zeta_{\max})^{\mathcal{R}_\zeta} & \text{for } \kappa = 1 \end{cases}. \quad (4.102)$$

4.4.7 Generation of Trial Evolution Scale

The new scale is generated as in the case of initial-initial antennae, see sec. 4.3.7.

4.4.8 Inverse Transforms

After a set of shower variables has been generated, the (t^{IF}, ζ) choices must be inverted to reobtain the branching invariants (s_{aj}, s_{jk}) which are used to construct the kinematics of the trial branching. These inversions are the following:

$$t_{\text{emit}}^{\text{IF}} \text{ with } \zeta_1: \quad s_{aj} = \frac{t_{\text{emit}}^{\text{IF}} \zeta_1}{\zeta_1 - 1} \quad s_{jk} = s_{AK}(\zeta_1 - 1) \quad (4.103)$$

$$t_{\text{emit}}^{\text{IF}} \text{ with } \zeta_2: \quad s_{aj} = s_{AK} \zeta_2 + t_{\text{emit}}^{\text{IF}} \quad s_{jk} = \frac{t_{\text{emit}}^{\text{IF}}}{\zeta_2} \quad (4.104)$$

$$t_{\text{emit}}^{\text{IF}} \text{ with } \zeta_3: \quad s_{aj} = t_{\text{emit}}^{\text{IF}} \left(\frac{1}{2} + \sqrt{\frac{1}{2} + \frac{\zeta_3 s_{AK}}{t_{\text{emit}}^{\text{IF}}}} \right) \quad s_{jk} = \frac{s_{aj}}{\zeta_3} \quad (4.105)$$

$$s_{aj} \text{ with } \zeta_1: \quad s_{aj} = t_{\text{conv}}^{\text{IF}} \quad s_{jk} = (\zeta_1 - 1)s_{AK} \quad (4.106)$$

$$s_{jk} \text{ with } \zeta_2: \quad s_{aj} = \zeta_2 (s_{AK} + t_{\text{conv}}^{\text{IF}}) \quad s_{jk} = t_{\text{conv}}^{\text{IF}} \quad (4.107)$$

Correcting Ordered Showers

The GKS MEC algorithm for combining the parton-shower approximation with LO matrix elements with different multiplicities has been discussed in chap. 4. However, this procedure requires the shower to populate phase-space regions that are beyond the reach of traditional ordered evolution. In this context, a consequence of the shower unitarity is the loss of soft, low-energy radiation due to increasing the emission rate in the hard part of phase space. In other words, if additional radiation is allowed in the unordered parts of the evolution, it is taken away from the ordered phase space. In addition, the smooth ordering restricts the branching range of ordered partons for higher multiplicities, as these partons restart the evolution at a scale that is, by definition, smaller or equal to the scale of the last branching. Due to the evolution of initial-state partons in unordered regions, no-emission probabilities arise that do not correspond to conventional terms of the PDF evolution in sec. 3.3.

Unordered branchings also potentially violate the assumption under which factorization has been proven. As discussed in sec. 2.4, factorizing the calculation of the hard process into the short-distance physics described by the partonic cross section and the long-distance physics described by universal PDFs, relies on approximations. Factorization uses a scale Q that is based on the kinematics of the hard scattering process, or energy flow through the corresponding Feynman diagram. For instance for the Drell-Yan process the “natural” scale is the mass of the lepton pair, $Q = m_{ll}$. The factorization theorem assumes that the factorization scale $\mu_F \sim Q$ correctly characterizes the process and that radiation with scales $\leq Q$ is resummed properly, see e.g. [140–143] and references therein. “Power showers” allow the production of partons with scales larger than the factorization scale of the underlying Born process, $t > \mu_F$, in the parton shower. While this concept might be interesting from a phenomenological point of view, if it constitutes the only option to populate the hard phase-space regions, it is in conflict with the factorization assumption described before and the additional parton is not well described by the collinear PDFs. In a similar way, unordered branchings with $t_{n+1} > t_n$ are in disagreement with the factorization condition.

Based on the arguments given in the preceding paragraphs, we introduce a new method to correct the ordered evolution of the parton shower and combine it with unordered phase-space points, while avoiding the smooth ordering of sec. 4.1 for

subsequent unordered emissions as well as the power-shower concept and the method of sec. 4.1 for the first emission of the parton shower. This is achieved by extending the MEC formalism of chap. 4 to purely ordered evolution. To fill the full phase space for the corrected orders, a prescription for adding events beyond the reach of the parton shower is required. An important feature in these events, probably the most important one, is the choice of factorization and renormalization scale, as has been shown e.g. in [144, 145]. In the publication in sec. 5.1 we develop a MEC formalism for ordered evolution, together with a new scale-setting scheme for unordered events which is based on ME as well as parton-shower information.

The algorithm discussed in the publication borrows from the CKKW-L [75, 76] method for merging ME calculations of different parton multiplicities with the parton shower. We implemented the necessary functionality in VINCIA by using the existing machinery of PYTHIA 8 and adjusting it to the QCD antenna picture of VINCIA. As a result, the CKKW-L approach can not only be applied in the context of sec. 5.1, but also standalone in the PYTHIA 8 + VINCIA framework. This method is therefore discussed in sec. 5.2 in the context of antennae.

5.1 Published Material

Combining states without scale hierarchies with ordered parton showers

Nadine Fischer and Stefan Prestel

Published in The European Physics Journal C 77 no. 9 (2017) 601

DOI: 10.1140/epjc/s10052-017-5160-7

e-Print: [arXiv:1706.06218](https://arxiv.org/abs/1706.06218) [hep-ph]

With kind permission of The European Physical Journal (EPJ).

Begins overleaf.

Combining states without scale hierarchies with ordered parton showers

Nadine Fischer^{1,a}, Stefan Prestel²

¹ School of Physics and Astronomy, Monash University, Clayton, VIC 3800, Australia

² Fermi National Accelerator Laboratory, Batavia, IL 60510-0500, USA

Received: 26 June 2017 / Accepted: 23 August 2017

© The Author(s) 2017. This article is an open access publication

Abstract We present a parameter-free scheme to combine fixed-order multi-jet results with parton-shower evolution. The scheme produces jet cross sections with leading-order accuracy in the complete phase space of multiple emissions, resumming large logarithms when appropriate, while not arbitrarily enforcing ordering on momentum configurations beyond the reach of the parton-shower evolution equation. This requires the development of a matrix-element correction scheme for complex phase-spaces including ordering conditions as well as a systematic scale-setting procedure for unordered phase-space points. The resulting algorithm does not require a merging-scale parameter. We implement the new method in the VINCIA framework and compare to LHC data.

1 Introduction

High-energy physics in the era of the Large Hadron Collider relies on accurate calculations of Standard-Model scattering signatures—both to determine backgrounds when directly searching for new physics and to allow for setting indirect bounds by comparing measurements to precision calculations. Since measurements at the LHC are typically sensitive to the formation and evolution of jets, much attention has been devoted to calculating QCD corrections. This has led to exquisite dedicated high-precision calculations, and to the development of general schemes to overcome the limited applicability of individual fixed-order QCD calculations by combining multiple calculations into a single consistent result. To this end, modern General Purpose Event Generators [1–4] include a variety of complex matching [5–16] and merging [17–35] schemes.

A unified Standard-Model prediction that is applicable for precision measurements and new-physics searches alike

must naturally include particle configurations that probe very different aspects of the calculation. The optimal perturbative description of very different particle (and momentum) configurations can consequently vary significantly within one measurement, so that care must be taken to avoid applying specialized arguments outside of their region of validity. Otherwise, the accuracy of the calculation is in jeopardy and its uncertainty might be underestimated. For example, applying QCD reasoning to events without large hierarchies in the hardness of jets can lead to problematic effects [36].

Standard-model calculations at the LHC can somewhat artificially be categorized as focussing on momentum configurations with or without large scale (hardness) hierarchies between jets. Fixed-order QCD calculations are often appropriate for the latter, while the former require a resummation of large perturbative enhancements by means of evolution equations. Both approaches have complementary strengths and should be combined for a state-of-the-art calculation. It is crucial to avoid bias when constructing a single calculation that describes very different limits.

In this article, we design a new algorithm to combine multiple fixed-order calculations for different parton multiplicities with each other and with (parton-shower) resummation of large logarithmic enhancements. The aim of this combined calculation is to simultaneously describe up to n hard, well-separated partons with fixed-order matrix elements while retaining the jet evolution given by the parton shower. We enforce strict requirements on the new scheme to improve on previous ideas:

1. The introduction of new parameters into the calculation is avoided. This is especially important when the correlation with existing parameters is not obvious.
2. The method should provide a uniform accuracy over the complete phase space for one particle multiplicity. For now, this means that the rate of n jets should be given

^a e-mail: nadine.fischer@monash.edu

with leading-order accuracy in QCD, irrespectively of the hardness of jets.

3. The method should be largely agnostic to parton-shower-inspired arguments when configurations without large scale hierarchies are discussed.

The resulting method borrows concepts from the CKKW-L method of merging matrix elements and parton showers [26–28], as well as from matrix-element correction schemes [37,38]. We provide a new solution to the treatment of phase-space regions beyond the reach of traditional shower evolution. Furthermore, we improve upon the structure of the combined calculation in the parton-shower region of soft and/or collinear emissions. Our new method consists of two main developments: the introduction (and implementation) of matrix-element corrections for ordered parton-shower evolution, and the definition of a general scale-setting prescription based on matrix elements for contributions without apparent scale hierarchies. The benefit of using matrix-element corrections for shower-like splitting sequences is that unitarity of fixed-order multi-jet cross sections is automatically guaranteed in these phase-space regions. This means that the inclusive rates for n jets will be correctly described with fixed-order accuracy, without the need for explicit subtractions of negative weight, even if the rate for $n + 1$ jets is also corrected with matrix elements. We will describe how the new method allows to achieve leading-order accuracy in QCD for multi-parton configurations. This establishes a baseline for future developments beyond leading-order QCD.

The new scheme relies on applying leading-order matrix-element corrections in phase-space regions that are accessible by a sequence of splittings ordered in a parton-shower evolution variable, supplemented with fixed-order results for configurations that cannot be reached by any such sequence. We will use the misnomer “shower configurations” for such states, and call states which cannot be reached by an ordered sequence of shower emissions “non-shower states”.

A very brief introduction to the parton-shower formalism and the notation is established in Sect. 2. The new method to iteratively correct parton showers with matrix elements is described in detail in Sect. 3. The combination of this scheme of matrix-element corrections for ordered parton-shower evolution with non-shower states is discussed in Sect. 4. An executive summary of the algorithm is given in Sect. 5, followed by a discussion of the impact of combining parton-shower-like and non-shower phase-space regions at parton level. Then results and data comparisons are presented in Sect. 6 before we summarize and give an outlook in Sect. 7. Additional details about the smoothly ordered showers and “GKS” matrix-element corrections previously used in VIN-CIA are collected in Appendix A, while a thorough validation

of new matrix-element corrections for ordered parton-shower evolution is given in Appendix B.

2 Parton showers and matrix-element corrections

To set the scene and establish notation, let us briefly review some parton-shower basics. We start by defining the effect of parton-shower evolution [39,40] on an arbitrary observable O (in the notation of [41]),

$$\mathcal{F}_{\vec{a}}(\Phi_n, t, t'; O) = \mathcal{F}_{\vec{a}}(\Phi_n, t, t') O(\Phi_n) + \int_t^{t'} \frac{d\bar{t}}{\bar{t}} \frac{d\mathcal{F}_{\vec{a}}(\Phi_n, \bar{t}, t')}{d \ln \bar{t}} \mathcal{F}_{\vec{a}'}(\Phi'_{n+1}, t, \bar{t}; O), \tag{1}$$

where $t \equiv t(\Phi_{n+1}/\Phi_n)$ is the shower evolution variable, and the shower generating functional \mathcal{F} depends on the list of parton flavors \vec{a} , and the corresponding n -particle momentum configuration Φ_n . Though not explicitly stated, any n -particle state contains an arbitrarily complicated Born state, $\Phi_n \equiv \Phi_{B+n}$. The first term in Eq. (1) encodes the contribution from no resolvable shower emissions, while the second piece includes one or more emissions. The parton flavors \vec{a}' of the $(n + 1)$ -particle momentum configuration Φ_{n+1} include the resolved emission and the partons \vec{a} , with momenta changed according to the recoil prescription of the parton shower and flavor changes where applicable. The generating functional obeys the evolution equation

$$\frac{d \ln \mathcal{F}_{\vec{a}}(\Phi_n, t, \mu^2)}{dt} = \sum_{i \in \text{IS}} \sum_{b=q,g} \int_{x_i}^{1-\varepsilon} \frac{dz}{z} \frac{\alpha_s(t)}{2\pi} P_{ba_i} \frac{f_b(x_i/z, t)}{f_{a_i}(x_i, t)} + \sum_{j \in \text{FS}} \sum_{b=q,g} \int_{\varepsilon}^{1-\varepsilon} dz \frac{\alpha_s(t)}{2\pi} P_{a_j b}, \tag{2}$$

where $z \equiv z(\Phi_{n+1}/\Phi_n)$ is an energy-sharing variable and x the momentum fraction of the incoming parton in Φ_n . The first term in Eq. (2) corresponds to evolution by initial-state radiation, while the second term represents final-state radiation. Backward evolution [39] for initial-state radiation introduces a ratio of parton distribution functions (PDFs) f in the first term. The quality of the shower real-radiation pattern is governed by the unregularized, dimensionful splitting kernels $P_{ij} \equiv P_{ij}(\Phi_{n+1}/\Phi_n)$.¹ For brevity, we will suppress the indices of the splitting functions. The shower will produce an accurate real-emission pattern if the sum of all products of

¹ We define $P_{ij}(\Phi_{n+1}/\Phi_n)$ as dimensionful to follow the convention used in the antenna literature [42,43]. Thus, P_{ij} corresponds to \hat{P}_{ij}/t in the notation of [41], leading to a marginally different notation compared to the latter.

splitting probabilities and transition probabilities $|\mathcal{M}(\Phi_n)|^2$ is a good approximation of the full real-emission probability $|\mathcal{M}(\Phi_{n+1})|^2$. For a transition from an n -particle to an $(n+1)$ -particle state, this can be achieved by the (symbolic) replacement

$$\begin{aligned} & \left[\sum_{\Phi_n} P(\Phi_{n+1}/\Phi_n) |\mathcal{M}(\Phi_n)|^2 \right] \\ & \rightarrow \left[\sum_{\Phi_n} P(\Phi_{n+1}/\Phi_n) |\mathcal{M}(\Phi_n)|^2 \right] \\ & \quad \times \frac{|\mathcal{M}(\Phi_{n+1})|^2}{\left(\sum_{\Phi'_n} P(\Phi_{n+1}/\Phi'_n) |\mathcal{M}(\Phi'_n)|^2 \right)} \\ & = \sum_{\Phi_n} \left[P(\Phi_{n+1}/\Phi_n) |\mathcal{M}(\Phi_n)|^2 \mathcal{R}(\Phi_{n+1}) \right]. \end{aligned} \quad (3)$$

Such a process- and multiplicity-dependent redefinition of the splitting kernel is called matrix-element correction (MEC). It is worth noting that this replacement changes both the shower no-emission probability and the real-emission pattern. The real-emission pattern is corrected to a target fixed-order accuracy. However, the accuracy of the parton-shower resummation of virtual corrections into Sudakov factors is not improved.

The impact of ME corrections is largest for hard, well-separated jets, as splitting kernels do not approximate the full fixed-order matrix element well for configurations with hard, well-separated jets. Thus, the most significant improvement of ME corrections can be obtained when correcting the n hardest splittings in the shower cascade. In practise, this means that hardness-ordered parton showers allow for simpler MEC schemes [44–46], which in particular do not require knowledge of high-multiplicity matrix elements as a function of evolution variables.² Instead, it is sufficient that the parton shower generates complete, physical intermediate momenta Φ_n that can be used to evaluate $|\mathcal{M}(\Phi_n)|^2$ numerically. Thus, we will limit our discussion to hardness-ordered shower programs. This will allow for a level of process-independence, and make the *iteration* of ME corrections possible.

The key technical difficulty for a consistent application of ME corrections is the construction of the sum over parton-shower paths in the denominator of the correction factor $\mathcal{R}(\Phi_{n+1})$. Since parton showers are formulated as Markov

processes, neither the weight nor the existence of each term in the sum is known a priori when the splitting governed by $P(\Phi_{n+1}/\Phi_n)$ is generated, and all terms have to be reconstructed explicitly.

3 Matrix-element corrections for ordered parton showers

The formalism of ME corrections for ordered parton showers (MOPS) is close in spirit to the idea of the iterative MEC approach of [37,38].³ These previous ideas rely on a history-independent parton shower that is able to fill the complete available phase space. This necessitates abandoning parton-shower ordering, i.e. the property that ensures the resummation of large logarithms in ratios of evolution scales. Sensible resummation properties then rely on the introduction of auxiliary functions. Furthermore, configurations with hard well-separated jets might contain poorly understood higher-order corrections. It is thus sensible to limit ME corrections for the parton shower to phase-space regions reachable by an ordered sequence of branchings. This means that we need to rederive appropriate MEC factors $\mathcal{R}(\Phi_n)$ that correctly encode the presence of complicated phase-space constraints due to ordering—making the resulting method substantially different from previous attempts.

To not overcomplicate the derivation of the MOPS formalism, we drop all coupling- and PDF factors in this section. These pieces are evaluated exactly as in an uncorrected parton shower (the probability of a splitting at evolution scale t includes a factor $\alpha_s(t)/2\pi$, splittings involving initial legs induce ratios of PDFs $f(\frac{x}{z}, t)/f(x, t)$, cf. Eq. (2)), and do not enter in the MEC factors. Similarly, Sudakov factors are not explicitly written out when demonstrating the MOPS method. The MOPS procedure is applied during the Sudakov veto-algorithm as a redefinition of the splitting kernels, meaning that both the (real) emission probability and the no-emission probabilities are ME corrected. This ensures the unitarity of the method, i.e. that corrections to higher parton multiplicities vanish in observables that are only sensitive to a lower multiplicity.

Consider an arbitrary Born process with factorization scale $t_{\text{fac}} \equiv t(\Phi_0)$ as starting point of the parton shower. The weight of the first branching is

$$P(\Phi_1/\Phi_0) \Theta(t(\Phi_0) - t(\Phi_1/\Phi_0)) |\mathcal{M}(\Phi_0)|^2 d\Phi_1, \quad (4)$$

where the shower is restricted to scales below the factorization scale. For processes that require regularizing cuts at Born level, the matrix element $|\mathcal{M}(\Phi_0)|^2$ can be suitably redefined to include the necessary Θ -functions. To correct the weight

² A scheme to correct the hardest emission in angular-ordered showers has been discussed in [47]. This scheme requires to apply the same correction repeatedly, to guarantee that the single hardest emission is corrected to leading-order accuracy. Although promising from the resummation standpoint, it is, however, not obvious how this scheme could be used to correct the n hardest emissions.

³ A short review of the GKS approach is given in Appendix A.

of the phase-space point Φ_1 to the full fixed-order matrix element, all possible emissions from “underlying” Born configurations Φ'_0 that could have produced the phase-space point Φ_1 that we want to correct have to be taken into account. A suitable multiplicative correction factor is thus

$$\mathcal{R}(\Phi_1) = \frac{|\mathcal{M}(\Phi_1)|^2}{\sum_{\Phi'_0} P(\Phi_1/\Phi'_0) \Theta(t(\Phi'_0) - t(\Phi_1/\Phi'_0)) |\mathcal{M}(\Phi'_0)|^2}. \tag{5}$$

Applying this correction to each individual splitting and summing over all shower contributions cancels the denominator of Eq. (5) and gives

$$\mathcal{R}(\Phi_1) \sum_{\Phi_0} P(\Phi_1/\Phi_0) \Theta(t(\Phi_0) - t(\Phi_1/\Phi_0)) |\mathcal{M}(\Phi_0)|^2 = |\mathcal{M}(\Phi_1)|^2. \tag{6}$$

The calculation of the correction factor for the weight of a second branching becomes more cumbersome,

$$\mathcal{R}(\Phi_2) = \frac{|\mathcal{M}(\Phi_2)|^2}{\sum_{\Phi'_1} P(\Phi_2/\Phi'_1) \mathcal{R}(\Phi'_1) \sum_{\Phi'_0} \Theta(t(\Phi'_1/\Phi'_0) - t(\Phi_2/\Phi'_1)) P(\Phi'_1/\Phi'_0) \Theta(t(\Phi'_0) - t(\Phi'_1/\Phi'_0)) |\mathcal{M}(\Phi'_0)|^2}. \tag{7}$$

Here, the denominator sums over all possible ways how the shower can populate the phase-space point Φ_2 , taking into account the allowed (ordered) paths through the Θ -functions with the ME corrected parton-shower weights of the intermediate +1-particle phase-space points. Consequently, $\mathcal{R}(\Phi_2)$ includes the correction factors of the previous order, $\mathcal{R}(\Phi'_1)$.

It is useful to illustrate how this relatively complicated recursive definition is obtained with an example. Consider the case of a +2-particle state shown in Fig. 1. The +2-particle state on top of the pyramid can be reached from the base of the pyramid by several splitting sequences or “paths”. The paths are not necessarily physical but rather serve the purpose of illustration. In Fig. 1a all paths directly contribute to the +2-particle state, as each path from the base to the top follows a decreasing (i.e. ordered) sequence of branchings scales. With the shorthands introduced in the caption of Fig. 1 the correction factors for the +1-particle states are

$$\mathcal{R}_1^1 = \frac{\mathcal{M}_1^1}{P_1^1 \mathcal{M}_0^1 + P_1^2 \mathcal{M}_0^2} \quad \text{and} \quad \mathcal{R}_1^2 = \frac{\mathcal{M}_1^2}{P_1^3 \mathcal{M}_0^3 + P_1^4 \mathcal{M}_0^4}. \tag{8}$$

Both factors contribute to the correction to the +2-particle state,

$$\mathcal{R}_2 = \frac{\mathcal{M}_2}{P_2^1 \mathcal{R}_1^1 (P_1^1 \mathcal{M}_0^1 + P_1^2 \mathcal{M}_0^2) + P_2^2 \mathcal{R}_1^2 (P_1^3 \mathcal{M}_0^3 + P_1^4 \mathcal{M}_0^4) + P_2^3 \mathcal{M}_1^3} = \frac{\mathcal{M}_2}{P_2^1 \mathcal{M}_1^1 + P_2^2 \mathcal{M}_1^2 + P_2^3 \mathcal{M}_1^3}. \tag{9}$$

Since all paths contribute, the nesting of the MOPS factors cancels and the denominator reduces to the sum of the splitting kernels, multiplied with the +1-particle matrix elements.

Some paths in Fig. 1b are unordered, which leads to +1 MOPS factors of

$$\mathcal{R}_1^1 = \frac{\mathcal{M}_1^1}{P_1^1 \mathcal{M}_0^1} \quad \text{and} \quad \mathcal{R}_1^2 = \frac{\mathcal{M}_1^2}{P_1^3 \mathcal{M}_0^3 + P_1^4 \mathcal{M}_0^4}. \tag{10}$$

Only one path (brown) contributes to the denominator of \mathcal{R}_1^1 —the other path (red) is unordered.

The correction to the +2-particle state is

$$\mathcal{R}_2 = \frac{\mathcal{M}_2}{P_2^1 \mathcal{R}_1^1 P_1^1 \mathcal{M}_0^1 + P_2^2 \mathcal{R}_1^2 P_1^4 \mathcal{M}_0^4} = \frac{\mathcal{M}_2}{P_2^1 \mathcal{M}_1^1 + P_2^2 \frac{\mathcal{M}_1^2}{P_1^3 \mathcal{M}_0^3 + P_1^4 \mathcal{M}_0^4} P_1^4 \mathcal{M}_0^4}. \tag{11}$$

The red path in Fig. 1b does not contribute at all to the +2-particle state since the first branching scale is exceeding the factorization scale, $t_1^2 > t_{\text{fac}}^2$. This leads to a cancellation in the first term of the denominator in Eq. (11). The green path is not contributing directly to the +2-particle state, as $t_1^2 > t_1^3$. However, since $t_1^3 < t_{\text{fac}}^3$, the path is present in \mathcal{R}_1^2 . Therefore, the MOPS factor for the +2-particle state depends on more than one “layer” in the paths, and can thus not be calculated by reconstructing only +1-particle states from the +2-particle state that should be corrected.

This example highlights the core features of the MOPS method. The recursive structure of the correction factor represents a crucial difference to the GKS method (see Appendix A). At first sight, it seems counter-intuitive that knowledge of ordered *and* unordered paths is required to correctly calculate the correction factor for a phase-space point that has been generated by an ordered sequence of splittings. However, the necessity becomes clear when the weight of intermediate states is taken into account.

To obtain a uniform accuracy over the complete n -parton phase space, states beyond the reach of the parton shower have to be included. We discuss the treatment of these non-shower states in the next section, and present the general formula for the MOPS factor in Sect. 5.

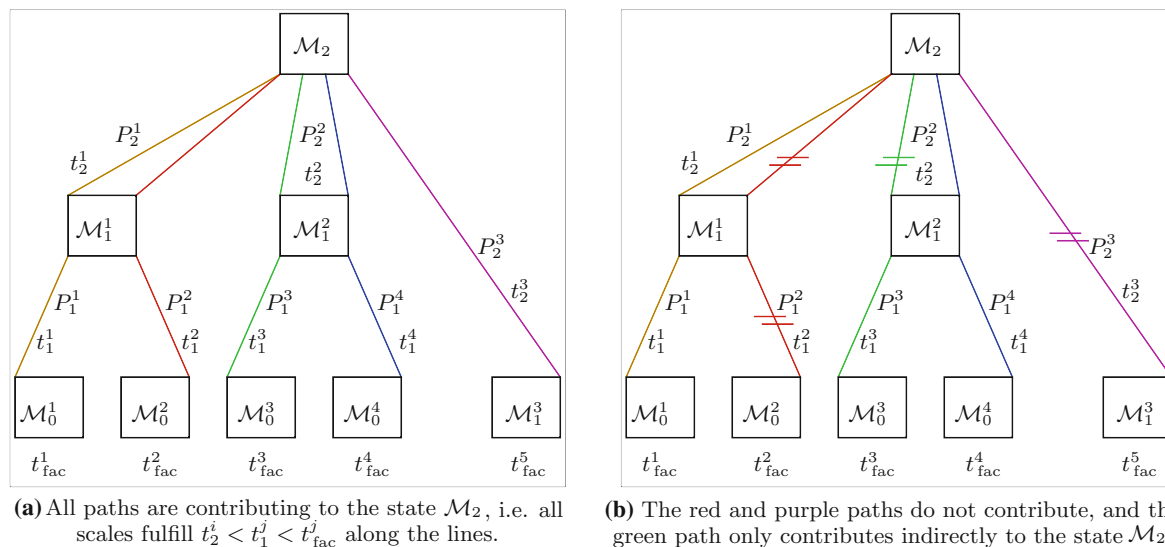


Fig. 1 History pyramid to illustrate different levels of contribution to the MOPS factor. The superscripts are numbering the different nodes. We use the shorthands $\mathcal{M}_X \equiv |\mathcal{M}(\Phi_X)|^2$, $t_X \equiv t(\Phi_X/\Phi_{X-1})$, and $P_X \equiv P(\Phi_X/\Phi_{X-1})$. The top layer is the main +2-particle state and the lower boxes represent the clustered states after one and two successive clusterings, respectively. The scales and splitting probabilities associated with the clusterings are noted along the lines. For illustrative purposes we included a path where the Born state is reached after one clustering (purple line), as present e.g. when combining QCD and electroweak clusterings

4 Completing the calculation with non-shower configurations

The MOPS formalism discussed in Sect. 3 only covers the parton-shower phase space characterized by an ordered sequence of splitting scales ($t_{\text{fac}} > t_1 > t_2 \dots$). As a consequence, a prescription for the missing phase space is required. The precise definition of these regions depends on the parton shower itself, the starting scale, definition of the evolution variable, and recoil strategy. Configurations can either be forbidden by restricting the first emission to scales below the factorization scale, cuts on lowest-multiplicity phase space points, or by the ordering property of the shower.

When combining non-shower and shower states, care has to be taken to avoid double- or under-counting. As discussed in Sect. 3, the shower off lowest-multiplicity events is treated without any restrictions apart from ordering emissions in the parton-shower evolution variable. Only those higher-multiplicity states that cannot be reproduced by showering lower-multiplicity states need to be added explicitly. This criterion supersedes algorithms that rely on the introduction of a merging cut.⁴ Uniform (leading-order) accuracy then is obtained across the complete emission phase space by also

applying a ME corrected shower when adding soft-collinear shower radiation to non-shower states. This will, if performed naively, introduce overlap between (the shower off) different non-shower states. Three steps are required to avoid the overlap:

1. Non-shower events are defined as unordered if no ordered path exists, i.e. if different paths to the same ME state are present, the event is only considered unordered if none of the paths can be reproduced with an ordered sequence of branchings scales.
2. Potential overlap between non-shower states with different parton multiplicities has to be removed, e.g. a maximally unordered +2-particle state may also be produced as a shower emission off a maximally unordered +1-particle state. The explanation how this overlap is identified and removed in the higher-multiplicity states, is deferred to the end of Sect. 5, since it is helpful to first discuss how non-shower states are showered.
3. States produced by ordered parton showers overlap with soft-collinear radiation attached to non-shower states if the “history” of a phase-space point contains both ordered and unordered paths. Therefore, both have to be ME cor-

⁴ An arbitrary shower will not correctly describe all sub-leading logs in its evolution variable, so that non-shower configurations may still contain (sub-leading) logarithmic divergences. One famous example of such configurations are the unordered, balancing soft-gluon emissions leading to Parisi-Petronzio scaling in p_{\perp} distributions [48,49].

Footnote 4 continued

To avoid such divergences in practice, we only include non-shower phase-space points if each scale at which partons could be recombined (as defined by the shower evolution variable) is above the parton-shower cut-off $t_{\text{cut}} \approx 1 \text{ GeV}$.

rected with correction factors taking into account both possibilities of population.

We now turn to the scale setting in non-shower events with two or more additional partons. From a parton-shower standpoint, there is no a priori guideline how non-shower configurations should be treated. However, since non-shower configurations easily dominate LHC observables depending on many well-separated jets, finding a sensible scale-setting prescription for arbitrary processes will greatly improve the ability of fixed-order + parton-shower calculations to describe data. Variations around the central scale can then be used to assess the precision of the calculation.

To obtain a flexible scale-setting prescription, we borrow the idea of constructing all possible event histories from the CKKW-L [26–28]. The aim of the procedure is twofold: define dynamical scales by exploiting the information about the phase-space points with the help of the weight and “sub-structure” of multi-jet matrix elements, while further ensuring a smooth inclusion of non-shower states with shower-accessible events.

For a sensible scale-setting prescription for non-shower states, we follow an argument similar to the derivation of the MOPS factor. However, ordering considerations should not be applied to non-shower states. Assume that a phase-space point Φ_{n+1} can be reached from multiple Φ'_n states by splitting an external leg. The contribution to the cross section due to splitting a single leg can be approximated by

$$\alpha_s(t(\Phi_{n+1}/\Phi'_n)) P(\Phi_{n+1}/\Phi'_n) \alpha_s^n(t_n^{\text{eff}}) |\mathcal{M}(\Phi'_n)|^2, \tag{12}$$

where t_n^{eff} is a suitable scale for the “underlying” n -particle state. To obtain the correct (leading-order) result when summing over all possible splittings $\Phi'_n \rightarrow \Phi_{n+1}$, we can apply the corrective factor

$$\mathcal{R}(\Phi_{n+1}) = \frac{\alpha_s^{n+1}(t_{n+1}^{\text{eff}}) |\mathcal{M}(\Phi_{n+1})|^2}{\sum_{\Phi'_n} \alpha_s(t(\Phi_{n+1}/\Phi'_n)) P(\Phi_{n+1}/\Phi'_n) \alpha_s^n(t_n^{\text{eff}}) |\mathcal{M}(\Phi'_n)|^2}, \tag{13}$$

where t_{n+1}^{eff} is the desired (currently unknown) scale for the $(n + 1)$ -particle state. To find a suitable scale, note that

- (a) if one splitting dominates over all other splittings, then a natural scale to capture the dynamics is strongly correlated with the relative jet separation of the dominant splitting,
- (b) if no splitting dominates, i.e. all splittings contribute democratically, there should be no strong preference for a scale, and a weighted average of jet separations seems appropriate.

Leaving aside the complications (and bias) induced by ordering constraints, an identical argument holds for parton-shower-produced states. In this case, the requirements above are fulfilled by keeping the characteristic shower-induced α_s factors for every ME corrected shower splitting. This would be guaranteed if the α_s factors in Eq. (13) would be identified by

$$\alpha_s^{n+1}(t_{n+1}^{\text{eff}}) = \frac{\sum_{\Phi'_n} \alpha_s(t(\Phi_{n+1}/\Phi'_n)) P(\Phi_{n+1}/\Phi'_n) \alpha_s^n(t_n^{\text{eff}}) |\mathcal{M}(\Phi'_n)|^2}{\sum_{\Phi'_n} P(\Phi_{n+1}/\Phi'_n) |\mathcal{M}(\Phi'_n)|^2}, \tag{14}$$

since then Eq. (13) is a simplified MEC factor. For ordered parton-shower sequences, Eq. (14) will not lead to the correct result. It is, however, well-suited as a scale-setting prescription for non-shower configurations. We will use Eq. (14) as the definition of the effective scales below, i.e. we set the renormalization and factorization scales for non-shower events to t^{eff} . The effective scale also serves as a shower (re)starting scale. The variation of the effective scale may act as an uncertainty estimate of the prescription.

An expression for the effective scale could also have been obtained by including PDF ratios in Eq. (13), which would mean that the choice of effective scale captured dynamics of underlying “hadronic” cross sections. We do not implement such a scale-setting prescription since we believe that the scale setting should be based on perturbative parton-level quantities.

Note that the scale-setting mechanism in Eq. (14) allows for $t_{\text{fac}} < t^{\text{eff}}$ if the scales entering the calculation are sufficiently large. An example of such a configuration are non-shower states with multiple hard (and possibly balancing) jets without p_{\perp} hierarchy. In this case, using a scale defined for the lowest-multiplicity process can result in pathologies [50]. It is desirable that t^{eff} is not bounded by t_{fac} , the factorization scale assigned to a fictitious lowest-multiplicity process. Instead, t^{eff} should provide a more “natural” scale for this genuine multi-jet configuration. Furthermore, t^{eff} is bound to remain in the perturbative region, since we only include non-shower phase space points for which clustering scales (as defined by the shower evolution variable) are above the parton-shower cut-off.

In Sect. 6 we will show that the scale setting outlined in this section results in a very good description of LHC data.

5 The complete algorithm

In this section, we summarize the combined fixed-order + parton-shower algorithm, and present the general form of the MOPS factor. The scheme introduces ME correction for

several ordered consecutive parton-shower emissions. This is in general obtained by applying the MOPS factor

result for small \vec{p}_\perp of the combined Born+ n -parton system. If instead a hierarchy $t_{\text{fac}} > t_{n-1}^{\text{eff}} > t_n$ can be constructed,

$$\begin{aligned} \mathcal{R}(\Phi_{n+1}) = & |\mathcal{M}(\Phi_{n+1})|^2 \left[\sum_{\Phi'_n} P(\Phi_{n+1}/\Phi'_n) \mathcal{R}(\Phi'_n) \sum_{\Phi'_{n-1}} \Theta(t(\Phi'_n/\Phi'_{n-1}) - t(\Phi_{n+1}/\Phi'_n)) P(\Phi'_n/\Phi'_{n-1}) \mathcal{R}(\Phi'_{n-1}) \right. \\ & \times \prod_{k=n-2}^{k \leq 1} \left(\sum_{\Phi'_k} \Theta(t(\Phi'_{k+1}/\Phi'_k) - t(\Phi'_{k+2}/\Phi'_{k+1})) P(\Phi'_{k+1}/\Phi'_k) \mathcal{R}(\Phi'_k) \right) \\ & \left. \sum_{\Phi'_0} \Theta(t(\Phi'_1/\Phi'_0) - t(\Phi'_2/\Phi'_1)) P(\Phi'_1/\Phi'_0) \Theta(t(\Phi'_0) - t(\Phi'_1/\Phi'_0)) |\mathcal{M}(\Phi'_0)|^2 \right]^{-1} \end{aligned} \quad (15)$$

to the splitting kernel. When including the correct weight of each possible path, the result exhibits a recursive structure, where $\mathcal{R}(\Phi_{n+1})$ includes the correction factors of all previous orders, $\mathcal{R}(\Phi'_n)$ to $\mathcal{R}(\Phi'_1)$. Once non-shower states are added, their contributions to the MOPS factor are taken into account as well.

Non-shower states are added as new configurations, with renormalization and factorization scales calculated through

$$\alpha_s^{n+1}(t_{n+1}^{\text{eff}}) = \frac{\sum_{\Phi'_n} \alpha_s(t(\Phi_{n+1}/\Phi'_n)) P(\Phi_{n+1}/\Phi'_n) \alpha_s^n(t_n^{\text{eff}}) |\mathcal{M}(\Phi'_n)|^2}{\sum_{\Phi'_n} P(\Phi_{n+1}/\Phi'_n) |\mathcal{M}(\Phi'_n)|^2} \quad (16)$$

This should ensure that the dynamics of the process are encoded in a sensible scale choice, without the scale-setting prescription being based on process- or multiplicity-dependent arguments.

Since non-shower states are included without a hard cut-off (e.g. a merging scale), the effective scale t^{eff} may differ significantly from the factorization scale t_{fac} . In this case, we further attach Sudakov factors by means of trial showering [26,27] to the non-shower states to include a sensible suppression due to the resummation of large logarithms of $t_{\text{fac}}/t^{\text{eff}}$. This is relatively straight-forward for +2-particle states—a Sudakov factor $\Delta(t_{\text{fac}}, t_2^{\text{eff}})$ is applied to ensure a sensible result if the \vec{p}_\perp of the combined Born+2-parton system is small. For higher-multiplicity non-shower states, more scale hierarchies arise, and a more detailed scheme is necessary to cover all relevant cases. However, only two types of scale hierarchies can remain after removing the overlap between n -particle non-shower events and states that are produced by showering lower-multiplicity non-shower configurations: the ordering $t_{\text{fac}} > t_n^{\text{eff}}$, or the ordering $t_{\text{fac}} > t_{n-1}^{\text{eff}} > t_n$.⁵ The hierarchy $t_{\text{fac}} > t_n^{\text{eff}}$ is again ameliorated by applying a single Sudakov factor $\Delta(t_{\text{fac}}, t_n^{\text{eff}})$ to produce a sensible

then a product of Sudakov factors $\Delta(t_{\text{fac}}, t_{n-1}^{\text{eff}})\Delta(t_{n-1}^{\text{eff}}, t_n)$ is appropriate. This guarantees a uniform weighting of $+n$ -particle events arising from either $+n$ -particle non-shower states or showered $+(n-1)$ -particle configurations. Note that the Sudakov factors $\Delta(t_{\text{fac}}, t^{\text{eff}})$ are unity if $t_{\text{fac}} < t^{\text{eff}}$.

The information about the different types of scale hierarchies are also used to remove the overlap between non-shower states with different parton multiplicities. States with scale hierarchies of the type $t_{n-m}^{\text{eff}} > t_{n-(m-1)} > \dots > t_n$ are removed for $m \geq 2$. For states that contain the hierarchy $t_{n-1}^{\text{eff}} > t_n$, the event is removed if the clustered $+(n-1)$ -particle state is itself an unordered state. Events without scale hierarchies that could have resulted from showering lower-multiplicity states are kept; that includes all +2-particle states with unordered scales $t_2 > t_1$ and +1-particle states with $t_1 > t_{\text{fac}}$. For the interested reader we include further methodological instructions in Appendix C.

6 Results

In this section, we present results obtained with the new method, including both the MOPS factor and the non-shower states (called “MOPS + unordered” in the following). A detailed validation can be found in Appendix B. The analyses are performed with RIVET [51]. We begin this section

⁵Footnote 5 continued

showering lower-multiplicity non-shower states. (a) If the reconstructed underlying +2-particle state is not shower-like (i.e. unordered), then the +4-particle state with the above hierarchy can be produced by adding two ordered shower emissions to the +2-particle state. Thus, the state is included by showering a non-shower +2-particle state. (b) If the reconstructed +2-particle state can be reached by an ordered sequence of emissions, and furthermore $t_3 > t_4$ then the “unordered” stems from the +2-particle to +3-particle transition. Thus, the +4-particle configuration can be reached by adding one ordered shower emission to a non-shower +3-particle state. In conclusion, the states with this more complex scale hierarchy should not be included through a non-shower +4-particle input, since this would result in over-counting.

⁵ Consider a non-shower (unordered) +4-particle state. After computing effective scales, it is possible that a scale hierarchy $t_{\text{fac}} > t_2^{\text{eff}} > t_3 > t_4$ exists. Such a configuration can be obtained in several ways

by studying the effect of the new method on jet separations, before moving to comparisons to LHC data. In both cases, we juxtapose the results with the GKS ME corrections implemented in VINCIA. The GKS MECs scheme includes emissions above the factorization scale t_{fac} (see Appendix A2 for how those are generated) as does the MOPS + unordered method by adding non-shower +1-particle states. Emissions with scales $t_1 > t_{\text{fac}}$ would not naturally be present in the pure or MOPS corrected shower, where Born states are showered beginning at t_{fac} . For the following results we add +1-particle states with scales $t_1 > t_{\text{fac}}$ explicitly to the pure and MOPS corrected shower, and shower these states using t_1 as shower starting scale. This decreases the significance of including non-shower states w.r.t comparing to a strictly ordered shower evolution, but should avoid using an “overly conservative” shower setup when comparing to default VINCIA.

6.1 Theory comparisons

Here, the general features of the new method are illustrated by discussing jet resolution scales. These variables show significant sensitivity to hard, well-separated jets as well as parton-shower resummation, and they can thus be used to gauge the effect of different pieces in the calculation. To not obscure the Sudakov shapes of the parton shower at low jet resolution, we do not include multiparton interactions.

Hadron-level results for hadronic Z decays and Drell–Yan events are presented in Fig. 2. The results have the expected behavior: at low jet resolution, parton-shower effects dominate, while non-shower states contribute mainly to large jet scales. Hence, the MOPS factor is dominating the observable at low scales. At LEP, shower states remain a dominant contribution even when modeling well-separated jets, and the effect of non-shower states remains at below 10% per bin. Results at the LHC are in stark contrast to this. There, the influence of shower configurations decreases substantially for large jet resolution, and non-shower phase-space regions become increasingly important. The uncertainty from varying the effective scale is not significant at LEP, and should thus not be considered a realistic uncertainty estimate. At LHC, the variation of t^{eff} ($= t_{\text{fac}} = t_{\text{ren}} = t_{\text{start}}$) is larger, and increases for high jet resolution, as expected from varying scales in a tree-level fixed-order variation. At low resolution, we observe a small increase in the scale uncertainty, which stems from the interplay of very large α_s values with the Sudakov factors that are applied to non-shower states.

By comparing with previous ideas below, we hope to understand the short-comings and benefits of our MOPS + unordered prescription. In Fig. 3 we compare the results of VINCIA2.2 without corrections, with the MOPS correction, MOPS + unordered scheme, and VINCIA2.0.01 with smooth ordering for the GKS ME corrected orders.

The MOPS correction for purely evolution-induced events is small for all jet resolutions. Differences are mostly at the level of 1–5%, illustrating that the uncorrected shower already describes the matrix elements well in phase-space regions reachable by showering. As discussed above, the jet resolution scales exhibit a Sudakov suppression for small values. In the Sudakov region, the corrected predictions should not deviate greatly from the “plain” shower result. This is indeed the case for both the MOPS + unordered and the GKS MECs method for very small resolution scales. The GKS MECs method generates more events with larger $d_{m,m+1}$ separation. Due to the unitarity of the shower, this leads to a depletion of events with small separation compared to the pure shower. The behavior is consistent with the findings in [38], where differences between strong and smooth ordering have been investigated. The impact of non-shower states in the MOPS + unordered scheme remains noticeable close to the peak of the distribution, although the modeling of the Sudakov region approaches the uncorrected shower more quickly than for the GKS MECs method. This means that the handling of non-shower states with large scale hierarchies (cf. end of Sect. 5) is important in our approach. Merging approaches commonly discard non-shower states with separation below a certain (merging) scale.

In conclusion, we believe that the MOPS + unordered scheme has desirable features, and that the choices in the method lead to the expected behavior.

6.2 Comparisons to data

To assess how the method performs for realistic observables, we now turn to Drell–Yan + jets measurements at the LHC. All curves employ the NNPDF2.1 LO PDF set [56] and use the corresponding strong coupling $\alpha_s(k_\mu, t)$ with one-loop running, $\alpha_s(m_Z^2) = 0.13$, and $k_\mu = 1$ for all branchings. We use these settings to compare all schemes on equal footing and choose $k_\mu = 1$ as required for the calculation of the effective scale.⁶ Soft-physics parameters are kept at their current VINCIA default values. The default VINCIA2.0.01 tune [38] corresponds to different α_s settings. While this results in a slightly better data description, it does not alter the general observations and conclusions of this section.

In Fig. 4 we confront the results of VINCIA2.2 without corrections, with the MOPS correction, MOPS + unordered scheme, and VINCIA2.0.01 with GKS ME corrections with ATLAS [52, 53] and CMS [54, 55] measurements.

As already seen in Sect. 6.1, the effect of the MOPS correction factor is small for all observables. This is of benefit for the description of the Drell–Yan p_\perp spectrum (upper left

⁶ Different k_μ values for different branching types invalidate the interpretation of the effective scale as a single parton-shower starting scale for subsequent showering.

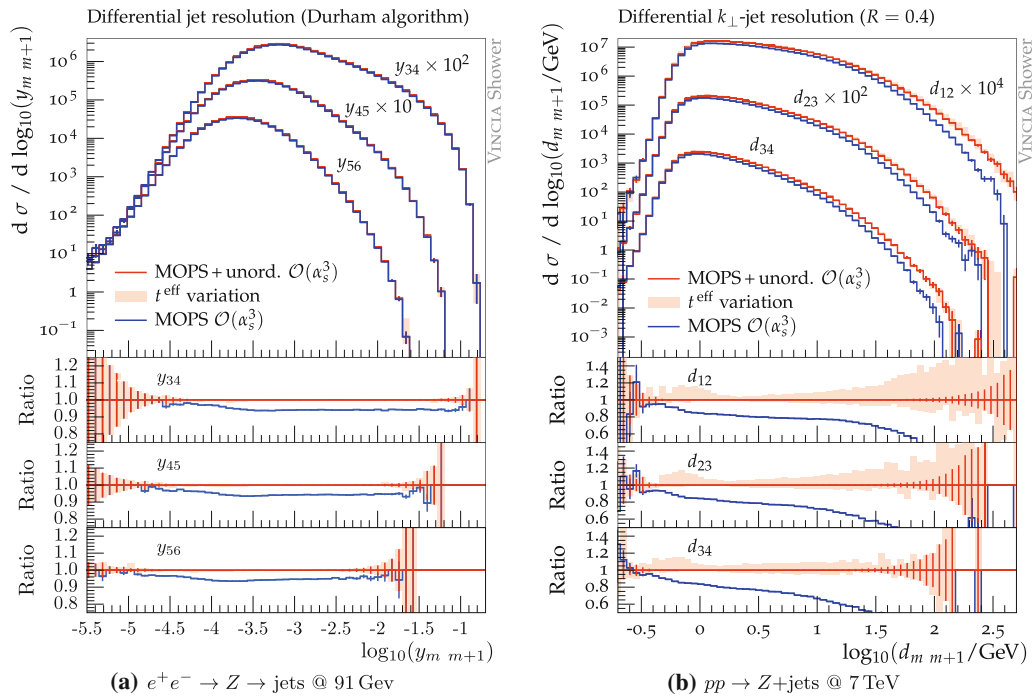


Fig. 2 PYTHIA8.2.26+VINCIA2.2 predictions for jet resolution measures $d_{m\ m+1}$ and $y_{m\ m+1}$ (the longitudinally invariant k_{\perp} jet algorithm with $R = 0.4$ for hadronic initial states and the Durham jet algorithm for lepton collisions). ME corrections are applied for ≤ 3 emissions. The red band is obtained by varying the effective scale t^{eff} [GeV] in non-shower events by factors of 2

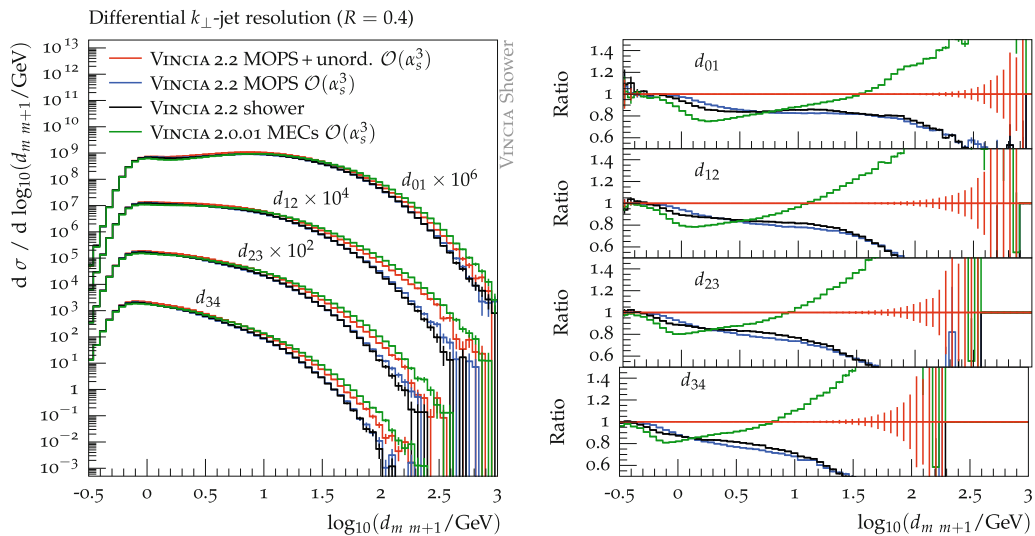


Fig. 3 PYTHIA8.2.26+VINCIA2.2 and PYTHIA8.2.15+VINCIA2.0.01 predictions for jet resolution measures in Drell-Yan events @ 7 TeV. ME corrections are applied for ≤ 3 emissions

panel of Fig. 4), for which the plain shower already offers a sensible data description. The quality of the description also remains unchanged for the MOPS + unordered scheme. The other observables in Fig. 4 test the existence of hard, well-

separated emissions in the tails of the distributions and are thus poorly modeled with the parton shower alone. We find a very good data description with the MOPS + unordered scheme. In particular, the quality of the data description in

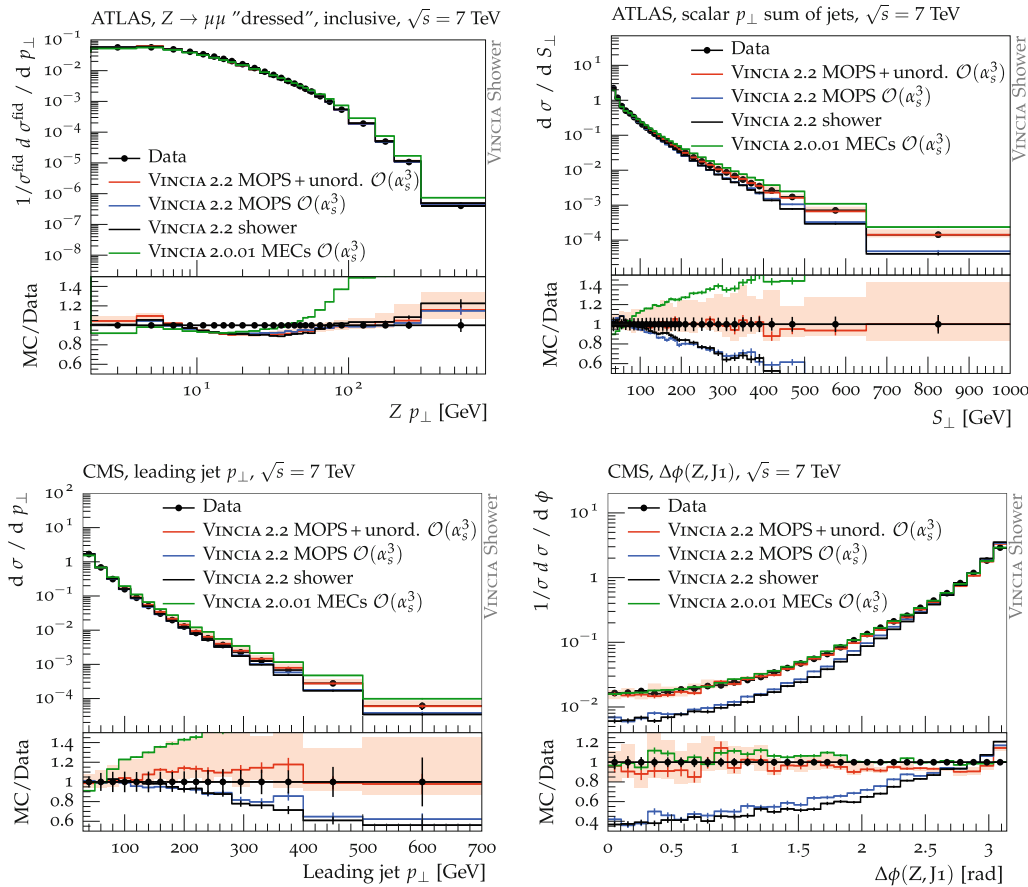


Fig. 4 PYTHIA8.2.26+VINCIA2.2 and PYTHIA8.2.15+VINCIA2.0.01 predictions compared to ATLAS data from [52, 53] and CMS data from [54, 55]. RIVET analyses ATLAS_2013_I1230812, ATLAS_2014_I1300647, CMS_2013_I1209721, and CMS_2015_I1310737. For the leading jet p_{\perp} and the scalar p_{\perp} sum of jets the predictions are rescaled to the experimental inclusive one-jet cross section. ME corrections are applied for ≤ 3 emissions. The red band is obtained by varying the effective scale t^{eff} [GeV] in non-shower events by factors of 2

our scheme relies crucially on the treatment of non-shower states. The scale-setting mechanism presented in Sect. 4 produces promising results, with the naive central scale choice close to the data, but with a large, leading-order-like uncertainty due to scale variations. We anticipate that the width of the band will decrease when performing a next-to-leading-order calculation with a similar scale choice. The uncertainty due to scale variations is largest in phase-space regions most sensitive to non-shower contributions. For the S_{\perp} and leading jet p_{\perp} distributions, the results of the GKS MECs approach touch the uncertainty bands attributed to non-shower events at low values, but are outside of the band in regions influenced by multiple hard jets. Both of these observables are much improved in the MOPS + unordered method, compared to the uncorrected shower. For the angle between the Z-boson and the hardest jet we observe a satisfactory data description for both our new method and VINCIA2.0.01.

7 Conclusions

We have presented an algorithm to obtain fixed-order accurate predictions combined with all-order parton-shower evolution that produces finite and non-overlapping results without introducing a merging scale. The new algorithm requires the introduction of a sophisticated matrix-element correction method for evolution-induced configurations. States beyond the reach of the parton shower are included with a systematic scale-setting procedure. This smoothly combines non-shower configurations and states produced in the ordered parton-shower evolution. The algorithm does not depend on specific properties of the parton shower and allows for arbitrary dead zones (which may be required by resummation considerations). The new fixed-order + parton-shower scheme has been implemented in the VINCIA parton shower

and will be made publicly available upon the VINCIA2.2 release.

The effect of including ME corrections for ordered parton-shower splittings is minor compared to the uncorrected shower. This means that the method does not deteriorate the shower resummation, and gives us confidence that the improvement does not interfere with other improvement strategies [57–59]. The main improvements stem from a careful treatment of contributions from phase-space regions that are not accessible by ordered parton showers. Such contributions are included with a sophisticated scale-setting prescription. For hadronic initial we find the scale setting to have a sizable influence on observables, since large parts of phase space are not shower accessible. We presented comparisons to data for the $pp \rightarrow Z + \text{jets}$ process and found the results of our new algorithm to be in good agreement with the data.

Acknowledgements We would like to thank Stefan Höche and Peter Skands for helpful discussions, and Peter Skands for comments on the manuscript. This work was supported by the Australian Research Council and by Fermi Research Alliance, LLC under Contract No. DE-AC02-07CH11359 with the U.S. Department of Energy, Office of Science, Office of High Energy Physics. NF thanks the SLAC and Fermilab theory divisions for hospitality during the course of this work.

Open Access This article is distributed under the terms of the Creative Commons Attribution 4.0 International License (<http://creativecommons.org/licenses/by/4.0/>), which permits unrestricted use, distribution, and reproduction in any medium, provided you give appropriate credit to the original author(s) and the source, provide a link to the Creative Commons license, and indicate if changes were made. Funded by SCOAP³.

Appendix A: Review of GKS matrix-element corrections

Iterative ME corrections have first been introduced in [37], and have been applied to colorless resonance decays [37] as well as to initial-state radiation [38]. Finite multiplicative correction factors are applied order by order in perturbation theory as the shower evolves. The MEC factor $\mathcal{R}(\Phi_{n+1})$ replaces the splitting kernels by a ratio of tree-level matrix elements. Symbolically, the correction factor can be written as

$$P(\Phi_{n+1}/\Phi_n) \longrightarrow \mathcal{R}(\Phi_{n+1}) P(\Phi_{n+1}/\Phi_n) \\ \equiv \frac{|\mathcal{M}(\Phi_{n+1})|^2}{\sum_{\Phi'_n} P(\Phi_{n+1}/\Phi'_n) |\mathcal{M}(\Phi'_n)|^2} P(\Phi_{n+1}/\Phi_n). \quad (\text{A1})$$

The denominator sums over all possible n -particle states through which the shower could have produced the $(n+1)$ -particle state.

A 1. Smoothly ordered showers

The MEC formalism in [37,38] requires a history-independent parton shower that covers the full phase space for the ME corrected orders. Therefore, VINCIA introduces the concept of smooth ordering. At any stage of the evolution the following procedure determines at which scale the shower off each parton in a $(n+1)$ -particle state is restarted:

- Find all physical clusterings $\Phi_{n+1} \rightarrow \Phi_n^i$ and their branching scales $t(\Phi_{n+1}/\Phi_n^i)$. The reference scale is the minimum of all scales, $\hat{t}(\Phi_{n+1}) = \min_i(t(\Phi_{n+1}/\Phi_n^i))$.
- Divide the $(n+1)$ -particle state into a set of “ordered” and “unordered partons”. For more details see [38].
- The evolution of “ordered partons” is restart at the reference scale \hat{t} . “Unordered partons” are allowed to radiate up to the phase-space maximum, but with the suppression factor

$$P_{\text{imp}}(\hat{t}(\Phi_{n+1}), t(\Phi_{n+2}/\Phi_{n+1})) \\ = \frac{\hat{t}(\Phi_{n+1})}{\hat{t}(\Phi_{n+1}) + t(\Phi_{n+2}/\Phi_{n+1})}. \quad (\text{A2})$$

When taking smooth ordering into account, the MEC factor (A1) should be defined as

$$\mathcal{R}(\Phi_{n+1}) = \frac{|\mathcal{M}(\Phi_{n+1})|^2}{\sum_{\Phi'_n} \mathcal{O}(\hat{t}(\Phi_n), t(\Phi_{n+1}/\Phi'_n)) P(\Phi_{n+1}/\Phi'_n) |\mathcal{M}(\Phi'_n)|^2}. \quad (\text{A3})$$

The ordering criterion reflects the different treatment of partons,

$$\mathcal{O}(\hat{t}(\Phi_n), t(\Phi_{n+1}/\Phi'_n)) \\ = \begin{cases} P_{\text{imp}}(\hat{t}(\Phi_n), t(\Phi_{n+1}/\Phi'_n)) & \text{for a branching of an “unordered parton”,} \\ \Theta(\hat{t}(\Phi_n) - t(\Phi_{n+1}/\Phi'_n)) & \text{for a branching of an “ordered parton”.} \end{cases}$$

The procedure guarantees a history-independent parton shower that covers the full kinematic range. However, it introduces complications that are hard to constrain from QCD considerations alone.

a. Sudakov factors in unordered regions

Consider the exclusive Born+jet cross section at the end of parton shower with the following evolution. The shower starts at the factorization scale of the Born process t_{fac} . After the branching at scale $t_1 < t_{\text{fac}}$, all partons explore their full kinematic range up to the scale t_{max} and are evolved down to the shower cut-off μ_c . Dropping the PDF factor for the second leg and suppressing most dependences of the splittings kernels, the exclusive cross section for this evolution sequence reads

$$d\sigma_1(\mu_c) = \Pi_1(t_{\max}, \mu_c) \cdot \alpha_s(t_1) P(t_1) \times \frac{f_1(x_1, t_1)}{f_0(x_0, t_1)} \Pi_0(t_{\text{fac}}, t_1) \cdot f_0(x_0, t_{\text{fac}}) |\mathcal{M}(\Phi_0)|^2 d\Phi_1. \tag{A4}$$

The no-emission probability $\Pi_1(t_{\max}, \mu_c)$ can be split up into an ordered part $\Pi_1(t_1, \mu_c)$ and a part that reflects the evolution in the unordered region $\Pi_1^{\text{uo}}(t_{\max}, t_1)$. We use the relation [60]

$$\Pi_n(t_n, t_{n+1}) = \frac{f_n(x_n, t_{n+1})}{f_n(x_n, t_n)} \Delta_n(t_n, t_{n+1}) \tag{A5}$$

to write the cross section in terms of Sudakov factors,

$$d\sigma_1(\mu_c) = \Pi_1^{\text{uo}}(t_{\max}, t_1) \cdot f_1(x_1, \mu_c) \Delta_1(t_1, \mu_c) \times \alpha_s(t_1) P(t_1) \Delta_0(t_{\text{fac}}, t_1) \cdot |\mathcal{M}(\Phi_0)|^2 d\Phi_1. \tag{A6}$$

The no-emission probability $\Pi_1^{\text{uo}}(t_{\max}, t_1)$ remains in the cross section. In VINCIA this factor is defined as

$$\Pi_1^{\text{uo}}(t_{\max}, t_1) = \exp\left(-\sum_{i \rightarrow 2} \int dz \int_{t_1}^{t_{\max}} dt \frac{f_2(x_2, t)}{f_1(x_1, t)} \alpha_s(t) P_{\text{imp}} P(t, z)\right). \tag{A7}$$

Here, the scale in the PDF ratio is fixed to the scale of the previous emission to ensure the proper cancellation between PDF factors for branchings in the unordered region. However, (A7) does not have a direct correspondence to any term in the DGLAP equation reformulated as a backwards evolution [39].

b. Missing evolution and configurations

For low multiplicities, all partons in the system are treated as unordered and explore their phase space up to the kinematics limit. However, starting for higher multiplicities, “ordered partons” are present which restart their evolution at the Markovian scale. By definition, this scale is smaller or equal to the scale of the last branching. The allowed branching range of “ordered partons” is therefore more restricted than in an ordered shower.

As with every parton shower that only contains QCD splittings, certain flavor configurations cannot be reached, independent of kinematic constraints. One such example is $q\bar{q} \rightarrow Wq'\bar{q}''$, where the W boson can only be radiated off the final-state legs. To include such a configuration within the MECs method an electroweak shower is necessary.

A 2. The treatment of hard jets

To avoid the concept of “power showers” and simultaneously allow jets with scales $t > t_{\text{fac}}$, VINCIA distinguishes between non-QCD and QCD processes. The latter category covers all hard processes with partons in the final state (except partons arising from resonance decay).

In non-QCD processes the input events are divided in two samples. The first one is associated with no hard jets, while the second sample contains at least one jet with $t > t_{\text{fac}}$. Because both samples are weighted differently, this introduces a non-smooth transition, see the left panel of Fig. 5. When more branchings are taken into account, the effect is washed out and the step barely visible as shown in the right panel of Fig. 5.

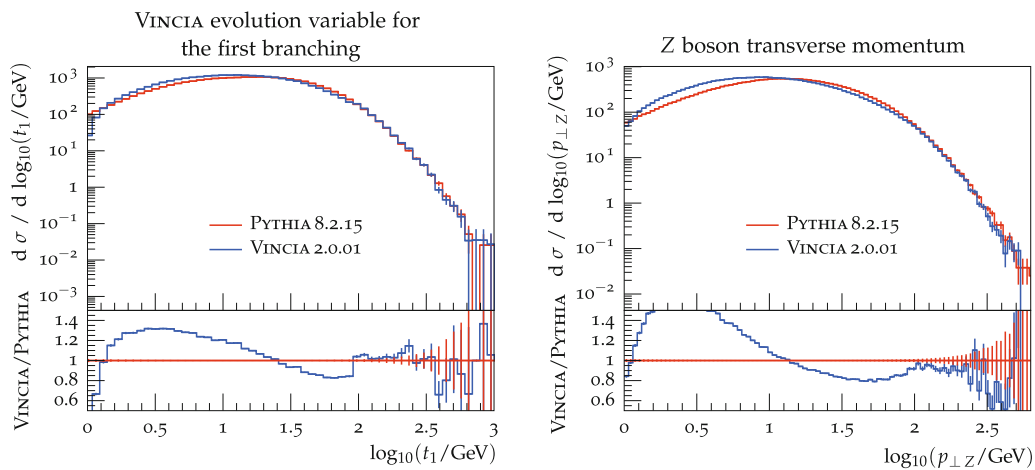


Fig. 5 Distribution of the VINCIA evolution variable after the first branching (left) and the Z boson transverse momentum (right) for $pp \rightarrow Z$ +jets at parton level

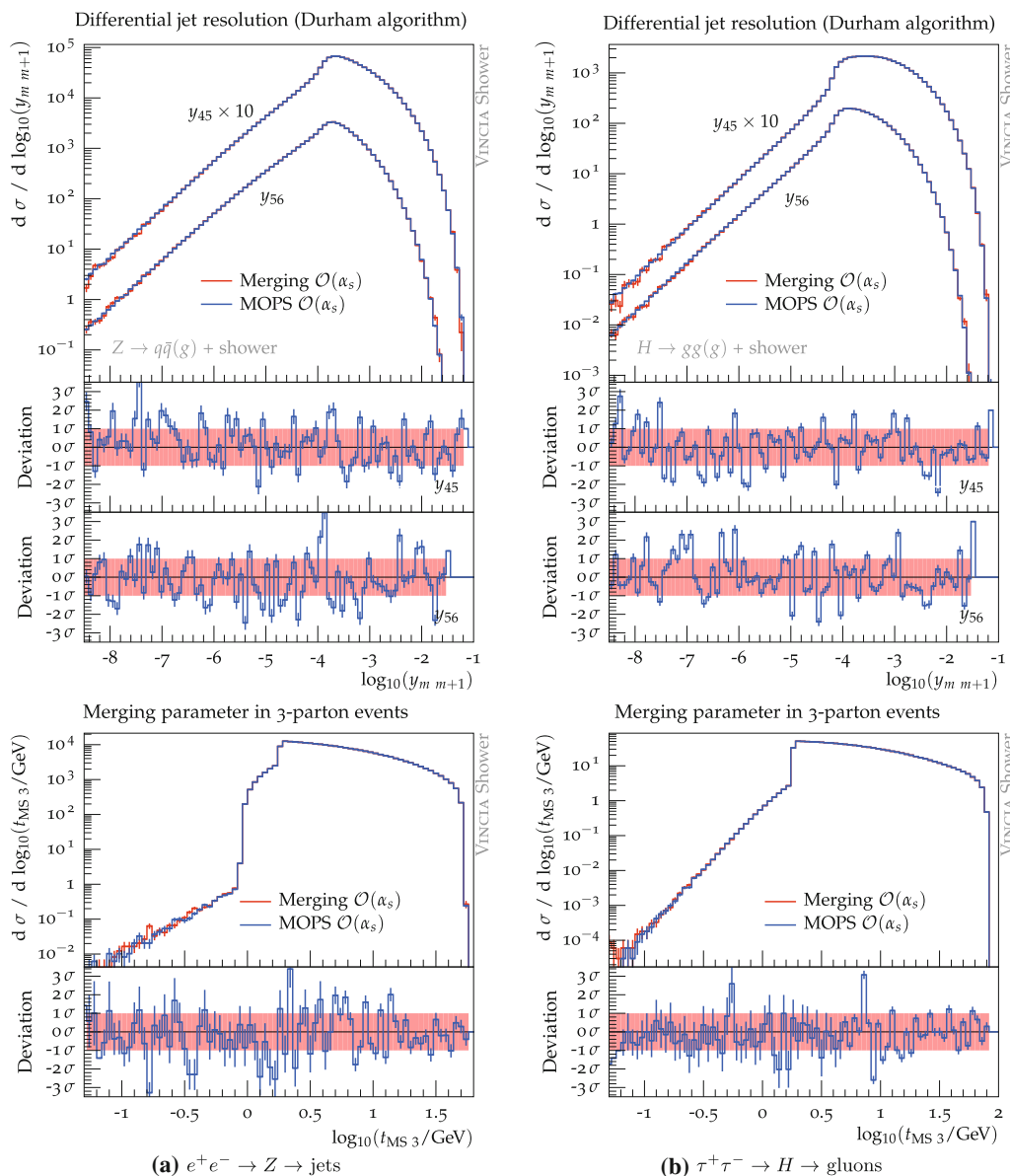


Fig. 6 Parton-level results: the distribution of the merging scale in exclusive 3-parton events (bottom) and the logarithmic distributions of differential jet resolutions (top). Merged predictions with a merging-scale value of 5 GeV are compared to predictions with the MOPS method

The first emission off a QCD $2 \rightarrow 2$ process is treated similar to the procedure summarized in Appendix A 1: all partons are allowed to explore their full phase space, but with a suppression of

$$P_{\text{imp}}(t_{\text{fac}}, t(\Phi_1/\Phi_0)) = \frac{t_{\text{fac}}}{t_{\text{fac}} + t(\Phi_1/\Phi_0)}. \tag{A8}$$

Here the factorization scale replaces the Markovian reference scale. This leads to similar, leftover no-emission probabilities from unordered regions as discussed in Appendix A 1.

Appendix B: Validation of matrix-element corrections for ordered emissions in VINCIA

In this section we validate the numerical implementation of the MOPS method in VINCIA by comparing it to merged predictions using the CKKW-L merging implementation in PYTHIA8 [28] applied to VINCIA. For the latter we define the merging scale as the minimum of all evolution scales, $t_{\text{MS}} = \min_i(t(\Phi_{n+1}/\Phi_n^i))$. No color information is used to

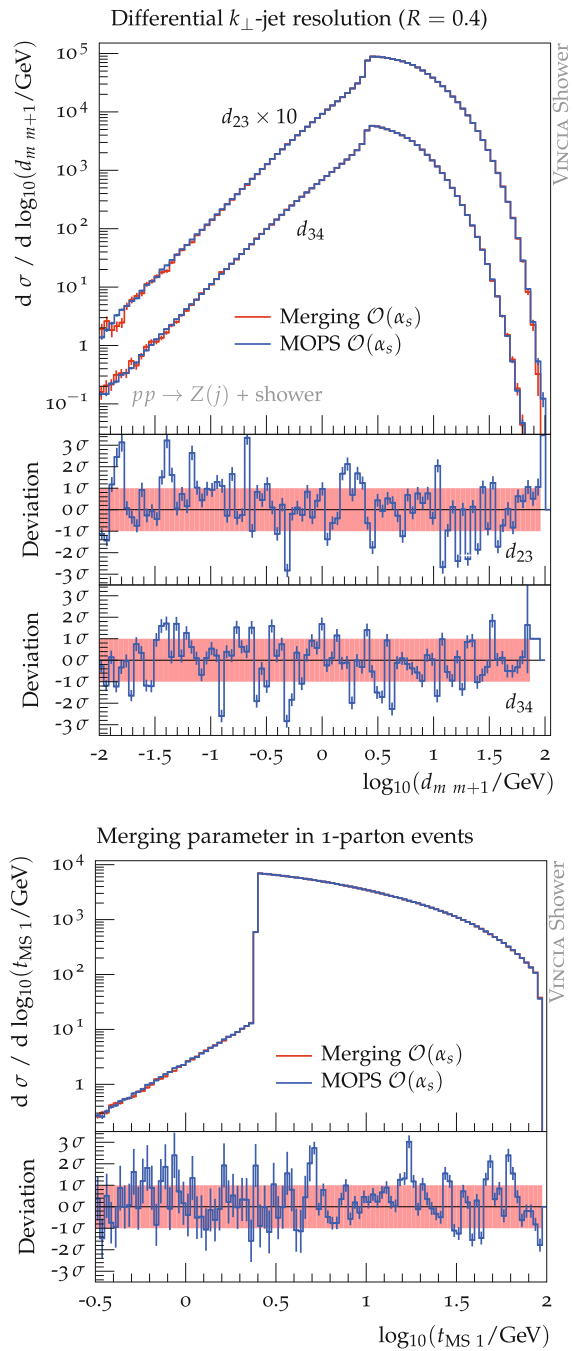


Fig. 7 Parton-level results for $pp \rightarrow Z+\text{jets}$: the distribution of the merging scale in exclusive 1-parton events (*bottom*) and the logarithmic distributions of differential jet resolutions (*top*). Merged predictions with a merging-scale value of 5 GeV are compared to predictions with the MOPS method

find possible clusterings. For the validation we use parton-level results with a fixed α_s for both methods and do not include events that cannot be reproduced by VINCIA with an

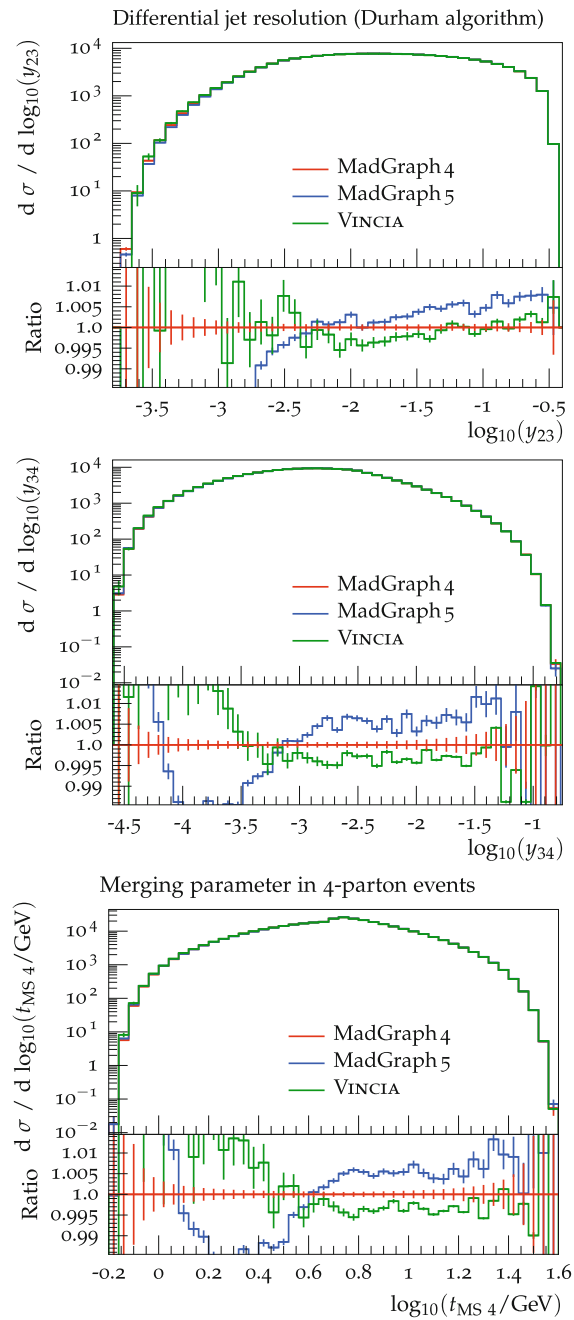


Fig. 8 Parton-level results for $e^+e^- \rightarrow Z \rightarrow q\bar{q}gg$: the distribution of the merging scale in exclusive 4-parton events (*bottom*) and the logarithmic distributions of differential jet resolutions. Comparison of MadGraph 4, MadGraph 5, and VINCIA+MadGraph 4+Rambo

ordered sequence of branching scales. To ensure the same Sudakov factors ME corrections are also applied in the case of merging.

Figures 6 and 7 show a comparison between the results of the MOPS method and merging including a ME corrected first emission. Each simulation contains at least 10^8 input events generated with MadGraph [61,62]. The lower panels present the deviation between the two methods, normalized to the statistical uncertainty of the merged prediction in the respective bin. As both methods should provide the same result, this distribution should exhibit statistical fluctuations only. Parton-level results for $e^+e^- \rightarrow Z \rightarrow \text{jets}$ and $\tau^+\tau^- \rightarrow H \rightarrow \text{gluons}$ are presented in Fig. 6. The deviation in the lower panels clearly show that both methods are identical up to statistical fluctuations.

Similar plots are shown for on-shell Z -boson production in Fig. 7. Note that we exclude branchings with scales above the factorization scale for comparison purposes. This is necessary due to how such emissions are generated in VINCIA, see Appendix A 2.

When correcting the second emission, we expect slight mismatches between the predictions of the two methods. The matrix elements in VINCIA are taken from MadGraph 4. It would thus be preferable to use MadGraph 4 input for the merging. However, MadGraph 4 is no longer developed and does not allow for linking against LHAPDF 5 [63], while PYTHIA8 requires LHAPDF 5 or higher. Thus, using the same PDF set for hadronic initial states means that the input for merging was generated with MadGraph 5. MadGraph 4 and 5 exhibit shape and normalization differences at the (sub-)percent level in the observables investigated for the validation, as discussed in the following. As an example, we compare the ME output of MadGraph 4 and 5 for $e^+e^- \rightarrow Z \rightarrow q\bar{q}gg$ with a cut on the invariant mass of jet pairs, $m_{jj} \geq 5$ GeV. We further include curves for the VINCIA matrix element integrated with RAMBO [64] (an implementation of which is included in VINCIA) and normalized to the MadGraph 4 cross section, as we are mainly interested in shape differences. The results are shown in Fig. 8. The ratio plots shown in the lower panels reveal differences between all three predictions, mostly at the level of around 0.5%. While those mismatches are irrelevant in practical studies, they deteriorate the quality the validation. Nevertheless the results of the validation are satisfactory. When correcting the third emission, we anticipate further differences between the two methods. In VINCIA, the color matrices for matrix elements with two identical quark pairs and at least one gluon are decomposed by hand; see [38]. Therefore, higher orders cannot be validated at the same level as the first order.

In Fig. 9 we show a comparison of merging and the MOPS method for three corrected emissions. The lower panels show the ratio of predictions with the MOPS method to merged

results. Small deviations between the two methods are visible at large scales. Considering that the differences are at most 3%, and that we expect some mismatches, and that the differences are mostly in a region where non-shower states have a very large impact (cf. Fig. 3), we find the methods in good agreement.

Appendix C: Identifying and removing the overlap between states with different multiplicities

As discussed in Sects. 4 and 5, overlap between (the shower off) non-shower states with different parton multiplicities exists and has to be removed. In this section we briefly explain, for interested readers and practitioners, how different states are treated to remove potential overlap.

+0-particle states: The shower is started at the factorization scale t_{fac} of the Born state and no further restrictions apply.

+1-particle states: Only events where all scales t_1 exceed the factorization scale, $t_1 > t_{\text{fac}}$, are taken into account. After a path is chosen, the shower off the +1-particle state starts at the scale t_1 .

+2-particle states: To avoid overlap with the shower off non-shower +1-particle states, an ordering of the clustering scales with respect to the factorization scale is not checked. Only events, where $t_2 > t_1$ holds for all paths, are taken into account and the effective scale t_2^{eff} is calculated. If $t_{\text{fac}} > t_2^{\text{eff}}$ a Sudakov factor $\Delta(t_{\text{fac}}, t_2^{\text{eff}})$ is attached by trial-showering the clustered Born state. The shower off the +2-particle state starts at t_2^{eff} .

+n-particle states ($n \geq 3$): As for the non-shower +2-particle states, an ordering of the clustering scales with respect to the factorization scale is not checked. Only events without an ordered path are taken into account. The effective scales $t_2^{\text{eff}}, t_3^{\text{eff}}, \dots, t_n^{\text{eff}}$ are calculated and the smallest $k \in \{2 \dots n\}$ which leads to an ordered sequence of scales, $t_k^{\text{eff}} > t_{k+1} > \dots > t_n$, is found. If $k \leq n - 2$, the event is removed from consideration due to overlap with showering lower-multiplicity non-shower states, see Sect. 5. If $k = n - 1$, i.e. $t_{n-1}^{\text{eff}} > t_n$, the event is removed, if the clustered $+(n - 1)$ -particle state is itself a non-shower state. For events that are not rejected we chose one of the paths for which $t_{n-1}^{\text{eff}} > t_n$ holds and attached the Sudakov factors $\Delta(t_{\text{fac}}, t_{n-1}^{\text{eff}})\Delta(t_{n-1}^{\text{eff}}, t_n)$. The shower off the $+n$ -particle state starts at t_n . If no scale hierarchy is found, the event is retained, the Sudakov factor $\Delta(t_{\text{fac}}, t_n^{\text{eff}})$ is attached, and the $+n$ -particle states is showered from t_n^{eff} .

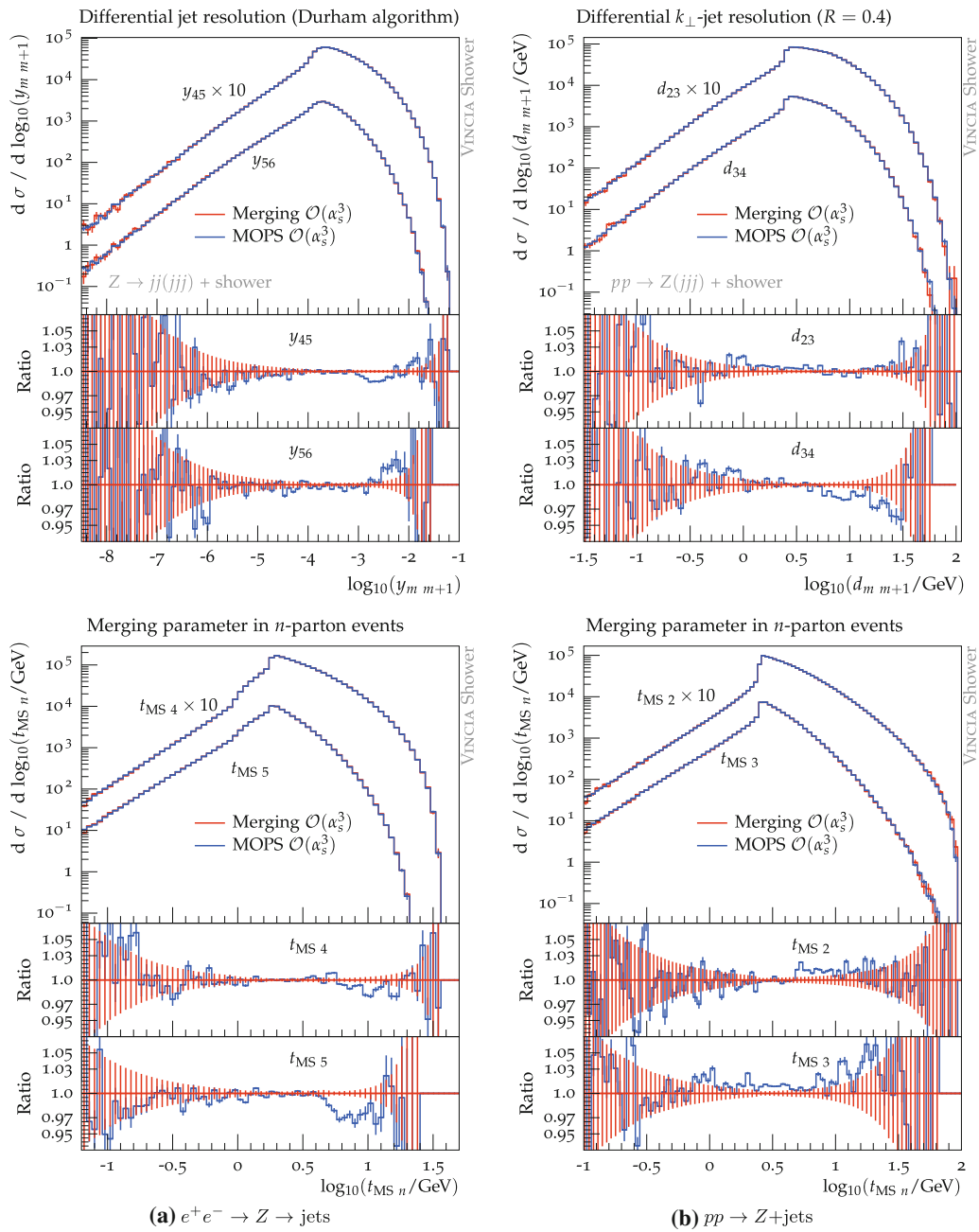


Fig. 9 Parton-level results: the distribution of the merging scale in exclusive 4- and 5-parton events (bottom) and the logarithmic distributions of differential jet resolutions (top). Merged predictions with a merging-scale value of 5 GeV are compared to predictions with the MOPS method

References

1. A. Buckley et al., Phys. Rep. **504**, 145 (2011). [arXiv:1101.2599](https://arxiv.org/abs/1101.2599) [hep-ph]
2. T. Gleisberg, S. Höche, F. Krauss, M. Schönherr, S. Schumann, F. Siegert, J. Winter, JHEP **02**, 007 (2009). [arXiv:0811.4622](https://arxiv.org/abs/0811.4622) [hep-ph]
3. T. Sjöstrand, S. Ask, J.R. Christiansen, R. Corke, N. Desai, P. Ilten, S. Mrenna, S. Prestel, C.O. Rasmussen, P.Z. Skands, Comput. Phys. Commun. **191**, 159 (2015). [arXiv:1410.3012](https://arxiv.org/abs/1410.3012) [hep-ph]
4. M. Bähr et al., Eur. Phys. J. C **58**, 639 (2008). [arXiv:0803.0883](https://arxiv.org/abs/0803.0883) [hep-ph]
5. S. Frixione, B.R. Webber, JHEP **0206**, 029 (2002). [arXiv:hep-ph/0204244](https://arxiv.org/abs/hep-ph/0204244)

6. P. Nason, JHEP **11**, 040 (2004). [arXiv:hep-ph/0409146](#)
7. S. Frixione, P. Nason, C. Oleari, JHEP **11**, 070 (2007). [arXiv:0709.2092](#) [hep-ph]
8. S. Frixione, F. Stoeckli, P. Torrielli, B.R. Webber, JHEP **1101**, 053 (2011). [arXiv:1010.0568](#) [hep-ph]
9. P. Torrielli, S. Frixione, JHEP **04**, 110 (2010). [arXiv:1002.4293](#) [hep-ph]
10. S. Alioli, P. Nason, C. Oleari, E. Re, JHEP **06**, 043 (2010). [arXiv:1002.2581](#) [hep-ph]
11. S. Höche, F. Krauss, M. Schönherr, F. Siegert, JHEP **04**, 024 (2011). [arXiv:1008.5399](#) [hep-ph]
12. S. Höche, F. Krauss, M. Schönherr, F. Siegert, JHEP **09**, 049 (2012). [arXiv:1111.1220](#) [hep-ph]
13. S. Plätzer, S. Gieseke, Eur. Phys. J. C **72**, 2187 (2012). [arXiv:1109.6256](#) [hep-ph]
14. J. Alwall, R. Frederix, S. Frixione, V. Hirschi, F. Maltoni, O. Mattelaer, H.S. Shao, T. Stelzer, P. Torrielli, M. Zaro, JHEP **07**, 079 (2014). [arXiv:1405.0301](#) [hep-ph]
15. S. Jadach, W. Placzek, S. Sapeta, A. Siodmok, M. Skrzypek, JHEP **10**, 052 (2015). [arXiv:1503.06849](#) [hep-ph]
16. M. Czakon, H.B. Hartanto, M. Kraus, M. Worek, JHEP **06**, 033 (2015). [arXiv:1502.00925](#) [hep-ph]
17. S. Catani, F. Krauss, R. Kuhn, B.R. Webber, JHEP **11**, 063 (2001). [arXiv:hep-ph/0109231](#)
18. M.L. Mangano, M. Moretti, R. Pittau, *Workshop on Monte Carlo Generator Physics for Run II at the Tevatron Batavia, Illinois, April 18-20, 2001*, Nucl. Phys. B **632**, 343 (2002). [arXiv:hep-ph/0108069](#)
19. S. Mrenna, P. Richardson, JHEP **05**, 040 (2004). [arXiv:hep-ph/0312274](#)
20. J. Alwall et al., Eur. Phys. J. C **53**, 473 (2008). [arXiv:0706.2569](#) [hep-ph]
21. K. Hamilton, P. Richardson, J. Tully, JHEP **11**, 038 (2009). [arXiv:0905.3072](#) [hep-ph]
22. K. Hamilton, P. Nason, JHEP **06**, 039 (2010). [arXiv:1004.1764](#) [hep-ph]
23. S. Höche, F. Krauss, M. Schönherr, F. Siegert, JHEP **08**, 123 (2011). [arXiv:1009.1127](#) [hep-ph]
24. N. Lavesson, L. Lönnblad, JHEP **12**, 070 (2008). [arXiv:0811.2912](#) [hep-ph]
25. L. Lönnblad, S. Prestel, JHEP **02**, 094 (2013). [arXiv:1211.4827](#) [hep-ph]
26. L. Lönnblad, JHEP **05**, 046 (2002). [arXiv:hep-ph/0112284](#)
27. N. Lavesson, L. Lönnblad, JHEP **07**, 054 (2005). [arXiv:hep-ph/0503293](#)
28. L. Lönnblad, S. Prestel, JHEP **03**, 019 (2012). [arXiv:1109.4829](#) [hep-ph]
29. S. Plätzer, JHEP **08**, 114 (2013). [arXiv:1211.5467](#) [hep-ph]
30. T. Gehrmann, S. Höche, F. Krauss, M. Schönherr, F. Siegert, JHEP **01**, 144 (2013). [arXiv:1207.5031](#) [hep-ph]
31. S. Höche, F. Krauss, M. Schönherr, F. Siegert, JHEP **04**, 027 (2013). [arXiv:1207.5030](#) [hep-ph]
32. L. Lönnblad, S. Prestel, JHEP **03**, 166 (2013). [arXiv:1211.7278](#) [hep-ph]
33. R. Frederix, S. Frixione, JHEP **12**, 061 (2012). [arXiv:1209.6215](#) [hep-ph]
34. S. Alioli, C.W. Bauer, C.J. Berggren, A. Hornig, F.J. Tackmann, C.K. Vermilion, J.R. Walsh, S. Zuberi, JHEP **09**, 120 (2013). [arXiv:1211.7049](#) [hep-ph]
35. J. Bellm, S. Gieseke, S. Plätzer, (2017). [arXiv:1705.06700](#) [hep-ph]
36. J.R. Christiansen, S. Prestel, Eur. Phys. J. C **76**, 39 (2016). [arXiv:1510.01517](#) [hep-ph]
37. W.T. Giele, D.A. Kosower, P.Z. Skands, Phys. Rev. D **84**, 054003 (2011). [arXiv:1102.2126](#) [hep-ph]
38. N. Fischer, S. Prestel, M. Ritzmann, P. Skands, Eur. Phys. J. C **76**, 589 (2016). [arXiv:1605.06142](#) [hep-ph]
39. T. Sjöstrand, Phys. Lett. B **157**, 321 (1985)
40. G. Marchesini, B.R. Webber, Nucl. Phys. B **310**, 461 (1988)
41. S. Höche, S. Prestel, Eur. Phys. J. C **75**, 461 (2015). [arXiv:1506.05057](#) [hep-ph]
42. D.A. Kosower, Phys. Rev. D **57**, 5410 (1998). [arXiv:hep-ph/9710213](#)
43. A. Gehrmann-De Ridder, T. Gehrmann, E.W.N. Glover, JHEP **09**, 056 (2005). [arXiv:hep-ph/0505111](#)
44. M. Bengtsson, T. Sjöstrand, Phys. Lett. B **185**, 435 (1987)
45. M. Bengtsson, T. Sjöstrand, Nucl. Phys. B **289**, 810 (1987)
46. G. Miu, T. Sjöstrand, Phys. Lett. B **449**, 313 (1999). [arXiv:hep-ph/9812455](#)
47. M.H. Seymour, Comput. Phys. Commun. **90**, 95 (1995). [arXiv:hep-ph/9410414](#)
48. G. Parisi, R. Petronzio, Nucl. Phys. B **154**, 427 (1979)
49. S. Frixione, P. Nason, G. Ridolfi, Nucl. Phys. B **542**, 311 (1999). [arXiv:hep-ph/9809367](#)
50. C.F. Berger, Z. Bern, L.J. Dixon, F. Febres Cordero, D. Forde, T. Gleisberg, H. Ita, D.A. Kosower, D. Maitre, Phys. Rev. D **80**, 074036 (2009). [arXiv:0907.1984](#) [hep-ph]
51. A. Buckley, J. Butterworth, L. Lönnblad, D. Grellscheid, H. Hoeth, J. Monk, H. Schulz, F. Siegert, Comput. Phys. Commun. **184**, 2803 (2013). [arXiv:1003.0694](#) [hep-ph]
52. G. Aad et al. (ATLAS), JHEP **07**, 032 (2013). [arXiv:1304.7098](#) [hep-ex]
53. G. Aad et al. (ATLAS), JHEP **09**, 145 (2014). [arXiv:1406.3660](#) [hep-ex]
54. S. Chatrchyan et al. (CMS), Phys. Lett. B **722**, 238 (2013). [arXiv:1301.1646](#) [hep-ex]
55. V. Khachatryan et al. (CMS), Phys. Rev. D **91**, 052008 (2015). [arXiv:1408.3104](#) [hep-ex]
56. R.D. Ball, V. Bertone, F. Cerutti, L. Del Debbio, S. Forte, A. Guffanti, J.I. Latorre, J. Rojo, M. Ubiali (NNPDF), Nucl. Phys. B **855**, 153 (2012). [arXiv:1107.2652](#) [hep-ph]
57. H.T. Li, P. Skands, Phys. Lett. B **771**, 59 (2017). [arXiv:1611.00013](#) [hep-ph]
58. S. Höche, S. Prestel, (2017). [arXiv:1705.00742](#) [hep-ph]
59. S. Höche, F. Krauss, S. Prestel, (2017). [arXiv:1705.00982](#) [hep-ph]
60. R.K. Ellis, W.J. Stirling, B.R. Webber, Camb. Monogr. Part. Phys. Nucl. Phys. Cosmol. **8**, 176 (1996)
61. J. Alwall, P. Demin, S. de Visscher, R. Frederix, M. Herquet, F. Maltoni, T. Plehn, D.L. Rainwater, T. Stelzer, JHEP **09**, 028 (2007). [arXiv:0706.2334](#) [hep-ph]
62. J. Alwall, M. Herquet, F. Maltoni, O. Mattelaer, T. Stelzer, JHEP **06**, 128 (2011). [arXiv:1106.0522](#) [hep-ph]
63. M.R. Whalley, D. Bourilkov, R.C. Group, in *HERA and the LHC: A Workshop on the Implications of HERA for LHC Physics. Proceedings, Part B*, p. 575 (2005). [arXiv:hep-ph/0508110](#)
64. R. Kleiss, W.J. Stirling, S.D. Ellis, Comput. Phys. Commun. **40**, 359 (1986)

5.2 CKKW-L Merging

This section sketches the relevant steps to perform the CKKW-L merging for combining the parton shower with LO matrix elements of different multiplicity. As an example, the process $pp \rightarrow Z + \leq 3$ jets is used in the context of the PYTHIA 8 + VINCIA framework. Event samples for $pp \rightarrow Z + n \cdot j$ ($n \in \{0 \dots 3\}$) with fixed renormalization and factorization scales, μ_{RME} and μ_{FME} , are generated, for instance with MADGRAPH. If the Z boson is accompanied by additional jets, the cross section has to be regularized by applying a cut. This is expressed as $\Theta(t_{ME}^n - t_{ME}^{\text{cut}})$, where t_{ME}^{cut} is the numerical value of the cut and the superscript n denotes the number of additional partons in the event sample. The definition of the cut t_{ME}^n is in principle arbitrary. However, if the functional form of t_{ME}^n is not identical to that of the merging scale t_{MS}^n , the full phase space might not be covered. Thus, we assume $t_{ME}^n \equiv t_{MS}^n$ and the cut in the ME to be more strict, compared to the cut in the merging, i.e. $t_{ME}^{\text{cut}} < t_{MS}^{\text{cut}}$.¹ The event samples for $pp \rightarrow Z + \leq 3$ jets are generated according to the differential cross sections

$$d\sigma_{pp \rightarrow Z+n \cdot j} = f_n(x_n, \mu_{FME}^2) \alpha_s^n(\mu_{RME}^2) |\mathcal{M}_{Z+n \cdot j}|^2 \Theta(t_{MS}^n - t_{MS}^{\text{cut}}) d\Phi_{Z+n \cdot j}. \quad (5.1)$$

For the sake of readability only one PDF factor is used. Flux factors are included in the phase-space and the strong coupling is explicitly written down. The sub- and superscripts n indicate how many final state partons exist. Simply showering and adding the events leads to the double counting problem introduced in sec. 3.4. Instead, the following procedure is applied to each event sample:

1. A complete history tree is set up by constructing all possible ways the event can be clustered back to the underlying Born state ($pp \rightarrow Z$). Such a history tree is shown in fig. 5.1 for $q\bar{q} \rightarrow Zgg$ and $q\bar{q}' \rightarrow Zq\bar{q}'$. In VINCIA only one clustering from $pp \rightarrow Zj$ to $pp \rightarrow Z$ exists.
2. A probability is assigned to each path in the tree, corresponding to the product of splitting functions A and the ME of the Born state, e.g. $P_1 = A_1^{(1)} A_2^{(1)} |\mathcal{M}_Z^{(1)}|^2$ and $P_2 = A_1^{(2)} A_2^{(2)} |\mathcal{M}_Z^{(2)}|^2$ for $q\bar{q} \rightarrow Zgg$. One path is selected among all, based on the relative probabilities. If ordered and unordered paths are present, e.g. if $t_1^{(1)} > t_2^{(1)}$ and $t_1^{(2)} < t_2^{(2)}$, only ordered paths are considered.
3. No-emission probabilities $\Pi_{pp \rightarrow Z}(\mu_F^{(p)}, t_1^{(p)}) \Pi_{pp \rightarrow Zj}(t_1^{(p)}, t_2^{(p)})$ are attached to the selected path p by means of trial showers [75]. The α_s reweighting factor for path p is

$$\prod_{i=1}^n \frac{\alpha_s(k_i^{(p)} t_i^{(p)})}{\alpha_s(\mu_{RME}^2)}. \quad (5.2)$$

¹At the beginning of the merging procedure, the cross section is recalculated, taking into account the looser cut due to the merging scale.

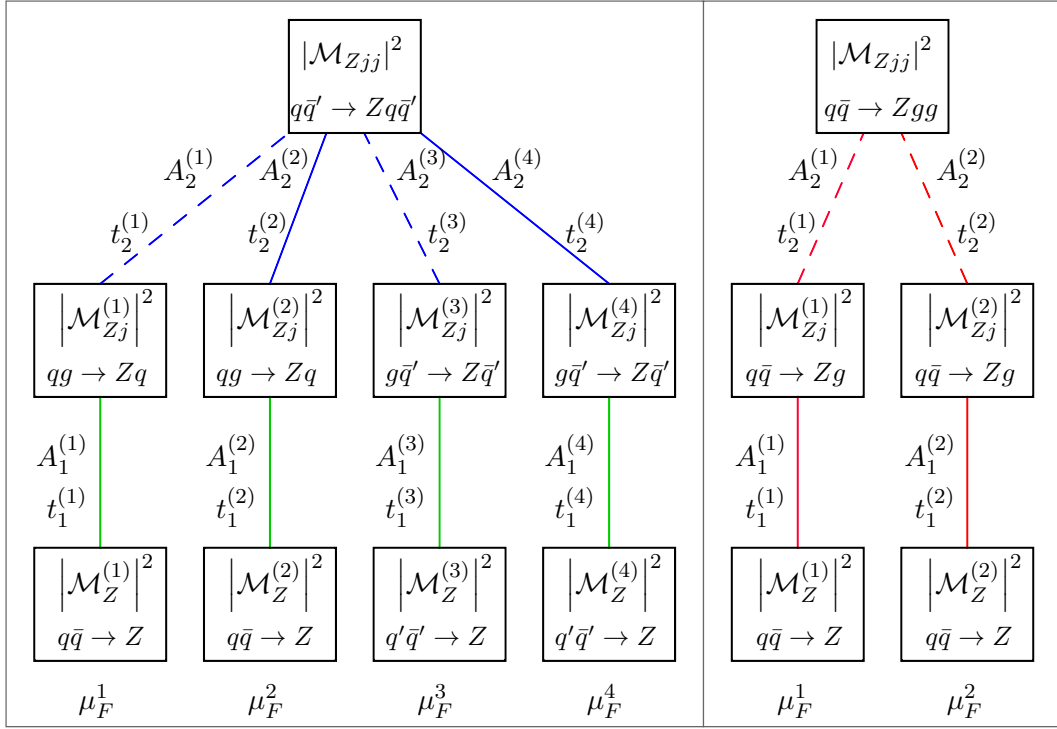


Figure 5.1: History trees for $q\bar{q}' \rightarrow Zq\bar{q}'$ (left) and a $q\bar{q} \rightarrow Zgg$ (right). The superscripts indicate a horizontal numbering within each tree. Solid (dashed) lines represent initial-initial (initial-final) clusterings: gluon emissions are red, gluons backwards evolving to quarks blue, and quarks backwards evolving to gluons green.

The product runs over the n segments of the selected path and replaces all α_s factors of the ME calculation with the couplings of the corresponding branching. With the superscript p dropped, the PDF reweighting factor is

$$\frac{f_0(x_0, \mu_F^2)}{f_n(x_n, \mu_{F, \text{ME}}^2)} \prod_{i=1}^n \frac{f_i(x_i, t_i)}{f_{i-1}(x_{i-1}, t_i)}. \quad (5.3)$$

The first PDF ratio replaces the PDFs in the ME calculation with the PDFs that the shower would have used as input for the Born state. The following PDF ratios reproduce the ones associated with each shower branching.

4. Further radiation is allowed through showering the event from $t_n^{(p)}$ (or μ_F for the lowest multiplicity sample). To avoid overlap between event samples with different multiplicities, the event is rejected if an additional branching results in a merging scale of $t_{\text{MS}} > t_{\text{MS}}^{\text{cut}}$, evaluated on the configuration after the branching. This cut is applied on all but the largest-multiplicity sample.

The selection and reweighting of the paths, together with the attached no-emission probabilities, reproduces the shower behaviour, see eq. (3.22). The emission patterns for $pp \rightarrow Z + \leq 3$ jets are now LO correct for scales above the merging cut.

Helicity Antenna Showers

The speed of the event generation is a crucial factor of MCEGs. The most computationally intense calculations performed in VINCIA are the ME evaluations during the MEC procedure discussed in chaps. 4 and 5. In Feynman-diagram based approaches, as implemented for instance in MADGRAPH, the ME result is obtained by taking into account all possible helicity configurations; summing over the helicities of outgoing particles and averaging over the incoming ones. Helicity is a gauge invariant quantum number and describes the projection of the spin onto the direction of momentum. The possible helicity states of partons are $+$ and $-$, whereas massive spin-1 objects have three, and spin-0 objects one possible helicity state. For massless particles, helicity is a “good quantum number”, i.e. it is a conserved quantity. The definition of the spin for massive particles is ambiguous though. Defining it by a projection onto a reference vector breaks Lorentz invariance and defining it by chirality (determined by the transformation property of a particle, see e.g. [146]) results in spin-flips. Chirality, however, has the advantage of being Lorentz invariant and equal to helicity for massless particles. In the current version of VINCIA the ambiguity is not taken into account as all partons are treated massless and the helicity of massive particles, such as the Z boson, is summed or averaged over. Calculating the ME by summing and averaging over helicities implies evaluating the amplitudes for an increasing number of different helicity configurations with increasing particle multiplicity. For instance, 48 helicity states exist for $pp \rightarrow Zjj$. If, however, the parton shower is capable of assigning explicit helicities to all partons, a significant increase in speed is achieved. Instead of summing over the helicity configurations, the amplitude has to be evaluated for only one state. This is possible as amplitudes with different external helicity states do not interfere.

A helicity-dependent antenna shower for final-state radiation has already been introduced in [147]. The extension to hadronic initial states is rather straightforward; we present a complete helicity-dependent antenna shower for initial- and final-state radiation in the publication in sec. 6.1, together with the corresponding antenna functions. A further small increase in speed is achieved by using Maximally Helicity Violating (MHV) amplitudes. A n -particle state, where all particles are considered outgoing, is in a MHV configuration if $n - 1$ particles have the same helicity. In this case the ME calculation reduces to a rather simple expression. A library of analytical MHV amplitudes for purely partonic external states and one lepton pair

plus partons has been implemented in VINCIA by Andrew Lifson. In the publication in sec. 6.1 we show how a helicity-dependent antenna shower for final- and initial-state radiation and MHV amplitudes are used to increase the speed of the parton shower with MECs. In addition, we introduce user-specifiable variations of the renormalisation scale and splitting kernels. Following the publication, sec. 6.2 shows how to obtain helicity-dependent antenna functions, given the unpolarized antenna functions and helicity-dependent DGLAP splitting kernels.

The helicity-dependence itself does not provide different radiation patterns, compared to the helicity-summed and -averaged parton shower. As will be shown in sec. 6.1, the singular terms of the generated radiation patterns are the same for both models. Therefore, the evolution of PDFs remains intact as the DGLAP limits of the antenna functions are not changed. By assigning explicit helicities to all partons, no unphysical helicity configurations are produced in the shower. However, there is no “consumer” of this information, i.e. neither the PDFs nor the fragmentation functions make use of it. The situation is fairly similar when MECs are applied: the parton-shower evolution is corrected such that all physical helicity states are generated according to the appropriate LO ME. The same holds for the helicity-independent shower, where unphysical helicity configurations do not contribute to the sum and average in the ME calculation.

6.1 Published Material

Helicity Antenna Showers for Hadron Colliders

Nadine Fischer, Andrew Lifson, and Peter Skands

Published in The European Physics Journal C 77 no. 10 (2017) 719

DOI: 10.1140/epjc/s10052-017-5306-7

e-Print: arXiv:1708.01736 [hep-ph]

Begins overleaf.

Helicity Antenna Showers for Hadron Colliders

Nadine Fischer^a, Andrew Lifson^{a,b}, Peter Skands^a

^a School of Physics and Astronomy, Monash University, Clayton, VIC 3800, Australia

^b ETH Zürich, Zürich, CH 8092, Switzerland

Abstract

We present a complete set of helicity-dependent $2 \rightarrow 3$ antenna functions for QCD initial- and final-state radiation. The functions are implemented in the VINCIA shower Monte Carlo framework and are used to generate showers for hadron-collider processes in which helicities are explicitly sampled (and conserved) at each step of the evolution. Although not capturing the full effects of spin correlations, the explicit helicity sampling does permit a significantly faster evaluation of fixed-order matrix-element corrections. A further speed increase is achieved via the implementation of a new fast library of analytical MHV amplitudes, while matrix elements from MADGRAPH are used for non-MHV configurations. A few examples of applications to QCD $2 \rightarrow 2$ processes are given, comparing the newly released VINCIA 2.200 to PYTHIA 8.216.

1 Introduction

The description of bremsstrahlung processes in parton-shower event generators typically starts from the probability density for unpolarised partons to emit unpolarised radiation, i.e., DGLAP kernels or dipole/antenna functions summed over outgoing and averaged over incoming polarisations/helicities. One way of incorporating nontrivial polarisation effects, used in PYTHIA [1], is to correlate the plane in which a gluon is produced, with the plane in which it subsequently branches, taking linear-polarisation effects into account on the intermediate propagator, and casting the result in terms of a non-uniform selection of the azimuthal φ angle around the direction of the branching gluon, see, e.g., [2]. A more complete, but also more cumbersome, alternative, used in HERWIG [3], is to keep track of spin correlations explicitly, using a spin-density matrix formalism [4–6]. In both cases, the nontrivial angular correlations ultimately arise from dot products between reference vectors expressing *linear* polarisations.

By contrast, a *helicity* basis does not rely on any external reference vectors, and hence helicity-dependence in and of itself does not generate any nontrivial angular correlations. Nonetheless, helicity-dependent radiation functions, as used for final-state radiation in VINCIA for a few years [7], do have some advantages: helicity conservation can be made explicit, allowing to trace helicities through the shower; unphysical helicity configurations are prevented from contributing to sums and averages; and the explicit helicity assignments allow faster evaluations of matrix-element correction (MEC) factors, since only a single (or a few) helicity amplitudes need to be evaluated for each ME-corrected parton state [7].

The concept of ME corrections was first developed to improve the description of radiation in PYTHIA (then called JETSET) outside the collinear region to agree with first-order matrix elements for $e^+e^- \rightarrow 3$ jets [8, 9], and was since extended to correct the first emission in a wide range of resonance-decay processes and some (colour-singlet) production processes [10, 11]. It was also used as a component of the first ME correction strategies in HERWIG [12, 13], and it forms the basis of the treatment of real corrections within the POWHEG

formalism [14, 15]. We note that, in these approaches, only the first shower emission is corrected, essentially by applying a multiplicative factor,

$$\mathcal{R}^{\text{MEC}} = \frac{\text{ME}}{\text{PS}}, \quad (1)$$

to the shower kernels, where ME is the relevant matrix-element expression (typically called “ R ” in POWHEG notation) and PS represents the (sum of) parton-shower contributions to the given phase-space point.

The limitation to single emissions was lifted by the development of iterated ME corrections [16]¹, implemented in VINCIA [17, 18], again first in the context of $e^+e^- \rightarrow \text{jets}$ [16] and subsequently for hadron collisions [18, 19]. Importantly, the most recent study in [19] extended the formalism to strongly-ordered and non-Markovian shower algorithms, expanding its applicability to essentially any shower algorithm in modern MC generators. Although a helicity-dependent (and hence computationally faster) version of the iterated-MEC algorithm was developed for final-state radiation [7], a fully-fledged helicity-dependent version for hadron collisions (and for strongly-ordered non-Markovian showers) has so far been missing. The aim of this paper is to develop this missing piece, while simultaneously presenting a complete set of helicity-dependent (and positive-definite) antenna functions for $2 \rightarrow 3$ branchings for both initial- and final-state radiation. In addition, some helicity configurations (called “maximally helicity violating”) can be expressed in compact analytical forms, hence we use such amplitudes for QCD $2 \rightarrow n$ processes whenever possible to speed up the calculation further. For non-MHV configurations, we use matrix elements from MADGRAPH 4 [20]. (Note that the use of MADGRAPH 4 puts some limitations on the configurations for which the relevant information for MEC factors can be extracted easily from the matrix elements. In particular, this is the case for amplitudes with multiple quark pairs. These limitations will be lifted by a new interface to MADGRAPH 5 which is currently under development [21].)

This article is organised as follows. In sec. 2, we give an overview over the helicity-dependent shower in VINCIA, including the extension to initial-state radiation and changes with respect to [18]. The matrix-element correction formalism is reviewed in short in sec. 3 together with a brief introduction to the MHV amplitudes in VINCIA. In sec. 4, we report on the new user-specifiable uncertainty variations. Results are presented in sec. 5, before giving some concluding remarks in sec. 6. The helicity-dependent antenna functions are given in app. A.

2 Helicity-Dependent Showers

A helicity-dependent antenna shower for final-state radiation has already been introduced in [7]. The extension to hadronic initial states is straightforward. We start with a brief review of how emissions are generated and helicities selected. In cases where an event with unpolarised partons is showered by VINCIA, a polariser function is first called, which uses helicity matrix elements to assign explicit helicities to all partons. Since the events are also assigned colour flows, we first define the joint probability to select a parton configuration with a colour flow i and a set of helicities h ,

$$P(h, i) = \underbrace{\frac{\text{FC}^h}{\sum_{h'} \text{FC}^{h'}}}_{\text{Helicity-Selection Factor}} \times \underbrace{\frac{\text{LC}_i^h}{\sum_j \text{LC}_j^h}}_{\text{Colour-Flow Selection Factor}}, \quad (2)$$

where the full-colour (FC) and leading-colour (LC) matrix elements squared are defined by

$$\text{FC}^h = \sum_{i,j} \mathcal{M}_i^h \mathcal{M}_j^{h*} \quad (3)$$

$$\text{LC}_i^h = |\mathcal{M}_i^h|^2 \quad (4)$$

¹We note that a form of iterated ME corrections is also used throughout the PYTHIA showers to impose quark-mass corrections [11], but the resulting process-dependent nonsingular terms will still only be fully correct for the first emission.

with \mathcal{M}_i the amplitude for colour-ordering i . We also make use of the notation

$$\text{VC}_i^h = \text{FC}^h \frac{\text{LC}_i^h}{\sum_j \text{LC}_j^h} \quad (5)$$

for the fraction of the full-colour helicity matrix element squared that is projected onto LC colour flow i .

As written here, the easiest would be to start by generating a helicity configuration, using the first factor in eq. (2) and then subsequently generate a colour flow using the second factor. For events which already have colour-flow assignments, the conditional probability for choosing helicity configuration h is simplest to define in terms of the redefined LC matrix elements,

$$P(h|i) = \frac{\text{VC}_i^h}{\sum_{h'} \text{VC}_i^{h'}}. \quad (6)$$

(If the corresponding matrix elements do not exist in VINCIA, the event will remain unpolarised and showered using helicity-averaged and -summed antenna functions.)

For events with explicit helicities, trial branchings are generated just as in the helicity-independent shower, i.e., using *unpolarised* trial-antenna function overestimates. After generating the post-branching kinematics (see, e.g., [17, 18]), the total probability for accepting a branching (denoting pre-branching partons by AB and post-branching ones by ijk)² is:

$$P_{\text{accept}} = \frac{\mathcal{A}_{\text{phys}}}{\mathcal{A}_{\text{trial}}} = \frac{\sum_{h_i, h_j, h_k} \mathcal{A}(h_A, h_B; h_i, h_j, h_k)}{\mathcal{A}_{\text{trial}}}, \quad (7)$$

for fixed helicities $h_{A,B}$ of the parent partons. The sum over daughter helicities, $h_{i,j,k}$, in the physical antenna function, $\mathcal{A}_{\text{phys}}$, runs over all possible (physical) helicities for the ijk partons, with each term, $\mathcal{A}(h_A, h_B; h_i, h_j, h_k)$, being a helicity-dependent antenna function. To avoid clutter, and for ease of reference, we collect the precise forms for these functions in the appendix. We note that some of the functions differ (by nonsingular terms) from those used in previous versions of VINCIA, in particular those in [7, 18]. We also note that the accept probability defined by eq. (7) is in general identical to the unpolarised one (i.e., where one averages over h_A and h_B as well), up to nonsingular terms. In case of initial-state radiation, eq. (7) will be multiplied with the accept probability for the PDF ratios, just as in the unpolarised case [18].

Explicit helicities are then selected for the daughters according to the relative probabilities given by the antenna functions,

$$P(h_A, h_B; h_i, h_j, h_k) = \frac{\mathcal{A}(h_A, h_B; h_i, h_j, h_k)}{\sum_{h_i, h_j, h_k} \mathcal{A}(h_A, h_B; h_i, h_j, h_k)}, \quad (8)$$

where the denominator is equal to the numerator in eq. (7). Helicities are assigned to initial-state partons as well, using the same formalism. With the assumption that positive-helicity partons appear equally often as negative-helicity ones in the (anti)proton, the algorithm does not require any modifications when considering initial-state partons.

Helicity conservation implies that, for gluon emission off (massless) quarks or final-state gluons, the parent partons do not change their helicities. A subtlety arises, however, for emissions off initial-state gluons. In the perspective of forwards evolution, such a branching looks like $g_i^I \rightarrow g_A^I g_j^F$, where superscript I (F) denotes an initial-state (final-state) parton; clearly, the helicity of parton i can be inherited by either parton j or parton A without violating helicity conservation. Hence the reader should not be confused by the appearance of physical initial-state antenna functions for which $h_A \neq h_i$ in apps. A.3 and A.4, with corresponding DGLAP limits given in app. A.6.

For completeness, we also report on the following changes in VINCIA with respect to [18]:

²This is the same labelling convention as used in the VINCIA reference for final-state helicity showers [7].

- The so-called “Ariadne factor” [22] for gluon splitting antennae has been removed completely, as it has only been applied to 4-jet events in hadronic Z decays and its influence cancels once ME corrections are used in the evolution.
- The CMW-rescaling of α_s [23] is no longer applied to the soft-eikonal terms of the antenna functions, but rather as a global rescaling of Λ_{QCD} , independent of the type of branching.
- By default the power shower approach is used for hard process without QCD partons in the final state. This obviates the need for a separate event sample containing jets associated with scales larger than the factorisation scale, which has been introduced in [18]. For QCD-type processes the shower starts the evolution at the factorisation scale.
- The so-called “smooth ordering”, which allows the shower to populate phase-space regions beyond the reach of traditional ordered showers, is no longer used. Consequently, the MECs formalism so far used in VINCIA is no longer applicable and the MECs method for ordered showers of [19] is applied. See sec. 3 for a brief review of the formalism.
- The CKKW-L merging implementation in PYTHIA 8 [24] is now also available in VINCIA, making use of the parameters in PYTHIA 8. This allows to supplement the MECs method for ordered showers with non-shower-like events, as discussed in [19]. Note however, that it is not possible to combine the merging procedure with the helicity-dependent shower.
- The hard-coded uncertainty variations have been replaced by the user-specifiable variations which are described in detail in sec. 4.

3 Matrix-Element Corrections and MHV amplitudes in Vincia

3.1 Matrix-Element Corrections

The GKS formalism for iterated matrix-element corrections [16] was originally based on so-called smoothly ordered showers, with a Markovian (history-independent) choice of restart scale after each branching. This allows the shower algorithm to generate phase-space points that violate the nominal ordering condition of the shower, at a suppressed but still non-zero rate, thus filling previously inaccessible regions of phase space; the correct (tree-level) emission rates can then be obtained via matrix-element corrections just as in the ordered part of phase space. However, general arguments indicate that the effective Sudakov factors for the non-ordered histories, are probably not correct [18, 25, 26]. Recent efforts [19, 26] have therefore shifted focus back to filling the phase space for multiple hard emissions while remaining within the paradigm of strong ordering. In particular, we take the strongly-ordered iterated-MEC formalism presented in [19] as our starting point, and adapt it to include explicit helicities.

The question of Markovian vs non-Markovian behaviour comes about since the value of the shower evolution parameter in conventional strongly-ordered showers depends on which parton was the last one to be emitted. This cannot be uniquely determined merely by considering a given parton configuration; the value is a function of what shower history (or path) led to the configuration in question; a non-Markovian aspect. In the context of iterated ME corrections, non-Markovianity implies that the MEC factors contain nested sums over shower histories involving clusterings all the way back to the Born configuration (while a Markovian algorithm only requires a single level of clusterings [16]).

Within the formalism presented in [19], the splitting kernels are redefined by multiplying them with the

correction factor

$$\begin{aligned} \mathcal{R}(\Phi_{n+1}) = |\mathcal{M}(\Phi_{n+1})|^2 & \left[\sum_{\Phi'_n} \mathcal{A}(\Phi_{n+1}/\Phi'_n) \mathcal{R}(\Phi'_n) \sum_{\Phi'_{n-1}} \Theta(t(\Phi'_n/\Phi'_{n-1}) - t(\Phi_{n+1}/\Phi'_n)) \mathcal{A}(\Phi'_n/\Phi'_{n-1}) \mathcal{R}(\Phi'_{n-1}) \right. \\ & \prod_{k=n-2}^{k \leq 1} \left(\sum_{\Phi'_k} \Theta(t(\Phi'_{k+1}/\Phi'_k) - t(\Phi'_{k+2}/\Phi'_{k+1})) \mathcal{A}(\Phi'_{k+1}/\Phi'_k) \mathcal{R}(\Phi'_k) \right) \\ & \left. \sum_{\Phi'_0} \Theta(t(\Phi'_1/\Phi'_0) - t(\Phi'_2/\Phi'_1)) \mathcal{A}(\Phi'_1/\Phi'_0) \Theta(t(\Phi'_0) - t(\Phi'_1/\Phi'_0)) |\mathcal{M}(\Phi'_0)|^2 \right]^{-1}. \quad (9) \end{aligned}$$

$|\mathcal{M}(\Phi_{n+1})|^2$ denotes the matrix element squared of the Φ_{n+1} state and $\mathcal{A}(\Phi_{n+1}/\Phi'_n)$ the antenna function, associated with the clustering $\Phi_{n+1} \rightarrow \Phi'_n$. The denominator sums over all possible ways the shower could have produced the $n+1$ -particle state Φ_{n+1} from a given Born state Φ'_0 , including the correct weights of every shower step on the way. This yields the recursive structure of eq. (9) and the dependence on the correction factors of the previous orders. In addition to the (process-dependent) scale $t(\Phi'_0)$, at which the shower starts the evolution off the Born state is taken into account.

For a helicity-dependent correction, we modify eq. (9) such that, for a given polarised Φ_n state, the sums over the intermediate states $\Phi_{n-1} \dots \Phi_0$ are extended to include all possible helicity configurations. As an example, consider a possible clustering of a final-state $q\bar{q}$ pair to a gluon. In the unpolarised case, one term corresponding to the clustering $q\bar{q} \rightarrow g$ contributes with the respective unpolarised antenna function and matrix element (which both implicitly involve helicity sums of course). For a polarised $q_+\bar{q}_-$ pair, two different clustered helicity states are possible, $q_+\bar{q}_- \rightarrow g_+$ and $q_+\bar{q}_- \rightarrow g_-$, each contributing according to their antenna function and matrix element. The evolution variable, however, is the same as in the unpolarised case. This concludes our discussion of helicity-dependent matrix element corrections.

3.2 MHV Basics

For fast evaluation of certain types of helicity configurations VINCIA uses Maximally Helicity Violating (MHV) amplitudes. MHV amplitudes have the advantage of being compact analytical expressions which are independent of Feynman diagrams; see [27, 28] for reviews. In this section, we briefly introduce the concepts and notation relevant to understanding the conventions and properties of the small library of MHV amplitudes implemented in VINCIA.

In the following we consider all particles to be outgoing and massless. We recall that in this limit a particle's helicity corresponds to its chirality, and define our spinors in the helicity basis:

$$v_{\mp}(p) = u_{\pm}(p) = \frac{1}{2} (1 \pm \gamma^5) u(p), \quad \overline{v_{\mp}(p)} = \overline{u_{\pm}(p)} = \overline{u(p)} \frac{1}{2} (1 \mp \gamma^5). \quad (10)$$

The notation $\langle ij \rangle$ and $[ij]$ is used for inner products of such spinors:

$$\overline{u_{-}(i)} u_{+}(j) \equiv \langle ij \rangle = \sqrt{p_j^+} e^{i\phi_i} - \sqrt{p_i^+} e^{i\phi_j}, \quad (11)$$

$$\overline{u_{+}(i)} u_{-}(j) \equiv [ij] = \langle ji \rangle^*, \quad (12)$$

in terms of the (light-cone) momentum $p_i^+ = p_i^0 + p_i^3$ and $e^{i\phi_i} = (p_i^1 + ip_i^2)/\sqrt{p_i^+}$. For more details about spinor inner products and their properties see e.g. [27, 28]. Note that in recent literature one often finds the convention $[ij] = \langle ij \rangle^*$, which is different to above (see e.g. [29]).

In the all-outgoing convention, helicity conservation implies that at least two pairs of opposite-helicity partons must exist for an n -parton amplitude to be nonzero³. If the remaining $n-4$ partons are all chosen to be of the same helicity (+ or -), the amplitude is called maximally helicity violating (MHV), and has

³E.g., think of $++ \rightarrow ++$ and cross the two incoming positive helicities to be outgoing negative ones.

a remarkably simple structure. The first MHV amplitude to be discovered was the all-gluon Parke-Taylor amplitude [30]. In the following years this was extended to include one [31, 32] and two [33–35] quark pairs, as well as to the case of a quark pair and a massive vector boson which decays leptonically [36, 37].

All-Gluon Amplitudes: To use these amplitudes we first note that the colour information can be factorised from the kinematics. In the n -point all-gluon case we use:

$$\mathcal{M}_n(g_1, g_2, \dots, g_n) = g_s^{n-2} \sum_{\sigma \in S_n/Z_n} \text{Tr}(t^{a_{\sigma(1)}} \dots t^{a_{\sigma(n)}}) A_n(\sigma(p_1^{h_1}), \dots, \sigma(p_n^{h_n})), \quad (13)$$

where g_s is the strong coupling ($g_s^2 = 4\pi\alpha_s$), the normalisation convention is $t^a = \lambda^a \sqrt{2}$ with λ^a being the generators of $SU(3)$, p_i is the gluon momentum, h_i the gluon helicity, $\text{Tr}(t^{a_{\sigma(1)}} \dots t^{a_{\sigma(n)}})$ the colour factor and $A_n(\sigma(p_1^{h_1}), \dots, \sigma(p_n^{h_n}))$ the kinematic part of the amplitude. The sum is over all non-cyclic permutations σ of the particles. The Parke-Taylor amplitude then describes the kinematic part of eq. (13) and is given by:

$$A_n(i^-, j^-) = i \frac{\langle ij \rangle^4}{\langle 12 \rangle \langle 23 \rangle \dots \langle n1 \rangle}, \quad (14)$$

where gluons i and j have negative helicity, and all other particles have positive helicity.

One Quark Pair: If we add a $q\bar{q}$ pair we require that the quark and antiquark have opposite helicities (consistent with the gluon having spin 1), and use the following colour basis:

$$\mathcal{M}_n(q, g_1, g_2, \dots, g_{n-2}\bar{q}) = g_s^{n-2} \sum_{\sigma \in S_{n-2}} (t^{a_{\sigma(1)}} \dots t^{a_{\sigma(n-2)}})_{ij} A_n(q^{h_q} \sigma(p_1^{h_1}), \dots, \sigma(p_{n-2}^{h_{n-2}}) \bar{q}^{h_{\bar{q}}}), \quad (15)$$

where q , h_q , and i (\bar{q} , $h_{\bar{q}}$, and j) are respectively the quark (anti-quark) momentum, helicity, and colour index; and the sum is over all permutations of the gluons. If the quark and gluon i each have negative helicity and all other particles positive helicity, then the kinematic amplitude is the given by:

$$A_n(q^-, i^-, \bar{q}^+) = \frac{\langle qi \rangle^3 \langle \bar{q}i \rangle}{\langle \bar{q}q \rangle \langle q1 \rangle \langle 12 \rangle \dots \langle (n-2)\bar{q} \rangle}, \quad (16)$$

where the numbers refer to the (colour-ordered) gluons. If we exchange the helicities on the quarks, it is sufficient to exchange the exponents in the numerator:

$$A_n(q^+, i^-, \bar{q}^-) = \frac{\langle qi \rangle \langle \bar{q}i \rangle^3}{\langle \bar{q}q \rangle \langle q1 \rangle \langle 12 \rangle \dots \langle (n-2)\bar{q} \rangle}. \quad (17)$$

Two Quark Pairs: The four-quark, $n-4$ gluon colour structure is given by:

$$\begin{aligned} \mathcal{M}_n(q, \bar{q}, Q, \bar{Q}, g_1, \dots, g_{n-4}) &= g_s^{n-2} \frac{A_0(h_q, h_Q, h_{\bar{q}})}{\{q\bar{q}\}\{Q\bar{Q}\}} \times \\ &\left(\sum_{\sigma \in S_{n-4}} (t^{a_{\sigma(1)}} \dots t^{a_{\sigma(k)}})_{q\bar{q}} (t^{a_{\sigma(k+1)}} \dots t^{a_{\sigma(n-4)}})_{Q\bar{Q}} \times A_n^{(0)}(q, 1, \dots, k, \bar{q}, Q, k+1, \dots, n-4, \bar{Q}) \right. \\ &\left. - \frac{1}{N_C} (t^{a_{\sigma(1)}} \dots t^{a_{\sigma(k')}})_{q\bar{q}} (t^{a_{\sigma(k'+1)}} \dots t^{a_{\sigma(n-4)}})_{Q\bar{Q}} \times A_n^{(1)}(q, 1, \dots, k', \bar{q}, Q, k'+1, \dots, n-4, \bar{Q}) \right), \end{aligned} \quad (18)$$

where $\{ij\} = \langle ij \rangle$ for positive-helicity gluons and $\{ij\} = [ji]$ for negative-helicity gluons; q and Q label the two quark lines; $A_0(h_q, h_Q, h_{\bar{q}})$ is a kinematic function which depends on the helicities of the two quarks and

the gluons,

$$\begin{array}{c|c} (h_q, h_Q, h_g) & A_0(h_q, h_Q, h_g) \\ \hline (+, +, +) & \langle \bar{q}Q \rangle^2 \\ (+, +, -) & [qQ]^2 \\ (+, -, +) & \langle \bar{q}Q \rangle^2 \\ (+, -, -) & [qQ]^2 \end{array}, \quad (19)$$

with opposite-helicity cases obtained using parity transformation $\langle ij \rangle \leftrightarrow [ji]$; and the two functions $A_n^{(0)}$ and $A_n^{(1)}$ are kinematic amplitudes, for which we have used the short-hand notation $q \equiv q^{h_q}$, $i \equiv \sigma(p_i^{h_i})$ etc.:

$$A_n^{(0)} = \frac{\{q\bar{Q}\}}{\{q1\}\{12\}\dots\{k\bar{Q}\}} \frac{\{Q\bar{q}\}}{\{Q(k+1)\}\{(k+1)(k+2)\}\dots\{(n-4)\bar{q}\}}, \quad (20)$$

$$A_n^{(1)} = \frac{\{q\bar{q}\}}{\{q1\}\{12\}\dots\{k\bar{q}\}} \frac{\{Q\bar{Q}\}}{\{Q(k+1)\}\{(k+1)(k+2)\}\dots\{(n-4)\bar{Q}\}}. \quad (21)$$

We must sum over all possible partitions of gluons between the two quark colour lines, and also over all possible permutations of gluons within those partitions. If there are no gluons propagating off a particular colour line, then that colour line is described by a Kronecker delta. Note that this decomposition only works for the MHV configuration.

Drell-Yan, DIS, and hadronic Z decays: To create MHV amplitudes with a single quark pair, a single lepton pair, and an arbitrary number of gluons, the four-quark amplitude can be recycled with all gluons coming from a single quark line. The second quark line is now equivalent to a $l\bar{l}$ pair up to couplings and an overall propagator factor. The amplitude then has the form

$$\mathcal{M}_n(h_q, h_l, h_g) = ig_s^{n-4} \sum_{\sigma \in S_{n-4}} (t^{a_{\sigma(1)}} \dots t^{a_{\sigma(n-4)}})_{ij} A_n(q^{h_q}, \sigma(p_1^{h_1}), \dots, \sigma(p_{n-4}^{h_{n-4}}), \bar{q}^{h_{\bar{q}}}, l^{h_l}, \bar{l}^{h_{\bar{l}}}), \quad (22)$$

where the sum is again over all gluon permutations. The kinematic amplitude is given by

$$A_n(q, 1, \dots, n-4, \bar{q}, l, \bar{l}) = \sum_{V=\gamma, Z, W^\pm} M_V^l(h_l, h_q, h_g) \frac{1}{\{q1\}\{12\}\dots\{(n-4)\bar{q}\}}, \quad (23)$$

where the braces have the same meaning as in eq. (21), and the function M_V^l is given by

$$M_V^l(h_l, h_q, h_g) = \frac{A_0(h_l, h_q, h_g) [\bar{l}l] (v_\pm^l)_V (v_\pm^q)_V}{\langle l\bar{l} \rangle [\bar{l}l] - M_V^2 + i\Gamma_V M_V}, \quad (24)$$

where $A_0(h_l, h_q, h_g)$ is given by eq. (19), $(v_\pm^l)_V$ ($(v_\pm^q)_V$) is the coupling of lepton l (quark q) with helicity \pm to vector V , and M_V and Γ_V are the mass and width of the vector boson respectively.

Finally, we remark that in all of the above expressions, flipping the helicity of every particle is equivalent to exchanging each $\langle ij \rangle \leftrightarrow [ji]$. This concludes our brief recapitulation of the basics of the MHV formalism and convention choices.

3.3 MHV within Vincia

The MHV amplitudes that are made available in standalone VINCIA are summarised in tab. 1. Note that these amplitudes are so far only used for QCD $2 \rightarrow n$ matrix-element corrections, and that the second quark pair must have a different flavour to the first.

The colour-summed squared matrix element is calculated using the following matrix equation:

$$\text{FC} = \sum_{ij} A_{\sigma_i}^\dagger C_{ij} A_{\sigma_j}, \quad (25)$$

Type of process	Number of particles
All-gluon	4-6
1 quark pair plus gluons	4-7
2 quark pairs plus gluons	4,5
1 lepton pair, 1 quark pair plus gluons	4-9

Table 1: The types of processes available in VINCIA's MHV library.

where FC stands for the full colour-summed matrix element squared as in eq. (3), C_{ij} is a colour matrix obtained by multiplying the colour factor from permutation σ_i onto the conjugate colour factor from σ_j , and the sum is over all colour orders. We optimise the all-gluon amplitudes by diagonalising C_{ij} for the 4 and 5-gluon matrix elements, and partially diagonalising C_{ij} for the 6-gluon matrix element as done in [27].

By default, VINCIA uses MHV amplitudes wherever possible to compute its matrix-element correction factors, thus ensuring the fastest possible run time. However, this can be turned off (e.g., for cross checks with amplitudes from MADGRAPH) using the flag `vincia:useMHVamplitudes`. To calculate an MHV ME correction, VINCIA actively crosses the initial-state partons into the final state, rearranges the partons into the correct colour order, calculates all of the explicit spinor products needed, and then calculates the matrix element squared.

The calculation of ME corrections for MHV configurations exhibits the nice feature that all clustered states in eq. (9) are MHV configurations as well. Helicity conservation does not allow $++ \rightarrow -$ nor $-- \rightarrow +$ clusterings (in the all-outgoing convention). This results in clustered states being either MHV configurations themselves or unphysical states with a vanishing amplitude. Consider n positive- and 2 negative-helicity outgoing partons as an example. Here clustered states contain either $n - 1$ positive- and 2 negative-helicity partons (MHV) or n positive- and 1 negative-helicity partons (unphysical).

For instructions on how to use VINCIA for calculating spinor products or MHV amplitude in a standalone context, see the online user guide [38].

3.4 Polarising events with MHV

The fact that VINCIA assigns helicities to unpolarised events, with relative probabilities according to the corresponding helicity matrix elements squared, was briefly discussed in sec. 2. An interesting simplification occurs when all of the contributing amplitudes are of the MHV kind, as is, e.g., the case for all QCD $2 \rightarrow 2$ and $2 \rightarrow 3$ processes. The simplification follows by noting that the full-colour (FC) MHV matrix elements squared all have the following form (so long as there is at most one quark pair):

$$\text{FC}^h = |A_n^h(1, \dots, n)|^2 \left| \sum_{\sigma} \frac{1}{\langle \sigma(1)\sigma(2) \rangle \dots \langle \sigma(n)\sigma(1) \rangle} \text{CF}(\sigma(1) \dots \sigma(n)) \right|^2 \equiv M_n^h \left| \sum_{\sigma} F(\sigma) \right|^2, \quad (26)$$

where h is a label denoting the helicity assignments, $M_n^h \equiv |A_n^h(1, \dots, n)|^2$ is some function of the helicities and momenta, σ is the relevant set of permutations, CF is the relevant colour factor at the amplitude level, and $|\sum_{\sigma} F(\sigma)|^2$ is the square of the sum over colour permutations. For example, in the all-gluon amplitude $A_n^h(1, \dots, n)$ could be $\langle ij \rangle^4$. We have therefore factored out the helicity information M_n^h from the colour information. This also works for the LC matrix elements LC_i^h which are given by eq. (26) above without the sum of permutations. That is, $\text{LC}_i^h = M_n^h |F(\sigma_i)|^2$. Recall that the conditional probability defined in (6) used to pick helicities for configurations that already have colour assignments has the form:

$$P(h|i) = \frac{\text{VC}_i^h}{\sum_{h'} \text{VC}_i^{h'}} = \frac{\text{FC}^h \text{LC}_i^h}{\sum_j \text{LC}_j^h} \left[\sum_{h'} \frac{\text{FC}^{h'} \text{LC}_i^{h'}}{\sum_k \text{LC}_k^{h'}} \right]^{-1}. \quad (27)$$

We can use eq. (26) to simplify this:

$$\begin{aligned}
P(h|i) &= \frac{M_n^h |\sum_{\sigma} F(\sigma)|^2 M_n^h |F(\sigma_i)|^2}{\sum_j M_n^h |F(\sigma_j)|^2} \left[\frac{\sum_{h'} M_n^{h'} |\sum_{\sigma'} F(\sigma')|^2 M_n^{h'} |F(\sigma_i)|^2}{\sum_k M_n^{h'} |F(\sigma_k)|^2} \right]^{-1} \\
&= M_n^h \frac{|\sum_{\sigma} F(\sigma)|^2 |F(\sigma_i)|^2}{\sum_j |F(\sigma_j)|^2} \left[\frac{|\sum_{\sigma'} F(\sigma')|^2 |F(\sigma_i)|^2}{\sum_k |F(\sigma_k)|^2} \sum_{h'} M_n^{h'} \right]^{-1} \\
&= \frac{M_n^h}{\sum_{h'} M_n^{h'}}.
\end{aligned} \tag{28}$$

This shows that our factorisation allows to use the much simpler expressions $M_n^h \equiv |A_n^h(1, \dots, n)|^2$ to polarise the process. QCD processes are non-chiral, so we explicitly calculate only half of the factors M_n^h to polarise them, since the other half are equal by parity. For the mostly-plus helicity case the factors $A_n^h(1, \dots, n)$ are

Process	Negative-helicity particles	$A_0^h(1, \dots, n)$
All-gluon	i, j	$\frac{1}{(ij)^4}$
Single Quark Pair	q, i	$\langle qi \rangle^3 \langle \bar{q}i \rangle$
Single Quark Pair	\bar{q}, i	$\langle q\bar{i} \rangle \langle \bar{q}i \rangle^3$
Quark Pair and Lepton Pair	–	$A_0(h_l, h_q, +)(v_{\pm}^l)_V (v_{\pm}^q)_V$

(29)

while the mostly plus factors are given by the usual parity relation.

Note that this also holds for the full-colour amplitudes used for selecting helicities at the colour-summed level, cf. eq. (2),

$$P(h) = \frac{\text{FC}^h}{\sum_{h'} \text{FC}^{h'}} = \frac{M_n^h}{\sum_{h'} M_n^{h'}} \frac{|\sum_{\sigma} F(\sigma)|^2}{|\sum_{\sigma'} F(\sigma')|^2} = \frac{M_n^h}{\sum_{h'} M_n^{h'}}. \tag{30}$$

The preceding argument also works for 4-quark MHV amplitudes with distinct quark pairs provided one changes eq. (26) to include the second colour connection. However, this doesn't work for all 4-quark MHV amplitudes because there is an extra colour-connection when two identical quarks have the same helicity. Hence the colour factor depends on the helicity and cannot be factorised.

3.5 Speed Comparisons

As a measure of the relative speed of helicity-dependent vs helicity-summed ME corrections, and the difference between using MHV matrix elements or MADGRAPH 4 ones, we consider the following specific (but fairly representative) benchmark case: $qg \rightarrow qg$ Born-level processes, with a minimum \hat{p}_{\perp} of 100 GeV, in pp collisions with $E_{\text{cm}} = 10$ TeV. A technical point is that, for this comparison, we switch $g \rightarrow q\bar{q}$ branchings off in the shower, so that the generated shower configurations are all of the simple $qg \rightarrow qg + \text{gluons}$ type. This allows us to illustrate speeds of ME corrections with up to three additional legs while, if $g \rightarrow q\bar{q}$ branchings had been switched on, the current version of VINCIA is restricted to ME corrections with up to two additional legs. (This restriction will be lifted in a future update.)

Fig. 1 illustrates the number of milliseconds it takes to generate one shower, as a function of the number of legs that are requested to be ME-corrected. The solid (red) line without symbols uses helicity-summed showers and matrix elements, while the two blue curves (with symbols) show the dependence of the helicity-dependent formalism, with or without enabling the library of MHV matrix elements, respectively. For reference, the thick dashed horizontal line shows the time it takes to generate multi-parton interactions (MPI) and hadronisation for the same events⁴. For 0 or 1 corrected emissions, the helicity-summed shower is actually slightly faster, since the Born-level polariser and the helicity selection in the shower take a little extra time and the first-order ME corrections are very quick to evaluate even when summing over helicities. At two legs, however, the helicity-dependent formalism is up to 30% quicker (with the MHV library switched

⁴The thickness of the dashed line reflects that the helicity-dependent showers result in slightly longer MPI generation times due to the slightly slower showering off the MPI systems.

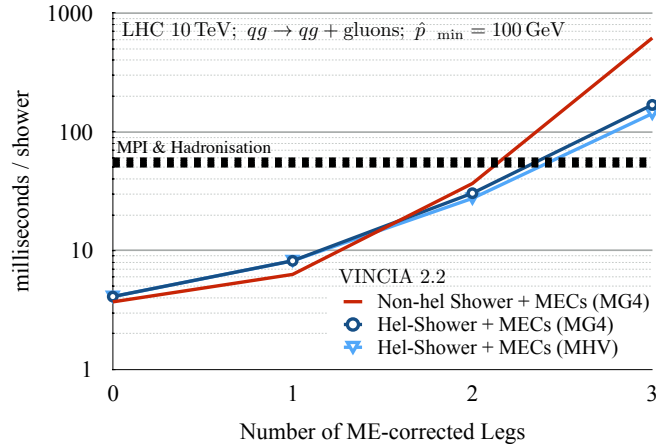


Figure 1: Speed comparison for helicity-independent (“Non-hel”) and helicity-dependent (“Hel”) showers as a function of the number of ME-corrected legs, for $q\bar{q} \rightarrow q\bar{q} + \text{gluons}$ with $\hat{p}_{\perp \text{min}} = 100$ GeV, for pp collisions at $E_{\text{cm}} = 10$ TeV. The dashed horizontal line indicates the time it takes to generate MPI and hadronisation for the same events. Results were obtained from 10,000 events generated for each run, on a single 2.9 GHz Intel Core i7 processor, using the `clang` compiler (v3.9), with `-O2` optimisation.

on) than the helicity-summed one. At three legs, the difference is a factor 4, with the MHV library allowing to shave an extra $\sim 15\%$ off the shower-generation time relative to using only MG4 matrix elements.

One also notices that by two corrected legs, the showering time is becoming comparable to the time it takes to generate MPI and hadronisation for the events, hence this is the point at which the showering speed would start to be felt in the context of generating full events. By three corrected legs, the ME corrections dominate the event-generation time. The default in the current version of VINCIA is that ME corrections are enabled for QCD $2 \rightarrow 2$ processes up to two additional legs; the event-generation time should therefore stay within roughly a factor 2 of that of the uncorrected algorithm. The complete set of matrix elements required for 3rd-order corrections will be provided in a future update. For hadronic Z , W , and H production or decay, the full set of 3rd-order matrix elements are already available in the current version. (We note that the implementation of the iterated-MEC algorithm itself is general and could in principle handle any number of legs, if provided with the required matrix elements.)

4 Automated Uncertainty Variations

Methods to deliver automated shower-uncertainty bands as vectors of alternative event weights, as first proposed in [16], were recently implemented in all of the main general-purpose event generators [39–41]. As a part of the work reported on here, we adapted the implementation in VINCIA to enable user-specifiable variations of the renormalisation scale and antenna functions using similar keywords as those defined in the PYTHIA 8 implementation [39]. The variation of the renormalisation scale is performed as

$$\alpha_s(t) \rightarrow \alpha_s(kt) . \quad (31)$$

The renormalisation-scale prefactor k can be chosen to be the same for all types of branchings or specific for the type of emission or splitting. For gluon emission we include an NLO-compensating term as

$$\alpha_s(t) \rightarrow \alpha_s(kt) \left(1 + \zeta \frac{\alpha_s(\mu_{\text{max}})}{2\pi} b_0 \ln(k) \right) , \quad (32)$$

where $b_0 = (11N_C - 2n_F)/3$ with $N_C = 3$ and n_F is the number of active flavours at the scale t . The scale μ_{\max} is defined as $\max(m_{\text{ant}}, kt)$ with m_{ant} the mass of the parent antenna. The prefactor is

$$\zeta = \begin{cases} 1 - s_{ik}/s_{IK} & \text{for a final-final branching } IK \rightarrow ijk \\ 1 - s_{AB}/s_{ab} & \text{for an initial-initial branching } AB \rightarrow ajb \\ 1 - s_{AK}/(s_{AK} + s_{jk}) & \text{for an initial-final branching } AK \rightarrow ajk \end{cases} \quad (33)$$

The user-specifiable keywords for the renormalisation-scale variations are the following:

Final-Final: `ff:muRfac`, `ff:QQemit:muRfac`, `ff:QGemit:muRfac`, `ff:GGemit:muRfac`, and `ff:XSsplit:muRfac`
Initial-Final: `if:muRfac`, `if:QQemit:muRfac`, `if:QGemit:muRfac`, `if:GGemit:muRfac`,
`if:GXconv:muRfac`, `if:QXsplit:muRfac`, and `if:XSsplit:muRfac`
Initial-Initial: `ii:muRfac`, `ii:QQemit:muRfac`, `ii:QGemit:muRfac`, `ii:GGemit:muRfac`,
`ii:GXconv:muRfac`, and `ii:QXsplit:muRfac`

We further include a variation of the antenna functions by nonsingular terms to represent unknown (and in general process-dependent) corrections to hard radiation,

$$\mathcal{A}(s_{12}, s_{23}, s_{\text{ant}}) \rightarrow \mathcal{A}(s_{12}, s_{23}, s_{\text{ant}}) + \frac{C_{\text{NS}}}{s_{\text{ant}}}, \quad (34)$$

with s_{12} and s_{23} the branching invariants and s_{ant} the invariant mass squared of the parent antenna. The additional nonsingular term $C_{\text{NS}}/s_{\text{ant}}$ is distributed evenly amongst all helicity configurations for a specific antenna function, i.e. all helicity-dependent antenna functions obtain the same fraction of the nonsingular term. As for the renormalisation-scale variation, C_{NS} can be chosen to be the same for all types of antenna functions, but we also include the possibility to specify different finite terms for each type. The user-specifiable keywords for the splitting-kernel variations are the following:

Final-Final: `ff:cNS`, `ff:QQemit:cNS`, `ff:QGemit:cNS`, `ff:GGemit:cNS`, and `ff:XSsplit:cNS`
Initial-Final: `if:cNS`, `if:QQemit:cNS`, `if:QGemit:cNS`, `if:GGemit:cNS`, `if:GXconv:cNS`,
`if:QXsplit:cNS`, and `if:XSsplit:cNS`
Initial-Initial: `ii:cNS`, `ii:QQemit:cNS`, `ii:QGemit:cNS`, `ii:GGemit:cNS`, `ii:GXconv:cNS`, and
`ii:QXsplit:cNS`

All variations can be combined arbitrarily for a comprehensive uncertainty study. Note also that the nonsingular-term variations are cancelled by ME corrections (up to the corrected order) and are therefore only carried out for uncorrected orders. Any significant remaining dependence on C_{NS} indicates a need for further corrections from hard matrix elements, while a significant dependence on the renormalisation scale indicates a need for further corrections at the loop level.

Finally, it is worth emphasising that the statistical fluctuations of the uncertainty variations are generally larger than for the central (non-varied) predictions. This is due to the central prediction being unweighted (in our setup) and the variations being computed by reweighting. See [40] for an example of how weighting (“biasing”) the central distribution can improve the relative statistical precision of the uncertainty bands.

5 Example Application

To illustrate the properties of the ME-corrected algorithm (and uncertainty variations) in the context of a realistic application, we consider showers off $gg \rightarrow gg$ Born-level events and compare PYTHIA 8.226 and VINCIA 2.200 on three observables sensitive to different aspects of the evolution: early branchings, late branchings, and a polarisation effect, respectively:

1. **Early branchings:** the 3-jet resolution scale, d_{23} , using the longitudinally invariant k_{\perp} -jet algorithm with $R = 0.4$.

2. **Late branchings:** the 6-jet k_{\perp} resolution scale, d_{56} , with the same jet algorithm as above.
3. **Gluon polarisation:** the angle between the event plane (characteristic of the original $gg \rightarrow gg$ Born-level event) and the plane of a subsequent $g \rightarrow b\bar{b}$ splitting. Here, the anti- k_{\perp} jet algorithm with $R = 0.2$ is used (so that the b jets can be resolved down to small separations), and we impose a minimum jet p_{\perp} of 50 GeV. (For further ideas on how to exploit heavy-flavour tags to probe $g \rightarrow q\bar{q}$ splittings at colliders, see e.g. [42, 43].)

The basic $2 \rightarrow 2$ QCD process is sampled with the cut $\hat{p}_{\perp} \geq 500$ GeV on the final-state partons. For consistency with the shower α_s parameters, VINCIA's default tune uses two-loop running for the strong coupling with $\alpha_s(m_Z^2) = 0.118$ for the hard process. To compare predictions on an equal footing we apply the same settings for the underlying Born process in PYTHIA. To focus on the showering off the hard process all comparisons are done with multiparton interactions switched off.

To obtain dimensionless variables, the jet resolution measures d_{23} and d_{56} are normalised by a factor $1/d_{12}$, i.e., they are effectively measured relative to a scale representing the \hat{p}_{\perp}^2 scale of the underlying Born process⁵. The resulting quantities exhibit a fixed-order behaviour for large values and a Sudakov suppression for low values. Especially for well-resolved radiation, we therefore expect these observables to be sensitive to low-order ME corrections, and hence the uncertainty associated with nonsingular-term variations should be reduced when VINCIA's ME corrections are switched on. (Note: PYTHIA does not incorporate ME corrections for QCD $2 \rightarrow 2$ processes.) Parton-level results for showered $gg \rightarrow gg$ events are presented in fig. 2 with uncertainty bands.

The ME corrections in strongly-ordered events exhibit a modest effect of up to 20% for large values of d_{23}/d_{12} and d_{56}/d_{12} , with the ME-corrected rate being larger than that of the pure VINCIA shower. Shape differences between the predictions of PYTHIA and VINCIA are visible throughout most of the distributions, with the uncorrected VINCIA shower generating a somewhat harder d_{23}/d_{12} spectrum than PYTHIA. ME corrections increase the rate for large d_{56}/d_{12} values, bringing the predictions of VINCIA closer to that of PYTHIA. Given the different choices of shower α_s parameters, evolution variable, and radiation functions, we do not consider this level of disagreement between the two models surprising. The evolution of the hard process starts at the factorisation scale for both showers. However, depending on the form of evolution variable, the hardest possible scales correspond to different values of d_{23} .

All predictions exhibit some rather large fluctuations in the uncertainty bands. The dijet system with the cut $\hat{p}_{\perp} \geq 500$ GeV as underlying hard process is typically accompanied by a large number of additional jets. Given the nature of the reweighting algorithm of [39] (and similarly for [40, 41]) this may easily result in fluctuating weights. In addition we expect larger fluctuations in the nonsingular-term variations for the helicity shower, compared to the helicity-independent one. As discussed in sec. 4, the additional nonsingular terms are distributed evenly between all helicity configurations. This results in a larger spread of weights, when considering helicity configurations that constitute either a large or a small fraction of the helicity-summed antenna functions. To mitigate the effects of weight fluctuations, we conclude that further development of these reweighting methods would be useful, in particular for large phase spaces (long shower chains). E.g., the authors in [40] have demonstrated that combining biasing with reweighting can improve the relative statistical precision of the uncertainty variations, at the price of generating some reasonably well-behaved weights for the central (non-varied) event sample.

The variation of the nonsingular terms (hashed bands) results in a larger band around small $|d_{23}/d_{12}|$ and $|d_{56}/d_{12}|$ for VINCIA without ME corrections, compared to PYTHIA. The ME corrections cancel the effect of varying the nonsingular terms in the radiation functions. Consequently, the respective uncertainty band for VINCIA with ME corrections is very narrow, especially for d_{23} . The renormalisation-scale variations (shaded bands) are quite similar in size for all predictions. They show the largest effect for small jet separation scales, where soft emissions and the Sudakov factor contribute to the distribution.

We now turn to an observable where polarisation effects are expected to contribute. In events with two b -jets a plane is defined by the two jets. A second plane is defined by the gluon-jet (the sum of the two b -jets) and the beam axis. In fig. 3 the angle between the two planes is shown. A flat distribution is obtained

⁵This is similar to how, e.g., m_Z^2 is used to normalise corresponding observables in e^+e^- collisions at the Z pole.

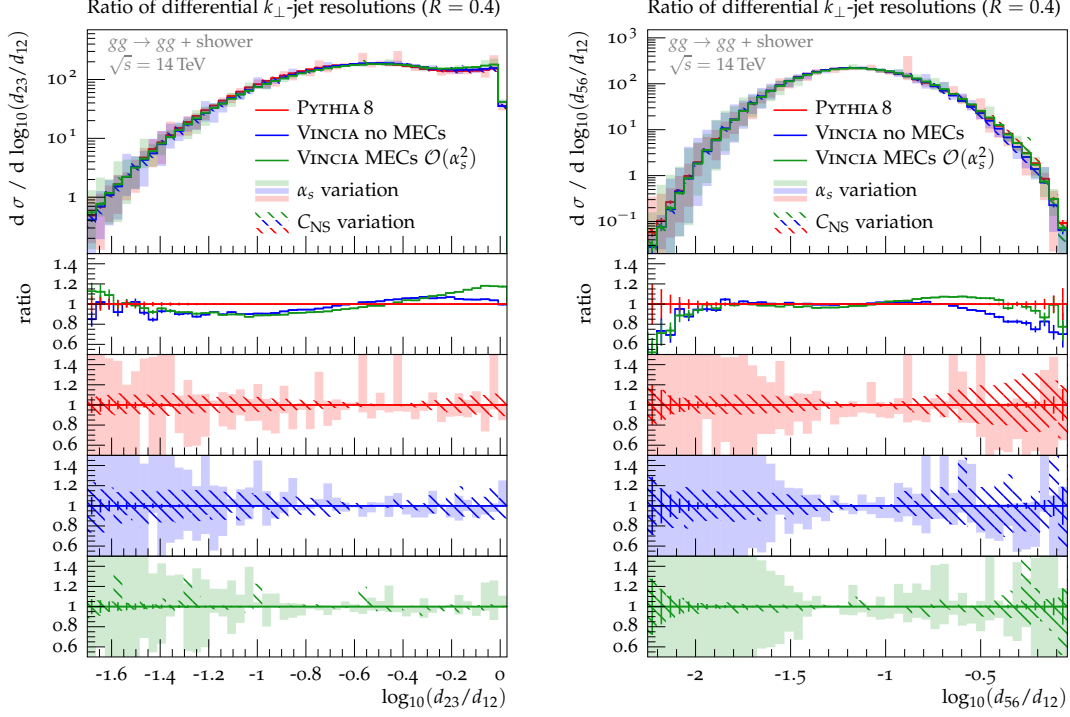


Figure 2: Logarithmic distributions of ratios of differential jet resolutions, d_{23}/d_{12} and d_{56}/d_{12} , for showering $gg \rightarrow gg$ events. Predictions of PYTHIA 8.226 and VINCIA 2.200 with and without ME corrections are shown. The solid bands present a renormalisation-scale variation with $k = 1/2$ and 2 and the hashed bands a variation of the nonsingular terms with $C_{NS} = \pm 2$.

with PYTHIA without gluon polarisation effects in the final-state shower and VINCIA without ME corrections. However, VINCIA produces an around 15% higher total rate, compared to PYTHIA. We note that both codes generate a similar total rate of $g \rightarrow b\bar{b}$ splittings in the shower, where the gluon splittings occur “later” in the evolution in PYTHIA (i.e., preceded by a larger number of other branchings). The b -quarks are therefore more likely to obtain a smaller invariant mass and might be clustered within the same jet. Together with the p_{\perp} and invariant mass cuts on the jets, this may cause a smaller rate of events with two b -jets. The polarisation effects in PYTHIA leave the total rate unchanged, but increase the amount of events where the angle is close to $\pi/2$. The ME corrections in VINCIA change the total rate by decreasing the number of events with splitting angles near 90 degrees. The qualitative effect is therefore the *opposite* of that in PYTHIA, where the total shower rate is preserved, but the region around 90 degrees is enhanced by the polarisation effect. We conclude that a measurement of this observable, and the development of alternative strategies for corrections beyond fixed order (e.g., along the lines proposed in [26]), would be desirable.

6 Conclusions

We have presented a helicity-dependent antenna shower for QCD initial- and final-state radiation, implemented in the VINCIA shower model. The iterated ME correction formalism of [7, 16, 18, 19] has been extended to cope with helicity-dependent clusterings and splitting kernels involving initial-state legs, and in this work has been applied to strongly ordered showers in a direct extension of the formalism presented in [19]. We

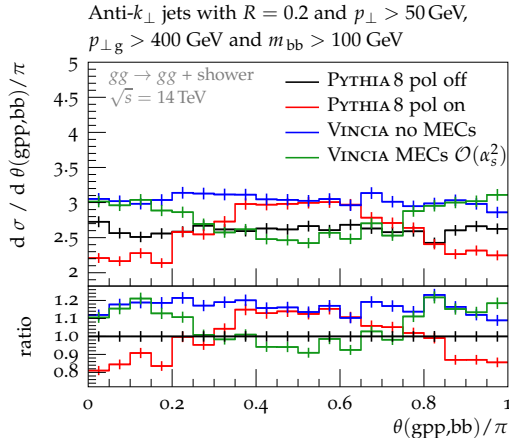


Figure 3: The angle between the plane of the two b -jets and the plane of the gluon jet and the beam axis. Predictions of PYTHIA 8.2.26 and VINCIA 2.2.0 with and without ME corrections are shown. In the labelling, “pol off” refers to the PYTHIA 8 parameters `TimeShower:phiPolAsym` and `TimeShower:phiPolAsymHard` being switched off and “pol on” to the default settings, where both parameters are switched on.

further reported on new, user-specifiable uncertainty variations in VINCIA, including renormalisation-scale and splitting-kernel variations.

The new approach and a library for tree-level MHV amplitudes enable a faster evaluation of MEC factors, as illustrated explicitly for the process $qg \rightarrow qg + \text{gluons}$. While the pure shower is slightly slower due to the additional step of helicity selection, the evaluation of ME corrections can be done significantly faster when only a single or a few helicity matrix elements need to be evaluated per trial branching, relative to when helicity-summed matrix elements are used.

To illustrate the effect of the iterated ME corrections and uncertainty variations within the helicity-dependent shower, we considered a few representative observables, based on showered $gg \rightarrow gg$ Born-level events. As expected, ME corrections reduce the overall amount of variation considerably in regions of relatively hard emissions, where process-dependent nonsingular terms (captured by the matrix elements) dominate over the universal logarithmic terms (captured by the showers). In regions of large scale hierarchies, the uncertainty due to renormalisation-scale variations dominates and remains uncompensated by tree-level ME corrections.

We also showed a more complex example, the angle between a Born-level $gg \rightarrow gg$ event plane and the plane of a subsequent $g \rightarrow b\bar{b}$ splitting. In PYTHIA, a general implementation of gluon polarisation effects implies an enhancement of such splittings at 90 degrees to the original event plane (while the total shower rate of $g \rightarrow b\bar{b}$ splittings is preserved); while in VINCIA, ME corrections dominantly act to suppress the overall rate of $g \rightarrow b\bar{b}$ splittings. Moreover, the suppression is most active for the most well-resolved branchings (at 90 degrees), leading to an opposite-sign effect than the one in PYTHIA. We conclude that there is a complex interplay between the rate and the angular dependence of these branchings, and intend to investigate this further in future studies.

Acknowledgments: AL and PS acknowledge support from the Monash-Warwick Alliance Development Fund Project “Collider Physics”. PS is the recipient of an Australian Research Council Future Fellowship, FT130100744.

A Helicity-Dependent Antenna Functions

A.1 Notation and Conventions

We use capital letters to denote partons in the pre-branching n -parton configuration and lower-case letters to denote partons in the post-branching $(n+1)$ -parton configuration. Incoming partons are denoted a, b , while final-state partons are denoted i, j, k . Thus, for example, an initial-final antenna branching is written $AK \rightarrow ajk$.

The scaled branching invariants for final-final antenna functions are

$$y_{ij} = \frac{s_{ij}}{m_{IK}^2}, \quad y_{jk} = \frac{s_{jk}}{m_{IK}^2}, \quad \text{and} \quad y_{ik} = \frac{s_{ik}}{m_{IK}^2}, \quad (35)$$

and the energy fractions

$$x_j = 1 - \frac{1}{1 - \mu_I^2} y_{ik} \quad \text{and} \quad x_k = 1 - \frac{1}{1 - \mu_I^2} y_{ij}, \quad (36)$$

with $\mu_I = m_i/m_{IK}$. The scaled branching invariants for initial-final antenna functions are

$$y_{aj} = \frac{s_{aj}}{m_{AK}^2 + s_{jk}}, \quad y_{jk} = \frac{s_{jk}}{m_{AK}^2 + s_{jk}}, \quad \text{and} \quad y_{ak} = \frac{s_{ak}}{m_{AK}^2 + s_{jk}}, \quad (37)$$

and for initial-initial antenna functions

$$y_{aj} = \frac{s_{aj}}{m_{AB}^2 + s_{aj} + s_{jb}}, \quad y_{jb} = \frac{s_{jb}}{m_{AB}^2 + s_{aj} + s_{jb}}, \quad \text{and} \quad y_{AB} = \frac{m_{AB}^2}{m_{AB}^2 + s_{aj} + s_{jb}}. \quad (38)$$

Note that, for gluon-emission antennae involving massive parent quarks, a helicity-independent negative correction to the eikonal is added, with helicity-summed average:

$$\Delta a_{\text{mass}}^{\text{eik}} = -\frac{2m_I^2}{s_{ij}^2} - \frac{2m_K^2}{s_{jk}^2}. \quad (39)$$

For gluon-splitting antennae ($Xg \rightarrow X\bar{q}_j q_k$), the mass correction is positive:

$$\Delta a_{\text{mass}}^{\text{split}} = \frac{m_j^2}{m_{jk}^4}. \quad (40)$$

A.2 $Q\bar{Q}$ parents: Gluon Emission

The helicity averages for $q\bar{q} \rightarrow qg\bar{q}$ antennae are

$$\mathbf{FF} : a(q_I q_K \rightarrow q_i g_j q_k) = \frac{1}{m_{IK}^2} \left[\frac{2y_{ik}}{y_{ij}y_{jk}} + \frac{y_{jk}}{y_{ij}} + \frac{y_{ij}}{y_{jk}} + 1 \right] = \frac{1}{m_{IK}^2} \left[\frac{(1-y_{ij})^2 + (1-y_{jk})^2}{y_{ij}y_{jk}} + 1 \right], \quad (41)$$

$$\mathbf{II} : a(\bar{q}_A q_B \rightarrow \bar{q}_a g_j q_b) = \frac{1}{s_{AB}} \left[\frac{2y_{AB}}{y_{aj}y_{jb}} + \frac{y_{jb}}{y_{aj}} + \frac{y_{aj}}{y_{jb}} + 1 \right] = \frac{1}{s_{AB}} \left[\frac{(1-y_{aj})^2 + (1-y_{jb})^2}{y_{aj}y_{jb}} + 1 \right], \quad (42)$$

$$\mathbf{IF} : a(q_A q_K \rightarrow q_a g_j q_k) = \frac{1}{s_{AK}} \left[\frac{(1-y_{aj})^2 + (1-y_{jk})^2}{y_{aj}y_{jk}} + \frac{3}{2} - \frac{y_{aj}^2}{2} - \frac{y_{jk}^2}{2} \right], \quad (43)$$

where the slightly different nonsingular terms chosen for the IF case ensure positivity of in particular the $(++ \rightarrow +-+)$ antenna function over all of the IF phase space, while the nonsingular terms for the FF and II cases result from averaging over the corresponding helicity matrix elements for Z and H decays.

The individual helicity contributions are:

$$a(++ \rightarrow +++) = \frac{1}{m_{IK}^2} \left[\frac{1}{y_{ij}y_{jk}} \right], \quad (44)$$

$$a(++ \rightarrow +-+) = \frac{1}{m_{IK}^2} \left[\frac{(1-y_{ij})^2 + (1-y_{jk})^2 - 1}{y_{ij}y_{jk}} + 2 \right], \quad (45)$$

FF :

$$a(+ - \rightarrow +++) = \frac{1}{m_{IK}^2} \left[\frac{(1-y_{ij})^2}{y_{ij}y_{jk}} \right], \quad (46)$$

$$a(+ - \rightarrow +- -) = \frac{1}{m_{IK}^2} \left[\frac{(1-y_{jk})^2}{y_{ij}y_{jk}} \right]. \quad (47)$$

$$a(++ \rightarrow +++) = \frac{1}{s_{AB}} \left[\frac{1}{y_{aj}y_{jb}} \right], \quad (48)$$

$$a(++ \rightarrow +-+) = \frac{1}{s_{AB}} \left[\frac{y_{AB}^2}{y_{aj}y_{jb}} \right], \quad (49)$$

II :

$$a(+ - \rightarrow +++) = \frac{1}{s_{AB}} \left[\frac{(1-y_{aj})^2}{y_{aj}y_{jb}} \right], \quad (50)$$

$$a(+ - \rightarrow +- -) = \frac{1}{s_{AB}} \left[\frac{(1-y_{jb})^2}{y_{aj}y_{jb}} \right]. \quad (51)$$

$$a(++ \rightarrow +++) = \frac{1}{s_{AK}} \left[\frac{1}{y_{aj}y_{jk}} \right], \quad (52)$$

$$a(++ \rightarrow +-+) = \frac{1}{s_{AK}} \left[\frac{(1-y_{aj})^2 + (1-y_{jk})^2 - 1}{y_{aj}y_{jk}} + 3 - y_{aj}^2 - y_{jk}^2 \right], \quad (53)$$

IF :

$$a(+ - \rightarrow +++) = \frac{1}{s_{AK}} \left[\frac{(1-y_{aj})^2}{y_{aj}y_{jk}} \right], \quad (54)$$

$$a(+ - \rightarrow +- -) = \frac{1}{s_{AK}} \left[\frac{(1-y_{jk})^2}{y_{aj}y_{jk}} \right]. \quad (55)$$

A.3 QG parents: Gluon Emission

The helicity averages for $qg \rightarrow qgg$ antennae are

$$\begin{aligned} \mathbf{FF} : a(q_I g_K \rightarrow q_i g_j g_k) &= \frac{1}{m_{IK}^2} \left[\frac{2y_{ik}}{y_{ij}y_{jk}} + \frac{y_{jk}}{y_{ij}} + \frac{y_{ij}(1-y_{ij})}{y_{jk}} + y_{ij} + \frac{y_{jk}}{2} \right] \\ &= \frac{1}{m_{IK}^2} \left[\frac{(1-y_{ij})^3 + (1-y_{jk})^2}{y_{ij}y_{jk}} - \frac{2\mu_I^2}{y_{ij}^2} + \frac{y_{ik}-y_{ij}}{y_{jk}} + 1 + y_{ij} + \frac{y_{jk}}{2} \right], \end{aligned} \quad (56)$$

$$\mathbf{II} : a(q_A g_B \rightarrow q_a g_j g_b) = \frac{1}{s_{AB}} \left[\frac{(1-y_{aj})^3 + (1-y_{jb})^2}{y_{aj}y_{jb}} + \frac{1+y_{aj}^3}{y_{jb}(1-y_{aj})} + 2 - y_{aj} - \frac{y_{jb}}{2} \right], \quad (57)$$

$$\mathbf{IF} : a(q_A g_K \rightarrow q_a g_j g_k) = \frac{1}{s_{AK}} \left[\frac{(1-y_{aj})^3 + (1-y_{jk})^2}{y_{aj}y_{jk}} + \frac{1-2y_{aj}}{y_{jk}} + \frac{3}{2} + y_{aj} - \frac{y_{jk}}{2} - \frac{y_{aj}^2}{2} \right], \quad (58)$$

$$\mathbf{IF} : a(g_A q_K \rightarrow g_a g_j q_k) = \frac{1}{s_{AK}} \left[\frac{(1-y_{jk})^3 + (1-y_{aj})^2}{y_{aj}y_{jk}} + \frac{1+y_{jk}^3}{y_{aj}(y_{AK}+y_{aj})} + \frac{3}{2} - \frac{y_{jk}^2}{2} \right]. \quad (59)$$

$$(60)$$

Note that for the initial-final case two antennae, $qg \rightarrow qgg$ and $gq \rightarrow ggq$, exist.

The individual helicity contributions are:

$$a(++ \rightarrow ++++) = \frac{1}{m_{IK}^2} \left[\frac{1}{y_{ij}y_{jk}} + (1-\alpha)(1-y_{jk}) \left(\frac{1-2y_{ij}-y_{jk}}{y_{jk}} \right) \right], \quad (61)$$

$$a(++ \rightarrow +-+) = \frac{1}{m_{IK}^2} \left[\frac{(1-y_{ij})y_{ik}^2}{y_{ij}y_{jk}} \right], \quad (62)$$

FF :

$$a(+ - \rightarrow +-+) = \frac{1}{m_{IK}^2} \left[\frac{(1-y_{ij})^3}{y_{ij}y_{jk}} \right], \quad (63)$$

$$a(+ - \rightarrow +--) = \frac{1}{m_{IK}^2} \left[\frac{(1-y_{jk})^2}{y_{ij}y_{jk}} + (1-\alpha)(1-y_{jk}) \left(\frac{1-2y_{ij}-y_{jk}}{y_{jk}} \right) \right]. \quad (64)$$

$$a(++ \rightarrow ++++) = \frac{1}{s_{AB}} \left[\frac{1}{y_{aj}y_{jb}} \frac{1-y_{jb}}{1-y_{aj}-y_{jb}} \right] = \frac{1}{s_{AB}} \left[\frac{1}{y_{aj}y_{jb}} + \frac{1}{y_{jb}y_{AB}} \right] \quad (65)$$

$$\xrightarrow{\text{sing}} \frac{1}{s_{AB}} \left[\frac{1}{y_{aj}y_{jb}} + \frac{1}{y_{jb}(1-y_{aj})} \right], \quad (66)$$

$$a(++ \rightarrow +-+) = \frac{1}{s_{AB}} \frac{1}{y_{aj}y_{jb}} \frac{y_{AB}^3}{1-y_{jb}} \frac{y_{AB}^3}{s_{AB}} \left[\frac{1}{y_{aj}y_{jb}} + \frac{1}{y_{aj}(1-y_{jb})} \right] \quad (67)$$

$$\xrightarrow{\text{sing}} \frac{1}{s_{AB}} \frac{1}{y_{aj}y_{jb}} \left[\frac{y_{AB}^3}{y_{aj}y_{jb}} + \frac{y_{AB}^2}{y_{aj}} \right] = \frac{1}{s_{AB}} \frac{(1-y_{aj})y_{AB}^2}{y_{aj}y_{jb}}, \quad (68)$$

$$a(+ - \rightarrow +++ -) = \frac{1}{s_{AB}} \left[\frac{(1-y_{aj})^3}{y_{aj}y_{jb}} + \frac{1-y_{jb}-y_{aj}^2}{1-y_{jb}} \right] \quad (69)$$

$$\xrightarrow{\text{sing}} \frac{1}{s_{AB}} \frac{(1-y_{aj})^3}{y_{aj}y_{jb}}, \quad (70)$$

II :

$$a(+ - \rightarrow +- -) = \frac{1}{s_{AB}} \frac{1}{y_{aj}y_{jb}} \frac{(1-y_{jb})^3}{1-y_{aj}-y_{jb}} = \frac{(1-y_{jb})^2}{s_{AB}} \left[\frac{1}{y_{aj}y_{jb}} + \frac{1}{y_{jb}(1-y_{aj}-y_{jb})} \right] \quad (71)$$

$$\xrightarrow{\text{sing}} \frac{1}{s_{AB}} \left[\frac{(1-y_{jb})^2}{y_{aj}y_{jb}} + \frac{1}{y_{jb}(1-y_{aj})} \right], \quad (72)$$

$$a(++ \rightarrow +- -) = \frac{1}{s_{AB}} \frac{y_{aj}^3}{y_{jb}(1-y_{jb})} \frac{1}{1-y_{aj}-y_{jb}}, \quad (73)$$

$$\xrightarrow{\text{sing}} \frac{1}{s_{AB}} \frac{y_{aj}^3}{y_{jb}(1-y_{aj})}, \quad (74)$$

$$a(+ - \rightarrow ++++) = a(++ \rightarrow +- -). \quad (75)$$

$$a(++ \rightarrow ++++) = \frac{1}{s_{AK}} \left[\frac{1}{y_{aj}y_{jk}} + \frac{1-2y_{aj}}{y_{jk}} \right], \quad (76)$$

$$a(++ \rightarrow +-+) = \frac{1}{s_{AK}} \left[\frac{(1-y_{aj})^3 + (1-y_{jk})^2 - 1}{y_{aj}y_{jk}} + 3 - y_{aj}^2 \right], \quad (77)$$

IF :

$$a(+ - \rightarrow +++ -) = \frac{1}{s_{AK}} \left[\frac{(1-y_{aj})^3}{y_{aj}y_{jk}} \right], \quad (78)$$

$$a(+ - \rightarrow +- -) = \frac{1}{s_{AK}} \left[\frac{(1-y_{jk})^2}{y_{aj}y_{jk}} + \frac{1-2y_{aj}}{y_{jk}} + 2y_{aj} - y_{jk} \right]. \quad (79)$$

$$a(++ \rightarrow ++++) = \frac{1}{s_{AK}} \left[\frac{1}{y_{aj}y_{jk}} + \frac{1}{y_{aj}(y_{AK} + y_{aj})} \right], \quad (80)$$

$$a(++ \rightarrow +-+) = \frac{1}{s_{AK}} \left[\frac{(1-y_{aj})^2 + (1-y_{jk})^3 - 1}{y_{aj}y_{jk}} + 3 - y_{jk}^2 \right], \quad (81)$$

$$a(+ - \rightarrow +++ -) = \frac{1}{s_{AK}} \left[\frac{(1-y_{aj})^2}{y_{aj}y_{jk}} + \frac{1}{y_{aj}(y_{AK} + y_{aj})} \right], \quad (82)$$

IF :

$$a(+ - \rightarrow +- -) = \frac{1}{s_{AK}} \left[\frac{(1-y_{jk})^3}{y_{aj}y_{jk}} \right], \quad (83)$$

$$a(++ \rightarrow - - +) = \frac{1}{s_{AK}} \frac{y_{jk}^3}{y_{aj}(y_{AK} + y_{aj})}, \quad (84)$$

$$a(+ - \rightarrow - - -) = a(++ \rightarrow - - +). \quad (85)$$

Note that for gluons in the initial-state an additional helicity configuration⁶ arises where the final-state gluon inherits the helicity.

A.4 GG parents: Gluon Emission

The helicity averages for $gg \rightarrow ggg$ antennae are

$$\begin{aligned} \mathbf{FF} : a(g_I g_K \rightarrow g_i g_j g_k) &= \frac{1}{m_{IK}^2} \left[\frac{2y_{ik}}{y_{ij}y_{jk}} + \frac{y_{jk}(1-y_{jk})}{y_{ij}} + \frac{y_{ij}(1-y_{ij})}{y_{jk}} + \frac{1}{2}y_{ij} + \frac{1}{2}y_{jk} \right] \\ &= \frac{1}{m_{IK}^2} \left[\frac{(1-y_{ij})^3 + (1-y_{jk})^3}{y_{ij}y_{jk}} + \frac{y_{ik}-y_{ij}}{y_{jk}} + \frac{y_{ik}-y_{jk}}{y_{ij}} + 2 + \frac{1}{2}y_{ij} + \frac{1}{2}y_{jk} \right], \end{aligned} \quad (86)$$

$$\mathbf{II} : a(g_A g_B \rightarrow g_a g_j g_b) = \frac{1}{s_{AB}} \left[\frac{(1-y_{aj})^3 + (1-y_{jb})^3}{y_{aj}y_{jb}} + \frac{1+y_{aj}^3}{y_{jb}(1-y_{aj})} + \frac{1+y_{jb}^3}{y_{aj}(1-y_{jb})} + 3 - \frac{3y_{aj}}{2} - \frac{3y_{jb}}{2} \right], \quad (87)$$

$$\mathbf{IF} : a(g_A g_K \rightarrow g_a g_j g_k) = \frac{1}{s_{AK}} \left[\frac{(1-y_{aj})^3 + (1-y_{jk})^3}{y_{aj}y_{jk}} + \frac{1+y_{jk}^3}{y_{aj}(y_{AK} + y_{aj})} + \frac{1-2y_{aj}}{y_{jk}} + 3 - 2y_{jk} \right]. \quad (88)$$

The individual helicity contributions are:

$$a(++ \rightarrow ++++) = \frac{1}{m_{IK}^2} \left[\frac{1}{y_{ij}y_{jk}} + (1-\alpha) \left((1-y_{ij}) \frac{1-2y_{jk}-y_{ij}}{y_{ij}} + (1-y_{jk}) \frac{1-2y_{ij}-y_{jk}}{y_{jk}} \right) \right], \quad (89)$$

$$a(++ \rightarrow +-+) = \frac{1}{m_{IK}^2} \left[\frac{y_{ik}^3}{y_{ij}y_{jk}} \right], \quad (90)$$

FF :

$$a(+ - \rightarrow +++ -) = \frac{1}{m_{IK}^2} \left[\frac{(1-y_{ij})^3}{y_{ij}y_{jk}} + (1-\alpha)(1-y_{ij}) \frac{1-2y_{jk}}{y_{ij}} \right], \quad (91)$$

$$a(+ - \rightarrow +- -) = \frac{1}{m_{IK}^2} \left[\frac{(1-y_{jk})^3}{y_{ij}y_{jk}} + (1-\alpha)(1-y_{jk}) \frac{1-2y_{ij}}{y_{jk}} \right]. \quad (92)$$

⁶Additional with respect to the final-state antenna functions.

$$a(++ \rightarrow ++++) = \frac{1}{s_{AB}} \left[\frac{1}{y_{aj}y_{jb}} + \frac{1}{y_{jb}(1-y_{aj})} + \frac{1}{y_{aj}(1-y_{jb})} \right], \quad (93)$$

$$a(++ \rightarrow +-+) = \frac{1}{s_{AB}} \frac{y_{AB}^3}{y_{aj}y_{jb}}, \quad (94)$$

$$a(+\rightarrow ++-) = \frac{1}{s_{AB}} \left[\frac{(1-y_{aj})^3}{y_{aj}y_{jb}} + \frac{1}{y_{aj}(1-y_{jb})} \right], \quad (95)$$

$$a(+\rightarrow +--) = \frac{1}{s_{AB}} \left[\frac{(1-y_{jb})^3}{y_{aj}y_{jb}} + \frac{1}{y_{jb}(1-y_{aj})} \right], \quad (96)$$

II :

$$a(++ \rightarrow +--) = \frac{1}{s_{AB}} \frac{y_{aj}^3}{y_{jb}(1-y_{aj})}, \quad (97)$$

$$a(++ \rightarrow -++) = \frac{1}{s_{AB}} \frac{y_{jb}^3}{y_{aj}(1-y_{jb})}, \quad (98)$$

$$a(+\rightarrow ++++) = a(++ \rightarrow +--), \quad (99)$$

$$a(+\rightarrow -++) = a(++ \rightarrow -++). \quad (100)$$

$$a(++ \rightarrow ++++) = \frac{1}{s_{AK}} \left[\frac{1}{y_{aj}y_{jk}} + \frac{1-2y_{aj}}{y_{jk}} + \frac{1}{y_{aj}(y_{AK}+y_{aj})} \right], \quad (101)$$

$$a(++ \rightarrow +-+) = \frac{1}{s_{AK}} \left[\frac{(1-y_{aj})^3 + (1-y_{jk})^3 - 1}{y_{aj}y_{jk}} + 6 - 3y_{aj} - 3y_{jk} + y_{aj}y_{jk} \right], \quad (102)$$

$$a(+\rightarrow ++-) = \frac{1}{s_{AK}} \left[\frac{(1-y_{aj})^3}{y_{aj}y_{jk}} + \frac{1}{y_{aj}(y_{AK}+y_{aj})} \right], \quad (103)$$

IF :

$$a(+\rightarrow +--) = \frac{1}{s_{AK}} \left[\frac{(1-y_{jk})^3}{y_{aj}y_{jk}} + \frac{1-2y_{aj}}{y_{jk}} + 3y_{aj} - y_{jk} - y_{aj}y_{jk} \right], \quad (104)$$

$$a(++ \rightarrow -++) = \frac{1}{s_{AK}} \frac{y_{jk}^3}{y_{aj}(y_{AK}+y_{aj})}, \quad (105)$$

$$a(+\rightarrow -++) = a(++ \rightarrow -++). \quad (106)$$

Note that for gluons in the initial-state an additional helicity configuration ⁷ arises where the final-state gluon inherits the helicity.

A.5 $G \rightarrow \bar{Q}Q$ Splittings

The helicity averages for $Xg \rightarrow X\bar{q}q$ antennae (final-state gluon splitting) are

$$\mathbf{FF} : a(X_I g_K \rightarrow X_i \bar{q}_j q_k) = \frac{1}{2m_{jk}^2} [(1-x_j)^2 + (1-x_k)^2] = \frac{1}{2m_{jk}^2} \left[\frac{y_{ik}^2 + y_{ij}^2}{(1-\mu_I^2)^2} \right], \quad (107)$$

$$\mathbf{IF} : a(X_A g_K \rightarrow X_a \bar{q}_j q_k) = \frac{1}{2m_{jk}^2} [y_{ak}^2 + y_{aj}^2]. \quad (108)$$

⁷Additional with respect to the final-state antenna functions.

The individual helicity contributions are:

$$a(X+ \rightarrow X-+) = \frac{1}{2m_{jk}^2} \frac{y_{ik}^2}{(1-\mu_I^2)^2} = \frac{(1-x_j)^2}{2m_{jk}^2}, \quad (109)$$

$$\mathbf{FF} : a(X+ \rightarrow X+-) = \frac{1}{2m_{jk}^2} \frac{y_{ij}^2}{(1-\mu_I^2)^2} = \frac{(1-x_k)^2}{2m_{jk}^2}. \quad (110)$$

$$a(X+ \rightarrow X-+) = \frac{y_{ak}^2}{2m_{jk}^2}, \quad (111)$$

$$\mathbf{IF} : a(X+ \rightarrow X+-) = \frac{y_{aj}^2}{2m_{jk}^2}. \quad (112)$$

The helicity averages for $qX \rightarrow g\bar{q}X$ antennae (quark backwards evolving to a gluon) are

$$\mathbf{II} : a(q_A X_B \rightarrow g_a \bar{q}_j X_b) = \frac{1}{s_{AB}} \frac{y_{AB}^2 + (1-y_{AB})^2}{y_{aj}}, \quad (113)$$

$$\mathbf{IF} : a(q_A X_K \rightarrow g_a \bar{q}_j X_k) = \frac{1}{s_{AK}} \frac{y_{AK}^2 + (1-y_{AK})^2}{y_{aj}}. \quad (114)$$

The individual helicity contributions are:

$$a(+X \rightarrow +-X) = \frac{1}{s_{AB}} \frac{y_{AB}^2}{y_{aj}}, \quad (115)$$

$$a(+X \rightarrow --X) = \frac{1}{s_{AB}} \frac{(1-y_{AB})^2}{y_{aj}}, \quad (116)$$

$$\mathbf{II} : a(-X \rightarrow -+X) = \frac{1}{s_{AB}} \frac{y_{AB}^2}{y_{aj}}, \quad (117)$$

$$a(-X \rightarrow ++X) = \frac{1}{s_{AB}} \frac{(1-y_{AB})^2}{y_{aj}}. \quad (118)$$

$$a(+X \rightarrow +-X) = \frac{1}{s_{AK}} \frac{y_{AK}^2}{y_{aj}}, \quad (119)$$

$$a(+X \rightarrow --X) = \frac{1}{s_{AK}} \frac{(1-y_{AK})^2}{y_{aj}}, \quad (120)$$

$$\mathbf{IF} : a(-X \rightarrow -+X) = \frac{1}{s_{AK}} \frac{y_{AK}^2}{y_{aj}}, \quad (121)$$

$$a(-X \rightarrow ++X) = \frac{1}{s_{AK}} \frac{(1-y_{AK})^2}{y_{aj}}. \quad (122)$$

The helicity averages for $gX \rightarrow qqX$ antennae (gluon backwards evolving to a quark) are

$$\mathbf{II} : a(g_A X_B \rightarrow q_a q_j X_b) = \frac{1}{s_{AB}} \frac{1 + (1-y_{AB})^2}{2y_{aj}(1-y_{jb})}, \quad (123)$$

$$\mathbf{IF} : a(g_A X_K \rightarrow q_a q_j X_k) = \frac{1}{s_{AK}} \frac{1 + (1-y_{AK})^2}{2y_{aj}(y_{AK} + y_{aj})}. \quad (124)$$

The individual helicity contributions are:

$$a(+X \rightarrow ++X) = \frac{1}{s_{AB}} \frac{1}{2y_{aj}(1-y_{jb})}, \quad (125)$$

$$a(+X \rightarrow --X) = \frac{1}{s_{AB}} \frac{(1-y_{AB})^2}{2y_{aj}(1-y_{jb})}, \quad (126)$$

II :

$$a(-X \rightarrow --X) = \frac{1}{s_{AB}} \frac{1}{2y_{aj}(1-y_{jb})}, \quad (127)$$

$$a(-X \rightarrow ++X) = \frac{1}{s_{AB}} \frac{(1-y_{AB})^2}{2y_{aj}(1-y_{jb})}. \quad (128)$$

$$a(+X \rightarrow ++X) = \frac{1}{s_{AK}} \frac{1}{2y_{aj}(y_{AK}+y_{aj})}, \quad (129)$$

$$a(+X \rightarrow --X) = \frac{1}{s_{AK}} \frac{(1-y_{AK})^2}{2y_{aj}(y_{AK}+y_{aj})}, \quad (130)$$

IF :

$$a(-X \rightarrow --X) = \frac{1}{s_{AK}} \frac{1}{2y_{aj}(y_{AK}+y_{aj})}, \quad (131)$$

$$a(-X \rightarrow ++X) = \frac{1}{s_{AK}} \frac{(1-y_{AK})^2}{2y_{aj}(y_{AK}+y_{aj})}. \quad (132)$$

A.6 Gluon Emission of Initial-State Gluons

As discussed in apps. A.3 and A.4, helicity configurations exist for which a final-state gluon inherits the helicity of an initial-state gluon. Thus, the helicity of a pre-branching initial-state gluon, A or B , can be different from that of the corresponding post-branching initial-state gluon, a or b , without violating helicity conservation.

For completeness, we give the DGLAP limits of antenna functions for gluon emission off initial-state gluons. The limits are independent of the other parent in the parent antenna. For initial-initial antennae the DGLAP limit corresponds to

$$y_{jb} = \frac{Q^2}{s_{ab}} \rightarrow 0, \quad z = y_{AB} = \frac{s_{AB}}{s_{ab}}, \quad \text{and} \quad y_{aj} \rightarrow 1 - z. \quad (133)$$

This gives the following limits of the helicity-dependent antenna functions in eqs. (93) to (100) (or eqs. (65) to (75)) for a parent with $+$ helicity,

$$\begin{aligned} a(X+ \rightarrow X++) &\rightarrow \frac{1}{Q^2} \frac{1}{z} \frac{1}{z(1-z)} = \frac{1}{Q^2} P_{g \rightarrow gg}^{\text{IS}}(+ \rightarrow ++), \\ a(X+ \rightarrow X-) &\rightarrow \frac{1}{Q^2} \frac{1}{z} \frac{z^3}{1-z} = \frac{1}{Q^2} P_{g \rightarrow gg}^{\text{IS}}(+ \rightarrow -+), \\ a(X+ \rightarrow X--) &\rightarrow \frac{1}{Q^2} \frac{1}{z} \frac{(1-z)^3}{z} = \frac{1}{Q^2} P_{g \rightarrow gg}^{\text{IS}}(+ \rightarrow +-). \end{aligned}$$

The same limits are obtained for initial-final antennae with

$$y_{aj} = \frac{Q^2}{m_{AK}^2 + s_{jk}} \rightarrow 0, \quad z = y_{AK} = \frac{m_{AK}^2}{m_{AK}^2 + s_{jk}}, \quad y_{jk} \rightarrow 1 - z, \quad \text{and} \quad y_{ak} \rightarrow 1. \quad (134)$$

References

- [1] T. Sjöstrand, S. Ask, J. R. Christiansen, R. Corke, N. Desai, P. Ilten, S. Mrenna, S. Prestel, C. O. Rasmussen, and P. Z. Skands, *An Introduction to PYTHIA 8.2*, *Comput. Phys. Commun.* **191** (2015) 159–177, [[arXiv:1410.3012](#)].
- [2] B. R. Webber, *Monte Carlo Simulation of Hard Hadronic Processes*, *Ann. Rev. Nucl. Part. Sci.* **36** (1986) 253–286.
- [3] J. Bellm et al., *Herwig 7.1 Release Note*, [arXiv:1705.0691](#).
- [4] I. G. Knowles, *Spin Correlations in Parton - Parton Scattering*, *Nucl. Phys.* **B310** (1988) 571–588.
- [5] I. G. Knowles, *A Linear Algorithm for Calculating Spin Correlations in Hadronic Collisions*, *Comput. Phys. Commun.* **58** (1990) 271–284.
- [6] P. Richardson, *Spin correlations in Monte Carlo simulations*, *JHEP* **11** (2001) 029, [[hep-ph/0110108](#)].
- [7] A. J. Larkoski, J. J. Lopez-Villarejo, and P. Skands, *Helicity-Dependent Showers and Matching with VINCIA*, *Phys. Rev. D* **87** (2013), no. 5 054033, [[arXiv:1301.0933](#)].
- [8] M. Bengtsson and T. Sjöstrand, *Coherent Parton Showers Versus Matrix Elements: Implications of PETRA - PEP Data*, *Phys. Lett. B* **185** (1987) 435.
- [9] M. Bengtsson and T. Sjöstrand, *A Comparative Study of Coherent and Noncoherent Parton Shower Evolution*, *Nucl. Phys. B* **289** (1987) 810.
- [10] G. Miu and T. Sjostrand, *W production in an improved parton shower approach*, *Phys. Lett.* **B449** (1999) 313–320, [[hep-ph/9812455](#)].
- [11] E. Norrbin and T. Sjostrand, *QCD radiation off heavy particles*, *Nucl. Phys.* **B603** (2001) 297–342, [[hep-ph/0010012](#)].
- [12] M. H. Seymour, *Matrix element corrections to parton shower algorithms*, *Comput. Phys. Commun.* **90** (1995) 95, [[hep-ph/9410414](#)].
- [13] G. Corcella and M. H. Seymour, *Matrix element corrections to parton shower simulations of heavy quark decay*, *Phys. Lett. B* **442** (1998) 417, [[hep-ph/9809451](#)].
- [14] P. Nason, *A New method for combining NLO QCD with shower Monte Carlo algorithms*, *JHEP* **11** (2004) 040, [[hep-ph/0409146](#)].
- [15] S. Frixione, P. Nason, and C. Oleari, *Matching NLO QCD computations with Parton Shower simulations: the POWHEG method*, *JHEP* **11** (2007) 070, [[arXiv:0709.2092](#)].
- [16] W. T. Giele, D. A. Kosower, and P. Z. Skands, *Higher-Order Corrections to Timelike Jets*, *Phys. Rev. D* **84** (2011) 054003, [[arXiv:1102.2126](#)].
- [17] W. T. Giele, D. A. Kosower, and P. Z. Skands, *A simple shower and matching algorithm*, *Phys. Rev.* **D78** (2008) 014026, [[arXiv:0707.3652](#)].
- [18] N. Fischer, S. Prestel, M. Ritzmann, and P. Skands, *Vincia for Hadron Colliders*, *Eur. Phys. J. C* **76** (2016), no. 11 589, [[arXiv:1605.0614](#)].
- [19] N. Fischer and S. Prestel, *Combining states without scale hierarchies with ordered parton showers*, [arXiv:1706.0621](#).

- [20] J. Alwall, P. Demin, S. de Visscher, R. Frederix, M. Herquet, F. Maltoni, T. Plehn, D. L. Rainwater, and T. Stelzer, *MadGraph/MadEvent v4: The New Web Generation*, *JHEP* **09** (2007) 028, [[arXiv:0706.2334](#)].
- [21] V. Hirschi et al. work in progress, 2017.
- [22] L. Lönnblad, *ARIADNE version 4: A Program for simulation of QCD cascades implementing the color dipole model*, *Comput. Phys. Commun.* **71** (1992) 15.
- [23] S. Catani, B. R. Webber, and G. Marchesini, *QCD coherent branching and semiinclusive processes at large x* , *Nucl. Phys. B* **349** (1991) 635.
- [24] L. Lönnblad and S. Prestel, *Matching Tree-Level Matrix Elements with Interleaved Showers*, *JHEP* **03** (2012) 019, [[arXiv:1109.4829](#)].
- [25] L. Hartgring, E. Laenen, and P. Skands, *Antenna Showers with One-Loop Matrix Elements*, *JHEP* **10** (2013) 127, [[arXiv:1303.4974](#)].
- [26] H. T. Li and P. Skands, *A framework for second-order parton showers*, *Phys. Lett.* **B771** (2017) 59–66, [[arXiv:1611.0001](#)].
- [27] M. L. Mangano and S. J. Parke, *Multiparton amplitudes in gauge theories*, *Phys. Rept.* **200** (1991) 301, [[hep-th/0509223](#)].
- [28] L. J. Dixon, *Calculating scattering amplitudes efficiently*, in *QCD and beyond. Proceedings, Theoretical Advanced Study Institute in Elementary Particle Physics, TASI-95, Boulder, USA, June 4-30, 1995*, pp. 539–584, 1996. [[hep-ph/9601359](#)].
- [29] L. J. Dixon, *A brief introduction to modern amplitude methods*, in *Proceedings, 2012 European School of High-Energy Physics (ESHEP 2012): La Pommeraye, Anjou, France, June 06-19, 2012*, pp. 31–67, 2014. [[arXiv:1310.5353](#)].
- [30] S. J. Parke and T. Taylor, *An Amplitude for n Gluon Scattering*, *Phys. Rev. Lett.* **56** (1986) 2459.
- [31] Z. Kunszt, *Combined Use of the Calkul Method and $N=1$ Supersymmetry to Calculate QCD Six Parton Processes*, *Nucl. Phys. B* **271** (1986) 333.
- [32] M. L. Mangano and S. J. Parke, *Quark - Gluon Amplitudes in the Dual Expansion*, *Nucl. Phys. B* **299** (1988) 673.
- [33] Z. Xu, D.-H. Zhang, and L. Chang, *Helicity Amplitudes for Multiple Bremsstrahlung in Massless Nonabelian Gauge Theories*, *Nucl. Phys. B* **291** (1987) 392.
- [34] J. F. Gunion and Z. Kunszt, *Four Jet Processes: Gluon-Gluon Scattering To Nonidentical quark - anti-quark pairs*, *Phys. Lett. B* **159** (1985) 167.
- [35] J. F. Gunion and Z. Kunszt, *Addendum Concerning the Four Quark Two Gluon Subprocess*, *Phys. Lett. B* **176** (1986) 477.
- [36] F. A. Berends and W. T. Giele, *Recursive Calculations for Processes with n Gluons*, *Nucl. Phys. B* **306** (1988) 759.
- [37] M. L. Mangano, *The Color Structure of Gluon Emission*, *Nucl. Phys. B* **309** (1988) 461.
- [38] P. Skands et al., *VINCIA User Reference*, 2017. [<http://vincia.hepforge.org/current/share/Vincia/html/doc/>].
- [39] S. Mrenna and P. Skands, *Automated Parton-Shower Variations in Pythia 8*, *Phys. Rev. D* **94** (2016), no. 7 074005, [[arXiv:1605.0835](#)].

- [40] J. Bellm, S. Plätzer, P. Richardson, A. Siódmok, and S. Webster, *Reweighting Parton Showers*, *Phys. Rev.* **D94** (2016), no. 3 034028, [[arXiv:1605.0825](#)].
- [41] E. Bothmann, M. Schönherr, and S. Schumann, *Reweighting QCD matrix-element and parton-shower calculations*, *Eur. Phys. J.* **C76** (2016), no. 11 590, [[arXiv:1606.0875](#)].
- [42] B. Nachman, *$g \rightarrow b\bar{b}$ Studies at the LHC*, in *Proceedings, Parton Radiation and Fragmentation from LHC to FCC-ee: CERN, Geneva, Switzerland, November 22-23, 2016*, pp. 139–143, 2017. [arXiv:1702.0132](#).
- [43] P. Ilten, N. L. Rodd, J. Thaler, and M. Williams, *Disentangling Heavy Flavor at Colliders*, [arXiv:1702.0294](#).

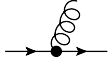
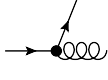
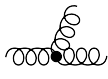
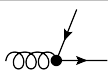
	$a \rightarrow Aj$ $K \rightarrow kj$	$+$ \rightarrow $++$	$+$ \rightarrow $+ -$	$+$ \rightarrow $- +$	sum
	$P_{q \rightarrow qg}$	$\frac{1}{1-z}$	$\frac{z^2}{1-z}$	0	$\frac{1+z^2}{1-z}$
	$P_{q \rightarrow gq}$	$\frac{1}{z}$	0	$\frac{(1-z)^2}{z}$	$\frac{1+(1-z)^2}{z}$
	$P_{g \rightarrow gg}$	$\frac{1}{z(1-z)}$	$\frac{z^3}{1-z}$	$\frac{(1-z)^3}{z}$	$\frac{1+z^4+(1-z)^4}{z(1-z)}$
	$P_{g \rightarrow q\bar{q}}$	0	z^2	$(1-z)^2$	$z^2 + (1-z)^2$

Table 6.1: Helicity-dependent DGLAP kernels with $p_A = z p_a$ and $p_k = z p_K$. The same expressions apply for $+$ \leftrightarrow $-$ or $q \leftrightarrow \bar{q}$.

6.2 Helicity-Dependent Antenna Functions from DGLAP Limits

In this section we discuss how the different helicity contributions to unpolarized initial-state antenna functions are constructed with the help of the helicity-dependent DGLAP splitting kernels and the unpolarized antenna functions. The results for initial-final antennae are presented in sec. 6.2.1 for the initial-state end and sec. 6.2.2 for the final-state end. Initial-initial antennae are discussed in sec. 6.2.3.

The helicity-dependent DGLAP kernels without colour factors are given in tab. 6.1. Note that for comparison with antenna functions, the kernel for $g \rightarrow gg$ includes an additional factor of 2 with respect to the function introduced in sec. 3.3.1. In other words, it does not include the symmetry factor of 1/2 for two identical bosons in the final state. The colour and coupling factors for DGLAP kernels, including dimensionless phase-space factors and the final-state $g \rightarrow gg$ symmetry factor, are

$$\begin{array}{cccc}
 q \rightarrow qq/q \rightarrow gq & g \rightarrow gg \text{ [FSR]} & g \rightarrow gg \text{ [ISR]} & g \rightarrow q\bar{q} \\
 C_F \frac{\alpha_s}{2\pi}, & \frac{1}{2} C_A \frac{\alpha_s}{2\pi}, & C_A \frac{\alpha_s}{2\pi}, & T_R \frac{\alpha_s}{2\pi}.
 \end{array} \quad (6.1)$$

The same expressions for antenna functions (which already include all relevant symmetry factors) are

$$\begin{array}{cccc}
 q \rightarrow qq/q \rightarrow gq & g \rightarrow gg \text{ [FSR]} & g \rightarrow gg \text{ [ISR]} & g \rightarrow q\bar{q} \\
 2 C_F \frac{\alpha_s}{4\pi}, & C_A \frac{\alpha_s}{4\pi}, & C_A \frac{\alpha_s}{4\pi}, & 2 T_R \frac{\alpha_s}{4\pi}.
 \end{array} \quad (6.2)$$

Except for gluon emission off initial-state gluons, the expressions are identical for antenna functions and DGLAP kernels, allowing a direct comparison between the two. We will come back to the difference in prefactors for the initial-state branching process $g \rightarrow gg$ below.

6.2.1 Initial-Final Antennae: Initial-State Side

In the antenna language, an initial-final branching is denoted by $AK \rightarrow ajk$, where AK is the parent antenna. When comparing to DGLAP kernels for initial-state radiation, note that the notation there uses a forward perspective, $a \rightarrow Aj$. The branching invariants in the DGLAP limit and the expression for the energy fraction of the branching parton, defined by $p_A = z p_a$, are

$$s_{aj} = Q^2 \rightarrow 0, \quad z = \frac{s_{AK}}{s_{AK} + s_{jk}}, \quad \text{and} \quad s_{jk} = s_{AK} \frac{1-z}{z}. \quad (6.3)$$

We now consider singularities in s_{aj} only, as finite terms and singularities in s_{jk} do not contribute to the DGLAP limit. The limits of the antenna functions are

$$\mathcal{A}_{qx \rightarrow qgx}^{\text{ISR}} \rightarrow 2 \frac{s_{AK}}{s_{aj}s_{jk}} + 2 \frac{1}{s_{aj}} + \frac{s_{jk}}{s_{AK}s_{aj}}, \quad (6.4)$$

$$\mathcal{A}_{gx \rightarrow qqx}^{\text{ISR}} \rightarrow \frac{1}{2} \frac{1}{s_{aj}} + \frac{s_{jk}}{s_{AK}s_{aj}} + \frac{s_{jk}^2}{s_{AK}^2 s_{aj}}, \quad (6.5)$$

$$\mathcal{A}_{gx \rightarrow ggx}^{\text{ISR}} \rightarrow 2 \frac{s_{AK}}{s_{aj}s_{jk}} + 2 \frac{1}{s_{aj}} + 2 \frac{s_{jk}}{s_{AK}s_{aj}} + 2 \frac{s_{jk}^2}{s_{AK}^2 s_{aj}} + 2 \frac{s_{jk}}{(s_{AK} + s_{jk})s_{aj}}, \quad (6.6)$$

$$\mathcal{A}_{qx \rightarrow g\bar{q}x}^{\text{ISR}} \rightarrow \frac{1}{s_{aj}} + \frac{s_{jk}}{s_{AK}s_{aj}} - 2 \frac{s_{jk}}{(s_{AK} + s_{jk})s_{aj}}. \quad (6.7)$$

These terms are easily rewritten by means of Q^2 and z ,

$$\mathcal{A}_{qx \rightarrow qgx}^{\text{ISR}} \rightarrow \frac{1}{Q^2} \frac{1}{z} \left[2 \frac{z^2}{1-z} + 2z + (1-z) \right], \quad (6.8)$$

$$\mathcal{A}_{gx \rightarrow qqx}^{\text{ISR}} \rightarrow \frac{1}{Q^2} \frac{1}{z} \left[\frac{1}{2} z + (1-z) + \frac{(1-z)^2}{z} \right], \quad (6.9)$$

$$\mathcal{A}_{gx \rightarrow ggx}^{\text{ISR}} \rightarrow \frac{1}{Q^2} \frac{1}{z} \left[2 \frac{z^2}{1-z} + 2z + 2(1-z) + 2 \frac{(1-z)^2}{z} + 2z(1-z) \right], \quad (6.10)$$

$$\mathcal{A}_{qx \rightarrow g\bar{q}x}^{\text{ISR}} \rightarrow \frac{1}{Q^2} \frac{1}{z} [z + (1-z) - 2z(1-z)]. \quad (6.11)$$

The DGLAP limits of the unpolarized antenna functions coincide with the DGLAP kernels in tab. 6.1,

$$\mathcal{A}_{qx \rightarrow qgx}^{\text{ISR}} \rightarrow \frac{1}{Q^2} \frac{1}{z} \frac{1+z^2}{1-z} = \frac{1}{Q^2} \frac{1}{z} P_{q \rightarrow qg}, \quad (6.12)$$

$$\mathcal{A}_{gx \rightarrow qqx}^{\text{ISR}} \rightarrow \frac{1}{Q^2} \frac{1}{z} \frac{1}{2} \frac{1+(1-z)^2}{z} = \frac{1}{Q^2} \frac{1}{z} \frac{1}{2} P_{q \rightarrow gq}, \quad (6.13)$$

$$\mathcal{A}_{gx \rightarrow ggx}^{\text{ISR}} \rightarrow \frac{1}{Q^2} \frac{1}{z} \frac{1+z^4+(1-z)^4}{z(1-z)} = \frac{1}{Q^2} \frac{1}{z} P_{g \rightarrow gg}, \quad (6.14)$$

$$\mathcal{A}_{qx \rightarrow g\bar{q}x}^{\text{ISR}} \rightarrow \frac{1}{Q^2} \frac{1}{z} [z^2 + (1-z)^2] = \frac{1}{Q^2} \frac{1}{z} P_{g \rightarrow q\bar{q}}. \quad (6.15)$$

The additional factor of $1/z$ is typically written as a phase-space contribution in the DGLAP language and does not appear in the splitting kernels. For the branching processes $gx \rightarrow ggx$ and $gx \rightarrow qqx$, the antenna function reproduces only half of the DGLAP kernel, as the parent gluon A participates in two antennae. For $gx \rightarrow ggx$, the difference is hidden in the prefactors of eqs. (6.1) and (6.2).

According to tab. 6.1, two different helicity configurations exist for the processes $q \rightarrow qq / q \rightarrow gq / g \rightarrow q\bar{q}$ and three for $g \rightarrow gg$. The contributions for $+$ \leftrightarrow $-$ have the same functional forms. The helicity of the parent parton A is averaged over to obtain the unpolarized splitting kernels from the polarized ones. Therefore, only the contributions with $+$ helicity of the parent parton A are of interest now. A general combination of terms in $Q^2 z \mathcal{A}_{Ax \rightarrow ajx}^{\text{ISR}}$ with the prefactors a to e reads

$$\begin{aligned} \mathcal{A}_{qx \rightarrow qqx}^{\text{ISR}} &: \frac{(2a - 2b + c)z^2 + (2b - 2c)z + c}{1 - z}, \\ \mathcal{A}_{gx \rightarrow qqx}^{\text{ISR}} &: \frac{1}{2} \frac{(a - 2b + 2c)z^2 + (2b - 4c)z + 2c}{z}, \\ \mathcal{A}_{gx \rightarrow ggx}^{\text{ISR}} &: 2 \frac{ez^4 + (a - b + c - d - 2e)z^3 + (b - 2c + 3d + e)z^2 + (c - 3d)z + d}{z(1 - z)}, \\ \mathcal{A}_{qx \rightarrow g\bar{q}x}^{\text{ISR}} &: 2cz^2 + (a - b - 2c)z + b. \end{aligned}$$

The helicity-dependent antenna functions can simply be read off by comparing to the DGLAP kernels,

$$\begin{aligned} \mathcal{A}_{qx \rightarrow qqx}^{\text{ISR}} &: [a = 0.5, b = c = 1] \text{ and } [a = 0.5, b = c = 0] \\ (+\times \rightarrow +\times) &\rightarrow \frac{s_{AK}}{s_{aj}s_{jk}} + 2 \frac{1}{s_{aj}} + \frac{s_{jk}}{s_{AK}s_{aj}} = \frac{1}{Q^2} \frac{1}{z} \frac{1}{1 - z}, \\ (+\times \rightarrow + - \times) &\rightarrow \frac{s_{AK}}{s_{aj}s_{jk}} = \frac{1}{Q^2} \frac{1}{z} \frac{z^2}{1 - z}, \\ \mathcal{A}_{gx \rightarrow qqx}^{\text{ISR}} &: [a = b = 1, c = 0.5] \text{ and } [a = b = 0, c = 0.5] \\ (+\times \rightarrow +\times) &\rightarrow \frac{1}{2} \frac{1}{s_{aj}} + \frac{s_{jk}}{s_{AK}s_{aj}} + \frac{1}{2} \frac{s_{jk}^2}{s_{AK}^2 s_{aj}} = \frac{1}{Q^2} \frac{1}{z} \frac{1}{2} \frac{1}{z}, \\ (+\times \rightarrow - - \times) &\rightarrow \frac{1}{2} \frac{s_{jk}^2}{s_{AK}^2 s_{aj}} = \frac{1}{Q^2} \frac{1}{z} \frac{1}{2} \frac{(1 - z)^2}{z}, \\ \mathcal{A}_{gx \rightarrow ggx}^{\text{ISR}} &: [a = d = 0.5, b = c = 1.5, e = 0], [a = e = 0.5, b = -0.5, c = d = 0], \\ &\text{and } [a = b = 0, c = d = e = 0.5] \\ (+\times \rightarrow +\times) &\rightarrow \frac{s_{AK}}{s_{aj}s_{jk}} + 3 \frac{1}{s_{aj}} + 3 \frac{s_{jk}}{s_{AK}s_{aj}} + \frac{s_{jk}^2}{s_{AK}^2 s_{aj}} = \frac{1}{Q^2} \frac{1}{z} \frac{1}{z(1 - z)}, \\ (+\times \rightarrow + - \times) &\rightarrow \frac{s_{AK}}{s_{aj}s_{jk}} - \frac{1}{s_{aj}} + \frac{s_{jk}}{(s_{AK} + s_{jk})s_{aj}} = \frac{1}{Q^2} \frac{1}{z} \frac{z^3}{1 - z}, \\ (+\times \rightarrow - - \times) &\rightarrow \frac{s_{jk}^2}{s_{AK}^2 s_{aj}} - \frac{s_{jk}}{s_{AK}s_{aj}} + \frac{s_{jk}}{(s_{AK} + s_{jk})s_{aj}} = \frac{1}{Q^2} \frac{1}{z} \frac{(1 - z)^3}{z}, \end{aligned}$$

$$\mathcal{A}_{qx \rightarrow g\bar{q}x}^{\text{ISR}} : [a = 0, b = 1, c = 0.5] \text{ and } [a = 1, b = 0, c = 0.5]$$

$$\begin{aligned} (+\times \rightarrow - - \times) &\rightarrow \frac{s_{jk}}{s_{AK}s_{aj}} - \frac{s_{jk}}{(s_{AK} + s_{jk})s_{aj}} = \frac{1}{Q^2} \frac{1}{z} (1-z)^2, \\ (+\times \rightarrow + - \times) &\rightarrow \frac{1}{s_{aj}} - \frac{s_{jk}}{(s_{AK} + s_{jk})s_{aj}} = \frac{1}{Q^2} \frac{1}{z} z^2. \end{aligned}$$

Averaging over the helicity of the parent parton gives the unpolarized antenna functions, e.g. for gluon emission off an initial-state quark,

$$\begin{aligned} \frac{1}{2} \left(\mathcal{A}_{qx \rightarrow qgq}^{\text{ISR}}(+\times \rightarrow ++\times) + \mathcal{A}_{qx \rightarrow qgq}^{\text{ISR}}(+\times \rightarrow +- \times) + \right. \\ \left. \mathcal{A}_{qx \rightarrow qgq}^{\text{ISR}}(-\times \rightarrow --\times) + \mathcal{A}_{qx \rightarrow qgq}^{\text{ISR}}(-\times \rightarrow -+\times) \right) = \mathcal{A}_{qx \rightarrow qgq}^{\text{ISR}}. \end{aligned} \quad (6.16)$$

6.2.2 Initial-Final Antennae: Final-State Side

We now turn to the discussion of the final-state limit, $K \rightarrow kj$. The branching invariants in the DGLAP limit and the expression for the energy fraction of the branching parton, defined by $p_k = z p_K$, are

$$s_{jk} = Q^2 \rightarrow 0, \quad z = \frac{s_{ak}}{s_{AK}}, \quad \text{and} \quad s_{aj} = s_{AK}(1-z). \quad (6.17)$$

Similar to sec. 6.2.1, only singularities in s_{jk} are considered. The expressions for the antenna functions of sec. 4.1 are

$$\mathcal{A}_{xq \rightarrow xgq}^{\text{FSR}} \rightarrow 2 \frac{s_{AK}}{s_{aj}s_{jk}} - 2 \frac{1}{s_{jk}} + \frac{s_{aj}}{s_{AK}s_{jk}}, \quad (6.18)$$

$$\mathcal{A}_{xg \rightarrow xgg}^{\text{FSR}} \rightarrow 2 \frac{s_{AK}}{s_{aj}s_{jk}} - 2 \frac{1}{s_{aj}} + \frac{s_{aj}}{s_{AK}s_{jk}} - \frac{s_{aj}^2}{s_{AK}^2 s_{jk}}, \quad (6.19)$$

$$\mathcal{A}_{xg \rightarrow x\bar{q}q}^{\text{FSR}} \rightarrow \frac{1}{2} \frac{1}{s_{jk}} - \frac{s_{aj}}{s_{AK}s_{jk}} + \frac{s_{aj}^2}{s_{AK}^2 s_{jk}}. \quad (6.20)$$

These terms are easily rewritten by means of Q^2 and z ,

$$\mathcal{A}_{xq \rightarrow xgq}^{\text{FSR}} \rightarrow \frac{1}{Q^2} \left[2 \frac{1}{1-z} - 2 + (1-z) \right], \quad (6.21)$$

$$\mathcal{A}_{xg \rightarrow xgg}^{\text{FSR}} \rightarrow \frac{1}{Q^2} \left[2 \frac{1}{1-z} - 2 + (1-z) - (1-z)^2 \right], \quad (6.22)$$

$$\mathcal{A}_{xg \rightarrow x\bar{q}q}^{\text{FSR}} \rightarrow \frac{1}{Q^2} \left[\frac{1}{2} - (1-z) + (1-z)^2 \right]. \quad (6.23)$$

The DGLAP limits of the unpolarized antenna functions coincide with the DGLAP kernels in tab. 6.1,

$$\mathcal{A}_{xq \rightarrow xgq}^{\text{FSR}} \rightarrow \frac{1}{Q^2} \frac{1+z^2}{1-z} = \frac{1}{Q^2} P_{q \rightarrow qg}, \quad (6.24)$$

$$\mathcal{A}_{xg \rightarrow xgg}^{\text{FSR}}(z) + \mathcal{A}_{xg \rightarrow xgg}^{\text{FSR}}(1-z) \rightarrow \frac{1}{Q^2} \frac{1+z^4 + (1-z)^4}{z(1-z)} = \frac{1}{Q^2} P_{g \rightarrow gg}, \quad (6.25)$$

$$\mathcal{A}_{xg \rightarrow x\bar{q}q}^{\text{FSR}}(z) + \mathcal{A}_{xg \rightarrow x\bar{q}q}^{\text{FSR}}(1-z) \rightarrow \frac{1}{Q^2} [z^2 + (1-z)^2] = \frac{1}{Q^2} P_{g \rightarrow q\bar{q}}. \quad (6.26)$$

For gluon emission off a gluon and gluon splitting to a $q\bar{q}$ pair, the DGLAP kernels are reproduced by summing over $j \leftrightarrow k$, which corresponds to summing over $z \leftrightarrow 1 - z$. As for the initial-state side, this is caused by the parent gluon K participating in two antennae.

Similar to the initial-side limit, a general combination of terms in $Q^2 z \mathcal{A}_{xK \rightarrow xjk}^{\text{FSR}}$ is

$$\begin{aligned} \mathcal{A}_{xq \rightarrow xqq}^{\text{FSR}} &: \frac{c z^2 + (2b - 2c)z + (2a - 2b + c)}{1 - z}, \\ \mathcal{A}_{xg \rightarrow xgg}^{\text{FSR}} &: \frac{d z^4 + (c - 3d)z^3 + (2b - 2c + 3d)z^2 + (2a - 2b + c - d)z}{z(1 - z)}, \\ \mathcal{A}_{xg \rightarrow xq\bar{q}}^{\text{FSR}} &: \frac{1}{2} (2c z^2 + (2b - 4c)z + (a - 2b + 2c)), \end{aligned}$$

The helicity-dependent antenna functions are read off by comparing to the DGLAP kernels,

$$\begin{aligned} \mathcal{A}_{xq \rightarrow xqq}^{\text{FSR}} &: [a = 0.5, b = c = 0] \text{ and } [a = 0.5, b = c = 1] \\ (\times+ \rightarrow \times++) &\rightarrow \frac{s_{AK}}{s_{aj}s_{jk}} = \frac{1}{Q^2} \frac{1}{1 - z}, \\ (\times+ \rightarrow \times-+) &\rightarrow \frac{s_{AK}}{s_{aj}s_{jk}} - 2 \frac{1}{s_{jk}} + \frac{s_{aj}}{s_{AK}s_{jk}} = \frac{1}{Q^2} \frac{z^2}{1 - z}, \\ \mathcal{A}_{xg \rightarrow xgg}^{\text{FSR}} &: [a = 0.5, b = -0.5, c = -2, d = 0] \text{ and } [a = 0.5, b = 1.5, c = 3, d = 1] \\ (\times+ \rightarrow \times++) &\rightarrow \frac{s_{AK}}{s_{aj}s_{jk}} + \frac{1}{s_{aj}} - 2 \frac{s_{aj}}{s_{AK}s_{jk}} = \frac{1}{Q^2} \frac{3z^2 - 2z^3}{z(1 - z)}, \\ (\times+ \rightarrow \times-+) &\rightarrow \frac{s_{AK}}{s_{aj}s_{jk}} - 3 \frac{1}{s_{aj}} + 3 \frac{s_{aj}}{s_{AK}s_{jk}} - \frac{s_{aj}^2}{s_{AK}^2 s_{jk}} = \frac{1}{Q^2} \frac{z^3}{1 - z}, \\ \mathcal{A}_{xg \rightarrow xq\bar{q}}^{\text{FSR}} &: [a = b = 0, c = 0.5] \text{ and } [a = b = 1, c = 0.5] \\ (\times+ \rightarrow \times+-) &\rightarrow \frac{1}{2} \frac{s_{aj}^2}{s_{AK}^2 s_{jk}} = \frac{1}{Q^2} \frac{1}{2} (1 - z)^2, \\ (\times+ \rightarrow \times-+) &\rightarrow \frac{1}{2} \frac{1}{s_{jk}} - \frac{s_{aj}}{s_{AK}s_{jk}} + \frac{1}{2} \frac{s_{aj}^2}{s_{AK}^2 s_{jk}} = \frac{1}{Q^2} \frac{1}{2} z^2. \end{aligned}$$

To obtain the correct result for $\mathcal{A}_{xg \rightarrow xgg}^{\text{FSR}}(\times+ \rightarrow \times++)$ for comparison with the DGLAP kernels, the permutations of the final-state gluons k and j have to be summed over,

$$\begin{aligned} &\mathcal{A}_{xg \rightarrow xgg}^{\text{FSR}}(\times+ \rightarrow \times++) (z) + \mathcal{A}_{xg \rightarrow xgg}^{\text{FSR}}(\times+ \rightarrow \times++) (1 - z) \\ &= \frac{1}{Q^2} \frac{1}{z(1 - z)} = \frac{1}{Q^2} P_{g \rightarrow gg}(+ \rightarrow ++). \end{aligned} \quad (6.27)$$

The configuration $\times+ \rightarrow \times+-$ is missing here, as it is taken care of by the permuted antenna function $\mathcal{A}_{xg \rightarrow xgg}^{\text{FSR}}(1 - z)$, when comparing to the full DGLAP kernels.

As before, averaging over the helicity of the parent parton gives the unpolarized antenna functions, e.g. for gluon emission off a final-state quark,

$$\frac{1}{2} \left(\mathcal{A}_{xq \rightarrow xgq}^{\text{FSR}}(\times + \rightarrow \times + +) + \mathcal{A}_{xq \rightarrow xgq}^{\text{FSR}}(\times + \rightarrow \times - +) + \mathcal{A}_{xq \rightarrow xgq}^{\text{FSR}}(\times - \rightarrow \times - -) + \mathcal{A}_{xq \rightarrow xgq}^{\text{FSR}}(\times - \rightarrow \times + -) \right) = \mathcal{A}_{xq \rightarrow xgq}^{\text{FSR}}. \quad (6.28)$$

6.2.3 Initial-Initial Antennae

An initial-initial branching is denoted by $AB \rightarrow ajb$, where AB is the parent antenna. The branching invariants in the DGLAP limit and the expression for the energy fraction of the branching parton, defined by $p_A = z p_a$, are

$$s_{aj} = Q^2 \rightarrow 0, \quad z = \frac{s_{AB}}{s_{ab}}, \quad \text{and} \quad s_{jb} = s_{AB} \frac{1-z}{z}. \quad (6.29)$$

As for initial-final antennae, only singularities in s_{aj} are considered. The expressions for the antenna functions of sec. 4.1 are

$$\mathcal{A}_{qx \rightarrow qgx}^{\text{ISR}} \rightarrow 2 \frac{s_{AB}}{s_{aj} s_{jb}} + 2 \frac{1}{s_{aj}} + \frac{s_{jb}}{s_{AB} s_{aj}}, \quad (6.30)$$

$$\mathcal{A}_{gx \rightarrow qqx}^{\text{ISR}} \rightarrow \frac{1}{2} \frac{1}{s_{aj}} + \frac{s_{jb}}{s_{AB} s_{aj}} + \frac{s_{jb}^2}{s_{AB}^2 s_{aj}}, \quad (6.31)$$

$$\mathcal{A}_{gx \rightarrow ggx}^{\text{ISR}} \rightarrow 2 \frac{s_{AB}}{s_{aj} s_{jb}} + 2 \frac{1}{s_{aj}} + 2 \frac{s_{jb}}{s_{AB} s_{aj}} + 2 \frac{s_{jb}^2}{s_{AB}^2 s_{aj}} + 2 \frac{s_{jb}}{(s_{ab} + s_{aj}) s_{aj}}, \quad (6.32)$$

$$\mathcal{A}_{qx \rightarrow g\bar{q}x}^{\text{ISR}} \rightarrow \frac{1}{s_{aj}} + \frac{s_{jb}}{s_{AB} s_{aj}} - \frac{2 s_{jb}}{(s_{AB} + s_{jb}) s_{aj}}. \quad (6.33)$$

These terms are easily rewritten by means of Q^2 and z ,

$$\mathcal{A}_{qx \rightarrow qgx}^{\text{ISR}} \rightarrow \frac{1}{Q^2} \frac{1}{z} \left[2 \frac{z^2}{1-z} + 2z + (1-z) \right], \quad (6.34)$$

$$\mathcal{A}_{gx \rightarrow qqx}^{\text{ISR}} \rightarrow \frac{1}{Q^2} \frac{1}{z} \left[\frac{1}{2} z + (1-z) + \frac{(1-z)^2}{z} \right], \quad (6.35)$$

$$\mathcal{A}_{gx \rightarrow ggx}^{\text{ISR}} \rightarrow \frac{1}{Q^2} \frac{1}{z} \left[2 \frac{z^2}{1-z} + 2z + 2(1-z) + 2 \frac{(1-z)^2}{z} + 2z(1-z) \right], \quad (6.36)$$

$$\mathcal{A}_{qx \rightarrow g\bar{q}x}^{\text{ISR}} \rightarrow \frac{1}{Q^2} \frac{1}{z} [z + (1-z) - 2z(1-z)]. \quad (6.37)$$

The DGLAP limits are exactly the same as as for initial-final antennae. Therefore, the helicity contributions can simply be taken over from sec. 6.2.1.

It is worth mentioning that the singularity

$$\frac{s_{jb}}{(s_{AB} + (n+1) s_{aj} + s_{jb}) s_{aj}} = \frac{s_{jb}}{(s_{ab} + n s_{aj}) s_{aj}}, \quad (6.38)$$

appearing with $n = \pm 1$ above, has the same limit for $s_{aj} \rightarrow 0$, independent of n . Thus, the choice of n is arbitrary when considering the DGLAP limit and here only fixed due to the choice of unpolarized antenna functions.

6.2.4 Summary

The limits of the helicity-dependent antenna functions in secs. 6.2.1 to 6.2.3 are combined for a consistent set of functions. The results are presented in tabs. 6.2 and 6.3. The shaded rows correspond to the unpolarized functions, obtained by averaging over parent and summing over daughter helicities. Note that no finite terms are added.

$AB \rightarrow ajb$	$\frac{s_{AB}}{s_{aj}s_{jb}}$	$\frac{1}{s_{aj}}$	$\frac{1}{s_{jb}}$	$\frac{\eta_{jb}}{s_{aj}}$	$\frac{\eta_{aj}}{s_{jb}}$	$\frac{\eta_{jb}^2}{s_{aj}}$	$\frac{\eta_{aj}^2}{s_{jb}}$	$\frac{s_{jb}/s_{aj}}{s_{ab} + ns_{aj}}$	$\frac{s_{aj}/s_{jb}}{s_{ab} + ns_{jb}}$
$q\bar{q} \rightarrow qg\bar{q}$	2	2	2	1	1	0	0	0	0
$++ \rightarrow +++$	1	2	2	1	1	0	0	0	0
$++ \rightarrow +-+$	1	0	0	0	0	0	0	0	0
$+- \rightarrow ++-$	1	2	0	1	0	0	0	0	0
$+- \rightarrow +--$	1	0	2	0	1	0	0	0	0
$qg \rightarrow qgg$	2	2	2	1	2	0	2	0	2
$++ \rightarrow +++$	1	2	3	1	3	0	1	0	0
$++ \rightarrow +-+$	1	0	-1	0	0	0	0	0	1
$+- \rightarrow ++-$	1	2	-1	1	0	0	0	0	1
$+- \rightarrow +--$	1	0	3	0	3	0	1	0	0
$++ \rightarrow +--$	0	0	0	0	-1	0	1	0	1
$+- \rightarrow +++$	0	0	0	0	-1	0	1	0	1
$gg \rightarrow ggg$	2	2	2	2	2	2	2	2	2
$++ \rightarrow +++$	1	3	3	3	3	1	1	0	0
$++ \rightarrow +-+$	1	-1	-1	0	0	0	0	1	1
$+- \rightarrow ++-$	1	3	-1	3	0	1	0	0	1
$+- \rightarrow +--$	1	-1	3	0	3	0	1	1	0
$++ \rightarrow --+$	0	0	0	-1	0	1	0	1	0
$++ \rightarrow +--$	0	0	0	0	-1	0	1	0	1
$+- \rightarrow ---$	0	0	0	-1	0	1	0	1	0
$+- \rightarrow +++$	0	0	0	0	-1	0	1	0	1
$xg \rightarrow xqq$	0	0	1/2	0	1	0	1	0	0
$++ \rightarrow +++$	0	0	1/2	0	1	0	1/2	0	0
$++ \rightarrow +--$	0	0	0	0	0	0	1/2	0	0
$+- \rightarrow +++$	0	0	0	0	0	0	1/2	0	0
$+- \rightarrow +--$	0	0	1/2	0	1	0	1/2	0	0
$x\bar{q} \rightarrow xqg$	0	0	1	0	1	0	0	0	-2
$++ \rightarrow +-+$	0	0	1	0	0	0	0	0	-1
$++ \rightarrow +--$	0	0	0	0	1	0	0	0	-1
$+- \rightarrow +++$	0	0	0	0	1	0	0	0	-1
$+- \rightarrow ++-$	0	0	1	0	0	0	0	0	-1

Table 6.2: Singular terms of the helicity-dependent initial-initial antennae with the shorthand notation $\eta_{aj/jb} = s_{aj/jb}/s_{AB}$.

$AK \rightarrow ajk$	$\frac{s_{AK}}{s_{aj}s_{jk}}$	$\frac{1}{s_{aj}}$	$\frac{1}{s_{jk}}$	$\frac{\eta_{jk}}{s_{aj}}$	$\frac{\eta_{aj}}{s_{jk}}$	$\frac{\eta_{jk}^2}{s_{aj}}$	$\frac{\eta_{aj}^2}{s_{jk}}$	$\frac{s_{jk}}{s_{aj}(s_{AK} + s_{jk})}$
$qq \rightarrow qqg$	2	2	-2	1	1	0	0	0
$++ \rightarrow +++$	1	2	0	1	0	0	0	0
$++ \rightarrow +-+$	1	0	-2	0	1	0	0	0
$+- \rightarrow +++$	1	2	-2	1	1	0	0	0
$+- \rightarrow +--$	1	0	0	0	0	0	0	0
$qg \rightarrow qgg$	2	2	-2	1	1	0	-1	0
$++ \rightarrow +++$	1	2	1	1	-2	0	0	0
$++ \rightarrow +-+$	1	0	-3	0	3	0	-1	0
$+- \rightarrow +++$	1	2	-3	1	3	0	-1	0
$+- \rightarrow +--$	1	0	1	0	-2	0	0	0
$gq \rightarrow ggq$	2	2	-2	2	1	2	0	2
$++ \rightarrow +++$	1	3	0	3	0	1	0	0
$++ \rightarrow +-+$	1	-1	-2	0	1	0	0	1
$+- \rightarrow +++$	1	3	-2	3	1	1	0	0
$+- \rightarrow +--$	1	-1	0	0	0	0	0	1
$++ \rightarrow --+$	0	0	0	-1	0	1	0	1
$+- \rightarrow ---$	0	0	0	-1	0	1	0	1
$gg \rightarrow ggg$	2	2	-2	2	1	2	-1	2
$++ \rightarrow +++$	1	3	1	3	-2	1	0	0
$++ \rightarrow +-+$	1	-1	-3	0	3	0	-1	1
$+- \rightarrow +++$	1	3	-3	3	3	1	-1	0
$+- \rightarrow +--$	1	-1	1	0	-2	0	0	1
$++ \rightarrow --+$	0	0	0	-1	0	1	0	1
$+- \rightarrow ---$	0	0	0	-1	0	1	0	1
$xg \rightarrow x\bar{q}q$	0	0	1/2	0	-1	0	1	0
$++ \rightarrow +++$	0	0	0	0	0	0	1/2	0
$++ \rightarrow +-+$	0	0	1/2	0	-1	0	1/2	0
$+- \rightarrow +++$	0	0	1/2	0	-1	0	1/2	0
$+- \rightarrow +-+$	0	0	0	0	0	0	1/2	0
$gx \rightarrow qqx$	0	1/2	0	1	0	1	0	0
$++ \rightarrow +++$	0	1/2	0	1	0	1/2	0	0
$++ \rightarrow --+$	0	0	0	0	0	1/2	0	0
$-+ \rightarrow +++$	0	0	0	0	0	1/2	0	0
$-+ \rightarrow --+$	0	1/2	0	1	0	1/2	0	0
$qx \rightarrow g\bar{q}x$	0	1	0	1	0	0	0	-2
$++ \rightarrow +-+$	0	1	0	0	0	0	0	-1
$++ \rightarrow --+$	0	0	0	1	0	0	0	-1
$-+ \rightarrow +++$	0	0	0	1	0	0	0	-1
$-+ \rightarrow -++$	0	1	0	0	0	0	0	-1

Table 6.3: Singular terms of the helicity-dependent initial-final antennae with the shorthand notation $\eta_{aj/jk} = s_{aj/jk}/s_{AK}$.

Constructing the helicity-dependent antenna functions as shown in secs. 6.2.1-6.2.3 automatically respects Bose-Einstein symmetry and the C and P invariance of QCD. The functions are symmetric when final-state gluons of the same helicity are exchanged, see $qg \rightarrow qgg$ and $gg \rightarrow ggg$ for initial-final antennae. The same functions apply for $+$ \leftrightarrow $-$ or $q \leftrightarrow \bar{q}$. These requirements are already encoded in the helicity-dependent DGLAP kernels in tab. 6.1 and consequently transferred to the antenna functions.

For initial-state radiation helicity configurations exist for which a final-state gluon inherits the helicity of an initial-state gluon, for instance $g_+q_\times \rightarrow g_-g_-q_\times$. From a physical point of view, there is no soft singularity associated with the final-state gluon. In a forwards perspective, the role of the “emission” is rather played by the initial-state gluon A , with the gluons a and j being the “emitter”. This is reflected in the antenna functions, where no soft terms $s_{AB}/(s_{aj}s_{jb})$ or $s_{AK}/(s_{aj}s_{jk})$ are present for $g_+x_\times \rightarrow g_-g_-x_\times$.

Finally, note that the initial-final antenna functions in tab. 6.3 have the same singularities in s_{jk} as the corresponding final-final antenna functions in [147] with $\alpha = 0$.

A Trip into Fragmentation

The predictions of PYTHIA 8 agree very well with a large range of LEP and early LHC data. New LHC measurements exhibit effects that are not included in the PYTHIA 8 string fragmentation, such as collective flow [148–150] or “the ridge” [151–153]. Furthermore, deviations between data and PYTHIA 8 in p_{\perp} spectra are present, for instance pions obtain a too hard p_{\perp} spectrum, whereas heavier hadrons obtain too little p_{\perp} .

The aim of the paper presented in sec. 7.1 is to implement modifications to the conventional string fragmentation framework in the PYTHIA 8 event generator and explore whether those can provide a step in the right direction to improve the description of new LHC data. In the current form of the fragmentation the string breaking is based on a tunneling analogy, where fluctuations of the form $g \rightarrow q\bar{q}$ break the string. The quark-antiquark pairs receive opposite and compensating kicks in p_{\perp} according to a Gaussian distribution, independently of their flavour. We implement a new model for generating the p_{\perp} of hadrons during the fragmentation in PYTHIA 8. It is inspired by thermodynamics and based on an exponential suppression of the hadronic transverse mass. It therefore naturally suppresses heavier hadrons with respect to lighter hadrons but they obtain a higher average p_{\perp} . We further added a simple model to take the close-packing of strings into account. By making the generation of the p_{\perp} dependent on the environment, hadrons in high-multiplicity events obtain more p_{\perp} . As a last addition we implement a simple model for hadron rescattering, where hadron pairs are allowed to scatter off each other dependent on their rapidity difference.

The modified predictions have been tested and validated with toy model studies as well as by comparing to LHC data, such as identified particle spectra. We tuned the newly introduced parameters to achieve an improved description of data. While the thermodynamical model provides a significantly improved description of some observables, compared the conventional model, the overall effects are not as large as hoped for and not all phenomena are included in the new model. Nevertheless the results point out that more physics is at play than assumed in the traditional Lund model with tunneling-based string breaks. The improvement due to the thermodynamical model implies that the string breaking is not governed solely by partons, but one should rather consider the hadrons themselves in the process. Taking into account the close-packing of string confirms that strings do affect each

other, especially in a dense environment. We do not claim that our simple model is necessarily the correct approach, but the improvements it causes point towards the right direction. The hadronic rescattering as a way of accounting for collective-flow effects contributes to the modelling of additional hadron-hadron interactions that occur on top of the string fragmentation.

The conclusions above are confirmed by the even more successful DIPSY generator, where the formation of colour ropes is a consequence of a more sophisticated model for the close-packing of strings [154]. In addition to the increased production of heavier hadrons and larger p_{\perp} values, the ridge phenomenon is included via a shoving mechanism [155]. Similar effects are achieved in the EPOS generator due to the formation of a quark-gluon plasma [156].

The new LHC measurements and successful models, which take into account string density, hadron rescattering, and/or quark-gluon plasma, point towards the physics of soft collective signals, including fragmentation, being similar for high-energy reactions with incoming hadrons and heavy ions. The effects are more obvious and dominant in heavy-ion collisions though. One may hope that the fragmentation in e^+e^- , pp , and heavy-ion collisions can be performed by the same underlying model, providing distinct predictions for the three different beam setups, based on arguments such as string density or energy. A recent article fits in this discussion by asking the question of whether the minimal conditions for collective effects are already met in e^+e^- collisions [157]. The authors predict results that “imply that in small collisions systems over a range of energies, a minimum of two strings is sufficient to generate collectivity signals.” Future studies will hopefully reveal the way how those effects are generated and therefore what underlying mechanisms are at play.

7.1 Published Material

Thermodynamical String Fragmentation

Nadine Fischer and Torbjörn Sjöstrand

Published in The Journal of High Energy Physics 01 (2017) 140

DOI: 10.1007/JHEP01(2017)140

e-Print: arXiv:1610.09818 [hep-ph]

Begins overleaf.



PUBLISHED FOR SISSA BY SPRINGER

RECEIVED: November 7, 2016

ACCEPTED: January 18, 2017

PUBLISHED: January 31, 2017

Thermodynamical string fragmentation

Nadine Fischer^{a,b} and Torbjörn Sjöstrand^a

^a*Theoretical Particle Physics, Department of Astronomy and Theoretical Physics, Lund University, Sölvegatan 14A, Lund, SE-223 62 Sweden*

^b*School of Physics and Astronomy, Monash University, Wellington Road, Clayton, VIC-3800 Australia*

E-mail: nadine.fischer@monash.edu, torbjorn@thep.lu.se

ABSTRACT: The observation of heavy-ion-like behaviour in pp collisions at the LHC suggests that more physics mechanisms are at play than traditionally assumed. The introduction e.g. of quark-gluon plasma or colour rope formation can describe several of the observations, but as of yet there is no established paradigm. In this article we study a few possible modifications to the PYTHIA event generator, which describes a wealth of data but fails for a number of recent observations. Firstly, we present a new model for generating the transverse momentum of hadrons during the string fragmentation process, inspired by thermodynamics, where heavier hadrons naturally are suppressed in rate but obtain a higher average transverse momentum. Secondly, close-packing of strings is taken into account by making the temperature or string tension environment-dependent. Thirdly, a simple model for hadron rescattering is added. The effect of these modifications is studied, individually and taken together, and compared with data mainly from the LHC. While some improvements can be noted, it turns out to be nontrivial to obtain effects as big as required, and further work is called for.

KEYWORDS: Phenomenological Models, QCD Phenomenology

ARXIV EPRINT: [1610.09818](https://arxiv.org/abs/1610.09818)

Contents

1	Introduction	1
2	Existing models and data	3
2.1	The Lund string model	3
2.2	Key data	6
3	The new models	9
3.1	Variations of the normal string model	9
3.2	The thermodynamical string model	13
3.3	The hadronic rescattering model	17
3.4	Results	20
4	Comparisons with data	25
4.1	Impact of the different effects	26
4.2	Results	28
5	Summary and outlook	35
A	Settings	37

1 Introduction

QCD, the theory of strong interactions, is at the origin of a wide range of phenomena. In one extreme, progress on high-energy perturbative calculations offers an increasingly precise and successful description of hard processes, as a large community is steadily improving calculational techniques. NLO calculations, once rare, are now standard, NNLO is getting there, and even N³LO is starting to appear (see e.g. [1] and references therein). In another extreme, the nonperturbative aspects of low-energy interactions are less well understood. Lattice QCD can be used to calculate static hadron properties, but not (yet?) dynamical processes. Specifically, the description of hadronization, the step whereby partons turn into hadrons in high-energy collisions, cannot be derived directly from the QCD Lagrangian within any currently known formalism. Instead string [2] and cluster [3–5] models, developed in the early eighties, have been used almost unchanged from PETRA/LEP e^+e^- events to Sp \bar{p} S/Tevatron/LHC $p\bar{p}/pp$ ones — the assumed “jet universality”. Differences have been attributed to the quite disparate parton-level configurations that undergo hadronization: while e^+e^- involves only hard process and final-state radiation (FSR), pp adds aspects such as initial-state radiation (ISR), multiparton interactions (MPIs), beam remnants and colour reconnection (CR).

Cracks have started to appear in this picture as new LHC data have been presented. Specifically, several studies have shown how high-multiplicity pp events have properties similar to those observed in heavy-ion AA collisions. Some observations may have an explanation within the current framework, e.g. CR may give some flow-like patterns [6], but others do not. An early example was the discovery of “the ridge”, an enhanced particle production around the azimuthal angle of a trigger jet, stretching away in (pseudo)rapidity [7–9]. A more recent example is the smoothly increasing fraction of strange baryon production with increasing charged multiplicity, a trend that lines up with pA data before levelling out at the AA results [10].¹ Conventional wisdom holds that the formation of a quark-gluon plasma (QGP) requires a larger volume and longer time for thermalization than pp or pA systems can offer, so such trends are unexpected, see e.g. [12].

It is therefore time to rethink the picture of hadronization in high-energy and high-multiplicity collisions. One possible approach is to imagine that a QGP is at least partly formed in pp collisions, such that individual colour fields (strings) cease to exist. Such a behaviour is already implemented in the EPOS model [13]. Another is to imagine that strings survive as a vehicle e.g. of short-range flavour correlations, but that their properties are modified. Colour ropes [14–16] is one such example, wherein several colour-triplet strings combine to a higher colour-representation field. A detailed implementation of rope dynamics is found in the DIPSY program [17]. Both EPOS and DIPSY qualitatively describe several of the new key features, such as the increasing rate of strangeness production at higher multiplicities.

With the studies described in this article we want to add to the set of alternative models that can be used to compare with data. At best it may offer some new insights, at worst it will act as a straw man model. Firstly, rather than the particle-mass-independent Gaussian p_{\perp} spectrum assumed in the standard string model, it introduces an exponential p_{\perp} dependence, $\exp(-p_{\perp}/T)$. This is split among possible flavours according to hadronic m_{\perp} , $\exp(-m_{\perp}/T)$. Such p_{\perp} and m_{\perp} shapes were used to describe early pp data, e.g. at the ISR [18], and has some foundation in the Hagedorn temperature [19–21] and in related [22] ideas. (Later powerlike p_{\perp} ansätze [21, 23, 24] or two-component exponential + powerlike ones [25] can be viewed as a consequence of perturbative jet production, and is in our framework generated as such, in an earlier stage than the nonperturbative hadronization.) Secondly, it assumes that the close-packing of several strings leads to an increased effective temperature and thereby both a changed particle composition and changed p_{\perp} spectra. In spirit this is close to the rope model, but it does not have to assume that the individual strings either fuse or melt away. Thirdly, if the fragmenting strings are close-packed this also implies the initial formation of a dense hadronic gas, wherein rescattering may lead to collective-flow effects. Such effects are simulated in a crude first approximation.

The impact of these mechanisms on experimental distributions is studied, in order to quantify their significance. As a prime example, consider the $\langle p_{\perp} \rangle (n_{\text{ch}})$ distribution, with a characteristic rising trend that has been proposed as a signal for colour reconnection [26].

¹Note that in [11] the authors obtain the same enhancement regardless of the system measured if the yield ratios are plotted against the estimated energy density.

Alternative interpretations are now offered in terms of close-packing of strings and/or hadrons, and these are presented and compared with data individually. At the end of the day, we should expect the “true” nature of high-multiplicity pp collisions to contain many contributing mechanisms, however. To be more more specific, in quantum mechanics any process that is not explicitly forbidden by some selection rule is bound to occur, the question is only with what rate. The final task therefore is try to constrain the relative importance of the mechanisms, not to prove a specific one “right” or “wrong”.

The new model components are implemented as options in the standard PYTHIA event generator [27, 28], which makes it easily accessible for further experimental tests. They should be viewed as a first iteration. Should they prove useful there is room for further improvements, as we will indicate.

The article is organized as follows. Section 2 outlines relevant features of the existing Lund string model and introduces key observables, with emphasis on those new ones that are not well described by the current PYTHIA generator. Section 3 introduces the alternative approaches explored in this article, and presents some first toy studies for simplified string topologies. Comparisons with data are presented in section 4, highlighting what seems to work where and what not. Finally section 5 contains a summary and outlook.

2 Existing models and data

2.1 The Lund string model

The Lund string fragmentation model [2] is very successful in many respects, but more so for the overall longitudinal fragmentation structure than for its description of the particle composition.

The central assumption in the string model is that of linear confinement, $V(r) = \kappa r$, with a string tension $\kappa \approx 1 \text{ GeV/fm}$. The word “string” should here not be taken literally; the physical object is a kind of flux tube stretched between the endpoints, with a typical transverse size of the order of the proton one, $r_p \sim 0.7 \text{ fm}$. The one-dimensional “mathematical” string should then be viewed as a description of the location of the center of the flux tube. By analogy with superconductivity the tube could be viewed as a vortex line like in a type II superconductor, alternatively as an elongated bag in a type I one.

In the case of a simple stable back-to-back $q\bar{q}$ system, with $m_q = p_{\perp q} = 0$, quarks move with the speed of light in “yo-yo”-mode oscillations, as energy moves between being stored in the endpoint quarks and in the intermediate string. If creation of new $q\bar{q}$ pairs is allowed the original system can break up into smaller ones, each a colour singlet in its own right. Denoting the original pair $q_0\bar{q}_0$, and ordering the new pairs $q_i\bar{q}_i$, $1 \leq i \leq n - 1$ from the quark end, results in the production of n hadrons $q_0\bar{q}_1, q_1\bar{q}_2, \dots, q_{n-1}\bar{q}_0$.

Aligning the x axis with the string axis, the breakup vertices are characterized by their location (t_i, x_i) . These vertices have a spacelike separation, and so have no unique time ordering. (Except for the original $(t_0, x_0) = (0, 0)$ of course. But here it is actually the turning points of the q_0 and \bar{q}_0 that define the vertices in eq. (2.1) below, and then spacelike separation is restored.) Two adjacent ones are correlated by the constraint that

the hadron produced should have the correct mass m_i :

$$\kappa^2((x_i - x_{i-1})^2 - (t_i - t_{i-1})^2) = m_i^2. \quad (2.1)$$

If the vertices are assigned from the quark end, say, each new vertex therefore corresponds to one degree of freedom, which should be selected according to some probability function. Imposing consistency constraints, mainly that results should be the same (on the average) if fragmentation is instead considered from the antiquark end, gives the solution [2]

$$f(z) \propto \frac{1}{z} (1-z)^a \exp(-bm^2/z), \quad (2.2)$$

with a and b two free parameters, and where $m^2 \rightarrow m_{\perp}^2$ once transverse momentum is introduced. Here z is the fraction of available lightcone momentum $E + p_x$ taken by a hadron, with the remainder $1-z$ retained by the string for subsequent particle production.

This ansatz leads to vertices having an equilibrium distribution (after having taken a few steps away from the endpoints)

$$P(\Gamma) \propto \Gamma^a \exp(-b\Gamma), \quad \Gamma = (\kappa\tau)^2 = \kappa^2(t^2 - x^2), \quad (2.3)$$

with the same a and b as above. (For the special case $a = 0$ this result agrees with the Artru-Mennessier model [29], which is based on constant decay probability per string area $dt dx$, without any mass constraint.) The associated probability for producing n particles can be written as [30]

$$dP_n \propto \left[\prod_{i=1}^n N d^2 p_i \delta(p_i^2 - m_i^2) \right] \delta^{(2)} \left(\sum_i p_i - p_{\text{tot}} \right) \exp(-b\kappa^2 A_{\text{tot}}), \quad (2.4)$$

where A_{tot} is the total space-time area under the breakup vertices. The relation between dP_n and dP_{n-1} (at a reduced c.m. energy) is then given by the fragmentation function eq. (2.2), where it is easy to show that the exponentials match, and somewhat less trivial that a larger N (i.e. larger weight for higher multiplicities) corresponds to a larger a (i.e. less momentum taken away in each step).

The simple $q\bar{q}$ fragmentation picture can be extended to $q\bar{q}g$ topologies if the gluon is viewed as having separate colour and anticolour indices, as in the $N_C \rightarrow \infty$ limit [31]. Then one string piece is stretched between the quark and the gluon, and another between the gluon and the antiquark. The absence of a string piece stretched directly between the quark and antiquark leads to predicted asymmetries in the particle production [32] that rapidly were observed experimentally [33]. In general, a string can stretch from a quark end via a number of intermediate gluons to an antiquark end. Technically the motion and fragmentation of such a string system can become rather complicated [34], but the fragmentation can be described without the introduction of any new principles or parameters. This is the most powerful and beautiful aspect of the string fragmentation framework. Note that the leading hadron in a gluon jet can take momentum from both the string pieces that attaches it to colour-adjacent partons. This is unlike cluster models, where gluons are forced to branch into $q\bar{q}$ pairs, such that smaller colour singlets are

formed rather than one single string winding its way between the partons. The string model is easily extended to closed gluon loops and, with rather more effort [35], to junction topologies, where three string pieces come together in a single vertex.

We now turn to the breakup mechanism. If a $q\bar{q}$ pair is massless and has no transverse momentum it can be produced on-shell, in a single vertex, and then the q and \bar{q} can move apart, splitting the string into two in the process. But if the q (and \bar{q}) transverse mass $m_{\perp q} = \sqrt{m_q^2 + p_{\perp q}^2} > 0$ this is no longer possible. By local flavour conservation the $q\bar{q}$ pair is still produced at a common vertex, but as virtual particles that each needs to tunnel out a distance $d = m_{\perp}/\kappa$. Using the WKB approximation [2] to calculate the tunneling probability for the pair gives a factor

$$\exp(-\pi m_{\perp q}^2/\kappa) = \exp(-\pi m_q^2/\kappa) \exp(-\pi p_{\perp q}^2/\kappa) , \quad (2.5)$$

where the Gaussian answer allows a convenient separation of the m and p_{\perp} dependencies (with implicit phase space d^2p_{\perp}).

The latter is implemented by giving the q and \bar{q} opposite and compensating p_{\perp} kicks, with $\langle p_{\perp q}^2 \rangle = \kappa/\pi = \sigma^2 \approx (0.25 \text{ GeV})^2$. A hadron receives its p_{\perp} as the vector sum of its q and \bar{q} constituent kicks, and thus $\langle p_{\perp \text{had}}^2 \rangle = 2\sigma^2$. Empirically the tuned σ value comes out larger than this, actually closer to $\sigma = 0.35 \text{ GeV}$. This implies that almost half of the p_{\perp}^2 kick is coming from other sources than tunneling. One source could be soft gluon radiation below the perturbative (parton shower) cutoff, where α_s becomes so big that perturbation theory breaks down [36]. Effectively radiation near the perturbative/nonperturbative border is thus shoved into an artificially enhanced tunneling answer, with the further assumption that the Gaussian shape and the p_{\perp} balancing inside each new $q\bar{q}$ pair still holds.

Uncertainties also arise in the interpretation of the mass suppression factor of eq. (2.5): what quark masses to use? If current quark masses then the u and d ones are negligible while the s is below 0.2 GeV , predicting less strangeness suppression than observed, while with constituent masses $m_u \approx m_d \approx 0.33 \text{ GeV}$ and $m_s \approx 0.51 \text{ GeV}$ [37] too much suppression is predicted. Intermediate masses and suppression factors closer to data can be motivated e.g. by noting that an expanding string corresponds to confinement in the two transverse dimensions but not in the longitudinal one. In the end, however, the s/u suppression is viewed as an empirical number to be tuned to data. Whichever values are used, c and b quark tunneling production is strongly suppressed, so this mechanism can be totally neglected relative to the perturbative ones.

Considering only mesons in radial and rotational ground states, i.e. only the pseudoscalar and vector multiplets, naive spin counting predicts relative rates $1 : 3$, whereas data prefers values closer to $1 : 1$, at least for $\pi : \rho$. It is possible to explain a suppression of the vector mesons based on the difference in the hadronic wave functions, from the spin-spin interaction term [2], but the amount has to be tuned to data. And further brute-force suppression factors are needed specifically for the η and η' mesons, which have “unnaturally” large masses owing to the $U(1)$ anomaly.

Baryon production can be introduced by allowing diquark-antidiquark breakups of the string [38], to be viewed as occurring in two consecutive $q\bar{q}$ creation steps [39]. A baryon

and the matching antibaryon would normally be nearest neighbours along the string, but the “popcorn mechanism” also allows one (or more) mesons to be produced in between. Diquark masses can be used to derive approximate suppressions, but again free parameters are used, for qq/q , sq/qq , qq_1/qq_0 and others. Unfortunately the tuned values do not always match so well with the tunneling-formula expectations.

In total $\mathcal{O}(20)$ parameters are used to describe the outcome of the string/tunneling mechanism for particle production. Notable is that the particle masses do not enter explicitly in these considerations. This is unlike cluster models, e.g., where hadron masses occur in the phase space available for different cluster decay channels. A fair overall description of the particle composition is then obtained with very few parameters [40, 41]. Note that while most fragmentation parameters in HERWIG++ exist in different copies for light (u, d, s), c, and b quarks, the ones for heavy quarks have either been set equal to the values of those for light quarks [40] or have not been included in further tuning processes [41].

The hadron masses can be explicitly introduced into the Lund framework by assuming that the integral $\int_0^1 f(z) dz$, with $f(z)$ given by eq. (2.2), provides the relative normalization of possible particle states. This concept has been developed successfully within the UCLA model [42, 43], in that particle rates come out quite reasonably with minimal further assumptions. There are some other issues with this approach, however, and we do not pursue it further here.

2.2 Key data

An immense number of studies have been published based on hadron collider data, and it is not the intention here to survey all of that. Instead we here bring up some of the key data and distributions that have prompted us to this study. Several of them will be shown repeatedly in the following. We note that all histograms we will present in this article are produced by utilizing RIVET [44].

The list of key observables includes:

- The change of flavour composition with event multiplicity. Specifically, high-multiplicity events have a higher fraction of heavier particles, meaning particles with a higher strangeness content [10]. PYTHIA contains no mechanism to generate such a behaviour. On the contrary, within a single fixed-energy string a higher multiplicity means more lighter particles, for phase space reasons. In pp collisions a higher multiplicity is predominantly obtained by more MPIs, however, so the composition stays rather constant.
- The average transverse momentum $\langle p_\perp \rangle$ is larger for heavier particles, both at RHIC [45] and LHC [46]. This is a behaviour that is present also in PYTHIA, and comes about quite naturally e.g. by lighter particles more often being decay products, with characteristic $\langle p_\perp \rangle$ values smaller than the primary particles in the string fragmentation. The mass dependence is underestimated, however. That is, π^\pm obtains a too large $\langle p_\perp \rangle$ in PYTHIA and baryons a too small one. Recently $\langle p_\perp \rangle$ has also been presented as a function of n_{ch} , inclusive [47] and for different hadron species [48], providing a more differential information on this mismatch. In figure 1 we show

these observables and compare default PYTHIA with data, with the above expected conclusions. Note that the data in figure 1 of [48] is not (yet) publicly available. To obtain an estimate of the data that is comparable to MC predictions we used an estimate of the logarithmic fits shown in figure 1 of [48] and used n_{ch} values on the x axis rather than $\langle dn_{\text{ch}}/d\eta \rangle_{|\eta|<0.5}$.

- The charged particle p_{\perp} spectrum is not correctly modelled at low p_{\perp} scales, with PYTHIA producing too few particles at very low values [47, 49, 50]. Often tunes then compensate by producing a bit too many at intermediate p_{\perp} scales. The issue shows up e.g. in minimum-bias $dn_{\text{ch}}/d\eta$ distributions, where it is not possible to obtain a good description for data analyzed with $p_{\perp} > 0.1$ GeV and $p_{\perp} > 0.5$ GeV simultaneously.
- In the p_{\perp} spectra for identified particles [51] it turns out that the deficit at low p_{\perp} is from too little π^{\pm} production. This is not unexpected, given the previous two points, but stresses the need to revise the mass dependence of p_{\perp} spectra.
- The Λ/K p_{\perp} spectrum ratio, measured by CMS [52], where PYTHIA is not able to reproduce the peak at ~ 2.5 GeV completely and overshoots the distribution for large- p_{\perp} values.
- The observation of a ridge in pp collisions was one of the major surprises in the 7 TeV data [7], and has been reconfirmed in the 13 TeV one [8, 9]. The ridge is most clearly visible at the very highest multiplicities, but more careful analyses hints the effect is there, to a smaller extent, also at lower multiplicities. Like in heavy-ion collisions one may also seek a description in terms of correlation functions, $C(\Delta\phi) \propto 1 + \sum_{n \geq 2} v_n \cos(n\Delta\phi)$, notably the v_2 coefficient, with a similar message. These phenomena are not at all described by PYTHIA: there is no mechanism that produces a ridge and, once the effects of back-to-back jet production have been subtracted, also no rise of v_2 .

There are also some other reference distributions that have to be checked. These are ones that already are reasonably well described, but that inevitably would be affected by the introduction of new mechanisms.

- The charged particle multiplicity distribution $P(n_{\text{ch}})$ is sensitive to all mechanisms in minimum-bias physics, but especially the MPI and CR modelling. A mismatch in $\langle n_{\text{ch}} \rangle$ is most easily compensated by modifying the $p_{\perp 0}$ scale of the MPI description. This parameter is used to tame the dp_{\perp}^2/p_{\perp}^4 divergence of the QCD cross section to a finite $dp_{\perp}^2/(p_{\perp 0}^2 + p_{\perp}^2)^2$ shape. It can be viewed as the the inverse of the typical colour screening distance inside the proton. A mismatch in the width of the n_{ch} distribution can be compensated by a modified shape of the b impact-parameter distribution of the two colliding protons. Specifically, a distribution more sharply peaked at $b = 0$ gives a longer tail towards high multiplicities.

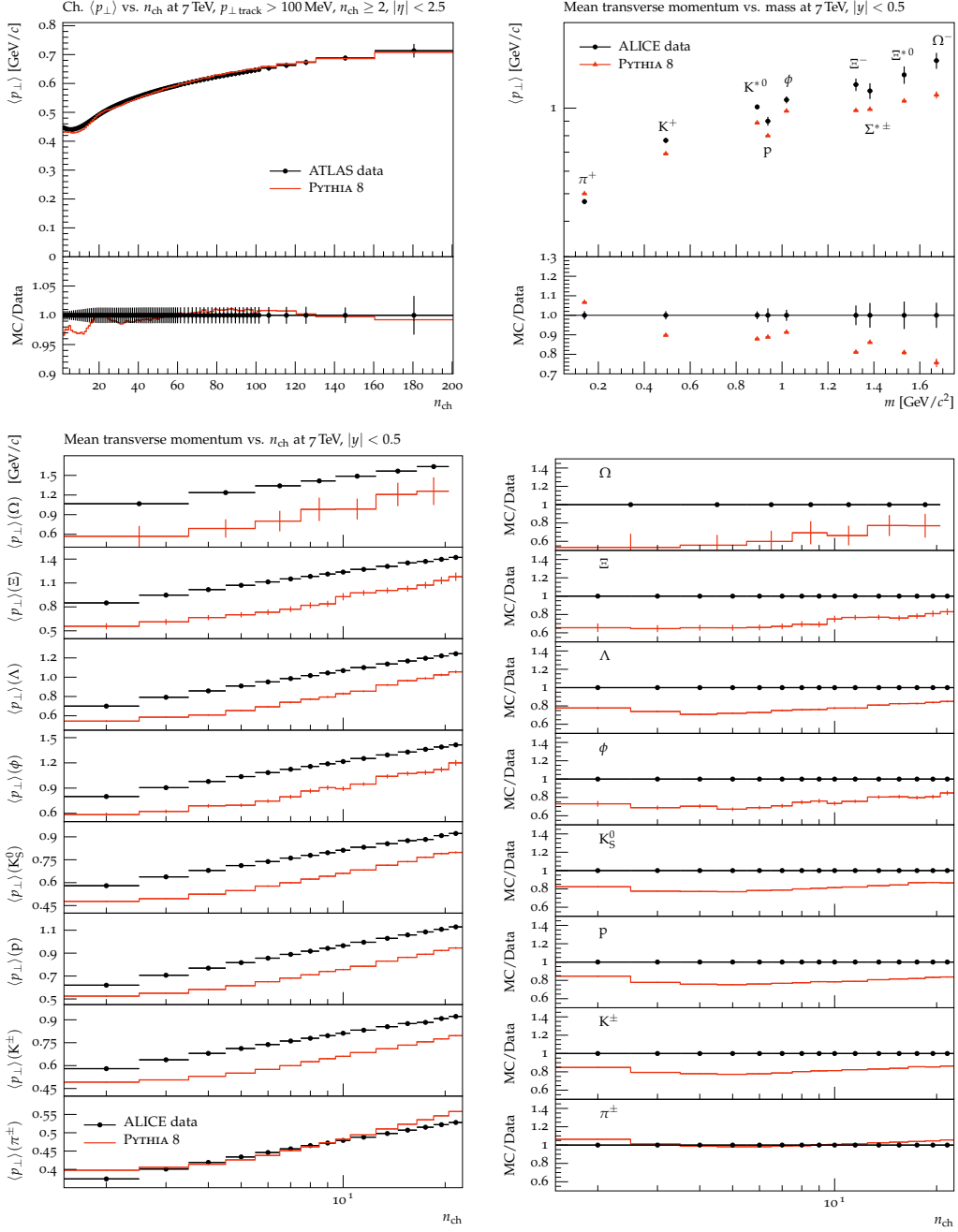


Figure 1. The mean transverse momentum as a function of the charged multiplicity (*top left* and *bottom left*) and the hadron mass (*top right* and *bottom right*). Predictions of default PYTHIA compared to ALICE [46, 48] and ATLAS [47] data. The data in the bottom plots is taken to be an estimate of the logarithmic fits in [48] and therefore no error bars are included.

- An $\langle p_{\perp} \rangle$ increasing with n_{ch} was noted already by UA1 [53], and has remained at higher energies [47, 48]. It offers a key argument for introducing CR in pp/p \bar{p} collisions, as follows [26]. The tail towards large n_{ch} is driven by events with more MPI activity, rather than e.g. by events with higher- p_{\perp} jets. If each MPI subcollision produces particles essentially independently the $\langle p_{\perp} \rangle(n_{\text{ch}})$ would be rather flat. CR implies that fewer and fewer extra particles are produced for each further MPI, as the possibilities to reduce the total string length by CR increase the more partons are already present. The amount of p_{\perp} from the MPIs thus increases faster than the n_{ch} , meaning more p_{\perp} per particle. (To this comes the normal hadronization p_{\perp} contribution, which raises the overall $\langle p_{\perp} \rangle$ level but does not contribute to the $\langle p_{\perp} \rangle(n_{\text{ch}})$ slope.) The exact nature of CR is not known, meaning that many models have been developed [26, 54, 55]. In most of them there is some overall CR strength parameter that can be adjusted to fit the $\langle p_{\perp} \rangle(n_{\text{ch}})$ slope.
- A natural reference for hadronization properties always is e^+e^- data. The principle of jet universality — or, in our case, string universality — is deeply rooted, so it is useful to check that no changes of fundamental string properties have too adverse an impact on e^+e^- . There is also a possibility of improvements in some places, like the inclusive $p_{\perp\text{in}}$ and $p_{\perp\text{out}}$ spectra; unfortunately these are not available for identified particles.

3 The new models

In this section we outline the basic ideas and implementations that we have developed to offer new options to the traditional PYTHIA hadronization framework. As we later compare with data we will have reason to go into more detail and discuss some variations.

3.1 Variations of the normal string model

As described above, the standard tunneling framework suggests a Gaussian suppression of the production of heavier quarks and diquarks, with a further suppression based on the hadronic spin state, but no obvious room for an explicit dependence on the hadron mass. It also provides a common Gaussian p_{\perp} spectrum for all new $q\bar{q}$ pairs. We will study a few variations of this framework, mainly as a reference for the thermodynamical ansatz below.

Firstly, consider a Gaussian suppression associated with the masses of the produced hadrons rather than with the quarks. That is, let the relative production rate of different hadron species be given by a factor $\exp(-m_{\perp\text{had}}^2/2\sigma^2)$, which factorizes into a species-independent p_{\perp} spectrum and an $\exp(-m_{\text{had}}^2/2\sigma^2)$ mass suppression. The question is then whether this would give the appropriate suppression for the production of heavier particles.

Secondly, the universal p_{\perp} spectrum could be broken by assigning a larger width in string breakups of the $s\bar{s}$ and $qq\bar{q}\bar{q}$ kinds, relative to the baseline $u\bar{u}$ and $d\bar{d}$ ones. The issue to understand here is how dramatic differences are required to get a better description of the individual π , K and p p_{\perp} spectra.

Thirdly, assume that more MPIs leads to a closer packing of strings in the event, but that each string “flux tube” remains as a separate entity. The transverse region of the

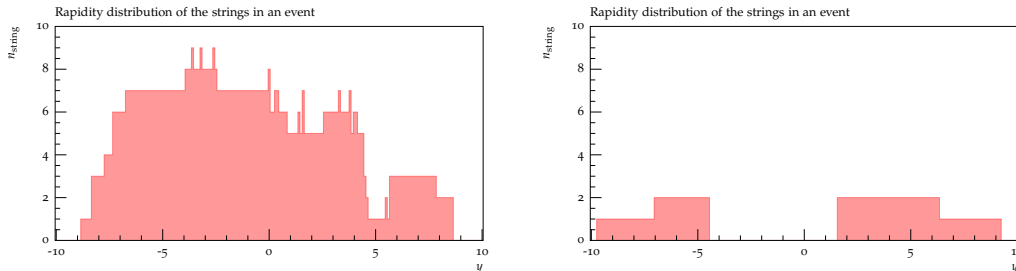


Figure 2. Rapidity distribution of the strings (added on top of each other) in a typical QCD event (*left*) and in a diffractive event (*right*).

string shrinks and, essentially by Heisenberg’s uncertainty relations, this should correspond to a higher energy, i.e. a larger string tension κ . (Such a relation comes out naturally e.g. for bag models of confinement [56].) Overall the dense-packing effect on κ and related parameters should scale as some power of n_{MPI} , i.e. the number of MPIs in the current event. Since n_{ch} and n_{MPI} are strongly correlated it is thus interesting to study how the particle composition and $\langle p_{\perp} \rangle$ depend on n_{ch} . For a more differential picture it should be preferable to estimate the number of strings in the neighbourhood of each new hadron being produced.

This is done by making a reasonable guess for the momentum of the hadron that is the next to be produced on the current string. Using an average hadron mass and p_{\perp} , defined in the frame of the parent string, and an average Γ value of $\langle \Gamma \rangle = (1+a)/b$, the momentum of the “average expected” hadron is calculated. Using this information, we determine the number of strings that cross the rapidity of the expected hadron. For this purpose the rapidity range that a string will populate is defined by the rapidity of the endpoint partons of each string piece,

$$y = \text{sgn}(p_z) \log \frac{E + |p_z|}{\sqrt{\max(m_{\perp}^2, m_{\text{min}}^2)}}, \quad (3.1)$$

where m_{min}^2 has the purpose to protect against strings with low- m_{\perp} endpoints from populating the full rapidity range. The rapidity-density measure is reasonable for low- p_{\perp} hadroproduction, but does not reflect the phase space inside a high- p_{\perp} jet, where close-packing of strings should be rare. Therefore the effective number of strings is calculated as

$$n_{\text{string}}^{\text{eff}} = 1 + \frac{n_{\text{string}} - 1}{1 + p_{\perp \text{had}}^2 / p_{\perp 0}^2}, \quad (3.2)$$

where $p_{\perp \text{had}}$ is the physical hadron p_{\perp} and $p_{\perp 0}$ is the MPI regularization parameter.

As two examples, the rapidity distribution of the strings in a typical QCD event and in a diffractive event are shown in figure 2. Using eq. (3.2), the string tension in eq. (2.5) is modified to be

$$\kappa \rightarrow \left(n_{\text{string}}^{\text{eff}} \right)^{2r} \kappa, \quad (3.3)$$

where the exponent r is left as a free parameter, that can be used to tune the model to data. Note that while junctions² contribute to the calculation of n_{string} by assuming one string stretched between the highest- and lowest-rapidity parton, their fragmentation does not make use of eq. (3.3). Junctions are rare in the models we study, so this is not a significant simplification.

The effect of modifying the string tension due to the local density has also been studied in other Monte Carlo programs, which are primarily for heavy-ion collisions. Some of them have hardly been used for pp physics as they miss out on other physics aspects such as QCD jet production. In the RQMD model [57] for studying relativistic nucleus-nucleus collisions, colour strings are allowed to fuse into ropes if they are overlapping, which weakens the suppression of strangeness and baryon production due to the increased string tension [58]. A similar model with string fusion into colour ropes is implemented in the DIPSY event generator [17] and shows improvement in the description of identified particle spectra in pp minimum bias data. For the UrQMD model [59, 60], used for relativistic heavy-ion and hadron-hadron collisions, the authors of [61] show that a better description of particle yields is achieved with an enhanced string tension. The effect of an increased string tension in a densely populated environment on strangeness and diquark production, antibaryon-to-baryon ratios and other observables has been investigated in [62]. In AMPT [63, 64], a Monte Carlo transport model for heavy-ion collisions at relativistic energies, parameters in the Lund string fragmentation model have been modified, as the string tension is expected to be increased in the dense matter formed in heavy-ion collisions [65]. In the PSM [66, 67] Monte Carlo model for simulating nuclear collisions, string fusion associated with high string densities is taken into account to reduce multiplicities and increase $\langle p_{\perp} \rangle$, baryon and strangeness production. Ref. [68] presents a model which introduces the interaction between strings via their fusion and percolation analytically. The $\langle p_{\perp} \rangle$ of the produced particles, and therefore also the string tension, depends on the string density and how much strings overlap [69–71].

3.1.1 One-string toy model

A very simple toy model is introduced to validate the modifications to the string tension in the conventional string model. A single string with energy m_Z is spanned along the z axis. The flavour of the endpoint quarks is chosen random from the set (u, d, s, c, b). The study includes only primary produced hadrons, i.e. no hadron decays, and also excludes the hadrons containing the endpoint quarks. (Such hadrons would have lower $\langle p_{\perp} \rangle$ since the endpoint quarks by definition have $p_{\perp} = 0$.)

The $\langle p_{\perp} \rangle$ and the mean multiplicity for different hadron species are shown in figure 3. As expected, increasing the string tension either for s quarks or for diquarks leads to an increased $\langle p_{\perp} \rangle$ value for the hadrons concerned. Note that for $\eta + \eta'$ the $\langle p_{\perp} \rangle$ is only increased slightly due to the $u\bar{u} + d\bar{d}$ quark component being more frequently produced compared to $s\bar{s}$. There is a slight reduction of the production probability for hadrons with s quarks or diquarks, shown in the top right plot in figure 3, due to the increased string

²A junction topology corresponds to an Y arrangement of strings, i.e. where three string pieces have to be joined up in a common vertex.

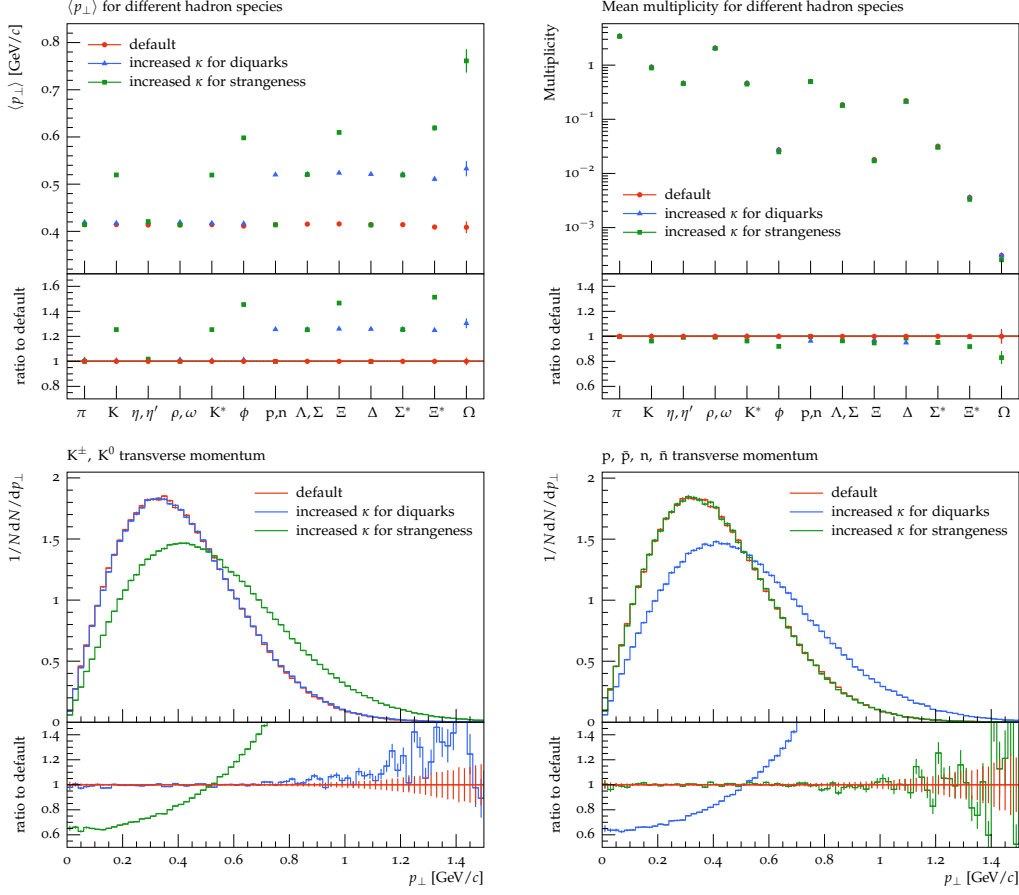


Figure 3. $\langle p_{\perp} \rangle$ (top left) and mean multiplicity (top right) for different hadron species and the K (bottom left) and p/n p_{\perp} (bottom right) spectra in the toy model. Predictions of the conventional string model without modifications are shown in red and with the string tension κ increased for diquarks in blue and strangeness in green.

tension leading to fewer particles being produced in affected events. The bottom row of figure 3 shows the K and p/n p_{\perp} spectra, shifted to larger values as the string tension for that hadron species is increased.

3.1.2 Multi-string toy model

To investigate the effect of the close-packing of strings, as in eq. (3.3), the above toy model is extended to include several strings along the z axis. The number of strings is picked randomly between two and eight and the string energies are chosen such that they sum up to 1 TeV. Figure 4 shows $\langle p_{\perp} \rangle$ as a function of the number of charged particles and the p_{\perp} distribution and compares the modified model to default PYTHIA. Two different choices for the baseline value for the string tension are made in case of taking the close-packing of strings into account. In the first case the tension is denoted with κ and its value is

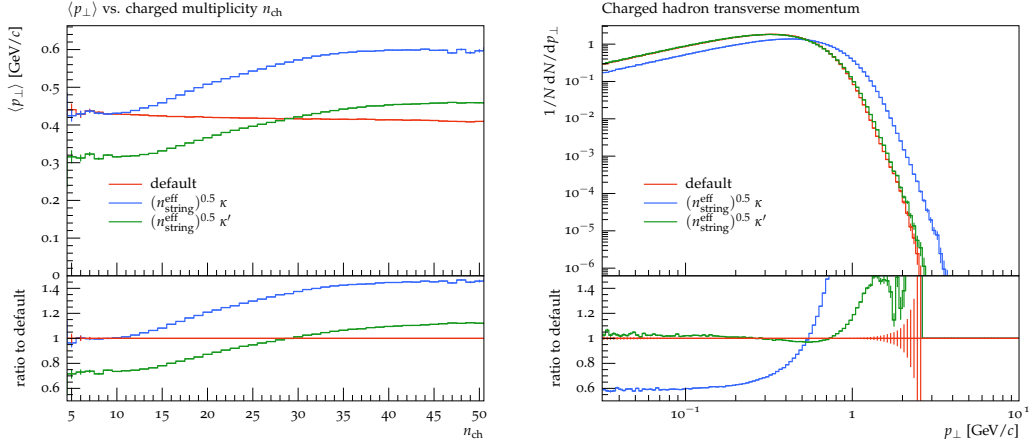


Figure 4. $\langle p_{\perp} \rangle$ as a function of the number of charged particles (*left*) and the p_{\perp} distribution (*right*) for the toy model with multiple strings along z axis. Predictions of the default model are shown in red and dependence of the string tension on the number of close strings in blue and green with two different string tensions $\kappa > \kappa'$.

adjusted such that $\langle p_{\perp} \rangle$ agrees with default PYTHIA for small values of n_{ch} . In the second case, where the string tension is denoted by κ' the value is adjusted to obtain the same $\langle p_{\perp} \rangle$, averaged over all hadrons and charged multiplicities. The latter case serves as a cross check when investigating the influence on the p_{\perp} spectrum of charged hadrons.

As expected the $\langle p_{\perp} \rangle$ increases with the charged multiplicity, eventually flattening out at large multiplicities. The left histogram in figure 4 also nicely shows that the rise is independent of the baseline string tension value.

When fitting the string tension such that the same overall $\langle p_{\perp} \rangle$ is reached as in the default model, the charged hadron p_{\perp} spectrum exhibits only small changes; making the spectrum somewhat broader.

3.1.3 Gaussian $m_{\perp\text{had}}^2$ suppression

To test the applicability of the Gaussian transverse mass suppression, the quark p_{\perp} is generated according to $\exp(-p_{\perp q}^2/\sigma^2)$, see eq. (2.5), with the hadron flavour chosen based on $\exp(-m_{\perp\text{had}}^2/2\sigma^2)$. The additional factor of two arises from the hadron receiving p_{\perp} contributions from two quarks. As the comparison to data is of interest here, realistic $e^+e^- \rightarrow$ jets events with $s = m_Z^2$ are investigated. In figure 5 the particle composition is shown as a function of mass. This clearly indicates that the suppression based on the transverse mass squared of the hadrons is suppressing heavier hadrons too much. We will therefore not consider this option further.

3.2 The thermodynamical string model

The most radical departure from standard Lund string principles that we explore in this article is to replace the Gaussian suppression factor in mass and p_{\perp} by an exponential one.

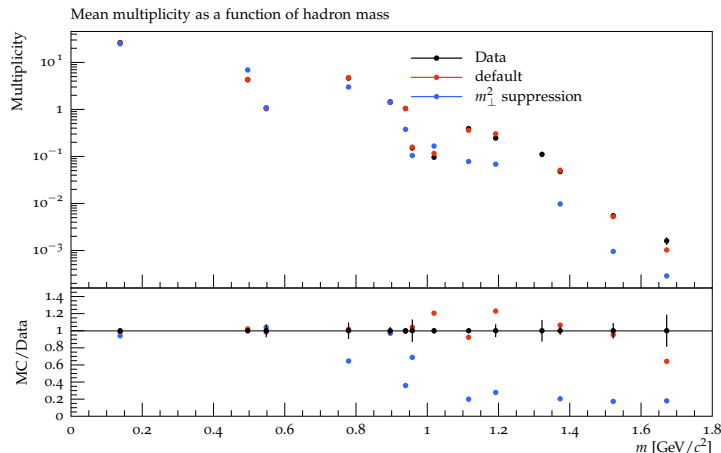


Figure 5. The conventional string model with its default options (red) and with the relative production rate of different hadron species given by a factor $\exp(-m_{\perp\text{had}}^2/2\sigma)$ (blue), compared to PDG data [72].

To be more explicit, instead of a quark-level suppression governed by eq. (2.5) there will be a hadron-level suppression

$$\exp(-m_{\perp\text{had}}/T) \quad \text{with} \quad m_{\perp\text{had}} = \sqrt{m_{\text{had}}^2 + p_{\perp\text{had}}^2}. \quad (3.4)$$

The inspiration clearly comes from a thermodynamical point of view, which is why we choose to associate the dimensional parameter with a temperature T . This association should not be taken too literally, however; there are many differences relative to a purely thermal model. The main one is that we keep the longitudinal string fragmentation structure unchanged, which ensures local flavour conservation. Another is that e.g. the Hagedorn approach [19, 20] is based on the assumption of a steeply increasing density of excited states as a function of mass, whereas we only include a few of the lowest multiplets. (By default only the ground states corresponding to no radial or orbital excitation, optionally also the lowest $L = 1$ meson multiplets.) This means that, although our T comes out to be a number of the order of the Hagedorn temperature, there is no exact correspondence between the two. Also, $T \sim \sqrt{\kappa/\pi} = \sigma$ from dimensional considerations, so our T could be viewed as a manifestation of the string energy per unit length, not directly linked to a temperature.

There is also an experimental historical background to the choice of an exponential shape, in that already fixed-target and ISR data showed that a distribution like $\exp(-Bp_{\perp})$ offered a good fit to the inclusive $dn_{\text{ch}}/dp_{\perp}^2$ spectrum, with $B \approx 6 \text{ GeV}^{-1}$ [18, 73–75]. With data split by particle type, a lower B value is noted for kaons and protons than for pions, but with the modified form $\exp(-Bm_{\perp})$ all the spectra can be described by almost the same $B \approx 6$ value.

As an aside, the preference for an exponential shape was and is not a show-stopper for the Gaussian approach in the normal string fragmentation. At larger p_{\perp} the spectrum is dominated by the fragmentation of (mini)jets, giving a larger rate than the nonperturbative

hadronization one. And at smaller p_{\perp} the pattern of decays makes the spectrum more steep than the Gaussian one of the primary hadrons. So at the end of the day a Gaussian ansatz lands not that far away from an exponential spectrum, although differences remain. See further section 3.4.1, in particular figure 9.

In more detail, our model is intended to give each new hadron in the string fragmentation a p_{\perp} according to an exponential distribution. We want to preserve the concept of local p_{\perp} conservation in each $q\bar{q}$ breakup vertex, so seek a distribution that convoluted with itself (in two transverse dimensions) gives an exponential,

$$f_{\text{had}}(p_{\perp\text{had}}) = \exp(-p_{\perp\text{had}}/T) = \int d^2p_{\perp 1} f_q(p_{\perp 1}) \int d^2p_{\perp 2} f_q(p_{\perp 2}) \delta(\mathbf{p}_{\perp\text{had}} - \mathbf{p}_{\perp 1} - \mathbf{p}_{\perp 2}). \quad (3.5)$$

Using Fourier transforms to turn the convolution into a product,

$$\begin{aligned} \tilde{f}_{\text{had}}(b_{\perp}) &= \frac{1}{2\pi} \int f_{\text{had}}(p_{\perp\text{had}}) \exp(-i\mathbf{b}_{\perp} \cdot \mathbf{p}_{\perp\text{had}}) d^2p_{\perp\text{had}} \\ &= 2\pi \tilde{f}_q^2(b_{\perp}) = \frac{1}{(1 + (b_{\perp}T)^2)^{3/2}}. \end{aligned} \quad (3.6)$$

The transformation back of \tilde{f}_q then gives [76]

$$f_q(p_{\perp q}) \propto \int \frac{\exp(ib(p_{\perp q}/T) \cos \varphi)}{(1 + b^2)^{3/4}} b db d\varphi \propto \int_0^{\infty} \frac{b J_0(b p_{\perp q}/T)}{(1 + b^2)^{3/4}} db \propto \frac{K_{1/4}(p_{\perp q}/T)}{(p_{\perp q}/T)^{1/4}}, \quad (3.7)$$

where $b = b_{\perp}T$, J_0 is a regular Bessel function of the first kind, and $K_{1/4}$ is the modified Bessel function of the second kind of order 1/4. An implementation of $K_{1/4}$ has been included in PYTHIA based on [77], using a power series for $p_{\perp q}/T < 2.5$ and an asymptotic expansion for $p_{\perp q}/T > 2.5$.

Consider the fragmentation of a string, where the quark q of one breakup has a certain $\mathbf{p}_{\perp 1}$. The transverse momentum $\mathbf{p}_{\perp 2}$ of the (di)quark of the next breakup pair $q'\bar{q}'$ is constructed by picking its absolute value according to eq. (3.7) and a random azimuthal angle. The partner anti(di)quark must thus have $-\mathbf{p}_{\perp 2}$ due to local momentum conservation. The hadron transverse momentum is simply the sum of the p_{\perp} of the two contributing quarks, $\mathbf{p}_{\perp\text{had}} = \mathbf{p}_{\perp 1} - \mathbf{p}_{\perp 2}$. Having $p_{\perp\text{had}}$ at hand we decide on the flavour of the breakup pair $q'\bar{q}'$, and therefore also on the hadron species, as follows: calculate the transverse mass $m_{\perp\text{had}}$ of all hadrons whose flavour content includes the incoming quark q and determine the basic probability for each hadron as

$$P_{\text{had}} = \exp(-m_{\perp\text{had}}/T). \quad (3.8)$$

Assuming the production of two hadrons with different masses m_1 and m_2 , then eq. (3.8) implies the same production rate for $p_{\perp} \gg m_1, m_2$, but more suppression of the heavier hadron at low p_{\perp} . Thus there is less production of heavier states, but they come with a larger $\langle p_{\perp} \rangle$.

As mentioned above, by default we only include the light-flavour (u, d, s) meson and baryon multiplets without radial or orbital excitation.³ However, if desired, more hadrons

³Heavy flavour hadrons are of course included to handle the endpoint quarks of the strings, where needed.

can be added to the procedure. Depending on the flavour content of the hadron, the probability in eq. (3.8) receives additional multiplicative factors:

- Due to spin-counting arguments vector mesons receive a factor of 3 and tensor mesons a factor of 5.
- For same-flavour mesons we include the diagonal meson mixing factors, similar to what has been done previously in the conventional Lund string model.
- Baryons receive a free overall normalization factor with respect to mesons, as well as an additional factor stemming from the SU(6) symmetry factors, see [38]. The relative weight of spin 1/2 baryons with respect to those with spin 3/2 is 2 : 4, similar to the factors for mesons arising from the spin-counting arguments in point 1.
- For the special case of octet baryons with three different flavours, e.g. Λ and Σ^0 , their probability for different internal spin configurations is taken into account.
- An extra suppression factor for hadrons with strange (di)quarks is included to get more control over the relative hadron production and thus a better description of data.

All probabilities are then rescaled to sum up to unity and the hadron species and therefore the flavour of the next (di)quark pair is chosen accordingly. Note that we have not (yet) implemented popcorn baryon production, i.e. no mesons are produced in between a baryon and its antibaryon partner.

Similar to eq. (3.3) the temperature can be modified as

$$T \rightarrow \left(n_{\text{string}}^{\text{eff}} \right)^r T, \quad (3.9)$$

with $n_{\text{string}}^{\text{eff}}$ given in eq. (3.2) to take into account the effect of close-packed strings. Note that in [78] the temperature has been related to the density in the context of the percolation of color sources (the density is however defined differently).

3.2.1 Asymmetry in different flavour transitions

Consider a very simple model, where only string breaks with $d\bar{d}$ and $s\bar{s}$ quark pairs are allowed to produce only pseudoscalar mesons, and the mixing of diagonal mesons is ignored. Then it is rather easy to see that the p_{\perp} spectra and $\langle p_{\perp} \rangle$ of the hadrons produced in $(d \rightarrow s)$ transitions is not the same as for $(s \rightarrow d)$ transitions, due to the difference in competition. In the first instance $(d \rightarrow s)$ competes with $(d \rightarrow d)$, and since the former produces the heavier meson it also obtains the higher $\langle p_{\perp} \rangle$. In the latter instance $(s \rightarrow d)$ instead competes with $(s \rightarrow s)$ and so gives the lighter meson and lower $\langle p_{\perp} \rangle$. Assuming that fragmentation is performed from the quark end inwards, $K^0 = d\bar{s}$ would thus obtain a harder p_{\perp} spectrum than $\bar{K}^0 = \bar{d}s$, which should not be the case. A simple solution for obtaining the same $\langle p_{\perp} \rangle$ for both $(d \rightarrow s)$ and $(s \rightarrow d)$ transitions is to adjust the temperature in eq. (3.8) in case of initial s/\bar{s} quarks such that $d\bar{s}$ and $\bar{d}s$ hadrons are produced with the same $\langle p_{\perp} \rangle$ value, higher than $d\bar{d}$, and $s\bar{s}$ becomes even higher than that.

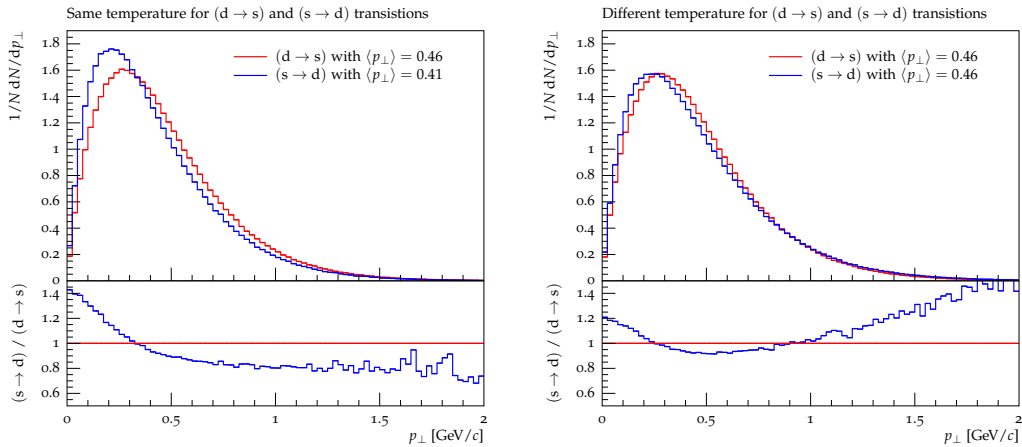


Figure 6. The inclusive hadron p_{\perp} spectrum for $(d \rightarrow s)$ and $(s \rightarrow d)$ transitions with the same temperature for both cases (*left*) and with the adjusted temperature (*right*).

In figure 6 we show the p_{\perp} spectra for both types of transitions with the same temperature and with the adjusted temperature. Note that though both transitions end up with the same $\langle p_{\perp} \rangle$ value, the shape of the p_{\perp} distribution still differs somewhat.

Unfortunately this is a price to pay for working with a recursive model, where flavour is conserved locally. A traditional thermal model based on eq. (3.8) would not conserve flavour or momentum, however, so is not an option here.

3.3 The hadronic rescattering model

A close-packing of fragmenting strings also implies a close-packing of the produced primary hadrons, i.e. a dense hadronic gas. This gives the possibility for hadrons to rescatter on the way out, in particular at the earliest times after hadronization. A detailed simulation of this mechanism would require a knowledge of where in space-time each hadron is produced. For a single string, say stretched along the z axis, it is straightforward to translate between the (E, p_z) values of the primary hadrons and the (t, z) coordinates of the string breakups. For the more realistic case, when a string is stretched between several partons and the string motion is considerably more complicated [34], appropriate rules have not been worked out. To this should be added ambiguities in the transverse production coordinates, both as a consequence of the transverse distribution of the MPIs and of transverse fluctuations inside each string. The modelling of all of these aspects is an interesting task for the future. In addition, the cross section for the scattering of two hadrons against each other varies between hadron kinds, and depends on the relative energy of the two, adding a further layer of complexity.

Here we want to avoid such a detailed model, but still be able to explore whether hadronic rescattering effects could contribute to the resolution of some of the effects that we are attempting to explain. Collective flow — whether dictated by properties of the QGP or by hadronic rescattering — is well-established in heavy-ion collisions, see e.g. [79–81]

and references therein. In particular, a common average radial velocity means that heavier particles have a higher $\langle p_{\perp} \rangle$ than lighter. Of course we do not expect as dramatic effects in pp, but they may still contribute to the same kind of $\pi/K/p$ p_{\perp} separation as in the thermodynamic scenario above, so it should be interesting to compare the two possibilities.

The simple modelling we have in mind is applied to the primary hadrons produced directly from the string fragmentation, before secondary decays are considered. Furthermore, for strings stretched along the z axis there is a strong correlation between the rapidity y of a particle and its space-time production vertex. Therefore, for a given hadron, the density of other hadrons at around the same rapidity is a reasonable (and longitudinally boost invariant) measure of how close-packed particle production is. If there is a contribution from particles coming from the same simple string it has presumably already been absorbed in the tuned fragmentation parameters, so we should disregard such pairs. Unlike e^+e^- events, however, it is common with topologies where a string consists of pieces stretched back and forth across the same rapidity range, and then the above argument does not apply. In practice, it is therefore more relevant to exclude rescattering only between close neighbours in the fragmentation chains.

One should further note that the rapidity density of hadrons refers to low- p_{\perp} particles. The hadronization of a scattered high- p_{\perp} parton mainly occurs at larger p_{\perp} scales, and these hadrons would be essentially unaffected.

The angular distribution of a rescattering, defined in the rest frame of the hadronic pair, should depend on the orbital angular momentum L . For simplicity, we restrict to s -wave isotropic scattering (i.e., $L = 0$) by requiring that the classical value of angular momentum $L = b|\mathbf{p}| < b|\mathbf{p}_{\max}| \sim 1$, where b is the impact parameter and \mathbf{p}_{\max} is the maximally allowed three-momentum of the hadrons in their rest frame, left as a (in principle) free parameter. We don't have access to b for each pair, but assume it is the same distribution for all combinations of hadron types. A common restriction on the three-momentum is thus introduced for all pairs, which is implemented as a cut on the invariant mass of the hadron pair,

$$m_{\text{inv}} < \sqrt{m_1^2 + |\mathbf{p}_{\max}|^2} + \sqrt{m_2^2 + |\mathbf{p}_{\max}|^2}, \quad (3.10)$$

with m_1 and m_2 being the masses of the hadrons and m_{inv} the physical invariant mass of the hadron pair. For all hadron pairs that are not excluded by eq. (3.10) we calculate the difference in rapidity, $\Delta y = |y_1 - y_2|$, and the rescattering probability. For hadrons that are *not* produced in the same string the latter is

$$P_{\text{ds}}(\Delta y) = P_{\text{ds}}^{\max} \left(1 - \frac{\Delta y}{\Delta y^{\max}} \right), \quad (3.11)$$

where the maximum scattering probability P_{ds}^{\max} and the maximum rapidity difference Δy^{\max} are left as free parameters. Eq. (3.11) simply means a probability of P_{ds}^{\max} for zero rapidity difference of the hadron pair, linearly decreasing to zero at a rapidity difference of Δy^{\max} .

As an alternative to eq. (3.11), without the cut on the invariant mass in eq. (3.10), the probability can be chosen to be

$$P_{\text{ds}}(\Delta y, \Delta\varphi) = P_{\text{ds}}^{\text{max}} \left(1 - \frac{\sqrt{(\Delta y)^2 + (\Delta\varphi)^2}}{R^{\text{max}}} \right), \quad (3.12)$$

with $\Delta\varphi$ being the difference in azimuth of the hadron pair and R^{max} the maximally allowed value of the radius $R = \sqrt{(\Delta y)^2 + (\Delta\varphi)^2}$.

For hadron pairs that are produced in the *same* string we introduce the difference in hadron index (called rank e.g. in [82]), $\Delta_{ij} = |i - j|$, to denote how close two hadrons are, i.e. two neighbours have $\Delta_{ij} = \Delta_{i \ i+1} = 1$, next-to-neighbours $\Delta_{ij} = \Delta_{i \ i+2} = 2$ and so on. The scattering probability for same-string hadrons is

$$P_{\text{ss}}(\Delta y) = P_{\text{ds}}(\Delta y) \cdot \begin{cases} P_{\text{ss}}^{\text{max}} & \text{if } \Delta_{ij} > \Delta_{ij}^{\text{max}} \\ \frac{P_{\text{ss}}^{\text{max}}(\Delta_{ij} - \Delta_{ij}^{\text{min}}) + P_{\text{ss}}^{\text{min}}(\Delta_{ij}^{\text{max}} - \Delta_{ij})}{\Delta_{ij}^{\text{max}} - \Delta_{ij}^{\text{min}}} & \text{if } \Delta_{ij}^{\text{min}} \leq \Delta_{ij} \leq \Delta_{ij}^{\text{max}} \\ 0 & \text{if } \Delta_{ij} < \Delta_{ij}^{\text{min}}, \end{cases} \quad (3.13)$$

where $P_{\text{ss}}^{\text{min/max}}$ is the minimum/maximum probability associated with the nearest/furthest neighbour, characterized by $\Delta_{ij}^{\text{min/max}}$, with a linear behaviour of the probability in between; zero probability for hadrons closer than Δ_{ij}^{min} and maximum probability for those further apart than Δ_{ij}^{max} . All four are left as free parameters. In the case where eq. (3.12) is applied, $P_{\text{ds}}(\Delta y)$ in eq. (3.13) has to be replaced by $P_{\text{ds}}(\Delta y, \Delta\varphi)$.

3.3.1 Multi-string toy model

In order to test the hadron scattering a simple toy model is applied: five strings, each with energy m_Z , are constructed along the z axis with different quark flavours for the endpoint quarks, and the primary produced hadrons are studied. As in section 3.1 the hadrons containing the endpoint quarks are excluded. The following plots are obtained by making use of eqs. (3.10) and (3.11); using eq. (3.12) instead leads to similar results, and thus the same conclusions.

Figure 7 shows the $\langle p_{\perp} \rangle$ for different hadron species. For the Gaussian hadronic p_{\perp} distribution without hadron scattering all hadrons receive the same p_{\perp} spectrum. Including hadron scattering, the $\langle p_{\perp} \rangle$ decreases for pions, the lightest hadrons, by about 20% and increases for heavy hadrons by up more than 40%. The same effect is present for the thermodynamical model, although changes only reach around 10%, as the $\langle p_{\perp} \rangle$ is higher for heavier hadrons already without hadron rescattering.

Figure 8 shows the normalized p_{\perp} spectra for all hadrons and, to exemplify the difference between light and heavy hadrons, the spectrum for pions, kaons, and protons/neutrons. Comparing the inclusive p_{\perp} spectrum for the Gaussian p_{\perp} , we notice that the distribution gets broader with hadron scattering, i.e. we get more pions with small p_{\perp} and more heavy hadrons with higher p_{\perp} .

As the thermodynamical model without hadron rescattering comes with a different starting point, compared to the Gaussian model, the effect of the rescattering is not as

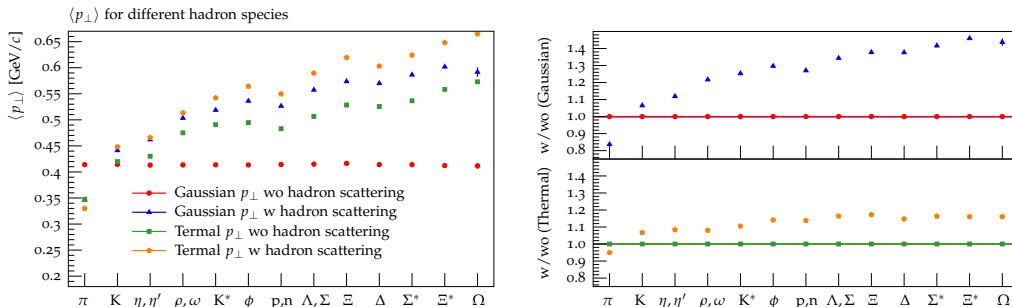


Figure 7. The $\langle p_{\perp} \rangle$ for different hadron species, with (blue triangles) and without (red dots) hadron scattering for the Gaussian p_{\perp} and with (orange pentagons) and without (green squares) hadron scattering for the thermal p_{\perp} in the toy model. The right plots show the ratio of the Gaussian model with to without hadron scattering in the upper panel and the same ratio for the thermodynamical model in the lower panel.

large, and shifts the p_{\perp} spectrum towards larger values. The exception is for pions only, where there is a slight broadening also towards smaller p_{\perp} values.

3.4 Results

3.4.1 The effect of decays

Hadron decays, such as $\rho \rightarrow \pi\pi$ or $\eta \rightarrow \pi^+\pi^-\pi^0$, influence the p_{\perp} spectra of the final state hadrons. As the decays are mostly dictated by kinematics, they constitute a limiting factor on the possibilities of modifying for instance the pion p_{\perp} spectrum during the fragmentation process. Even though the primary hadrons follow a Gaussian or exponential p_{\perp} distribution, the spectra obtained after decays do not, and become more similar. In addition, in realistic events the effects of perturbative jet production leads to a p_{\perp} broadening and the emergence of a powerlike high- p_{\perp} tail.

To investigate this smearing of the p_{\perp} spectra, we consider realistic $e^+e^- \rightarrow$ jets events and inelastic pp collisions, where the previously discussed effects of string density and hadron rescattering are not taken into account. The normalized transverse momentum distributions of π^{\pm} and p, \bar{p} are shown in figure 9 for the Gaussian and the thermodynamical model. Comparing the p_{\perp} spectra to the previous plots (note the different range of x and y axis) reveals how much the p_{\perp} distributions have moved to higher p_{\perp} values, as mentioned above. Four different ratio plots are included for each histogram to investigate different effects: the ratio of distributions after hadronic decays with respect to before, for both models, and the ratio of the thermodynamical with respect to the Gaussian model, with and without decays.

Decays shift the p_{\perp} spectra towards smaller values, where the Gaussian model shows a larger change, compared to the thermodynamical model. For LEP the difference between the predictions with and without decays is limited to around 50% at most, while for LHC the changes are rather large, especially for small and large p_{\perp} values. Figure 9 also nicely shows that the differences between the Gaussian and thermodynamical model become

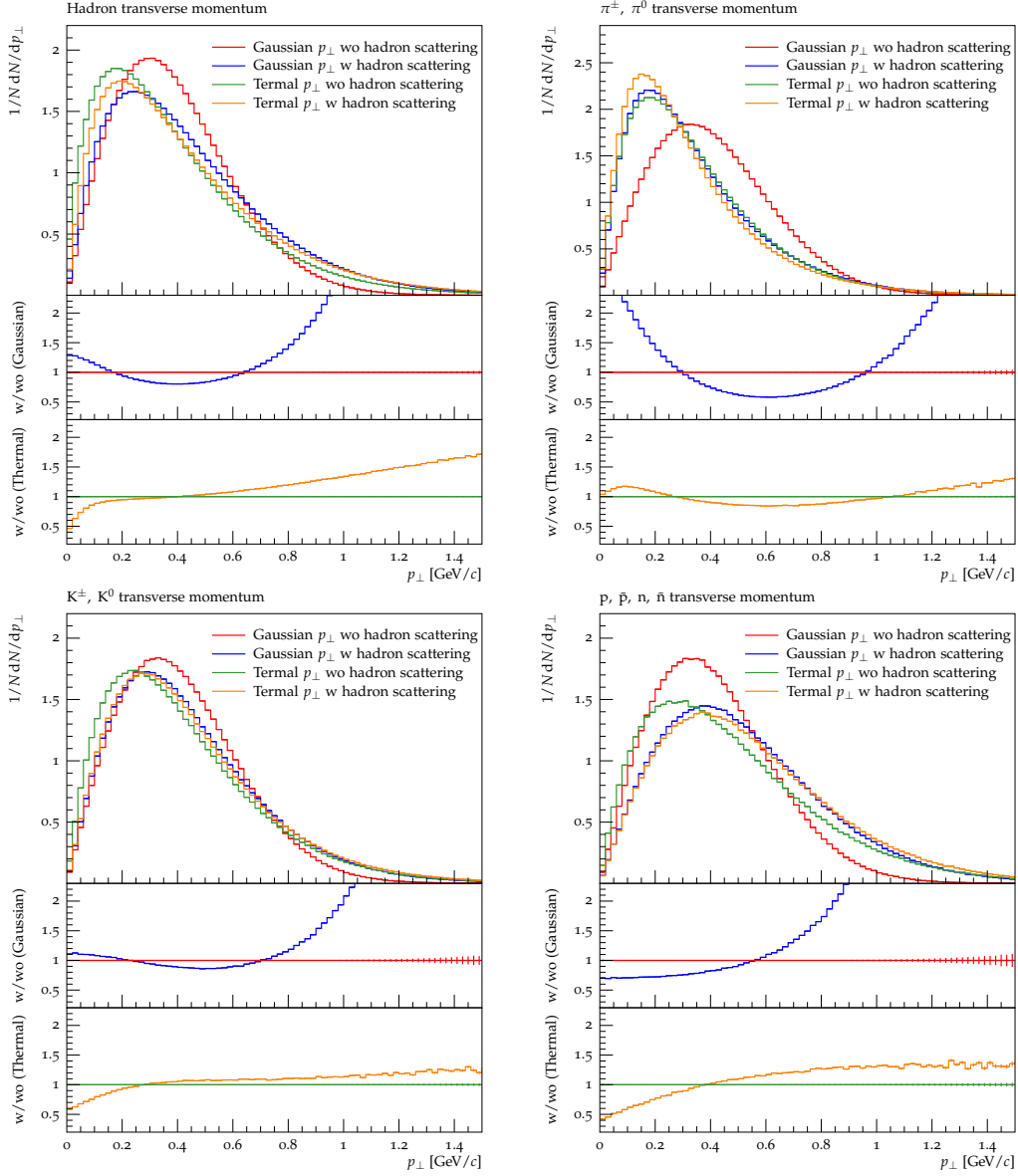


Figure 8. The p_{\perp} spectrum for all hadrons (*top left*), pions (*top right*), kaons (*bottom left*) and protons and neutrons (*bottom right*), with (blue) and without (red) hadron scattering for the Gaussian p_{\perp} and with (orange) and without (green) hadron scattering for the thermal p_{\perp} in the toy model.

more than a factor of two smaller when hadronic decays are included, where, as before, the differences are more pronounced for LHC events. Unfortunately, this will limit the impact of the modifications previously discussed in this section.

Another question is how much of the hadron rescattering effect on the primary hadrons survives the decays. Note that some of the primary hadrons, such as the ρ meson, are so

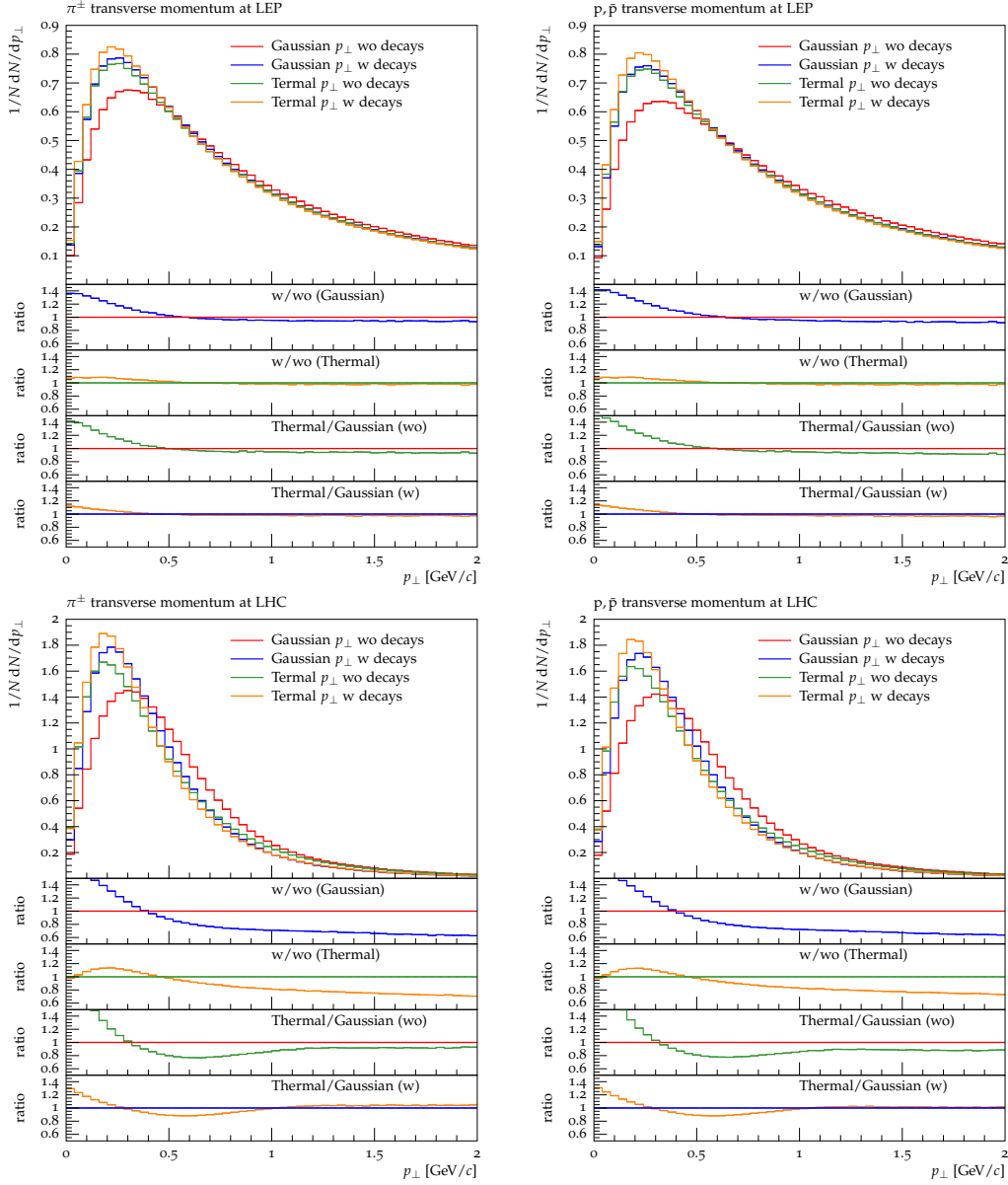


Figure 9. The p_\perp spectrum for charged pions (*left*) and protons (*right*), with (blue) and without (red) hadronic decays for the Gaussian and with (orange) and without (green) hadronic decays for the thermal model in $e^+e^- \rightarrow$ jets (*top*) and inelastic pp collisions (*bottom*).

short-lived that some of their decay products could rescatter which would influence the p_\perp spectra further. A realistic interleaving of rescattering and decays would require a detailed space-time picture, however, which is for the future.

In figure 10 the pion and proton p_\perp spectra are shown again for LHC events with hadron rescattering. The same ratio plots as before are included. The ratio of predictions

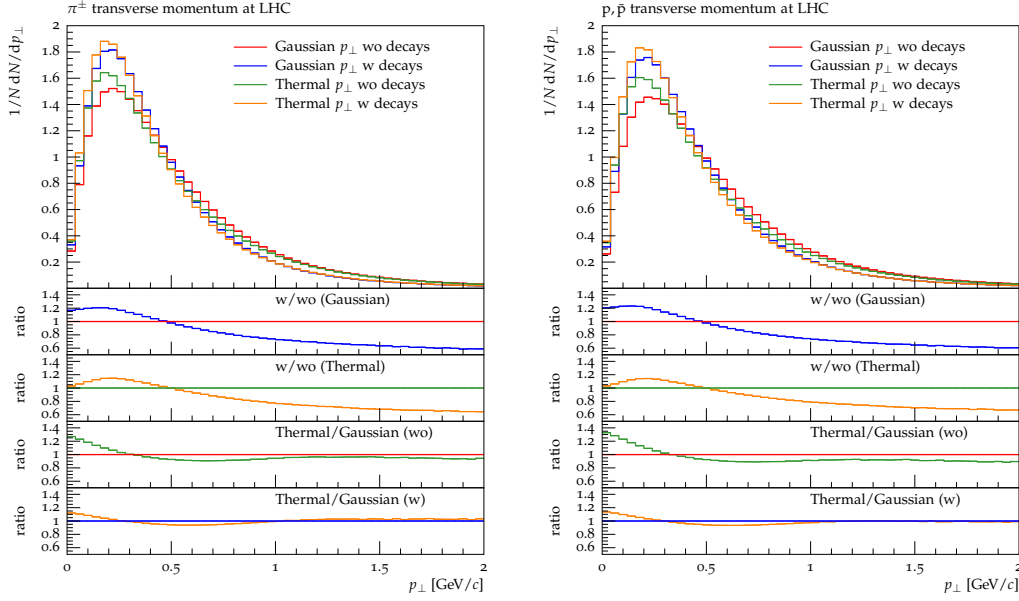


Figure 10. The p_{\perp} spectrum for charged pions (*left*) and protons (*right*), with (blue) and without (red) hadronic decays for the Gaussian and with (orange) and without (green) hadronic decays for the thermal model in inelastic pp collisions (*bottom*) with hadron rescattering.

with to without hadron decays shows a similar behaviour as the plots before, where no rescattering was included. The difference between the two models without hadronic decays becomes smaller when hadron rescattering is included. This is not surprising since the effect of the rescattering, that of shuffling some p_{\perp} from lighter to heavier hadrons, is smaller in the thermodynamical model where more massive hadrons obtain more p_{\perp} already from the beginning. Including decays brings the predictions of the two models even closer together.

3.4.2 Adding more hadrons

We now briefly investigate the effect of including additional hadrons in the flavour picking process in the thermodynamical model. $e^+e^- \rightarrow$ jets events at $\sqrt{s} = m_Z$ are analyzed with the effects of string density and hadron rescattering not being used. As discussed in section 3.2, by default only hadrons with u/d/s quarks and no radial or orbital excitation are included.

Firstly, consider including hadrons with charm quarks. To obtain a rough estimate of the suppression of c production in string breaks, compared to that of s quarks, the rates of D and K mesons and their ratios are analyzed; similar for vector mesons and baryons. The results in figure 11 show that the c hadrons are suppressed by more than an order of magnitude compared to s hadrons, although a bit less when only vector mesons are considered. In absolute numbers the amount of extra charm production is non-negligible, and probably inconsistent with both LEP and LHC observed rates. Recall that an additional suppression factor for s quarks was introduced for the hadron rates in section 3.2; we would

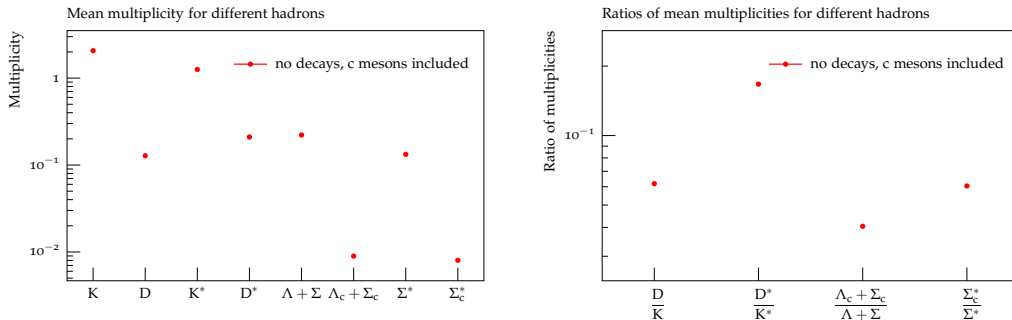


Figure 11. Mean multiplicities and their ratios for different groups of hadrons. Predictions of the thermodynamical model with c hadrons included in the fragmentation process and no hadronic decays.

therefore expect that a similar, even stronger factor is needed when including c quarks in the thermodynamical model. Given this, neither charm nor bottom production is included in the nonperturbative hadronization in the rest of our studies.

Secondly, consider excited mesons by including all of the following meson multiplets, where by default only the first two are present,

- pseudoscalar multiplet with $L = 0$, $S = 0$, $J = 0$,
- vector multiplet with $L = 0$, $S = 1$, $J = 1$,
- pseudovector multiplet with $L = 1$, $S = 0$, $J = 1$,
- scalar multiplet with $L = 1$, $S = 1$, $J = 0$,
- pseudovector multiplet with $L = 1$, $S = 1$, $J = 1$,
- tensor multiplet with $L = 1$, $S = 1$, $J = 2$,

with J denoting the sum of the spin S and orbital angular momentum L in the nonrelativistic approximation. In figure 12 the mean multiplicity of the different multiplets is shown, together with the p_\perp spectra of pions and protons. Note that including excited mesons leads to an increase of the total meson multiplicity after decays. All $L = 1$ multiplets are suppressed by more than an order of magnitude with respect to the pseudoscalar multiplet, with the scalar mesons being suppressed the most due to the combination of them being the heaviest of the considered hadrons and their smaller spin-state weight $2J + 1$. The normalized p_\perp spectra exhibit slight shifts towards smaller values, as the now included heavier mesons decay to more lighter hadrons. The excited mesons combined constitute a fraction of roughly 10% of the total meson multiplicity. Given that in addition those mesons and their decay channels are not very well understood, we consider it reasonable to not include those in further studies. In default PYTHIA the suppression of light vector mesons with respect to pseudoscalar mesons is ~ 0.5 . The thermodynamical naturally comes with a fairly similar value of ~ 0.35 .

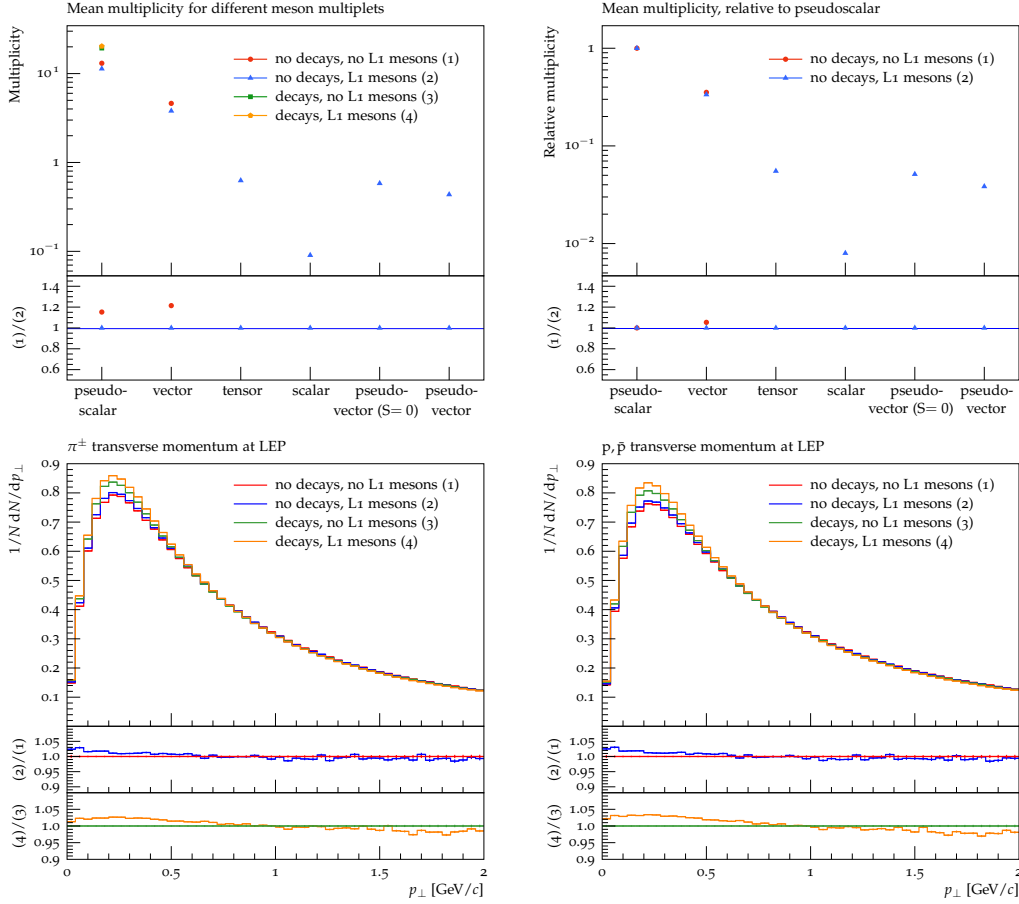


Figure 12. Mean multiplicities and ratios for the different meson multiplets (*top*). The p_\perp spectrum for charged pions (*bottom left*) and protons (*bottom right*). Predictions of the thermodynamical are shown, where decays are either switched on or off and $L = 1$ mesons are included or not.

4 Comparisons with data

We now proceed to compare the models with data. Note that, in a first step, there is no ambition to obtain a better overall description than the one achieved in several of the standard tunes that come with PYTHIA. It is rather to explore how the modelling of the new mechanisms impacts selected distributions, notably the ones discussed in section 2.2. That is, whether the mechanisms have the potential to improve the agreement with data in some crucial respects. Only in a second step there some attempt to combine the various mechanisms, but still without the ambition of a full-fledged tune. In section 4.1 we present a comparison of the different effects we have discussed so far, while section 4.2 gives an overview of the results obtained by combining the effects into a more complete picture. Note that the new mechanisms will be available in the next public PYTHIA release.

4.1 Impact of the different effects

Based on a limited set of LHC observables, this section presents the impact of the new mechanisms outlined in section 3 on the description of data. The observables have been chosen to illustrate the effects of the change of the Gaussian width or temperature, respectively, depending on the close-packing of strings as in eqs. (3.3) and (3.9), of hadron rescattering, and of colour reconnection. The latter has been included as it serves a similar purpose and shows a somewhat comparable behaviour. The baseline prediction, which serves as the main comparison for both models, is obtained by switching off all of the aforementioned effects. For a clear picture of the influence of the individual mechanisms, only one of them is switched on at a time. Note that the prediction of the Gaussian model with colour reconnection, labelled “Gaussian p_{\perp} ColRec” in the plots, corresponds to default PYTHIA 8. Recall that the results presented in this subsection are not obtained with parameter settings that optimize the data description but rather illustrate their general effect. The average transverse momentum $\langle p_{\perp} \rangle$ as a function of the hadron mass and the charged multiplicity are shown in figure 13, together with the charged particle p_{\perp} spectrum.

For both models, the description of $\langle p_{\perp} \rangle$ as a function of mass improves for each of the different mechanisms, compared to the baseline prediction, as heavier hadrons obtain larger $\langle p_{\perp} \rangle$ values. The thermodynamical model provides a somewhat better description of this observable, compared to the Gaussian model, which comes naturally due to the exponential hadronic transverse-mass suppression.

The baseline prediction for $\langle p_{\perp} \rangle (n_{\text{ch}})$ plateaus at small multiplicities, therefore underestimating $\langle p_{\perp} \rangle$ for values $n_{\text{ch}} \gtrsim 25$. All of the effects investigated in this study have a somewhat similar effect, in the sense that they are able to push up the prediction, compared to the baseline settings. While including the $n_{\text{string}}^{\text{eff}}$ -dependence significantly improves the description, it is still slightly worse than the prediction with colour reconnection. The hadron rescattering provides a fairly good description of $\langle p_{\perp} \rangle$ for small n_{ch} values, but clearly overshoots the distribution at high multiplicities.

Similar to the previous observable, the $n_{\text{string}}^{\text{eff}}$ -dependence and colour reconnection improve the description of the inclusive p_{\perp} spectrum. The Gaussian model without additional effects switched on produces a bump at $p_{\perp} \sim 0.5 \text{ GeV}/c$ and a broad dip at $p_{\perp} \sim 2.5 \text{ GeV}/c$. While colour reconnection removes the dip almost completely, the bump is still clearly visible. The $n_{\text{string}}^{\text{eff}}$ -dependence somewhat reduces both bump and dip, but at the cost of introducing another dip towards very small p_{\perp} values. The baseline prediction of the thermodynamical model, compared with the Gaussian one, has the same dip at $p_{\perp} \sim 2.5 \text{ GeV}/c$, while the bump is much less visible. Both colour reconnection and the $n_{\text{string}}^{\text{eff}}$ -dependence reduce the dip quite substantially and provide a very good description of the data. The hadron rescattering, while somewhat improving the description in the low- p_{\perp} region, overestimates mid- p_{\perp} values by around 20% before undershooting the distribution.

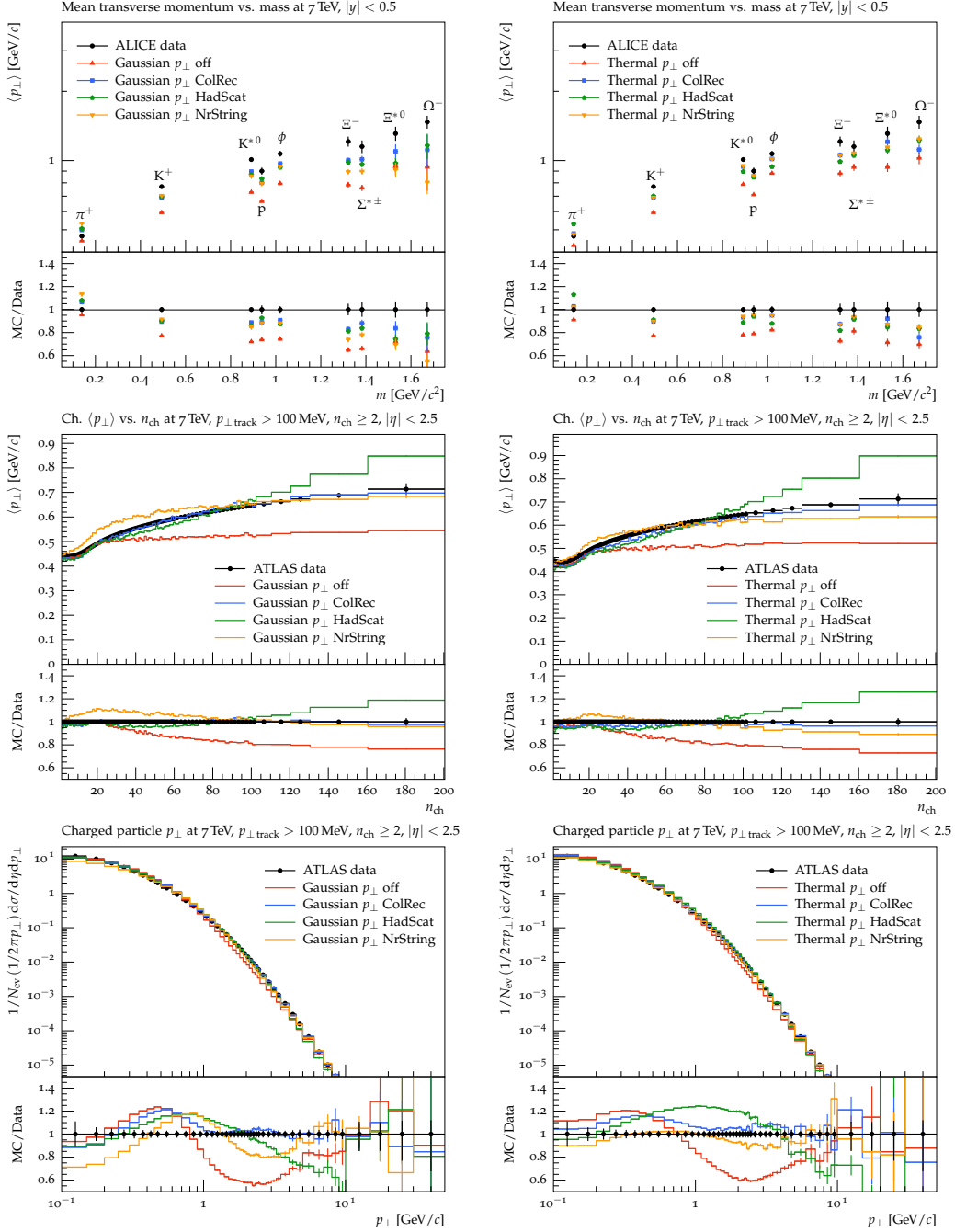


Figure 13. Comparisons to ALICE [46] and ATLAS [47] data: $\langle p_{\perp} \rangle$ as a function of the hadron mass (*top*), charged multiplicity (*middle*), and the charged particle p_{\perp} (*bottom*). Predictions with the Gaussian (thermodynamical) model are shown in the *left* (*right*) plots. ColRec / HadScat / NrString means that only colour reconnection / hadron rescattering / n_{string}^{eff} -dependence is switched on, otherwise everything is switched off.

4.2 Results

Using the information of the last subsection we adjust the parameters associated with the new mechanisms to obtain a good data description, with the main focus lying on p_{\perp} spectra of pions, kaons, and protons. We begin with LHC data, as this is the motivation for the thermodynamical model, the $n_{\text{string}}^{\text{eff}}$ -dependence, and the hadron rescattering, and continue with a cross-check of some LEP and SLC observables.

4.2.1 LHC

The new parameters are adjusted such that an improvement of the p_{\perp} spectra of π^{\pm} , K^{\pm} and p, \bar{p} , measured with ALICE [51], is achieved, while still giving a reasonable description of the charged particle p_{\perp} distribution and $\langle p_{\perp} \rangle$ as a function of the multiplicity, both measured with ATLAS [47]. The corresponding settings and values can be found in appendix A. The LHC data set presented here includes the aforementioned p_{\perp} spectra and the Λ to K_S^0 ratio shown in figure 14, $\langle p_{\perp} \rangle$ as a function of the hadron mass and the charged multiplicity, both inclusive and for different hadrons, shown in figure 15, and the ratio of yields with respect to $(\pi^+ + \pi^-)$ as a function of the charged multiplicity for different hadrons, shown in figure 16. The predictions of default PYTHIA are compared to the Gaussian and thermodynamical model with the modifications outlined in section 3.

Default PYTHIA describes the ATLAS charged particle p_{\perp} distribution very well for values of $p_{\perp} > 1 \text{ GeV}/c$, but shows a bump at around $0.5 \text{ GeV}/c$. The Gaussian model with modifications gives a similar shape and reduces the bump somewhat, while undershooting the distribution large p_{\perp} by a few %. The thermodynamical model improves the description quite substantially, especially for low- p_{\perp} values, where the aforementioned bump is almost gone. The predictions for the CMS charged hadron p_{\perp} spectrum behave mostly similar, with the same bump visible for default PYTHIA and the Gaussian model.

For default PYTHIA, pions obtain a too hard p_{\perp} spectrum. The modifications to the Gaussian model improve the distribution slightly, but there is still no good overall description. With the thermodynamical model the spectrum improves for low- p_{\perp} values quite a bit; however, it is still a bit too high in the large- p_{\perp} region. The K^{\pm} p_{\perp} spectrum shows the opposite behaviour: too many soft and too few hard kaons. The Gaussian model with modifications improves the description in the soft region somewhat, compared to default PYTHIA. Both the Gaussian and thermodynamical model change the shape of the spectrum slightly, but do not provide a better overall description of the K^{\pm} p_{\perp} . The prediction of both models for the p, \bar{p} p_{\perp} spectrum are better compared to default PYTHIA, where especially the thermodynamical model improves the low- p_{\perp} region quite substantially.

While the prediction of the thermodynamical model for the Λ/K_S^0 ratio is somewhat flatter with respect to the data, especially in the low- p_{\perp} region, the normalization is off by almost a factor of two due to the combination of producing slightly too many K_S^0 and not enough Λ . The observable could be improved by adjusting the overall normalization factor of baryons with respect to mesons. The value of this parameter has been fixed using the proton p_{\perp} spectrum, however.

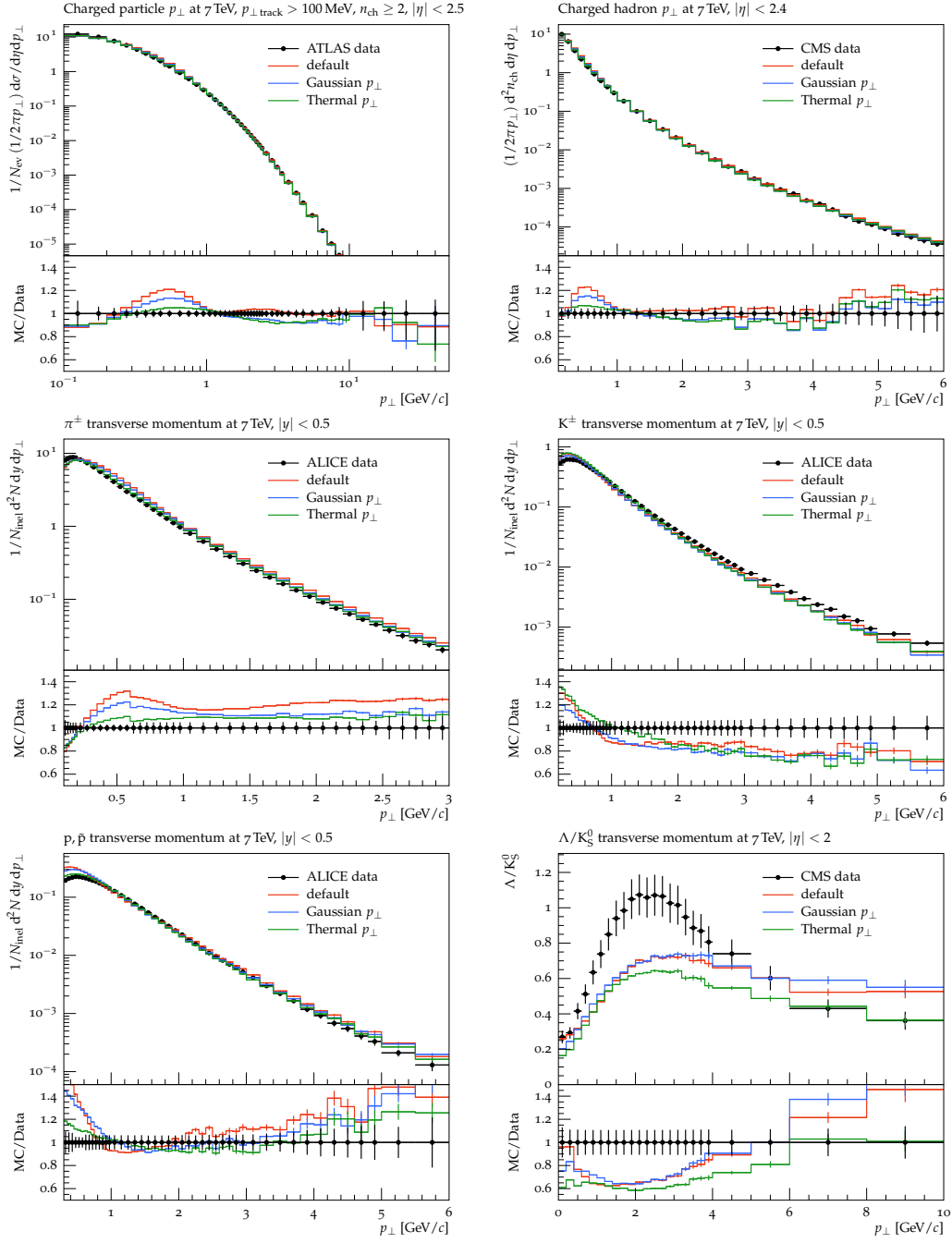


Figure 14. Inclusive (*top*), π^\pm , K^\pm , and p, \bar{p} (*middle and bottom left*) p_\perp spectra and the Λ to K_S^0 ratio (*bottom right*). Predictions of default PYTHIA, the Gaussian and thermodynamical model with modifications, compared to ATLAS [47], CMS [52, 83] and ALICE data [51].

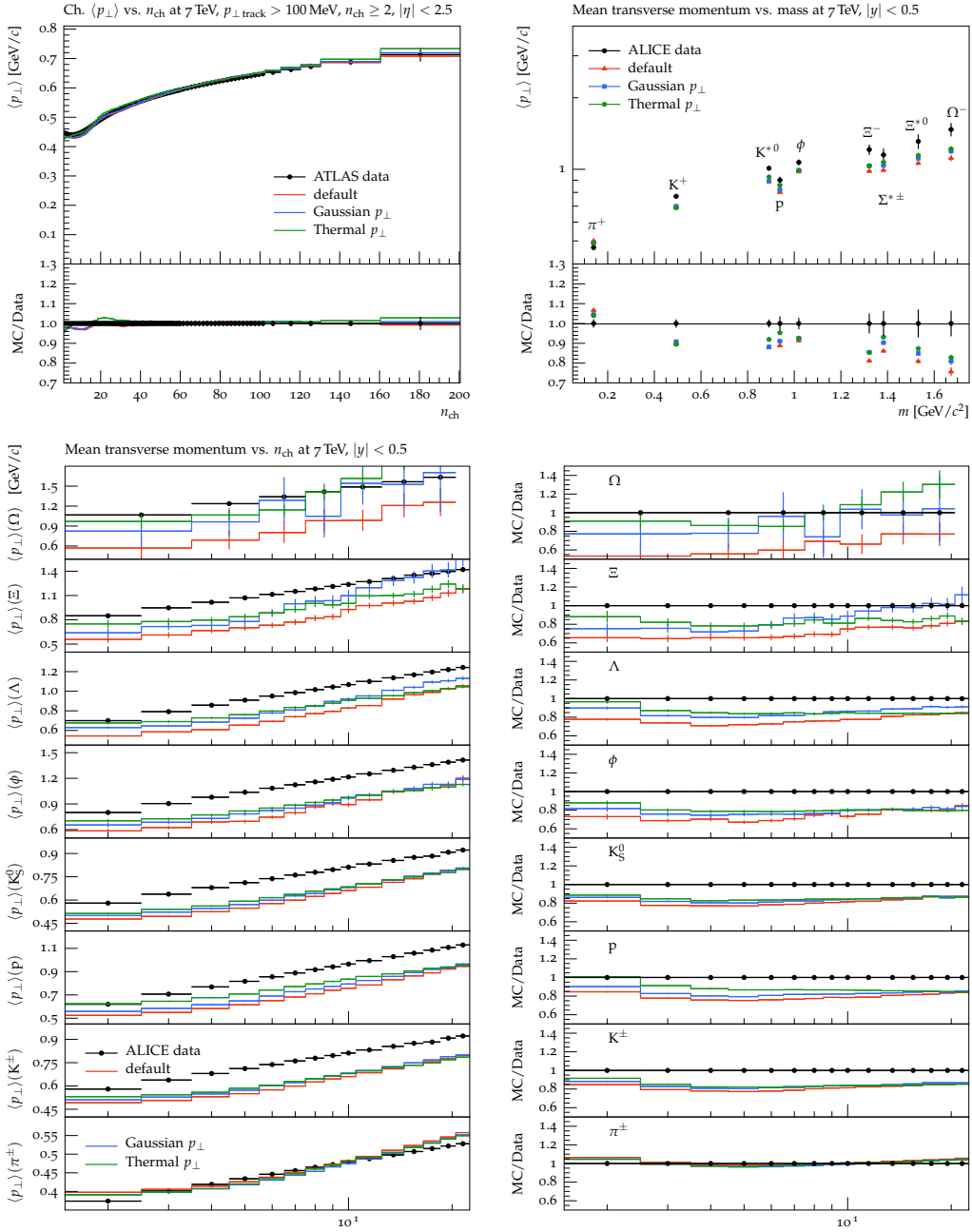


Figure 15. The mean transverse momentum as a function of the charged multiplicity (*top left*) and the hadron mass (*top right*) and (*bottom*). Predictions of default PYTHIA, the Gaussian and thermodynamical model with modifications, compared to ALICE [46, 48] and ATLAS [47] data. The data in the bottom plots is taken to be an estimate of the logarithmic fits in [48] and therefore no error bars are included.

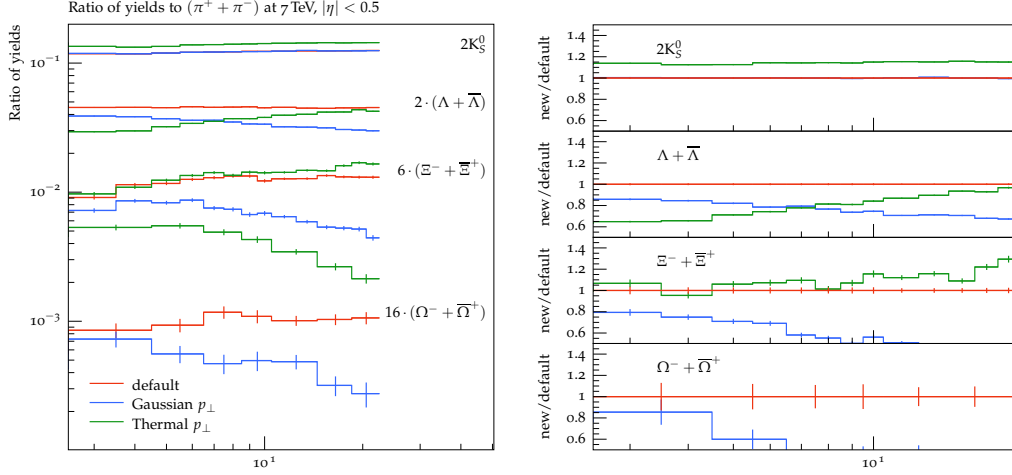


Figure 16. Ratio of yields with respect to $(\pi^+ + \pi^-)$ as a function of the charged multiplicity. Predictions of default PYTHIA, the Gaussian and thermodynamical model with modifications. The ALICE measurement can be found in [10].

All models give very similar predictions for $\langle p_\perp \rangle$ as a function of n_{ch} , with an extremely good description of the region $n_{\text{ch}} > 20$, but too low $\langle p_\perp \rangle$ for smaller multiplicities. It is quite obvious that the description of this observable could be further improved by choosing a larger value for the width or temperature respectively and simultaneously lowering the $n_{\text{string}}^{\text{eff}}$ -dependence and hadron rescattering. This would however come hand in hand with worse descriptions of other observables. For default PYTHIA, pions obtain a too large $\langle p_\perp \rangle$ and heavier hadrons a too small one. While the thermodynamical model improves the predictions for $\langle p_\perp \rangle(m)$, there is still no full agreement with data. The Gaussian model lies in between default PYTHIA and the thermodynamical model. We observe a similar behaviour for the $\langle p_\perp \rangle(n_{\text{ch}})$ distribution for individual hadrons. The pion $\langle p_\perp \rangle$ is described fairly well with a slope that is slightly too steep. The main difference of the other hadrons with respect to pions is that they obtain a too small $\langle p_\perp \rangle$ over the whole n_{ch} range. As for pions, the slopes tend to be too steep.

ALICE [10] found that the production of strange and multi-strange hadrons is enhanced with increasing multiplicity. While default PYTHIA is not able to reproduce such a behaviour, figure 16 shows that the thermodynamical model achieves an increase of strangeness with charged multiplicity for K_S^0 , Λ , and Ξ , but not for Ω . Except for the latter, we therefore expect the thermodynamical model to give an improved description of the data presented in [10]. The Gaussian model with modifications shows the opposite effect, a decrease with growing multiplicity. These findings can be explained as follows: in default PYTHIA all (primary) hadrons are produced with a probability that is independent of the multiplicity or number of strings. In the thermodynamical model heavier hadrons are produced preferably at large p_\perp values. Including the $n_{\text{string}}^{\text{eff}}$ -dependence leads to potentially higher temperatures for events with large n_{ch} , where heavy hadrons have a higher probability to be produced, compared to low- n_{ch} events. With the modifications

to the Gaussian model, all hadrons obtain more p_{\perp} in events with large values of $n_{\text{string}}^{\text{eff}}$. Due to phase-space constraints heavier hadrons might be rejected more often compared to lower-mass hadrons, leading to the decrease with growing multiplicity. This might also be the reason for the slight drop towards large n_{ch} for Ω in the thermodynamical model, as it eventually dominates over the effect of the $n_{\text{string}}^{\text{eff}}$ -dependence.

4.2.2 LEP and SLC

While the main motivation for introducing the exponential p_{\perp} distribution is arising from LHC data, the valid question of whether the same model is able to describe e^+e^- observables as well remains. The effect of the close-packing of strings and hadron rescattering are not included for e^+e^- data as we do not expect them to represent relevant physics here. Furthermore the string dependence relies on rapidity differences and an event axis aligned with the beam, which is not present in e^+e^- collisions.

The parameters of the thermodynamical model are adjusted using the charged particle momentum spectrum as well as the scaled momenta of π^{\pm} , K^{\pm} and p, \bar{p} , measured with SLD [84], while the ALEPH event shapes [85] served as cross checks. For the Gaussian model the width and prefactors for strange and diquarks have been adjusted such that the mean charged multiplicities agrees with the value obtained with the thermodynamical model. The corresponding settings and values can be found in appendix A. The e^+e^- data set presented here includes the aforementioned momenta and mean multiplicities for different hadrons shown in figure 17, as well as the charged multiplicity distribution, scaled momentum and the inclusive $p_{\perp\text{in}}$ and $p_{\perp\text{out}}$ spectra shown in figure 18. The predictions of default PYTHIA are compared to the Gaussian and thermodynamical model as described above.

The only difference between default PYTHIA and the prediction labelled as “Gaussian p_{\perp} ” is an adjusted value for the Gaussian width and its prefactors for s and diquarks, i.e. there is no change of the flavour selection parameters. Therefore, the values of the mean multiplicities remain, leading to overlapping data and Monte Carlo histogram points in figure 17, which are thus not fully visible. With the thermodynamical model we obtain a fairly good description of most hadrons, with the notable exceptions of producing too many heavy baryons. Note however, that the Gaussian model comes with around 20 parameter for selecting the flavour of new hadrons, whereas the thermodynamical model makes use of only three parameters: the temperature, the overall normalization factor of baryons with respect to mesons, and the additional suppression factor for hadrons with strange quarks, see section 3.2. Hence, the result is fairly acceptable.

The predictions of the two models for the charged particle momentum agree very well with data in the soft region; there is only some small deviation for medium and large momenta, where especially the thermodynamical model predicts somewhat too many particles in the hard region. The same effect is even clearer visible in the scaled momentum spectrum of pions. For kaons and protons we observe the opposite effect: the new model predicts too few hadrons with large momenta.

Similar to the charged particle momentum, the predictions of both models for the logarithm of the scaled momentum agrees well with data, with some small deviation for

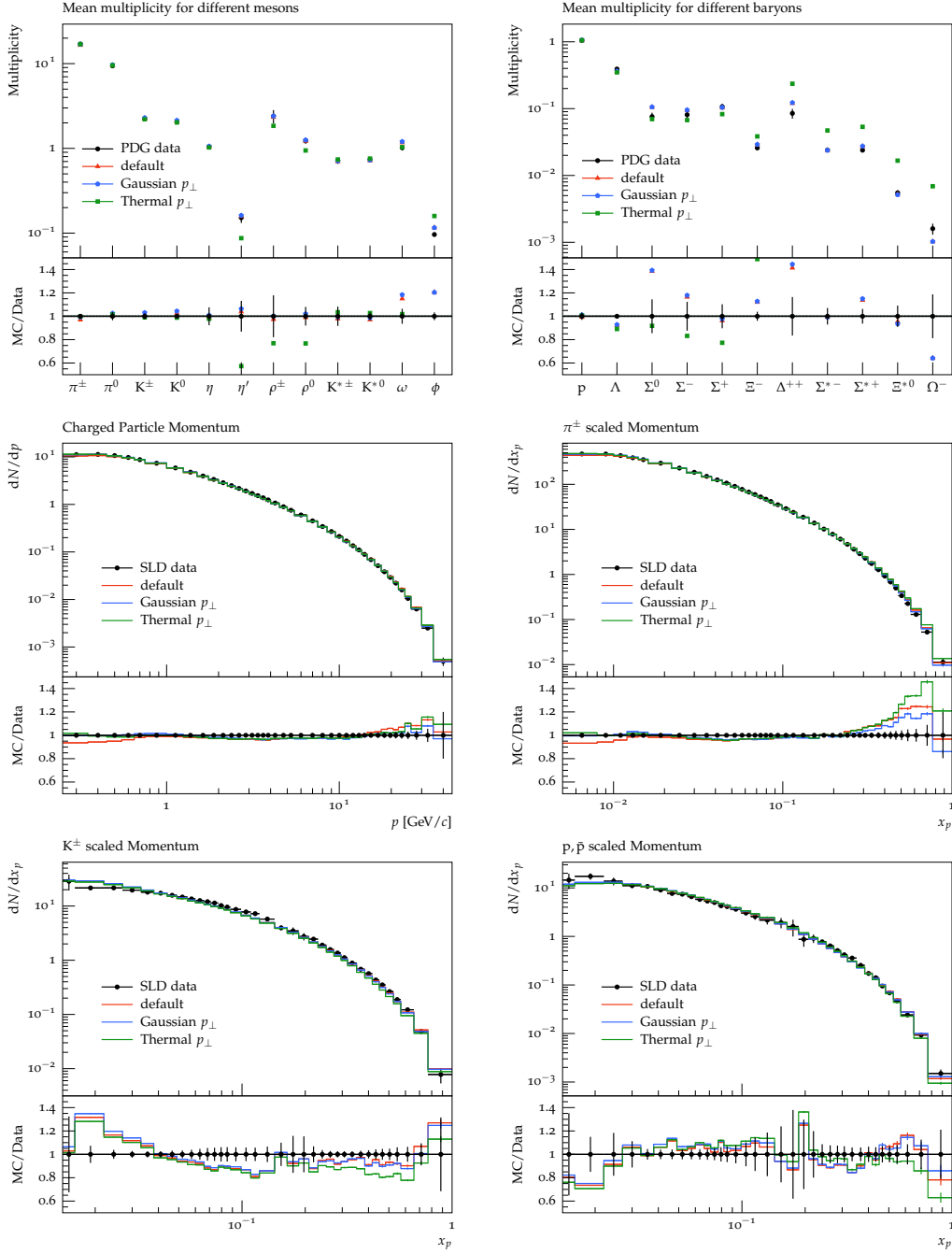


Figure 17. Mean hadron multiplicities (*top*), charged particle momentum (*middle left*), and scaled momenta $x_p = 2|\mathbf{p}|/E_{\text{cm}}$ of π^\pm (*middle right*), K^\pm (*bottom left*) and p, \bar{p} (*bottom right*). Predictions of default PYTHIA 8, the Gaussian and thermodynamical model compared to PDG [72] and SLD data [84].

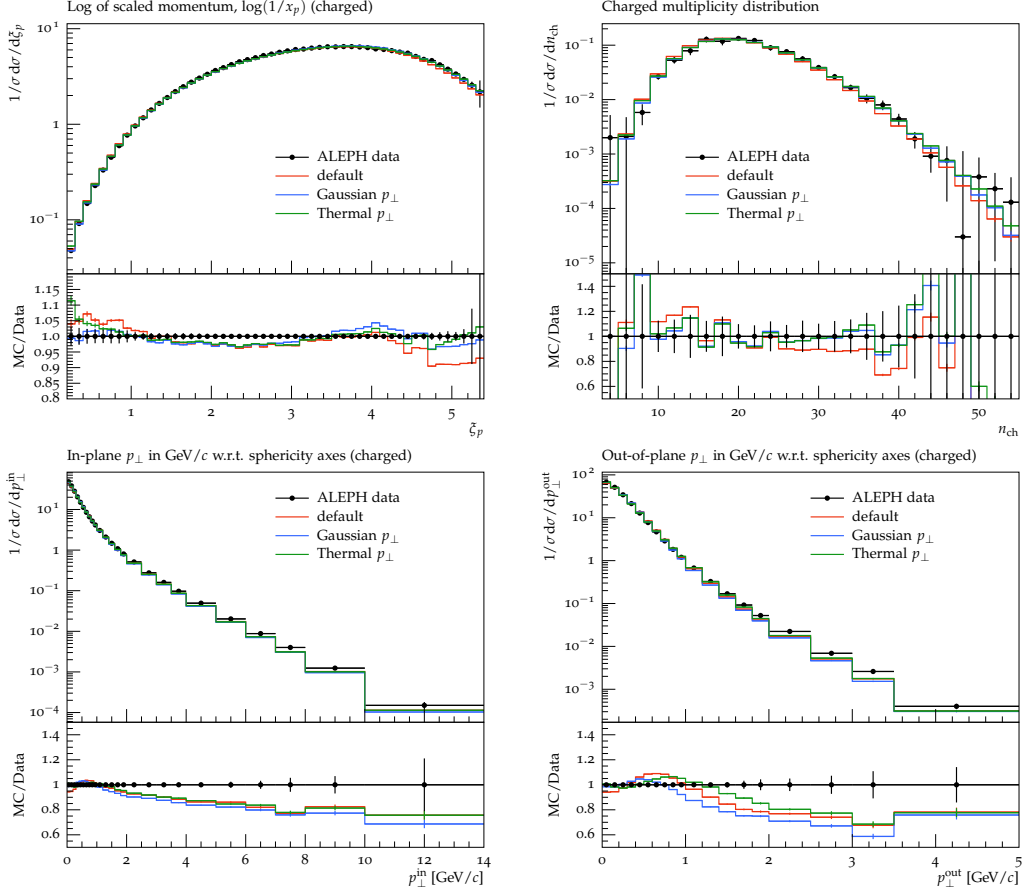


Figure 18. Charged multiplicity distribution (*top left*), scaled momentum (*top right*) and the inclusive $p_{\perp\text{in}}$ and $p_{\perp\text{out}}$ spectra (*bottom*). Predictions of default PYTHIA 8, the Gaussian and thermodynamical model compared to ALEPH data [85].

medium and large values. However, the sudden drop in the ratio of the Monte Carlo prediction to data at around $\xi_p = 4.7$ remains almost unchanged. The description of the charged multiplicity distribution improves slightly, compared to default PYTHIA, towards having less events with small multiplicities and more events with larger ones. This is due to having an increased mean charged multiplicity. While both models describe the low- p_{\perp} region of the inclusive $p_{\perp\text{in}}$ and $p_{\perp\text{out}}$ spectra very well, they underestimate the amount of events with larger p_{\perp} values. The thermodynamical model provides a better description of especially the $p_{\perp\text{out}}$ spectrum, compared to the Gaussian model.

To summarize we note that the thermodynamical model is able to provide predictions for event shapes and momentum spectra in e^+e^- events that are of a similar quality as those by the Gaussian model. Nevertheless, the hadron decomposition is not described well, a price to pay for reducing the amount of flavour selection parameters.

5 Summary and outlook

The understanding of soft hadronic physics is changing under the onslaught of LHC pp data. Of course, there has never been an approach that could describe all aspects of pp physics perfectly, but before LHC it was often assumed that all the basic concepts were in place, and that what remained was successive refinements. Now we see that there is still much left to learn. There have already been several surprises, and further data analyses may well produce more.

In view of this we have revisited some of the basic soft-physics assumptions of the PYTHIA event generator, which has been quite successful in predicting and describing many aspects of the data, but now starts to show cracks. New approaches have here been studied for some areas, to understand how much room for improvements there would be, without any claim that either of them would necessarily be the one and only right way to go.

A central pillar of PYTHIA has been the Lund string fragmentation model, where a tunneling mechanism for string breakups leads to a universal Gaussian p_{\perp} spectrum. In this work a thermodynamical model is implemented as an alternative, where p_{\perp} instead follows an exponential distribution. For an already selected p_{\perp} , the hadron flavour is picked based on an exponential m_{\perp} weight, with additional factors due to spin-counting rules and so on. This approach suppresses the production of heavier hadrons, and gives them a larger $\langle p_{\perp} \rangle$. Such a pattern is observed in data, and exists in the Gaussian approach mainly owing to particle decays, but there undershoots data.

Making the Gaussian p_{\perp} width, or temperature in case of the thermodynamical model, dependent on the close-packing of strings allows for modelling the influence of strings on each other in a simple way. An effective number of density of strings is introduced for low p_{\perp} 's, while high- p_{\perp} fragmentation tends to occur outside the close-packed string region and is left unaffected. Such a mechanism could e.g. be used to explain a changing flavour composition at high multiplicities.

Finally we implemented a simple model for hadronic rescattering, applied to the primary hadrons, before decays. The probability of two hadrons to rescatter is based on how close they are in phase space. By favouring a shift towards equal transverse velocities, it should also give higher $\langle p_{\perp} \rangle$ for heavy hadrons and lower for pions.

Not surprisingly we found the hadronic decays to limit the hoped-for effects. Specifically, most pions come from decays of heavier hadrons, and so the mechanisms intended to give less p_{\perp} to pions and more to kaons and protons are largely nullified. The mechanisms are also not simply additive; starting out from the thermodynamical model with its already-existing mass differentiation, the further effects of varying temperatures or hadronic rescattering are smaller than corresponding effects in the Gaussian approach.

Nevertheless the thermodynamical model is able to provide reasonable descriptions of observables such as the p_{\perp} spectrum of charged hadrons, the average transverse momentum as a function of the hadron mass, or the recently measured enhanced production of strange and multi-strange hadrons with increasing multiplicity. These observables have so far been described rather poorly by PYTHIA. And, given the small number of flavour parameters in

the thermodynamical model, it is able to describe a reasonable number of e^+e^- data rather well, even if it can not compete with the many-more-parameter tunes of default PYTHIA.

It should be noted that we have not compared with all relevant available data, by far. Notably, the ridge effect was not described by the existing PYTHIA model, and our current changes do not introduce any mechanism to induce it. The ridge was first observed in AA collisions [86–89], where nuclear geometry and hydrodynamical expansion offer natural starting points [90, 91], although the range of detailed models is too vast to cover here [92]. In the field of pp physics [93], the EPOS model addresses the issue by having an inner core that can push strings in the outer corona [94], whereas a recent extension of DIPSY [95] provides a corresponding shove from the excess energy of central overlapping strings that form ropes. In a similar spirit, our higher string tension could introduce a push also without rope formation. A detailed modelling is not trivial, however, and we have not pursued it for now.

To advance to the next level of sophistication within the line of research advocated here, it would be necessary to do a microscopic tracing of the full space-time evolution of the event, both for partons and for hadrons, and including both production and decay vertices. This is nontrivial beyond the simple one-string picture, even in the cleaner e^+e^- events, and the further complications of MPIs and CR in hadronic events will make it even worse. What it would allow is a more detailed understanding of the close-packing both of strings and of hadrons. Combined with a more detailed modelling of hadronic rescattering, a more realistic picture may emerge.

Some of the limitations encountered here are likely still to remain, so further mechanisms may be at play, in addition to the ones studied here. This would not be the first time where a cocktail of smaller effects combine to give a significant signal. What is less likely is actually the opposite, that one single mechanism does it all. Specifically, whatever else may be going on, the close-packing of strings and hadrons appears unavoidable in high-multiplicity pp events, and collective-flow effects are here to stay. In sum, we have an interesting and challenging time ahead of us, where some of the most unexpected new LHC observations may well come in the low- p_\perp region rather than the in high- p_\perp one.

Acknowledgments

Helpful discussions with Peter Skands are gratefully acknowledged. Work supported by the MCnetITN FP7 Marie Curie Initial Training Network, contract PITN-GA-2012-315877. This project has also received funding in part by the Swedish Research Council, contract number 621-2013-4287, and in part from the European Research Council (ERC) under the European Union’s Horizon 2020 research and innovation programme (grant agreement No 668679).

A Settings

Table 1 gives a list of the settings that have been changed with respect to default PYTHIA to obtain the results presented in section 4.2.

	LHC			LEP and SLC	
	Default	Gaussian	Thermal	Gaussian	Thermal
Switch to thermal model?					
StringPT:thermalModel	off	off	on	off	on
Gaussian width $\sigma = \sqrt{\kappa/\pi}$					
StringPT:sigma	0.335	0.33	-	0.295	-
σ prefactor for s quarks					
StringPT:widthPreStrange	1.0	1.2	-	1.2	-
σ prefactor for diquarks					
StringPT:widthPreDiquark	1.0	1.2	-	1.2	-
Fraction with enhanced σ					
StringPT:enhancedFraction	0.01	0.0	-	0.0	-
Temperature T					
StringPT:temperature	-	-	0.21	-	0.205
Baryon normalization factor					
StringFlav:BtoMratio	-	-	0.357	-	0.625
Suppression factor for s hadrons					
StringFlav:StrangeSuppression	-	-	0.5	-	0.45
r parameter in eq. (3.3) or (3.9)					
StringPT:expNSP	0.0	0.01	0.13	0.0	0.0
Range of MPI-based CR scheme					
ColourReconnection:range	1.8	1.8	1.1	-	-
Hadron rescattering (HR) on?					
HadronLevel:HadronScatter	off	on	on	off	off
HR with eq. (3.10) and (3.11)					
HadronScatter:mode	-	0	0	-	-
P_{ds}^{\max} parameter in eq. (3.11)					
HadronScatter:maxProbDS	-	0.25	0.5	-	-
MPI regularization parameter					
MultipartonInteractions:pT0Ref	2.28	2.34	2.5	-	-

Table 1. PYTHIA 8 parameters and their values for tuning to LHC and LEP/SLC observables.

Open Access. This article is distributed under the terms of the Creative Commons Attribution License ([CC-BY 4.0](https://creativecommons.org/licenses/by/4.0/)), which permits any use, distribution and reproduction in any medium, provided the original author(s) and source are credited.

References

- [1] G.P. Salam, *QCD Theory Overview — Towards Precision at LHC*, (2016), <https://indico.cern.ch/event/442390/contributions/1095992/>.
- [2] B. Andersson, G. Gustafson, G. Ingelman and T. Sjöstrand, *Parton Fragmentation and String Dynamics*, *Phys. Rept.* **97** (1983) 31 [[INSPIRE](#)].
- [3] R.D. Field and S. Wolfram, *A QCD Model for e^+e^- Annihilation*, *Nucl. Phys. B* **213** (1983) 65 [[INSPIRE](#)].
- [4] T.D. Gottschalk, *An Improved Description of Hadronization in the QCD Cluster Model for e^+e^- Annihilation*, *Nucl. Phys. B* **239** (1984) 349 [[INSPIRE](#)].
- [5] B.R. Webber, *A QCD Model for Jet Fragmentation Including Soft Gluon Interference*, *Nucl. Phys. B* **238** (1984) 492 [[INSPIRE](#)].
- [6] A. Ortiz Velasquez, P. Christiansen, E. Cuautle Flores, I. Maldonado Cervantes and G. Paic, *Color Reconnection and Flowlike Patterns in pp Collisions*, *Phys. Rev. Lett.* **111** (2013) 042001 [[arXiv:1303.6326](#)] [[INSPIRE](#)].
- [7] CMS collaboration, *Observation of Long-Range Near-Side Angular Correlations in Proton-Proton Collisions at the LHC*, *JHEP* **09** (2010) 091 [[arXiv:1009.4122](#)] [[INSPIRE](#)].
- [8] ATLAS collaboration, *Observation of Long-Range Elliptic Azimuthal Anisotropies in $\sqrt{s} = 13$ and 2.76 TeV pp Collisions with the ATLAS Detector*, *Phys. Rev. Lett.* **116** (2016) 172301 [[arXiv:1509.04776](#)] [[INSPIRE](#)].
- [9] CMS collaboration, *Evidence for collectivity in pp collisions at the LHC*, *Phys. Lett. B* **765** (2017) 193 [[arXiv:1606.06198](#)] [[INSPIRE](#)].
- [10] ALICE collaboration, *Multiplicity-dependent enhancement of strange and multi-strange hadron production in proton-proton collisions at $\sqrt{s} = 7$ TeV*, [arXiv:1606.07424](#) [[INSPIRE](#)].
- [11] E. Cuautle and G. Paic, *The energy density representation of the strangeness enhancement from $p+p$ to $Pb+Pb$* , [arXiv:1608.02101](#) [[INSPIRE](#)].
- [12] P. Braun-Munzinger and J. Stachel, *The quest for the quark-gluon plasma*, *Nature* **448** (2007) 302 [[INSPIRE](#)].
- [13] T. Pierog, I. Karpenko, J.M. Katzy, E. Yatsenko and K. Werner, *EPOS LHC: Test of collective hadronization with data measured at the CERN Large Hadron Collider*, *Phys. Rev. C* **92** (2015) 034906 [[arXiv:1306.0121](#)] [[INSPIRE](#)].
- [14] T.S. Biro, H.B. Nielsen and J. Knoll, *Color Rope Model for Extreme Relativistic Heavy Ion Collisions*, *Nucl. Phys. B* **245** (1984) 449 [[INSPIRE](#)].
- [15] A. Bialas and W. Czyz, *Chromoelectric Flux Tubes and the Transverse Momentum Distribution in High-energy Nucleus-nucleus Collisions*, *Phys. Rev. D* **31** (1985) 198 [[INSPIRE](#)].
- [16] B. Andersson and P.A. Henning, *On the dynamics of a color rope: The fragmentation of interacting strings and the longitudinal distributions*, *Nucl. Phys. B* **355** (1991) 82 [[INSPIRE](#)].
- [17] C. Bierlich, G. Gustafson, L. Lönnblad and A. Tarasov, *Effects of Overlapping Strings in pp Collisions*, *JHEP* **03** (2015) 148 [[arXiv:1412.6259](#)] [[INSPIRE](#)].

- [18] P. Capiluppi, G. Giacomelli, A.M. Rossi, G. Vannini and A. Bussiere, *Transverse momentum dependence in proton proton inclusive reactions at very high-energies*, *Nucl. Phys. B* **70** (1974) 1 [INSPIRE].
- [19] R. Hagedorn, *Statistical thermodynamics of strong interactions at high-energies*, *Nuovo Cim. Suppl.* **3** (1965) 147 [INSPIRE].
- [20] R. Hagedorn, *Remarks on the thermodynamical model of strong interactions*, *Nucl. Phys. B* **24** (1970) 93 [INSPIRE].
- [21] R. Hagedorn, *Multiplicities, p_T Distributions and the Expected Hadron \rightarrow quark-gluon Phase Transition*, *Riv. Nuovo Cim.* **6N10** (1983) 1 [INSPIRE].
- [22] S. Barshay and Y.A. Chao, *Longitudinal mass, inclusive transverse-momentum distributions, proton proton elastic diffraction slopes and the total cross-section*, *Phys. Lett. B* **38** (1972) 225 [INSPIRE].
- [23] C. Tsallis, *Possible Generalization of Boltzmann-Gibbs Statistics*, *J. Statist. Phys.* **52** (1988) 479 [INSPIRE].
- [24] J. Cleymans, *On the Use of the Tsallis Distribution at LHC Energies*, [arXiv:1609.02289](https://arxiv.org/abs/1609.02289) [INSPIRE].
- [25] A.A. Bylinkin and A.A. Rostovtsev, *Parametrization of the shape of hadron-production spectra in high-energy particle interactions*, *Phys. Atom. Nucl.* **75** (2012) 999 [INSPIRE].
- [26] T. Sjöstrand and M. van Zijl, *A Multiple Interaction Model for the Event Structure in Hadron Collisions*, *Phys. Rev. D* **36** (1987) 2019 [INSPIRE].
- [27] T. Sjöstrand, S. Mrenna and P.Z. Skands, *PYTHIA 6.4 Physics and Manual*, *JHEP* **05** (2006) 026 [[hep-ph/0603175](https://arxiv.org/abs/hep-ph/0603175)] [INSPIRE].
- [28] T. Sjöstrand et al., *An Introduction to PYTHIA 8.2*, *Comput. Phys. Commun.* **191** (2015) 159 [[arXiv:1410.3012](https://arxiv.org/abs/1410.3012)] [INSPIRE].
- [29] X. Artru and G. Mennessier, *String model and multiproduction*, *Nucl. Phys. B* **70** (1974) 93 [INSPIRE].
- [30] B. Andersson, G. Gustafson and B. Soderberg, *A Probability Measure on Parton and String States*, *Nucl. Phys. B* **264** (1986) 29 [INSPIRE].
- [31] G. 't Hooft, *A Planar Diagram Theory for Strong Interactions*, *Nucl. Phys. B* **72** (1974) 461 [INSPIRE].
- [32] B. Andersson, G. Gustafson and T. Sjöstrand, *How to Find the Gluon Jets in e^+e^- Annihilation*, *Phys. Lett. B* **94** (1980) 211 [INSPIRE].
- [33] JADE collaboration, W. Bartel et al., *Experimental study of jets in electron-positron annihilation*, *Phys. Lett. B* **101** (1981) 129 [INSPIRE].
- [34] T. Sjöstrand, *Jet Fragmentation of Nearby Partons*, *Nucl. Phys. B* **248** (1984) 469 [INSPIRE].
- [35] T. Sjöstrand and P.Z. Skands, *Baryon number violation and string topologies*, *Nucl. Phys. B* **659** (2003) 243 [[hep-ph/0212264](https://arxiv.org/abs/hep-ph/0212264)] [INSPIRE].
- [36] B. Andersson, G. Gustafson and T. Sjöstrand, *On Soft Gluon Emission and the Transverse Momentum Properties of Final State Particles*, *Z. Phys. C* **12** (1982) 49 [INSPIRE].
- [37] F.E. Close, *An Introduction to Quarks and Partons*, Academic Press, London (1979).
- [38] B. Andersson, G. Gustafson and T. Sjöstrand, *A Model for Baryon Production in Quark and Gluon Jets*, *Nucl. Phys. B* **197** (1982) 45 [INSPIRE].

- [39] B. Andersson, G. Gustafson and T. Sjöstrand, *Baryon Production in Jet Fragmentation and Υ Decay*, *Phys. Scripta* **32** (1985) 574 [INSPIRE].
- [40] S. Platzer and S. Gieseke, *Dipole Showers and Automated NLO Matching in HERWIG++*, *Eur. Phys. J. C* **72** (2012) 2187 [arXiv:1109.6256] [INSPIRE].
- [41] P. Richardson and D. Winn, *Investigation of Monte Carlo Uncertainties on Higgs Boson searches using Jet Substructure*, *Eur. Phys. J. C* **72** (2012) 2178 [arXiv:1207.0380] [INSPIRE].
- [42] S. Chun and C. Buchanan, *A Simple plausible path from QCD to successful prediction of $e^+e^- \rightarrow$ hadronization data*, *Phys. Rept.* **292** (1998) 239 [INSPIRE].
- [43] S. Abachi, C. Buchanan, A. Chien, S. Chun and B. Hartfiel, *UCLA space-time area law model: A persuasive foundation for hadronization*, *Eur. Phys. J. C* **49** (2007) 569 [hep-ph/0612103] [INSPIRE].
- [44] A. Buckley et al., *Rivet user manual*, *Comput. Phys. Commun.* **184** (2013) 2803 [arXiv:1003.0694] [INSPIRE].
- [45] STAR collaboration, B.I. Abelev et al., *Systematic Measurements of Identified Particle Spectra in pp, d^+ Au and Au+Au Collisions from STAR*, *Phys. Rev. C* **79** (2009) 034909 [arXiv:0808.2041] [INSPIRE].
- [46] ALICE collaboration, *Production of $\Sigma(1385)^\pm$ and $\Xi(1530)^0$ in proton-proton collisions at $\sqrt{s} = 7$ TeV*, *Eur. Phys. J. C* **75** (2015) 1 [arXiv:1406.3206] [INSPIRE].
- [47] ATLAS collaboration, *Charged-particle multiplicities in pp interactions measured with the ATLAS detector at the LHC*, *New J. Phys.* **13** (2011) 053033 [arXiv:1012.5104] [INSPIRE].
- [48] ALICE collaboration, *Strangeness production as a function of charged particle multiplicity in proton-proton collisions*, *Nucl. Phys. A* **956** (2016) 777 [arXiv:1604.06736] [INSPIRE].
- [49] CMS collaboration, *Charged particle transverse momentum spectra in pp collisions at $\sqrt{s} = 0.9$ and 7 TeV*, *JHEP* **08** (2011) 086 [arXiv:1104.3547] [INSPIRE].
- [50] ALICE collaboration, *Pseudorapidity and transverse-momentum distributions of charged particles in proton-proton collisions at $\sqrt{s} = 13$ TeV*, *Phys. Lett. B* **753** (2016) 319 [arXiv:1509.08734] [INSPIRE].
- [51] ALICE collaboration, *Measurement of pion, kaon and proton production in proton-proton collisions at $\sqrt{s} = 7$ TeV*, *Eur. Phys. J. C* **75** (2015) 226 [arXiv:1504.00024] [INSPIRE].
- [52] CMS collaboration, *Strange Particle Production in pp Collisions at $\sqrt{s} = 0.9$ and 7 TeV*, *JHEP* **05** (2011) 064 [arXiv:1102.4282] [INSPIRE].
- [53] UA1 collaboration, C. Albajar et al., *A Study of the General Characteristics of $p\bar{p}$ Collisions at $\sqrt{s} = 0.2$ TeV to 0.9 TeV*, *Nucl. Phys. B* **335** (1990) 261 [INSPIRE].
- [54] T. Sjöstrand and V.A. Khoze, *On color rearrangement in hadronic $W^+ W^-$ events*, *Z. Phys. C* **62** (1994) 281 [hep-ph/9310242] [INSPIRE].
- [55] J.R. Christiansen and P.Z. Skands, *String Formation Beyond Leading Colour*, *JHEP* **08** (2015) 003 [arXiv:1505.01681] [INSPIRE].
- [56] A. Chodos, R.L. Jaffe, K. Johnson, C.B. Thorn and V.F. Weisskopf, *A New Extended Model of Hadrons*, *Phys. Rev. D* **9** (1974) 3471 [INSPIRE].
- [57] H. Sorge, H. Stoecker and W. Greiner, *Poincaré Invariant Hamiltonian Dynamics: Modeling Multi-Hadronic Interactions in a Phase Space Approach*, *Annals Phys.* **192** (1989) 266 [INSPIRE].

- [58] H. Sorge, M. Berenguer, H. Stoecker and W. Greiner, *Color rope formation and strange baryon production in ultrarelativistic heavy ion collisions*, *Phys. Lett. B* **289** (1992) 6 [INSPIRE].
- [59] S.A. Bass et al., *Microscopic models for ultrarelativistic heavy ion collisions*, *Prog. Part. Nucl. Phys.* **41** (1998) 255 [nucl-th/9803035] [INSPIRE].
- [60] M. Bleicher et al., *Relativistic hadron hadron collisions in the ultrarelativistic quantum molecular dynamics model*, *J. Phys. G* **25** (1999) 1859 [hep-ph/9909407] [INSPIRE].
- [61] S. Soff et al., *Enhanced strange particle yields - signal of a phase of massless particles?*, *J. Phys. G* **27** (2001) 449 [nucl-th/0010103] [INSPIRE].
- [62] S. Soff, J. Randrup, H. Stoecker and N. Xu, *Effects of strong color fields on baryon dynamics*, *Phys. Lett. B* **551** (2003) 115 [nucl-th/0209093] [INSPIRE].
- [63] B. Zhang, C.M. Ko, B.-A. Li and Z.-w. Lin, *A multiphase transport model for nuclear collisions at RHIC*, *Phys. Rev. C* **61** (2000) 067901 [nucl-th/9907017] [INSPIRE].
- [64] Z.-W. Lin, C.M. Ko, B.-A. Li, B. Zhang and S. Pal, *A multi-phase transport model for relativistic heavy ion collisions*, *Phys. Rev. C* **72** (2005) 064901 [nucl-th/0411110] [INSPIRE].
- [65] Z.-w. Lin, S. Pal, C.M. Ko, B.-A. Li and B. Zhang, *Charged particle rapidity distributions at relativistic energies*, *Phys. Rev. C* **64** (2001) 011902 [nucl-th/0011059] [INSPIRE].
- [66] N.S. Amelin, M.A. Braun and C. Pajares, *Multiple production in the Monte Carlo string fusion model*, *Phys. Lett. B* **306** (1993) 312 [INSPIRE].
- [67] N.S. Amelin, N. Armesto, C. Pajares and D. Sousa, *Monte Carlo model for nuclear collisions from SPS to LHC energies*, *Eur. Phys. J. C* **22** (2001) 149 [hep-ph/0103060] [INSPIRE].
- [68] M.A. Braun and C. Pajares, *Particle production in nuclear collisions and string interactions*, *Phys. Lett. B* **287** (1992) 154 [INSPIRE].
- [69] M.A. Braun and C. Pajares, *Implications of percolation of color strings on multiplicities, correlations and the transverse momentum*, *Eur. Phys. J. C* **16** (2000) 349 [hep-ph/9907332] [INSPIRE].
- [70] M.A. Braun and C. Pajares, *Transverse momentum distributions and their forward backward correlations in the percolating color string approach*, *Phys. Rev. Lett.* **85** (2000) 4864 [hep-ph/0007201] [INSPIRE].
- [71] C. Pajares, *String and parton percolation*, *Eur. Phys. J. C* **43** (2005) 9 [hep-ph/0501125] [INSPIRE].
- [72] PARTICLE DATA GROUP collaboration, C. Amsler et al., *Review of Particle Physics*, *Phys. Lett. B* **667** (2008) 1 [INSPIRE].
- [73] BRITISH-SCANDINAVIAN collaboration, B. Alper et al., *Production Spectra of π^\pm , K^\pm , ρ^\pm at Large Angles in Proton Proton Collisions in the CERN Intersecting Storage Rings*, *Nucl. Phys. B* **100** (1975) 237 [INSPIRE].
- [74] BRITISH-SCANDINAVIAN-MIT collaboration, K. Guettler et al., *Inclusive Production of Low-Momentum Charged Pions at $x = 0$ at the CERN Intersecting Storage Rings*, *Phys. Lett. B* **64** (1976) 111 [INSPIRE].
- [75] G. Giacomelli and M. Jacob, *Physics at the CERN ISR*, *Phys. Rept.* **55** (1979) 1 [INSPIRE].
- [76] I.S. Gradshteyn and I.M. Ryzhik, *Table of Integrals, Series, and Products*, fourth edition, Academic Press, London (1980).

- [77] M. Abramowitz and I. Stegun, *Handbook of Mathematical Functions with Formulas, Graphs, and Mathematical tables*, Dover Publications, New York (1965).
- [78] J. Dias de Deus and C. Pajares, *Percolation of color sources and critical temperature*, *Phys. Lett. B* **642** (2006) 455 [[hep-ph/0607101](#)] [[INSPIRE](#)].
- [79] M. Gyulassy and L. McLerran, *New forms of QCD matter discovered at RHIC*, *Nucl. Phys. A* **750** (2005) 30 [[nucl-th/0405013](#)] [[INSPIRE](#)].
- [80] U. Heinz and R. Snellings, *Collective flow and viscosity in relativistic heavy-ion collisions*, *Ann. Rev. Nucl. Part. Sci.* **63** (2013) 123 [[arXiv:1301.2826](#)] [[INSPIRE](#)].
- [81] G. Roland, K. Safarik and P. Steinberg, *Heavy-ion collisions at the LHC*, *Prog. Part. Nucl. Phys.* **77** (2014) 70 [[INSPIRE](#)].
- [82] R.D. Field and R.P. Feynman, *A Parametrization of the Properties of Quark Jets*, *Nucl. Phys. B* **136** (1978) 1 [[INSPIRE](#)].
- [83] CMS collaboration, *Transverse-momentum and pseudorapidity distributions of charged hadrons in pp collisions at $\sqrt{s} = 7$ TeV*, *Phys. Rev. Lett.* **105** (2010) 022002 [[arXiv:1005.3299](#)] [[INSPIRE](#)].
- [84] SLD collaboration, K. Abe et al., *Production of π^+ , π^- , K^+ , K^- , p and \bar{p} in light (uds), c and b jets from Z^0 decays*, *Phys. Rev. D* **69** (2004) 072003 [[hep-ex/0310017](#)] [[INSPIRE](#)].
- [85] ALEPH collaboration, R. Barate et al., *Studies of quantum chromodynamics with the ALEPH detector*, *Phys. Rept.* **294** (1998) 1 [[INSPIRE](#)].
- [86] STAR collaboration, J. Adams et al., *Distributions of charged hadrons associated with high transverse momentum particles in pp and Au + Au collisions at $\sqrt{s_{NN}} = 200$ GeV*, *Phys. Rev. Lett.* **95** (2005) 152301 [[nucl-ex/0501016](#)] [[INSPIRE](#)].
- [87] STAR collaboration, B.I. Abelev et al., *Long range rapidity correlations and jet production in high energy nuclear collisions*, *Phys. Rev. C* **80** (2009) 064912 [[arXiv:0909.0191](#)] [[INSPIRE](#)].
- [88] PHOBOS collaboration, B. Alver et al., *High transverse momentum triggered correlations over a large pseudorapidity acceptance in Au+Au collisions at $\sqrt{s_{NN}} = 200$ GeV*, *Phys. Rev. Lett.* **104** (2010) 062301 [[arXiv:0903.2811](#)] [[INSPIRE](#)].
- [89] CMS collaboration, *Long-range and short-range dihadron angular correlations in central PbPb collisions at a nucleon-nucleon center of mass energy of 2.76 TeV*, *JHEP* **07** (2011) 076 [[arXiv:1105.2438](#)] [[INSPIRE](#)].
- [90] J.-Y. Ollitrault, *Anisotropy as a signature of transverse collective flow*, *Phys. Rev. D* **46** (1992) 229 [[INSPIRE](#)].
- [91] S. Voloshin and Y. Zhang, *Flow study in relativistic nuclear collisions by Fourier expansion of Azimuthal particle distributions*, *Z. Phys. C* **70** (1996) 665 [[hep-ph/9407282](#)] [[INSPIRE](#)].
- [92] Y. Akiba et al., *The Hot QCD White Paper: Exploring the Phases of QCD at RHIC and the LHC*, [arXiv:1502.02730](#) [[INSPIRE](#)].
- [93] W. Li, *Observation of a ‘Ridge’ correlation structure in high multiplicity proton-proton collisions: A brief review*, *Mod. Phys. Lett. A* **27** (2012) 1230018 [[arXiv:1206.0148](#)] [[INSPIRE](#)].
- [94] K. Werner, I. Karpenko and T. Pierog, *The ‘Ridge’ in Proton-Proton Scattering at 7 TeV*, *Phys. Rev. Lett.* **106** (2011) 122004 [[arXiv:1011.0375](#)] [[INSPIRE](#)].
- [95] C. Bierlich, G. Gustafson and L. Lönnblad, *A shoving model for collectivity in hadronic collisions*, [arXiv:1612.05132](#) [[INSPIRE](#)].

Summary and Conclusions

The work of this thesis has been performed in the context of general-purpose Monte Carlo event generators, indispensable tools in high-energy collider physics. Their primary goal is to provide an as detailed and precise picture as possible of the complete final-state dynamics in collider events, which is crucial for the understanding of Standard Model as well as new physics processes. The contributions of the thesis span both the perturbative and the non-perturbative side of the event simulation.

In chap. 2 the theoretical background of the Standard Model has been reviewed with emphasis on Quantum Chromodynamics. The notion of the cross section has been introduced to calculate the probability for certain scattering processes to occur. The main features of Monte Carlo event generators have been discussed in chap. 3, with the main focus on parton showers and different matching and merging strategies. These topics, together with the concept of fragmentation, constitute the basis for the following chapters including published material.

In the first paper, presented in chap. 4, the VINCIA antenna shower for final-state radiation has been extended to emissions involving initial-state legs. The functions driving the radiation have been taken from a previous publication [158]. Phase-space convolutions and kinematic maps have been calculated for emissions off antennae, where either both partons are in the initial state or one parton is the initial and one in the final state. The parton-shower approximation is systematically improved by means of iterated matrix-element corrections, which had so far only applied to colourless resonance decays [80]. Some modifications and improvements with respect to [80] have been made, such as the handling of interference terms or making the shower history independent, which is important for maintaining a fast code. The implementation has been published with the release of VINCIA 2.001, making it the first publicly available antenna shower for initial-state radiation. Iterated matrix-element corrections have been applied to LHC processes for the first time.

The matrix-element corrections approach has been revised in chap. 5, such that the purely ordered evolution of the parton shower remains undistorted. This requires the development of a correction scheme for complex, evolution-induced phase spaces. Configurations beyond the reach of the parton shower are included with a systematic scale-setting procedure to supplement the parton-shower states.

The resulting algorithm does not depend on specific properties of the shower, allows arbitrary dead zones, and does not require a merging scale for unordered states. Comparisons to LHC data for the process $pp \rightarrow Z + \text{jets}$ have been presented and the new algorithm has been found to be in good agreement with the data. The new method has been implemented in the VINCIA framework and made public with the release of VINCIA 2.200.

The matrix-element evaluations required for correcting the parton shower constitute a fairly large amount of computing time when generating collider events. To increase the speed of the calculation, chap. 6 uses a helicity-dependent shower to assign explicit helicities to all partons in the event. Instead of summing over all possible helicity configurations, the matrix element has to be evaluated for only one constellation. For so-called maximally-helicity violation configurations, a dedicated set of amplitudes coded in VINCIA is applied. This allows a further, modest decrease of the evaluation time. The code has been made public with the release of VINCIA 2.200.

In chap. 7 a new model has been developed to take over parts of the Lund string fragmentation model. While in the conventional model the transverse momentum of hadrons is modelled flavour-independently according to a Gaussian distribution, the new model is based on an exponential suppression of the hadronic transverse mass. Therefore, heavier hadrons are naturally suppressed in rate with respect to lighter hadrons, but they obtain a higher average transverse momentum. To take the close-packing of strings into account, a simple model has been added, which generates the transverse momentum dependent on the environment, i.e. hadrons in events with large multiplicities obtain more transverse momentum. As a last addition a simple model for hadron rescattering has been implemented, where hadron pairs are allowed to scatter off each other dependent on their rapidity difference. The predictions have been tested and validated with toy model studies and by comparing to LHC data. The newly introduced parameters have been adjusted such that they result in an improved description of data. The study showed that the new models have the capability to describing some observables better, compared to the conventional model. However, given the reduced set of parameters, weaknesses in describing particle multiplicities exist. The methods and results have been published and the code has been made public with the release of PYTHIA 8.223.

Event generators are widely used as a research tool for exploring phenomenological aspects of and beyond the Standard Model. Processes involving quarks and gluons are ubiquitous in the high-energy particle collisions at current machines, as well as possible future colliders such as the Future Circular Collider at CERN. Matching the increasing precision of experimental measurements implies that generators have to model the effects of Quantum Chromodynamics both precisely and accu-

rately. This allows sophisticated predictions and comparisons to data, as required to extract conclusions from experimental measurements. Therefore, the development of improved parton-shower models and their combination with fixed-order matrix elements is crucial. As an example, the publication in chap. 5 nicely shows that observables such as the sum of scalar transverse momenta of jets or the leading jet transverse momentum are in need of a well-defined parton-shower + matrix-element scheme, as otherwise the data cannot be described properly.

As the quarks and gluons at the end of the parton shower provide the input for the fragmentation step, improved perturbative models also allow for clearer interpretations of non-perturbative phenomena. In addition, new or revised fragmentation models are clearly required as shown by recent measurements such as the enhanced production of strange and multi-strange hadrons in high-multiplicity events [159]. The development and testing of different models and their confrontation with data is a key aspect in investigating and understanding non-perturbative phenomena in leptonic, hadronic, as well as heavy-ion collisions.

A further application of event generators is the correction of data for detector effects. The generator output is passed through a detector simulation and the results are used to perform an unfolding of the data. Improved theoretical models allow to optimize the unfolding procedure and thereby decrease the systematic uncertainties of measurements.

With the Standard Model being firmly validated by current experiments, the primary goal of many particle physicists is to investigate what physics beyond the Standard Model may look like. In hadronic collider experiments, a potential new particle would most likely be produced in association with known particles. This is particularly pressing when considering the composite nature of the beam particles. A difficult task is therefore to distinguish such a signal event from much more frequent Standard-Model-like background events. Multijet events often represent the most difficult Standard Model background for new-physics searches at the LHC. Improvements in the reliability of event generators can help to better constrain the background, aiding new-physics searches at both current and future high-energy colliders. Better measurements at collider experiments can also help other fields of particle physics, e.g. the search for Dark Matters candidates, carried out through, for instance, gamma-ray observations and cosmic-ray measurements.

Possible Future Work

The development and improvement of event generators is an open-ended research field. Among the possible areas to improve is the development of a run-time interface to a matrix-element provider, which allows to matrix-element correct arbitrary processes up to arbitrary orders. Supplementing the shower with higher-order

corrections in VINCIA is so far limited to including leading-order matrix elements with different parton multiplicities. A general description for next-to-leading order matching and merging is required. Apart from improving the predictive power of VINCIA in that respect, further modifications to the shower itself would add to the value of the code. Those include the possibility of electroweak radiation as well as taking the quark masses in the shower into account, i.e. implementing massive radiation functions and a massive phase-space factorization for the initial state.

A lot of new and updated LHC measurements have become available during the last year. There are now several signals of collective flow in pp collisions, rather unexpected and in need of a deep understanding. Models exist that describe some of the effects, but not yet any consensus. The results of the PYTHIA fragmentation study showed that more work has to be done for a fully convincing description of LHC data. A microscopic tracing of the full space-time evolution of the event in PYTHIA, for partons and hadrons as well as for all production and decay vertices would provide the information for a more detailed understanding and modelling of the close-packing of strings and hadrons as well as the hadronic rescattering. This should lead to a more realistic picture of the soft structure of LHC events and therefore hopefully an improved description of data.

Bibliography

- [1] **ATLAS** Collaboration, G. Aad et al., *Observation of a new particle in the search for the Standard Model Higgs boson with the ATLAS detector at the LHC*, *Phys. Lett. B* **716** (2012) 1.
- [2] **CMS** Collaboration, S. Chatrchyan et al., *Observation of a new boson at a mass of 125 GeV with the CMS experiment at the LHC*, *Phys. Lett. B* **716** (2012) 30.
- [3] V. N. Gribov and L. N. Lipatov, *Deep inelastic $e p$ scattering in perturbation theory*, *Sov. J. Nucl. Phys.* **15** (1972) 438. [*Yad. Fiz.*15,781(1972)].
- [4] Y. L. Dokshitzer, *Calculation of the Structure Functions for Deep Inelastic Scattering and $e^+ e^-$ Annihilation by Perturbation Theory in Quantum Chromodynamics.*, *Sov. Phys. JETP* **46** (1977) 641. [*Zh. Eksp. Teor. Fiz.* 73, 1216 (1977)].
- [5] G. Altarelli and G. Parisi, *Asymptotic Freedom in Parton Language*, *Nucl. Phys. B* **126** (1977) 298.
- [6] G. Gustafson and U. Pettersson, *Dipole Formulation of QCD Cascades*, *Nucl. Phys. B* **306** (1988) 746.
- [7] Y. I. Azimov, Y. L. Dokshitzer, V. A. Khoze, and S. I. Troian, *The String Effect and QCD Coherence*, *Phys. Lett. B* **165** (1985) 150.
- [8] D. A. Kosower, *Antenna factorization of gauge theory amplitudes*, *Phys. Rev. D* **57** (1998) 5410.
- [9] A. Gehrmann-De Ridder, T. Gehrmann, and E. W. N. Glover, *Antenna subtraction at NNLO*, *JHEP* **09** (2005) 056.
- [10] S. Catani and M. H. Seymour, *The Dipole formalism for the calculation of QCD jet cross-sections at next-to-leading order*, *Phys. Lett. B* **378** (1996) 287.
- [11] S. Catani and M. H. Seymour, *A General algorithm for calculating jet cross-sections in NLO QCD*, *Nucl. Phys. B* **485** (1997) 291. [Erratum: *Nucl. Phys. B* 510, 503 (1998)].
- [12] B. Andersson, G. Gustafson, G. Ingelman, and T. Sjöstrand, *Parton Fragmentation and String Dynamics*, *Phys. Rept.* **97** (1983) 31.
- [13] T. Sjöstrand, *Jet Fragmentation of Nearby Partons*, *Nucl. Phys. B* **248** (1984) 469.
- [14] B. R. Webber, *A QCD Model for Jet Fragmentation Including Soft Gluon Interference*, *Nucl. Phys. B* **238** (1984) 492.
- [15] R. P. Feynman, R. B. Leighton, and M. Sands, *The Feynman Lectures on Physics*. 1963.
- [16] T. P. Cheng and L. F. Li, *Gauge Theory of Elementary Particle Physics*. 1984.
- [17] F. Mandl and G. Shaw, *Quantum Field Theory*. 1985.
- [18] M. E. Peskin and D. V. Schroeder, *An Introduction to Quantum Field Theory; 1995 ed.* Westview, Boulder, CO, 1995.
- [19] D. Griffiths, *Introduction to Elementary Particles*. John Wiley & Sons Inc, Hoboken, NJ, 1987.
- [20] D. J. Gross and F. Wilczek, *Ultraviolet Behavior of Nonabelian Gauge Theories*, *Phys. Rev. Lett.* **30** (1973) 1343.

- [21] H. D. Politzer, *Reliable Perturbative Results for Strong Interactions?*, *Phys. Rev. Lett.* **30** (1973) 1346.
- [22] W. E. Caswell, *Asymptotic Behavior of Nonabelian Gauge Theories to Two Loop Order*, *Phys. Rev. Lett.* **33** (1974) 244.
- [23] D. R. T. Jones, *Two Loop Diagrams in Yang-Mills Theory*, *Nucl. Phys. B* **75** (1974) 531.
- [24] W. A. Bardeen, A. J. Buras, D. W. Duke, and T. Muta, *Deep Inelastic Scattering Beyond the Leading Order in Asymptotically Free Gauge Theories*, *Phys. Rev. D* **18** (1978) 3998.
- [25] **Particle Data Group** Collaboration, C. Patrignani et al., *Review of Particle Physics*, *Chin. Phys. C* **40** (2016), no. 10 100001.
- [26] P. W. Higgs, *Broken Symmetries and the Masses of Gauge Bosons*, *Phys. Rev. Lett.* **13** (1964) 508.
- [27] F. Englert and R. Brout, *Broken Symmetry and the Mass of Gauge Vector Mesons*, *Phys. Rev. Lett.* **13** (1964) 321.
- [28] G. T. Bodwin, *Factorization of the Drell-Yan Cross-Section in Perturbation Theory*, *Phys. Rev. D* **31** (1985) 2616. [Erratum: *Phys. Rev. D* **34**, 3932 (1986)].
- [29] J. C. Collins, D. E. Soper, and G. F. Sterman, *Factorization for Short Distance Hadron - Hadron Scattering*, *Nucl. Phys.* **261** (1985) 104.
- [30] J. C. Collins, D. E. Soper, and G. F. Sterman, *Soft Gluons and Factorization*, *Nucl. Phys. B* **308** (1988) 833.
- [31] J. C. Collins, D. E. Soper, and G. F. Sterman, *All Order Factorization for Drell-Yan Cross-sections*, *Phys. Lett. B* **134** (1984) 263.
- [32] J. C. Collins and G. F. Sterman, *Soft Partons in QCD*, *Nucl. Phys. B* **185** (1981) 172.
- [33] T. Kinoshita, *Mass singularities of Feynman amplitudes*, *J. Math. Phys.* **3** (1962) 650–677.
- [34] T. D. Lee and M. Nauenberg, *Degenerate Systems and Mass Singularities*, *Phys. Rev.* **133** (1964) B1549. [25(1964)].
- [35] E. C. Poggio and H. R. Quinn, *The Infrared Behavior of Zero-Mass Green's Functions and the Absence of Quark Confinement in Perturbation Theory*, *Phys. Rev. D* **14** (1976) 578.
- [36] G. F. Sterman, *Kinoshita's Theorem in Yang-Mills Theories*, *Phys. Rev. D* **14** (1976) 2123.
- [37] S. Weinberg, *Feynman Rules for Any Spin*, *Phys. Rev.* **133** (1964) B1318–B1332.
- [38] C. W. Bernard, *Feynman Rules for Gauge Theories at Finite Temperature*, *Phys. Rev. D* **9** (1974) 3312.
- [39] F. Maltoni and T. Stelzer, *MadEvent: Automatic event generation with MadGraph*, *JHEP* **0302** (2003) 027.
- [40] T. Sjöstrand, S. Mrenna, and P. Skands, *A Brief Introduction to PYTHIA 8.1*, *Comput. Phys. Commun.* **178** (2008) 852.
- [41] T. Sjöstrand, S. Ask, J. R. Christiansen, R. Corke, N. Desai, P. Ilten, S. Mrenna, S. Prestel, C. O. Rasmussen, and P. Z. Skands, *An Introduction to PYTHIA 8.2*, *Comput. Phys. Commun.* **191** (2015) 159.
- [42] M. Bähr, S. Gieseke, M. Gigg, D. Grellscheid, K. Hamilton, et al., *Herwig++ Physics and Manual*, *Eur. Phys. J. C* **58** (2008) 639.
- [43] T. Gleisberg, S. Höche, F. Krauss, M. Schönherr, S. Schumann, et al., *Event generation with SHERPA 1.1*, *JHEP* **0902** (2009) 007.
- [44] T. Gleisberg and S. Hoeche, *Comix, a new matrix element generator*, *JHEP* **12** (2008) 039.
- [45] K. Arnold, M. Bähr, G. Bozzi, F. Campanario, C. Englert, et al., *VBFNLO: A Parton level Monte Carlo for processes with electroweak bosons*, *Comput. Phys. Commun.* **180** (2009) 1661.

- [46] J. M. Campbell and R. K. Ellis, *An Update on vector boson pair production at hadron colliders*, *Phys. Rev. D* **60** (1999) 113006.
- [47] J. M. Campbell, R. K. Ellis, and C. Williams, *Vector boson pair production at the LHC*, *JHEP* **07** (2011) 018.
- [48] E. Boos, M. Dobbs, W. Giele, I. Hinchliffe, J. Huston, et al., *Generic user process interface for event generators*, [arXiv:hep-ph/0109068](https://arxiv.org/abs/hep-ph/0109068).
- [49] J. Alwall, A. Ballestrero, P. Bartalini, S. Belov, E. Boos, et al., *A Standard format for Les Houches event files*, *Comput. Phys. Commun.* **176** (2007) 300.
- [50] S. Plätzer and S. Gieseke, *Dipole Showers and Automated NLO Matching in Herwig++*, *Eur. Phys. J. C* **72** (2012) 2187.
- [51] **ATLAS** Collaboration, G. Aad et al., *Study of Jet Shapes in Inclusive Jet Production in pp Collisions at $\sqrt{s} = 7$ TeV using the ATLAS Detector*, *Phys. Rev. D* **83** (2011) 052003.
- [52] **CMS** Collaboration, V. Khachatryan et al., *First Measurement of Hadronic Event Shapes in pp Collisions at $\sqrt{s} = 7$ TeV*, *Phys. Lett. B* **699** (2011) 48.
- [53] **ATLAS** Collaboration, G. Aad et al., *Measurement of underlying event characteristics using charged particles in pp collisions at $\sqrt{s} = 900$ GeV and 7 TeV with the ATLAS detector*, *Phys. Rev. D* **83** (2011) 112001.
- [54] **CMS** Collaboration, S. Chatrchyan et al., *Measurement of the Underlying Event Activity at the LHC with $\sqrt{s} = 7$ TeV and Comparison with $\sqrt{s} = 0.9$ TeV*, *JHEP* **09** (2011) 109.
- [55] R. K. Ellis, W. J. Stirling, and B. R. Webber, *QCD and collider physics*, *Camb. Monogr. Part. Phys. Nucl. Phys. Cosmol.* **8** (1996).
- [56] S. Catani and M. Grazzini, *Infrared factorization of tree level QCD amplitudes at the next-to-next-to-leading order and beyond*, *Nucl. Phys. B* **570** (2000) 287.
- [57] Z. Bern, V. Del Duca, W. B. Kilgore, and C. R. Schmidt, *The infrared behavior of one loop QCD amplitudes at next-to-next-to leading order*, *Phys. Rev. D* **60** (1999) 116001.
- [58] R. D. Field, *Applications in Perturbative QCD*. Addison-Wesley Publishing Company, Inc., Boston, MA, 1989.
- [59] S. Höche, *Introduction to parton-shower event generators*, in *TASI 2014, Boulder, Colorado, 2014*.
- [60] T. Sjöstrand, *A Model for Initial State Parton Showers*, *Phys. Lett. B* **157** (1985) 321.
- [61] G. Dissertori, I. G. Knowles, and M. Schmelling, *Quantum chromodynamics: high energy experiments and theory*. International series of monographs on physics. Oxford Univ. Press, Oxford, 2002.
- [62] Y. L. Dokshitzer, V. S. Fadin, and V. A. Khoze, *Coherent Effects in the Perturbative QCD Parton Jets*, *Phys. Lett. B* **115** (1982) 242.
- [63] B. Andersson, G. Gustafson, L. Lonnblad, and U. Petterson, *Coherence Effects in Deep Inelastic Scattering*, *Z. Phys. C* **43** (1989) 625.
- [64] S. Catani, F. Fiorani, and G. Marchesini, *QCD Coherence in Initial State Radiation*, *Phys. Lett. B* **234** (1990) 339.
- [65] G. Marchesini and B. R. Webber, *Simulation of QCD Jets Including Soft Gluon Interference*, *Nucl. Phys. B* **238** (1984) 1.
- [66] M. Bengtsson and T. Sjöstrand, *A Comparative Study of Coherent and Noncoherent Parton Shower Evolution*, *Nucl. Phys. B* **289** (1987) 810.
- [67] L. Lönnblad, *ARIADNE version 4: A Program for simulation of QCD cascades implementing the color dipole model*, *Comput. Phys. Commun.* **71** (1992) 15.

- [68] W. T. Giele, D. A. Kosower, and P. Z. Skands, *A simple shower and matching algorithm*, *Phys. Rev. D* **78** (2008) 014026.
- [69] S. Schumann and F. Krauss, *A Parton shower algorithm based on Catani-Seymour dipole factorisation*, *JHEP* **03** (2008) 038.
- [70] S. Plätzer and S. Gieseke, *Coherent Parton Showers with Local Recoils*, *JHEP* **01** (2011) 024.
- [71] S. Höche and S. Prestel, *The midpoint between dipole and parton showers*, *Eur. Phys. J. C* **75** (2015), no. 9 461.
- [72] M. H. Seymour, *A Simple prescription for first order corrections to quark scattering and annihilation processes*, *Nucl. Phys. B* **436** (1995) 443.
- [73] M. H. Seymour, *Matrix element corrections to parton shower algorithms*, *Comput. Phys. Commun.* **90** (1995) 95.
- [74] S. Catani, F. Krauss, R. Kuhn, and B. R. Webber, *QCD matrix elements + parton showers*, *JHEP* **11** (2001) 063.
- [75] L. Lönnblad, *Correcting the color dipole cascade model with fixed order matrix elements*, *JHEP* **05** (2002) 046.
- [76] N. Lavesson and L. Lönnblad, *W+jets matrix elements and the dipole cascade*, *JHEP* **07** (2005) 054.
- [77] M. L. Mangano, M. Moretti, F. Piccinini, and M. Treccani, *Matching matrix elements and shower evolution for top-quark production in hadronic collisions*, *JHEP* **01** (2007) 013.
- [78] S. Mrenna and P. Richardson, *Matching matrix elements and parton showers with HERWIG and PYTHIA*, *JHEP* **05** (2004) 040.
- [79] M. Bengtsson and T. Sjöstrand, *Coherent Parton Showers Versus Matrix Elements: Implications of PETRA - PEP Data*, *Phys. Lett. B* **185** (1987) 435.
- [80] W. T. Giele, D. A. Kosower, and P. Z. Skands, *Higher-Order Corrections to Timelike Jets*, *Phys. Rev. D* **84** (2011) 054003.
- [81] S. Frixione and B. R. Webber, *Matching NLO QCD computations and parton showers simulations*, *JHEP* **0206** (2002) 029.
- [82] S. Frixione, F. Stoeckli, P. Torrielli, B. R. Webber, and C. D. White, *The MC@NLO 4.0 Event Generator*, [arXiv:1010.0819](https://arxiv.org/abs/1010.0819).
- [83] P. Nason, *A New method for combining NLO QCD with shower Monte Carlo algorithms*, *JHEP* **11** (2004) 040.
- [84] K. Hamilton, P. Nason, C. Oleari, and G. Zanderighi, *Merging H/W/Z + 0 and 1 jet at NLO with no merging scale: a path to parton shower + NNLO matching*, *JHEP* **05** (2013) 082.
- [85] L. Lönnblad and S. Prestel, *Merging Multi-leg NLO Matrix Elements with Parton Showers*, *JHEP* **03** (2013) 166.
- [86] R. Frederix and K. Hamilton, *Extending the MINLO method*, *JHEP* **05** (2016) 042.
- [87] S. Alioli, C. W. Bauer, C. Berggren, F. J. Tackmann, J. R. Walsh, and S. Zuberi, *Matching Fully Differential NNLO Calculations and Parton Showers*, *JHEP* **06** (2014) 089.
- [88] K. Hamilton, P. Nason, E. Re, and G. Zanderighi, *NNLOPS simulation of Higgs boson production*, *JHEP* **10** (2013) 222.
- [89] S. Höche, Y. Li, and S. Prestel, *Drell-Yan lepton pair production at NNLO QCD with parton showers*, *Phys. Rev. D* **91** (2015), no. 7 074015.
- [90] S. Höche, Y. Li, and S. Prestel, *Higgs-boson production through gluon fusion at NNLO QCD with parton showers*, *Phys. Rev. D* **90** (2014), no. 5 054011.

- [91] R. D. Field and R. P. Feynman, *Quark Elastic Scattering as a Source of High Transverse Momentum Mesons*, *Phys. Rev. D* **15** (1977) 2590.
- [92] R. D. Field and R. P. Feynman, *A Parametrization of the Properties of Quark Jets*, *Nucl. Phys. B* **136** (1978) 1.
- [93] X. Artru and G. Mennessier, *String model and multiproduction*, *Nucl. Phys. B* **70** (1974) 93.
- [94] L. Susskind, *Lattice Models of Quark Confinement at High Temperature*, *Phys. Rev. D* **20** (1979) 2610–2618.
- [95] K. D. Born, E. Laermann, R. Sommer, P. M. Zerwas, and T. F. Walsh, *The Interquark potential: A QCD lattice analysis*, *Phys. Lett. B* **329** (1994) 325–331.
- [96] Y. Koma and M. Koma, *Precise determination of the three-quark potential in SU(3) lattice gauge theory*, *Phys. Rev. D* **95** (2017), no. 9 094513.
- [97] N. Isgur and J. E. Paton, *A Flux Tube Model for Hadrons*, *Phys. Lett. B* **124** (1983) 247.
- [98] N. Isgur and J. E. Paton, *A Flux Tube Model for Hadrons in QCD*, *Phys. Rev. D* **31** (1985) 2910.
- [99] A. Di Giacomo, M. Maggiore, and S. Olejnik, *Evidence for Flux Tubes From Cooled QCD Configurations*, *Phys. Lett. B* **236** (1990) 199–202.
- [100] A. Di Giacomo, M. Maggiore, and S. Olejnik, *Confinement and Chromoelectric Flux Tubes in Lattice QCD*, *Nucl. Phys. B* **347** (1990) 441.
- [101] G. S. Bali, K. Schilling, and C. Schlichter, *Observing long color flux tubes in SU(2) lattice gauge theory*, *Phys. Rev. D* **51** (1995) 5165–5198.
- [102] F. E. Close and P. R. Page, *The Production and decay of hybrid mesons by flux tube breaking*, *Nucl. Phys. B* **443** (1995) 233.
- [103] **TkL, TXL** Collaboration, G. S. Bali et al., *Glueballs and string breaking from full QCD*, *Nucl. Phys. Proc. Suppl.* **63** (1998) 209.
- [104] C. E. Detar, O. Kaczmarek, F. Karsch, and E. Laermann, *String breaking in lattice quantum chromodynamics*, *Phys. Rev. D* **59** (1999) 031501.
- [105] F. D. R. Bonnet, D. B. Leinweber, A. G. Williams, and J. M. Zanotti, *Towards string breaking in the static quark potential*, [arXiv:hep-lat/9912044](https://arxiv.org/abs/hep-lat/9912044).
- [106] B. Bolder, T. Struckmann, G. S. Bali, N. Eicker, T. Lippert, B. Orth, K. Schilling, and P. Ueberholz, *A High precision study of the Q anti-Q potential from Wilson loops in the regime of string breaking*, *Phys. Rev. D* **63** (2001) 074504.
- [107] A. Duncan, E. Eichten, and H. Thacker, *String breaking in four-dimensional lattice QCD*, *Phys. Rev. D* **63** (2001) 111501.
- [108] **UKQCD** Collaboration, P. Pennanen and C. Michael, *String breaking in zero temperature lattice QCD*, [arXiv:hep-lat/0001015](https://arxiv.org/abs/hep-lat/0001015).
- [109] C. W. Bernard, T. A. DeGrand, C. E. Detar, P. Lacock, S. A. Gottlieb, U. M. Heller, J. Hetrick, K. Orginos, D. Toussaint, and R. L. Sugar, *Zero temperature string breaking in lattice quantum chromodynamics*, *Phys. Rev. D* **64** (2001) 074509.
- [110] **SESAM** Collaboration, G. S. Bali, H. Neff, T. Duessel, T. Lippert, and K. Schilling, *Observation of string breaking in QCD*, *Phys. Rev. D* **71** (2005) 114513.
- [111] D. Amati and G. Veneziano, *Preconfinement as a Property of Perturbative QCD*, *Phys. Lett. B* **83** (1979) 87.
- [112] S. Frixione, P. Nason, and C. Oleari, *Matching NLO QCD computations with Parton Shower simulations: the POWHEG method*, *JHEP* **11** (2007) 070.
- [113] S. Frixione, F. Stoeckli, P. Torrielli, and B. R. Webber, *NLO QCD corrections in Herwig++ with MC@NLO*, *JHEP* **1101** (2011) 053.

- [114] P. Torrielli and S. Frixione, *Matching NLO QCD computations with PYTHIA using MC@NLO*, *JHEP* **04** (2010) 110.
- [115] S. Alioli, P. Nason, C. Oleari, and E. Re, *A general framework for implementing NLO calculations in shower Monte Carlo programs: the POWHEG BOX*, *JHEP* **06** (2010) 043.
- [116] S. Höche, F. Krauss, M. Schonherr, and F. Siegert, *Automating the POWHEG method in Sherpa*, *JHEP* **04** (2011) 024.
- [117] J. Alwall, R. Frederix, S. Frixione, V. Hirschi, F. Maltoni, O. Mattelaer, H. S. Shao, T. Stelzer, P. Torrielli, and M. Zaro, *The automated computation of tree-level and next-to-leading order differential cross sections, and their matching to parton shower simulations*, *JHEP* **07** (2014) 079.
- [118] M. L. Mangano, M. Moretti, and R. Pittau, *Multijet matrix elements and shower evolution in hadronic collisions: $Wb\bar{b} + n$ jets as a case study*, *Nucl. Phys. B* **632** (2002) 343.
- [119] J. Alwall et al., *Comparative study of various algorithms for the merging of parton showers and matrix elements in hadronic collisions*, *Eur. Phys. J. C* **53** (2008) 473.
- [120] N. Lavesson and L. Lonnblad, *Merging parton showers and matrix elements: Back to basics*, *JHEP* **04** (2008) 085.
- [121] K. Hamilton, P. Richardson, and J. Tully, *A Modified CKKW matrix element merging approach to angular-ordered parton showers*, *JHEP* **11** (2009) 038.
- [122] K. Hamilton and P. Nason, *Improving NLO-parton shower matched simulations with higher order matrix elements*, *JHEP* **06** (2010) 039.
- [123] S. Höche, F. Krauss, M. Schonherr, and F. Siegert, *NLO matrix elements and truncated showers*, *JHEP* **08** (2011) 123.
- [124] L. Lonnblad and S. Prestel, *Unitarising Matrix Element + Parton Shower merging*, *JHEP* **02** (2013) 094.
- [125] S. Plätzer, *Controlling inclusive cross sections in parton shower + matrix element merging*, *JHEP* **08** (2013) 114.
- [126] N. Lavesson and L. Lonnblad, *Extending CKKW-merging to One-Loop Matrix Elements*, *JHEP* **12** (2008) 070.
- [127] T. Gehrmann, S. Höche, F. Krauss, M. Schonherr, and F. Siegert, *NLO QCD matrix elements + parton showers in $e^+e^- \rightarrow$ hadrons*, *JHEP* **01** (2013) 144.
- [128] S. Höche, F. Krauss, M. Schonherr, and F. Siegert, *QCD matrix elements + parton showers: The NLO case*, *JHEP* **04** (2013) 027.
- [129] S. Alioli, C. W. Bauer, C. J. Berggren, A. Hornig, F. J. Tackmann, C. K. Vermilion, J. R. Walsh, and S. Zuberi, *Combining Higher-Order Resummation with Multiple NLO Calculations and Parton Showers in GENEVA*, *JHEP* **09** (2013) 120.
- [130] R. Frederix and S. Frixione, *Merging meets matching in MC@NLO*, *JHEP* **12** (2012) 061.
- [131] M. Dinsdale, M. Ternick, and S. Weinzierl, *Parton showers from the dipole formalism*, *Phys. Rev. D* **76** (2007) 094003.
- [132] Z. Nagy and D. E. Soper, *A parton shower based on factorization of the quantum density matrix*, *JHEP* **06** (2014) 097.
- [133] G. Marchesini and B. R. Webber, *Monte Carlo Simulation of General Hard Processes with Coherent QCD Radiation*, *Nucl. Phys. B* **310** (1988) 461.
- [134] S. Gieseke, P. Stephens, and B. Webber, *New formalism for QCD parton showers*, *JHEP* **12** (2003) 045.
- [135] T. Sjöstrand and P. Z. Skands, *Transverse-momentum-ordered showers and interleaved multiple interactions*, *Eur. Phys. J. C* **39** (2005) 129.

- [136] R. Kuhn, F. Krauss, B. Ivanyi, and G. Soff, *APACIC++: A Parton Cascade In C++, version 1.0*, *Comput. Phys. Commun.* **134** (2001) 223.
- [137] F. Krauss, A. Schaliche, and G. Soff, *APACIC++ 2.0: A Parton cascade in C++*, *Comput. Phys. Commun.* **174** (2006) 876.
- [138] T. Sjöstrand, S. Mrenna, and P. Z. Skands, *PYTHIA 6.4 Physics and Manual*, *JHEP* **05** (2006) 026.
- [139] *Mathematica 11.0*. Wolfram Research, Inc., Champaign, Illinois, 2016.
- [140] J. C. Collins, D. E. Soper, and G. F. Sterman, *Transverse Momentum Distribution in Drell-Yan Pair and W and Z Boson Production*, *Nucl. Phys. B* **250** (1985) 199.
- [141] J. C. Collins, D. E. Soper, and G. F. Sterman, *Factorization of Hard Processes in QCD*, *Adv. Ser. Direct. High Energy Phys.* **5** (1989) 1.
- [142] P. M. Nadolsky, D. R. Stump, and C. P. Yuan, *Semiinclusive hadron production at HERA: The Effect of QCD gluon resummation*, *Phys. Rev. D* **61** (2000) 014003. [Erratum: *Phys. Rev. D* **64**, 059903 (2001)].
- [143] G. F. Sterman, *Some Basic Concepts of Perturbative QCD*, *Acta Phys. Polon. B* **39** (2008) 2151.
- [144] J. R. Christiansen and S. Prestel, *Merging weak and QCD showers with matrix elements*, *Eur. Phys. J. C* **76** (2016), no. 1 39.
- [145] A. Schaliche and F. Krauss, *Implementing the ME+PS merging algorithm*, *JHEP* **07** (2005) 018.
- [146] G. Sterman, *An Introduction to Quantum Field Theory*. Cambridge Univ. Press, Cambridge, 1993.
- [147] A. J. Larkoski, J. J. Lopez-Villarejo, and P. Skands, *Helicity-Dependent Showers and Matching with VINCIA*, *Phys. Rev. D* **87** (2013), no. 5 054033.
- [148] M. Gyulassy and L. McLerran, *New forms of QCD matter discovered at RHIC*, *Nucl. Phys. A* **750** (2005) 30.
- [149] U. Heinz and R. Snellings, *Collective flow and viscosity in relativistic heavy-ion collisions*, *Ann. Rev. Nucl. Part. Sci.* **63** (2013) 123.
- [150] G. Roland, K. Safarik, and P. Steinberg, *Heavy-ion collisions at the LHC*, *Prog. Part. Nucl. Phys.* **77** (2014) 70.
- [151] CMS Collaboration, V. Khachatryan et al., *Observation of Long-Range Near-Side Angular Correlations in Proton-Proton Collisions at the LHC*, *JHEP* **09** (2010) 091.
- [152] ATLAS Collaboration, G. Aad et al., *Observation of Long-Range Elliptic Azimuthal Anisotropies in $\sqrt{s} = 13$ and 2.76 TeV pp Collisions with the ATLAS Detector*, *Phys. Rev. Lett.* **116** (2016), no. 17 172301.
- [153] CMS Collaboration, V. Khachatryan et al., *Evidence for collectivity in pp collisions at the LHC*, *Phys. Lett. B* **765** (2017) 193.
- [154] C. Bierlich, G. Gustafson, L. Lönnblad, and A. Tarasov, *Effects of Overlapping Strings in pp Collisions*, *JHEP* **03** (2015) 148.
- [155] C. Bierlich, G. Gustafson, and L. Lönnblad, *A shoving model for collectivity in hadronic collisions*, [arXiv:1612.05132](https://arxiv.org/abs/1612.05132).
- [156] T. Pierog, I. Karpenko, J. M. Katzy, E. Yatsenko, and K. Werner, *EPOS LHC: Test of collective hadronization with data measured at the CERN Large Hadron Collider*, *Phys. Rev. C* **92** (2015), no. 3 034906.
- [157] J. L. Nagle, R. Belmont, K. Hill, J. Orjuela Koop, D. V. Perepelitsa, P. Yin, Z.-W. Lin, and D. McGlinchey, *Are minimal conditions for collectivity met in e^+e^- collisions?*, [arXiv:1707.02307](https://arxiv.org/abs/1707.02307).

- [158] M. Ritzmann, D. A. Kosower, and P. Skands, *Antenna Showers with Hadronic Initial States*, *Phys. Lett. B* **718** (2013) 1345.
- [159] **ALICE** Collaboration, J. Adam et al., *Enhanced production of multi-strange hadrons in high-multiplicity proton-proton collisions*, *Nature Phys.* **13** (2017) 535.